SUM FREQUENCY MIXING AND QUANTUM INTERFERENCE IN THREE-LEVEL ATOMS

Richard R. Moseley

A Thesis Submitted for the Degree of PhD
at the
University of St Andrews

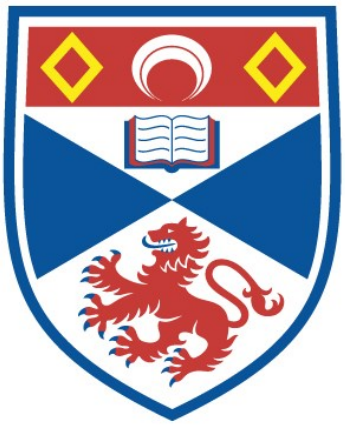

1995

Sum Frequency Mixing and Quantum Interference in Three-Level Atoms

A thesis presented by

Richard R. Moseley, B.Sc

to the

University of St. Andrews

in application for the degree of

Doctor of Philosophy

September 1994

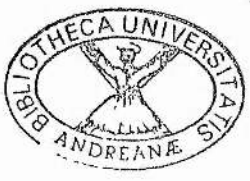

ProQuest LLC.
789 East Eisenhower Parkway
P.O. Box 1346
Ann Arbor, MI 48106 – 1346

Declarations

I, Richard Robert Moseley, hereby certify that this thesis has been composed by myself, that it is a record of my own work, and that it has not been accepted in partial or complete fulfillment of any other degree or professional qualification. I was admitted to the Faculty of Science of the University of St. Andrews under Ordinance General No. 12 in October 1991 and as a candidate for the degree of Ph.D. in October 1992.

Richard R. Moseley
September 1994

I hereby certify that the candidate has fulfilled the conditions of the Resolution and Regulations appropriate to the Degree of Ph.D.

Malcolm H. Dunn
September 1994

In submitting this thesis to the University of St. Andrews I understand that I am giving permission for it to be made available for use in accordance with the regulations of the University Library for the time being in force, subject to any copyright vested in the work not being affected thereby. I also understand that the title and abstract will be published, and that a copy of the work may be made and supplied to any *bona fide* library or research worker.

Abstract

This work contains theoretical and experimental studies of the properties of three-level atoms subjected to two single-frequency, continuous-wave laser sources with special emphasis on magnetic-field-induced sum frequency mixing (SFM) and electromagnetically-induced transparency (EIT).

In sodium vapour, two resonant-enhancement routes for SFM were experimentally studied. In one route (3S–3P–3D) the output is generated on a quadrupole-allowed transition and on the other (3S–3P–4P), a dipole-allowed transition. Phase matching conditions are studied in detail. On the second route, the two contributions to the phase mismatch can combine to heavily distort the spectroscopic lineshapes observed.

Doubly-resonant SFM is considered and two paths for excitation of the output coherence are identified. Control of their relative strength, via the input laser strengths, is predicted, as well as interference between them. These are both experimentally observed on the $3S_{1/2}$–$3P_{1/2}$– $3D_{3/2}$ transition scheme in sodium.

Theory is presented to show how the use of a strong upper laser in resonant SFM can, by EIT, greatly reduce the absorption on the lower transition without similarly reducing the nonlinear process. A significant increase in conversion efficiency is predicted.

Theory is also presented on the inclusion of the local field correction, which is relevant for high vapour densities, in the Bloch equations for the three-level atom. Nonlinear coherence cross-coupling terms arise and the generalised equations are then used for two case studies; one concerning EIT, the other SFM.

EIT is experimentally studied using continuous-wave lasers in rubidium vapour. Focusing and de-focusing were observed on the probe laser beam as it tunes through the transparency window at close, but separate, detunings. This is attributed to the radial intensity profile of the coupling laser which imposes a spatial refractive index modulation on the medium at the probe laser wavelength.

Dad

for his love, enthusiasm and interest,

and for *the chance...*

Acknowledgements

I wish to gratefully thank my supervisors, Prof. Malcolm Dunn and Dr. Bruce Sinclair, for their guidance, suggestions, patience and physical insight displayed during the course of this work. I owe a large debt of gratitude to Dr. Sara Shepherd for her ideas, our frequent discussions and tuition in the art of tweaking. I would also acknowledge useful discussions and encouragement from Dr. Christoph Keitel regarding the work on EIT in this thesis. I would like to thank the Department of Physics and Astronomy for its technical backup and assistance, especially Les and Derek for the loan of equipment.

I wish to extend my gratitude to The Carnegie Trust for the Universities of Scotland who provided my scholarship to carry out this work.

Moreover, I thank all the students and postdocs in the department for their help and good humour (plus a good few bits of borrowed equipment!) during this time, but especially: Sara, David, Gordon and Neil. Finally, I wish to thank my family and Kay for their encouragement, support and love, and particularly, Dick for the PC.

Table of Contents

Chapter 1

Introduction

1. INTRODUCTION

1.1. Background

The work presented in this thesis concerns the interaction of light with the atoms in a gas. It is by no means the first work in this area.

The modern view of this field was born when Fraunhofer discovered, experimentally, that the spectrum of light emitted by the sun contained numerous, narrow well-defined dark bands. Later work showed that each line was unique to an element and that a study of the wavelength of these spectral features, whether in light emitted from a sample, or from incident light absorbed within a sample, could be used to determine the composition of the sample. Furthermore, it could tell a great deal about the atom itself. Nowadays this form of study is called spectroscopy and it has a variety of applications in all physical sciences. This thesis is concerned with furthering the understanding of how atoms react to strong, coherent, narrow-bandwidth optical radiation when applied at two separate wavelengths simultaneously. It is, therefore, spectroscopy but also falls into the more precise classification of non-linear optics.

In 1917 Einstein postulated basic principles for the interaction of radiation with the discrete energy levels in atoms [1]. These principles were basically incoherent in nature and involved the rate of transfer of population between the energy levels, whether spontaneous or stimulated. These rules underpinned the later development of the laser in 1960, the use of which has opened a new chapter in the interaction of light with atomic systems. Laser radiation is characterised by its excellent coher-

ence, high intensity and narrow bandwidth and, when subjected to such radiation, atoms react in ways that cannot always be explained under a rate equation analysis. Coherent excitation [1], as this regime is called, leads to a variety of phenomena, such as the Rabi flopping of populations [2] and Autler-Townes splitting [3] (also called the ac Stark effect). Its hallmark is that the atomic wavefunction that is produced can hold a definite phase relationship to the oscillating fields of the incident electromagnetic wave. We say that the atom has "coherences" induced between the wavefunctions of its discrete levels. This is possible only when the incident light is both coherent and monochromatic.

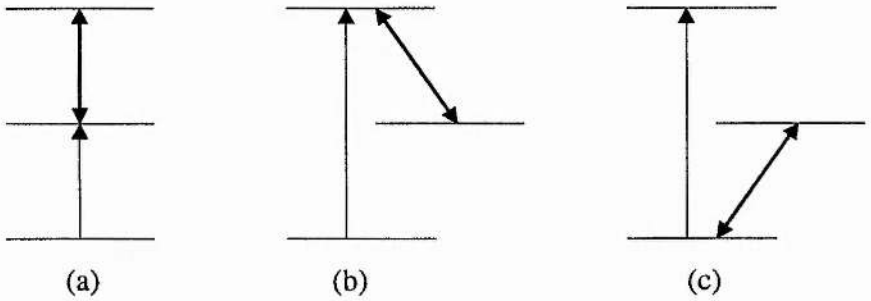

Figure 1.1: Three possible three-level atom configurations: (a) cascade, (b) lambda (Λ) and (c) vee (V). The arrows denote near-resonant fields incident on dipole-allowed transitions. The third, unprobed, transition in each configuration is assumed to be dipole forbidden.

The conceptual framework for analytical study in this area is usually a simplified atom of generally two or three isolated energy levels, basically a sub-set of a real atomic system. The three-level atom can come in three configurations: the cascade, lambda (Λ) or vee (V) as shown in figure 1.1. This work looks at three-level atoms, both theoretically and experimentally, in which both transitions are excited by coherent, near-resonant laser sources. The way that the cascade system can produce a higher frequency of light by combing the two input waves in a sum frequency mixing process is looked at in detail. Also, how the atom responds to input light on one

transition, while suffering strong perturbation on the other transition is studied in regard to interference between the two coherent excitation processes.

1.2. Non-Linear Optics

When light impinges on a medium a polarisation is set up within the atoms of that medium. Usually the light intensity is low enough that a linear relation between the polarisation induced in the medium, P, and the electric field of the light, E, is an accurate description:

$$P = \epsilon_0 \chi^{(1)} E \tag{1.1}$$

The constant, $\chi^{(1)}$, is termed the linear susceptibility of the medium and depends strongly on the medium and the wavelength of the light. However, if the incident light is particularly intense, and a laser output often is, this linear relation breaks down and we must express the polarisation as a power series containing higher-order terms:

$$P = \epsilon_0 \chi^{(1)} E + \epsilon_0 \chi^{(2)} E^2 + \epsilon_0 \chi^{(3)} E^3 \ldots \tag{1.2}$$

The study of the effects of these higher-order terms is called non-linear optics and is motivated by a number of scientific and commercial objectives. Among the most important consequence of the $\chi^{(2)}$ term, the second-order nonlinear susceptibility, is the ability of the medium to generate new frequencies of light [4] by: doubling the input frequency (second harmonic generation); subdiving the input frequency into two additive parts (parametric oscillation); or combing two separate input waves to produce a sum or difference frequency. Similarly, the third-order susceptibility, $\chi^{(3)}$, can lead to the generation of new frequencies of light — among other applications [5].

1.2.1. Second-Order Wave Mixing in Vapours

The principle application of second-order nonlinear processes is the generation of laser-like light at frequencies where no convenient laser source exists. A simple

symmetry argument [6] shows that a centrosymmetric medium, of either a gas or appropriate crystal structure, cannot mediate a second-order process, and for such media $\chi^{(2)} = 0$. Therefore, it is usual to use an appropriate non-centrosymmetric crystal with a large second-order nonlinear coefficient for such experiments. However, despite the intrinsic symmetry of an atomic vapour, second-order nonlinear processes can be observed in them if the vapour symmetry is broken by some external means. While vapours have lower conversion efficiencies than crystals in general, with tighter tuning restrictions and being bulky in physical dimensions (generally requiring vacuum equipment), they do have some advantages. Principally, they allow generation in the ultra-violet, vacuum-ultra-violet and X-ray regions of the spectra, below the absorption cut-off point in nonlinear crystals around 200nm. Furthermore, they are able to withstand very high input intensities that would damage conventional crystals and are scalable to large physical dimensions. For these reasons vapours have become widely established for third-order wave mixing processes [5, 7], but second-order processes can be as efficient [8] and have been the subject of detailed research (see Sinclair [9] for a review). The required symmetry breaking can be obtained by a variety of means including: transverse magnetic or electric fields; high intensity focused laser pulses; or non-collinear beam geometries.

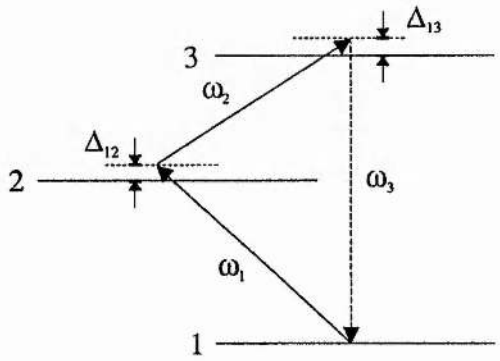

Figure 1.2: A generic atomic level scheme for sum frequency mixing

In order to realise a useful conversion efficiency, the input wavelengths in a

gaseous wave mixing process must be tuned close to resonant transitions, as in figure 1.2. This is highlighted by the simplified equation for the second-order susceptibility in a gas [8, 9, 10]:

$$\chi^{(2)} \propto \frac{\mu_{12}\mu_{23}\mu_{13}}{(\Delta_{12} - i\gamma_{12})(\Delta_{13} - i\gamma_{13})} \tag{1.3}$$

wherein μ_{ij} are the transition matrix elements, Δ_{ij} the detunings, and γ_{ij} the decay rates. For the sum frequency mixing (SFM) process shown in figure 1.2 the conversion efficiency is increased by several orders of magnitude when either Δ_{12} or Δ_{13} are near zero, ie. when either single-photon or two-photon resonance conditions are satisfied. Also evident from this expression is the role of the transition matrix elements. The product of these must be as high as possible for efficient conversion. Unfortunately, selection rules require that in a closed three-level atomic system one of these transitions cannot be dipole-allowed. However, use of a quadrupole-allowed transition can still lead to efficient conversion [8, 11].

This work seeks to extend earlier studies of magnetic-field-induced second harmonic generation and sum frequency mixing using continuous-wave (cw) lasers [9, 10, 12, 13, 14, 15, 16]. The use of cw lasers allowed a detailed, high-resolution comparison between the observed and calculated lineshapes for the output. By using two independent dye laser sources, Poustie [10] demonstrated a very high nonlinearity, rivaling that of a crystal, by tuning separate lasers on to resonance with the 3S–3P and 3P–4D transitions in sodium. This work uses the 3S–3P and 3P–3D transitions, as they have stronger matrix elements, and attains even higher conversion efficiencies. The ability to probe this system stems from the development of a titanium sapphire laser source [12] which is capable of producing the appropriate wavelength for the 3P–3D transition, 819nm. Furthermore, this laser allowed a comparison of two contrasting transition schemes for near-resonant SFM, differing in the placing of the quadrupole transition: 3S–3P–3D and 3S–3P–4P. This study highlights the role of phase matching in such processes and shows that lineshapes may be radically altered by this under appropriate conditions. It also clearly demon-

strates the advantage of having the quadrupole transition on the output. This work constitutes chapter 4.

1.3. Atomic Coherence and Quantum Interference

By pushing the nonlinear process to simultaneous single and two-photon resonance a new realm of atomic conditions is entered. The approximations made in deriving equation 1.3 break down and the coherences generated on each transition are strongly influenced by each other. The possibility of interference between the coherences arises and the SFM process needs to be re-evaluated in light of this. This is presented in chapter 5. The wider context of atomic coherence and quantum interference phenomena is relevant to this work, and as background to the work presented in later chapters concerning electromagnetically-induced transparency. A summary of relevant pioneering work is, therefore, given below.

An early study of a quantum interference effect concerned the problem of a discrete state placed within a continuum. In his 1961 treatment of such "autoionising" states, Fano [17] introduced the concept of the phase of the interaction between the state and the continuum. This was shown to vary across the state's linewidth and markedly asymmetrical absorption curves, which had zeros in the absorption to one side of the main peak, were predicted in agreement with experimental work. A straightforward physical view of this cancellation in the absorption is of the excitation through the two routes to the end product — an ionised atom — interfering. The two routes in this case are (a) direct photo-ionisation, and (b) excitation to the discrete state followed by rapid decay and, hence, ionisation. Later measurements by Austin and Marr [18, 19] of the vacuum ultra-violet absorption spectra of cadmium and zinc vapours respectively, showed sharp interference features between close autoionising lines. These showed dramatically that neighbouring lines in the continuum could lead to interference, and thus cancellation in absorption, as well.

Some time later, in 1976, experiments in sodium at Pisa, Italy discovered a co-

herent quantum interference within a closed atomic system [20, 21, 22]. In this work a multimode dye laser was used to excite sodium atoms in a magnetic field on the 589nm D_1 line transition. When the magnetic field was such that the hyperfine spacing of the ground state of sodium matched the mode spacing of the laser, a sharp dip in the population of the upper level was observed. Density matrix theory was presented and showed that the effect was due to the coherences set up between the three atomic levels and the important role of the coherence induced between the ground states (not directly excited or probed by any radiation) elucidated. This work was complemented by detailed theory, and later experiments, within a beam of sodium (to avoid Doppler broadening) by Gray, Whitley and Stroud [23, 24]. These results clearly showed the sharp interference feature that occurred at the two-photon resonance condition in the lambda level scheme they were using. The physical explanation presented gave rise to the concept of coherent population trapping. Briefly, they considered the system via the joint Hamiltonian for the atom and its interaction with the field, and this gave a basis of states wherein the two ground states mapped to two new states, one of which was decoupled from the radiation. Population was then optically pumped into this state via decay from the upper state and became trapped there, removed from the possibility of excitation. An alternative view, via electromagnetically-induced transparency (EIT), will be discussed below. Further work on coherent population trapping tended to concern multi-photon ionisation, and the maximisation of yields therein, so the transfer of population was of prime interest [25]. The important analogy between the interference within the atomic systems and that of Fano interference was made by Coleman and Knight [26] who also detailed how a bound state could be embedded in the photo-ionisation continuum by a strong laser, altering ion yields. This idea was dubbed "laser induced continuum structure" and was recently observed by two groups [27, 28].

1.4. Electromagnetically-Induced Transparency (EIT)

Recent work in this area has tended to concentrate not so much on the transfer of population, but on the absorption and emission properties of systems displaying this form of quantum interference. Generally the conceptual and experimental structures revolve around a three level atom which is being excited by a strong laser on one transition (the "coupling" field), and the effect that this has on the absorption on the other transition, which is monitored by a weak probe field.

1.4.1. The Rabi frequency and Autler-Townes Splitting

A central parameter to the majority of this work is the Rabi frequency [2, 29]. The Rabi frequency, Ω, is basically a measure of the strength of the interaction between the atom and the incident radiation. It is defined as:

$$\Omega = \frac{\mu_{ij} E}{\hbar} \tag{1.4}$$

where E is the strength of the electric field of the incident light and μ_{ij} is the transition matrix element, as before. It corresponds to the rate the population would flop back and forward between the levels of an undamped system. (See [1, 2] for a comprehensive introduction.)

It also corresponds to the splitting of the atomic level caused by the interaction of strong, resonant, monochromatic light. This splitting is termed the Autler-Townes (or ac Stark) effect [1, 3, 29] and is the high frequency analogue of the dc Stark effect. More generally, the levels at each end of the transition split into two components separated by $\tilde{\Omega}$, which is given by:

$$\tilde{\Omega} = \sqrt{\Delta^2 + \Omega^2} \tag{1.5}$$

where Δ is the detuning of the coupling field from resonance. This splitting has been observed in the optical range for some time (eg. see [30, 31, 32]) in both beam and vapour experiments. However, it was not realised until fairly recently that the

absorption lineshape for transitions to an Autler-Townes doublet was not necessarily just the addition of two, appropriately split, sub-components but that between the two components an interference was created leading to a greatly reduced absorption probability: electromagnetically-induced transparency. This sharp interference feature occurs even when the Autler-Townes splitting is less than the homogeneous linewidth (although not when the splitting is less than the inhomogeneous linewidth) and appears as a narrow transparency window within the absorption profile. The position of the feature is set by the two-photon resonance, the width by the coupling field Rabi frequency, and the reduction in absorption by a combination of the coupling field strength and the two-photon dephasing. See section 2.4.2 for some example lineprofiles and some explanation of the dependance on these parameters.

1.4.2. Initial Work on EIT

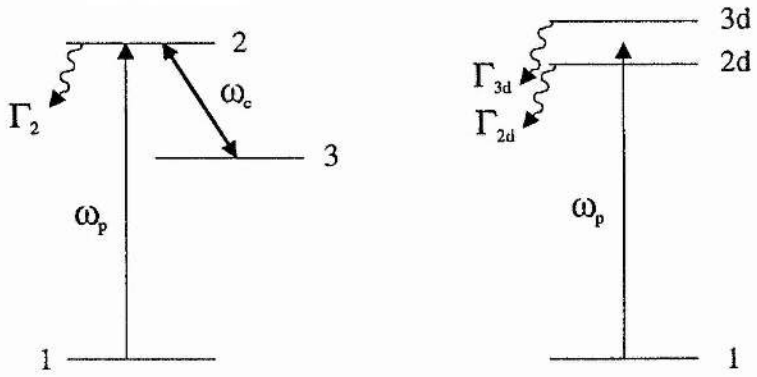

Figure 1.3: On the left the bare state scheme considered for EIT, and on the right, the corresponding dressed state view.

The concept of EIT can be traced to a paper by Imamoğlu and Harris [33] in which the authors considered the possibility of lasing without inversion in a three-level atomic system. The bare and dressed state views of the problem are shown in figure 1.3. They considered the atomic response to light at ω_p which is tuned across the 1–2 transition while a strong, resonant field couples the 2–3 transition. They

showed that a strong interference occurred at the two-photon resonance condition and explained the phenomenon via the spontaneous decay of lifetime-broadened dressed states, in keeping with their earlier work [34, 35, 36]. However, it was the first two observations using an optical frequency coupling field [37, 38] that demonstrated the power and robust nature of EIT.

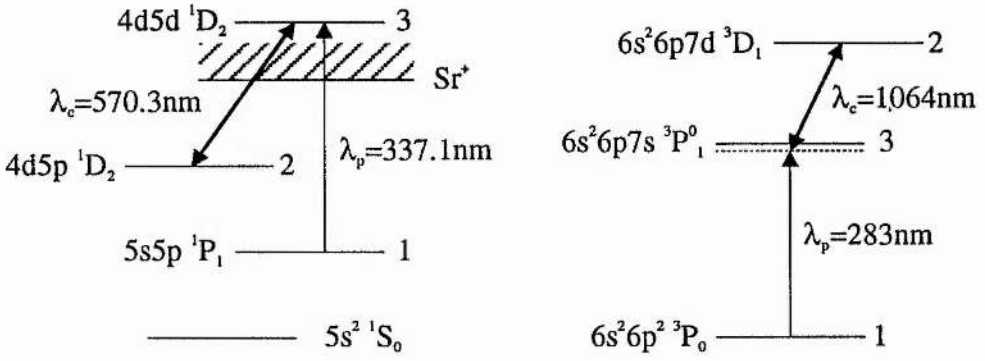

Figure 1.4: The atomic schemes used in the Stanford demonstrations of EIT. On the left the strontium system using an autoionising state and on the right the collisionally-broadened lead vapour system using the near coincidence in coupling transition wavelength to the wavelength of the Nd:YAG laser.

Figure 1.4 shows the schemes used in these first two experiments at Stanford. The strontium experiment [37] used an autoionising state as the intermediate level due to its large lifetime-broadened linewidth and demonstrated an increase in the transmission from an optically thick $\exp(-20)$ to $\exp(-1)$. The following experiment in dense lead vapour [38] extended observations into the predominantly collisionally broadened regime, as opposed to the overwhelming natural broadening encountered in the first experiment. This was an important step and demonstrated conclusively that the probe transition linewidth was unimportant in the EIT process, rather it was the two-photon coherence decay (from their labelling scheme, γ_{12}) that controlled the transparency. Both experiments used pulsed dye lasers pumped by a Q-switched injection-seeded Nd:YAG laser. The coherence requirements of the coupling laser

were stressed and single-longitudinal mode operation of this laser was critical to the experimental success.

1.4.3. Differing Views of EIT

A description of the physics behind EIT can come from different, but equivalent, viewpoints. Three of these are summarised below:

- *Coherent Population Trapping.* EIT is an alternative manifestation of coherent population trapping, ie. observation of this by the transition susceptibilities rather than the level populations. This view is in keeping with the historical references of the work at Pisa and Rochester [20, 21, 22, 23, 24].

- *Interference Between the Dressed States.* By including both the bare atom and the atom-field interaction in the system Hamiltonian a new basis set of levels are generated, called "dressed states" [1, 39, 40, 41]. Since the atom-field interaction is included in the Hamiltonian, this basis includes Autler-Townes splitting intrinsically and consists of pairs of levels separated by $\tilde{\Omega}$ (see equation 1.5). (These pairs of levels are analogous to the two Autler-Townes components in the bare state view.) EIT is the manifestation an interference between the pair of closely spaced dressed states coupled by their lifetime-broadening [33].

- *Interference Between Two Routes.* A conceptually useful viewpoint is that of an interference between two absorption paths [42], a similar explanation to that for Fano interference and, as presented in chapter 5 of this thesis, interference of excitation paths in resonant sum frequency mixing. The two routes are direct absorption to the intermediate level and a hyper-Raman process involving a cycle of the coupling transition, see figure 1.5. Density matrix perturbation chains (of the sort presented in Berman [43, 44] and chapter 5 of

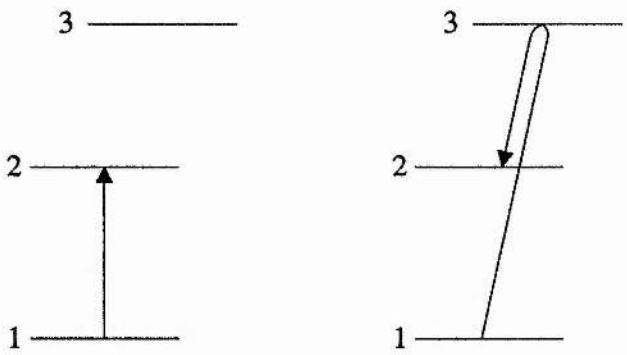

Figure 1.5: The two interfering routes for absorption that combine to give EIT.

this work) can serve to highlight this. The direct absorption route is:

$$\rho_{11} \overset{\Omega_{12}}{\Rightarrow} \left\{ \begin{array}{c} \tilde{\rho}_{12} \\ \tilde{\rho}_{21} \end{array} \right\} \overset{\Omega_{12}}{\Rightarrow} \rho_{22}$$

while the second route via the coupled transition is:

$$\rho_{11} \overset{\Omega_{12}}{\Rightarrow} \left\{ \begin{array}{c} \tilde{\rho}_{12} \\ \tilde{\rho}_{21} \end{array} \right\} \overset{\Omega_{23}}{\Rightarrow} \left\{ \begin{array}{c} \tilde{\rho}_{13} \\ \tilde{\rho}_{31} \end{array} \right\} \overset{\Omega_{23}}{\Rightarrow} \left\{ \begin{array}{c} \tilde{\rho}_{12} \\ \tilde{\rho}_{21} \end{array} \right\} \overset{\Omega_{12}}{\Rightarrow} \rho_{22}$$

If the density matrix system is simplified and solved by strictly following these perturbation paths then EIT is predicted confirming that these are the principle paths involved. The central role of $\tilde{\rho}_{13}$, the two-photon coherence, in EIT is highlighted by this analysis. This construction also clearly shows the interference to occur in the generation of $\tilde{\rho}_{12}$, which then leads to ρ_{22} and the population effects, ie. it shows EIT to be fundamental to coherent population trapping effects. Furthermore, it shows why the coherence decay rate of the two-photon transition, γ_{13}, is so important in determining the strength of the EIT feature. If this parameter is high then the second route will have a low strength and therefore the interference effect is proportionately reduced.

1.4.4. Review of Subsequent EIT Literature

Since the original observations of EIT in 1991 there have been several advances and extensions to the theoretical background, and some interesting consequences of the process have been presented. This includes work on EIT in nonlinear processes which will be treated separately in the next section. The related topics of inversionless lasing and phasonium are discussed in section 1.6.

A review of the initial EIT experiments, placing them in the wider context of other work, appeared soon after the Stanford experiments in Physics Today [45]. This is a helpful introduction to the area, accessible to the non-specialist. Thereafter, a series of papers were written by the Stanford group on various aspects of the phenomena. To begin with, Harris, Field and Kasapi [46] considered the consequences of the highly dispersive conditions experienced by the probe pulse during the EIT window. They predicted that probe pulses would propagate with unusually slow group velocities — a sample atomic scheme led to a prediction of up to 250 times less than the speed of light. (A recent result from the group claims a measurement of a factor of 126 between the speed of light and the group velocity of the probe pulse [47].)

An important set of papers concerns the mutual propagation of coupling and probe radiation pulses within the context of EIT. Harris pointed out that pulses with matched amplitude profiles [48] would set up a state where, after a characteristic distance, both pulses would propagate without loss. This includes the Fourier frequency components of the probe pulse which lie outside the single-atom transparency window. Further work by Harris discerned the two normal modes that are such that one is driven to zero and the other is independent of space and time in propagation for this situation [49]. Simultaneously, the concept of dressed-field pulses (a direct analogue of the dressed states in a population trapped system) was advanced by Eberly, Pons and Haq [50] in which the combination of coupling and probe pulse that propagates without interaction with the media was isolated

(equivalent to one of Harris' normal modes).

Field introduced the possibility of observing EIT without a coupling field by using an ultra-high finesse resonant cavity to induce vacuum Rabi splitting [51], and hence, inversionless lasing without any externally injected coherent field. Field and Imamoğlu also investigated the properties of spontaneous emission from the intermediate state in the presence of EIT [52]. Emission from the state is unaffected by the interference that leads to EIT and, thus, the observed spontaneous emission should be unusually bright due to the lack of re-absorption.

The noise properties of EIT, and the possibility of squeezing, has occupied other workers. Gheri and Walls [53] and, later, Fleischhauer, Rathe and Scully [54] predicted that 50% phase-noise squeezing was possible for the probe light, if the system was contained in a resonant cavity. Two studies of EIT due to quantized fields have appeared recently [55, 56] and predict matched photon statistics and correlation of high frequency phase fluctuations respectively. Taking EIT into the solid-state domain, the possibility of EIT, and inversionless lasing, on an intersubband transition in semiconductor quantum wells has recently been advanced [57].

Another theoretical initiative has been the proposal of radiative renormalisation [58] to EIT [59]. This theoretical structure involves less coupled equations and is designed to be well suited to the study of strong field nonlinear optical problems. It involves taking the Fourier transform of the Liouville equation (see chapter 2 or [6]) and substituting the resulting expression for $\rho(\omega)$ into itself. This gives a second order result and causes a simplification of the theoretical system.

1.5. EIT in Nonlinear Optical Processes

Among the first of the applicable consequences of EIT to be realised was its use in enhancing nonlinear wave mixing processes in gases. Harris, Field and Imamoğlu [60] considered a four-wave sum frequency mixing process (as shown in figure 1.6) in which the main limiting factor was the re-absorption of the generated sum-frequency

wave. They illustrated that use of a strong coupling laser on the last transition could induce EIT, hence removing the re-absorption, but that this did not also nullify the nonlinear conversion process at the same time. While between the Autler-Townes components the absorption sees an interference in routes, the nonlinear process does not and sees the constructive addition of the wings of the two components. Hence, the ratio of nonlinear generation to re-absorption takes a sharp rise when the Autler-Townes splitting is in excess of any inhomogeneous broadening inherent in the system, and a large increase in conversion efficiency (of up to 4 orders of magnitude) results.

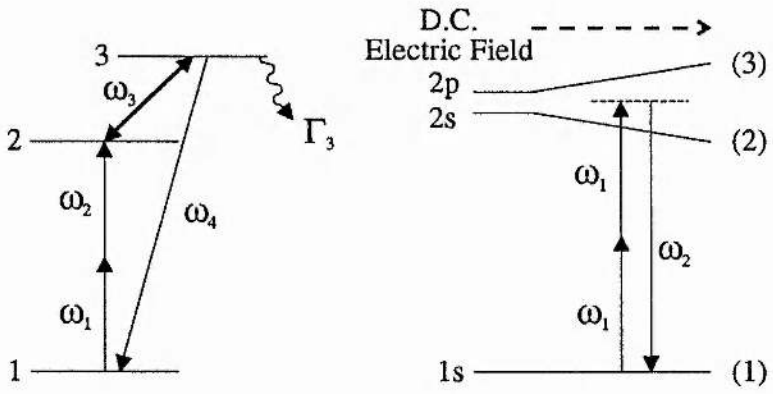

Figure 1.6: On the left, the original four-wave mixing system considered by Harris et al. for the enhancement of nonlinear processes by EIT. While, on the right, the dc electric field coupled system in hydrogen on which it was first observed.

The first demonstration of an enhancement in nonlinear wave mixing by quantum interference was actually via Fano interference, and not EIT, in 1990 [61]. However, a clear demonstration of the asymmetry in the linear (absorption) and nonlinear susceptibilities under EIT was made by Hakuta, Marmet and Stoicheff [62] three months later. This work used a dc electric field as the coupling radiation field to create the transparency and the re-absorption of second harmonic generation resonant with the 1s–2s,p transition in hydrogen (see figure 1.6) was radically reduced.

Actual demonstration of an increase in the conversion efficiency required an increased particle density and interaction length product and was indicated in a later work giving a fuller description of the theory and experiment [63]. The development of the experiment by substitution of an optical frequency coupling field instead of the dc electric field was later presented [64] and again the separate behaviours of the linear and nonlinear susceptibilities clearly demonstrated. The predicted phase matching point at the centre of EIT was used to demonstrate that a nonlinear process could be enhanced by a strong laser, even off resonance, and an increase of a factor of 59 in the nonlinear conversion efficiency was observed in lead vapour [65].

Around this time various theoretical works emerged which also have a bearing in this area. An earlier paper by Tewari and Agarwal in 1986 [66] discussed the effect of using an additional strong laser to change the phase matching properties and re-absorption in a four-wave mixing process. While not using a field actually involved in the wave mixing process, the concepts and consequences are the same [67]. Later works by the same authors [68, 69] continue this theme and, moreover, include the effects of possible amplification without inversion on the fundamental waves to further enhance the nonlinear process. The effect of the various laser linewidths on the enhancement of nonlinear processes was treated analytically by Lakshmi and Swain [70] and in particular a narrow coupling laser linewidth was shown to be of critical importance. The properties of the hydrogen experiment were considered by Gheri, Saavedra and Walls [71], this experiment was shown to be capable of producing the second harmonic field with highly squeezed quantum fluctuations.

The application of EIT to reduce the *input* wave absorption in a second-order three-wave mixing experiment is presented in chapter 6 of this thesis and is shown to give a similar enhancement to that possible by reduction of the output wave re-absorption.

1.6. Inversionless Lasing and Phasonium

The wider context of this subject area embraces the concept of lasing without inversion. A very substantial body of theoretical work has been built up in the past five years and, recently, there have been demonstrations of transient gain without population inversion [72, 73, 74, 75]. The development of the various schemes has been reviewed by Kocharovskaya [76] and further references may be found in this, reference [77], and in the review by Mandel [78]. The basic principles of amplification without inversion are that there must be small signal gain with no population inversion in the bare states in the presence of all the appropriate coherent coupling and incoherent pump fields and that there must be some extraction of energy from the medium. This last specification is necessary to deliniate between this field and that of enhanced nonlinear processes.

Briefly, two mechanisms for amplification without inversion have been isolated [79, 80]. Firstly, several proposals involve coherent population trapping and a hidden inversion in the dressed state basis (eg. see [76, 81, 82, 83, 84, 85, 86] and references therein). Other proposals give amplification without inversion in any basis set, so called amplification by atomic coherence, (eg. see [53, 76, 87, 88, 89, 90] and references therein). Some proposals can be made to exhibit amplification by both mechanisms (eg. [80]) and the driving force to this work is the possibility of the generation of light at new wavelengths, especially in the UV, VUV and X-ray regions of the spectrum. Additionally, the application of these ideas to the direct production of γ-rays via quantum coherence at nuclear-level crossings has been proposed [91].

Another relevant concept is that of accessing the resonantly-enhanced refractive index close to an atomic transition without the accompanying absorption [92]. An atomic system prepared in this way has been dubbed "phasonium" as its only effect on the probe is one of refraction. Scully initially proposed this concept and recently reviewed theoretical progress [42]. No direct observation of a system prepared in this way has been made to date. Various schemes have been proposed relying on the

differing inversionless laser schemes [93]. Proposed applications include improved resolution in optical microscopy, inverse Cerenkov detection in particle accelerators and magnetometry [42, 94] (although the latter could be argued to be more an application of EIT than the concepts central to phasonium).

It is in this area that chapter 8 has its impact. The spatial consequences of an EIT experiment are studied and lensing induced by the radial profile of the coupling laser on the probe laser is seen. This observation has relevance for the design of all experiments and devices in this field.

1.7. The Local Field Effect

In most gaseous nonlinear optics, and all of the above work, it is generally assumed that the microscopic, local field experienced by an atom is equal to the injected macroscopic electric field. However, at very high particle densities, $\mathcal{N}$, such that:

$$\mathcal{N}\lambda^3 \gg 10 \tag{1.6}$$

where λ is the transition wavelength, it is known to be inaccurate. At densities satisfying this inequality the polarisation induced in the surrounding atoms has a significant feedback effect on the local field experienced by an atom and this must be included in the formulation of the atomic response. This is termed the local field correction, or near-dipole-dipole effect, and is an important phenomenon in the solid-state [95, 96]. In dense atomic vapours it can also be important and the local electric field, E_L, should be expressed in terms of both the injected macroscopic electric field, E, and the polarisation induced in the sample, P, thus:

$$E_L = E + \frac{P}{3\epsilon_0} \tag{1.7}$$

This is the Lorentz-Lorenz equation and has been shown to be valid for arbitrary time-dependent fields in a nonlinear medium [97, 98]. It is responsible for several interesting optical effects such as the possibility of intrinsic optical bistability [99], ultrafast optical switching [100] and resonance line shifts [101, 102].

This high density correction is relevant in the context of this thesis due to EIT. Usually the resonance-line absorption in media of sufficient density for this effect to be relevant is very severe (with penetration depths of less than one wavelength of the incident light) but with the reduction of absorption due to EIT such densities can now be probed. Therefore, the effect of the local-field correction is important to include in the three-level atom model, used to provide the theoretical background for EIT, and this is done in chapter 7 of this work.

1.8. A Guide to the Following Chapters

In the following chapters of this thesis the work introduced above will be dealt with in detail. The contribution of each principle chapter was mentioned in the appropriate context above, but a short summary of the flow is given here.

Immediately following this introduction are two general chapters giving, firstly, the background to the theoretical structures and numerical computations used in the remainder of the thesis (chapter 2 and appendix A) and, secondly, a description of the experimental equipment and atomic systems used in the experimental studies (chapter 3). Thereafter, chapter 4 contains an experimental study of near-resonant, $\chi^{(2)}$, sum frequency mixing in sodium vapour. Emphasis is placed on the bulk phase matching properties of the experiment and two possible resonant enhancement routes, which differ in the placing of the dipole-forbidden transition, are contrasted. This is followed in chapter 5 by a detailed consideration of doubly-resonant sum frequency mixing. Two possible excitation paths for the output coherence are identified and their independent control is postulated. Theoretical work and numerical calculations predict interference between these two routes, and an experimental study verifies both the control and interference of the pathways. Two theoretical studies follow. Firstly, in chapter 6, the enhancement of resonant, second-order sum frequency mixing by using EIT to reduce a parasitic input wave absorption is predicted. Formal theory is developed, numerical calculations presented, and possibilities, and

attendant problems, for experimental observation are given. Secondly, the inclusion of the local field correction in the density matrix equations for a three-level cascade atom is described. This general theoretical extension for high densities is then used to look at two case studies, EIT and SFM. Chapter 8 returns to the experimental work with the observation of EIT in rubidium vapour using continuous-wave lasers. Focusing and de-focusing is observed on the probe laser beam and this is traced to the spatial profile of the other, coupling laser beam. This novel effect, and its implications, are discussed in detail. Finally, chapter 9 concludes the work and proposes some areas of possible future investigation.

REFERENCES

[1] Bruce W. Shore, *The Theory of Coherent Atomic Excitation* (Wiley, New York, 1990).

[2] R. Loudon, *The Quantum Theory of Light, Oxford Science Publications*, 2 ed. (Oxford University Press, Oxford, 1991).

[3] S. H. Autler and C. H. Townes, Stark effect in rapidly varying fields *Phys Rev* **100**, 703 (1955).

[4] Y. R. Shen, *The Principles of Nonlinear Optics* (Wiley, New York, 1984).

[5] D. C. Hanna, M. A. Yuratich, and D. Cotter, *Nonlinear Optics of Free Atoms and Molecules* (Springer Verlag, Berlin, 1979).

[6] Amnon Yariv, *Optical Electronics*, 3 ed. (Holt-Saunders, New York, 1985).

[7] R. B. Miles and S. E. Harris, Optical third-harmonic generation in alkali metal vapors *IEEE J Quantum Electron* **QE-9**, 470 (1973).

[8] D. S. Bethune, R. W. Smith, and Y. R. Shen, Optical quadrupole sum-frequency generation in sodium vapour *Phys Rev Lett* **37**, 431 (1976).

[9] Bruce D. Sinclair, *Second Harmonic Generation in Sodium Vapour Induced by a Magnetic Field*, PhD thesis, University of St. Andrews, 1987.

[10] Alistair J. Poustie, *Magnetic Field Induced Sum Frequency Mixing in Sodium Vapour*, PhD thesis, University of St. Andrews, 1990.

[11] H. Uchiki, H. Nakatsuka, and M. Matsuoka, Optical second harmonic generation in gases in magnetic field *J Phys Soc Japan* **52**, 3010 (1983).

[12] Sara Shepherd, *Use and Development of a CW Titanium Sapphire Laser for Non-Linear Optics*, PhD thesis, University of St. Andrews, 1993.

[13] M. H. Dunn, Continuous-wave, single-frequency, second harmonic generation in sodium vapour *Opt Commun* **45**, 346 (1983).

[14] B. D. Sinclair and M. H. Dunn, Continuous-wave second-harmonic generation in sodium vapour *Phys Rev A* **34**, 3989 (1986).

[15] B. D. Sinclair and M. H. Dunn, Magnetic field gradients and particle density effects in second-harmonic generation in sodium vapour *J. Mod. Opt.* **35**, 517 (1988).

[16] A. J. Poustie and M. H. Dunn, Magnetic field induced sum frequency mixing in sodium vapour *Phys Rev A* **47**, 1365 (1993).

[17] U. Fano, Effects of configuration interaction on intensities and phase shifts *Phys Rev* **124**, 1866 (1961).

[18] G. V. Marr and J. M. Austin, Absorption cross-section measurements on the vacuum ultraviolet spectrum of cadmium vapour *Proc Roy Soc A* **310**, 137 (1969).

[19] G. V. Marr and J. M. Austin, Absorption cross-section measurements on the vacuum ultra-violet spectrum of zinc vapour *J Phys B: At Mol Phys* **2**, 107 (1969).

[20] E. Arimondo and G. Orriols, Nonabsorbing atomic coherences by coherent two-photon transitions in a three-level optical pumping. *Nouvo Cimento Lettere* **17**, 333 (1976).

[21] G. Alzetta, L. Moi, and G. Orriols, Nonabsorption hyperfine resonances in a sodium vapour irradiated by a multimode dye-laser *Il Nuovo Cimento B* **52 B**, 209 (1979).

[22] G. Orriols, Nonabsorption resonances by nonlinear coherent effects in a three-level system *Il Nuovo Cimento B* **53B**, 1 (1979).

[23] R. M. Whitley and C. R. Stroud Jr., Double optical resonance *Phys Rev A* **14**, 1498 (1976).

[24] H. R. Gray, R. M. Whitley, and C. R. Stroud Jr, Coherent trapping of atomic populations *Opt Lett* **3**, 218 (1978).

[25] P. M. Radmore and P. L. Knight, Population trapping and dispersion in a three-level system *J Phys B* **15**, 561 (1982).

[26] P. E. Coleman and P. L. Knight, Population trapping in photoionisation to dressed continuum states *J Phys B: At Mol Phys* **15**, L235 (1982).

[27] Y. L. Shao, D. Charalambidis, C. Fotakis, Jian Zhang, and P. Lambropoulos, Observation of laser-induced continuum structure in ionization of sodium *Phys Rev Lett* **67**, 3669 (1991).

[28] S. Cavalieri, F. S. Pavone, and M. Matera, Observation of a laser-induced resonance in the photoionization spectrum of sodium *Phys Rev Lett* **67**, 3673 (1991).

[29] P. L. Knight and P. W. Milonni, The Rabi frequency in optical spectra *Phys Rep* **66**, 21 (1980).

[30] J. L. Picqué and J. Pinard, Direct observation of the Autler-Townes effect in the optical range *J Phys B: At Mol Phys* **9**, L77 (1976).

[31] R. E. Grove, F. Y. Wu, and S. Ezekiel, Measurement of the spectrum of resonance fluorescence from a two-level atom in an intense monochromatic field *Phys Rev A* **15**, 227 (1977).

[32] H. R. Gray and C. R. Stroud Jr., Autler-Townes effect in double optical resonance *Opt Commun* **25**, 359 (1978).

[33] A. Imamoğlu and S. E. Harris, Lasers without inversion : Interference of dressed lifetime-broadened states *Opt Lett* **14**, 1344 (1989).

[34] S. E. Harris, Lasers without inversion : Interference of lifetime-broadened resonances *Phys Rev Lett* **62**, 1033 (1989).

[35] A. Imamoğlu, Interference of radiatvely broadened resonances *Phys Rev A* **40**, 2835 (1989).

[36] S. E. Harris and J. .J. Macklin, Lasers without inversion : Single-atom transient response *Phys Rev A* **40**, 4135 (1989).

[37] K.-J. Boller, A. Imamoğlu, and S. E. Harris, Observation of electromagnetically induced transparency *Phys Rev Lett* **66**, 2593 (1991).

[38] J. E. Field, K. H. Hahn, and S. E. Harris, Observation of electromagnetically induced transparency in collisionally broadened lead vapour *Phys Rev Lett* **67**, 3062 (1991).

[39] Claude Cohen-Tannoudji and Serge Reynaud, Dressed-atom description of resonance fluorescence and absorption spectra of a multi-level atom in an intense laser beam *J Phys B: At Mol Phys* **10**, 345 (1977).

[40] Claude Cohen-Tannoudji and Serge Reynaud, Modification of resonance raman scattering in very intense laser fields *J Phys B: At Mol Phys* **10**, 365 (1977).

[41] P. R. Berman and Rainer Salomaa, Comparison between dressed-atom and bare-atom pictures in laser spectroscopy *Phys Rev A* **25**, 2667 (1982).

[42] Marlan O. Scully, From lasers and masers to phaseonium and phasers *Phys Rep* **219**, 191 (1992).

[43] P. R. Berman, Effects of collisions on linear and non-linear spectroscopic line shapes *Phys Rep* **43**, 101 (1978).

[44] Paul R. Berman, Theory of collisional effects in Doppler-free spectroscopy *Phys Rev A* **13**, 2191 (1976).

[45] Barbara Goss Levi, Some benefits of quantum interference become transparent *Physics Today* **45**, 17 (1992).

[46] S. E. Harris, J. E. Field, and A. Kasapi, Dispersive properties of electromagnetically induced transparency *Phys Rev A* **46**, R29 (1992).

[47] A. Kasapi, G. Y. Yin, M. Jain, A. Merriman, and S. E. Harris, in *International Conference on Quantum Electronics Technical Digest* (Optical Society of America, Washington DC, 1994), Vol. 10.

[48] S. E. Harris, Electromagnetically induced transparency with matched pulses *Phys Rev Lett* **70**, 552 (1993).

[49] S. E. Harris, Normal modes for electromagnetically induced transparency *Phys Rev Lett* **72**, 52 (1993).

[50] J.H. Eberly, M. L. Pons, and H. R. Haq, Dressed-field pulses in an absorbing medium *Phys Rev Lett* **72**, 56 (1994).

[51] J.E. Field, Vacuum-Rabi-splitting-induced transparency *Phys Rev A* **47**, 5064 (1992).

[52] J. E. Field and A. Imamoğlu, Spontaneous emission into an electromagnetically induced transparency *Phys Rev A* **48**, 2486 (1993).

[53] K. M. Gheri and D. F. Walls, Squeezed lasing without inversion or light amplification by coherence *Phys Rev A* **45**, 6675 (1992).

[54] M. Fleischhauer, U. Rathe, and M. O. Scully, Phase-noise squeezing in electromagnetically induced transparancy *Phys Rev A* **46**, 5856 (1992).

[55] Girish S. Agarwal, Coherent population trapping states of a system interacting with quantized fields and the production of the photon statistics matched fields *Phys Rev Lett* **71**, 1351 (1993).

[56] Michael Fleischhauer, Correlation of high-frequency phase fluctuations in electromagnetically induced transparency *Phys Rev Lett* **72**, 989 (1994).

[57] Yang Zhao, Danhong Huang, and Cuakai Wu, Electric-field-induced quantum coherence on the intersubband transition in semiconductor quantum wells *Opt Lett* **19**, 816 (1994).

[58] O. Blum, P. Harshman, T. K. Gustafson, and P. L. Kelley, Application of radiative renormalization to strong-field resonant nonlinear optical interactions *Phys Rev A* **47**, 5165 (1993).

[59] P. J. Harshman, O. Blum, T.K. Gustafson, and P. L. Kelley, Application of radiative renormalisation to electromagnetically induced transparency *Opt Lett* **18**, 1706 (1993).

[60] S .E. Harris, J. E. Field, and A. Imamoğlu, Nonlinear optical processes using electromagnetically induced transparency *Phys Rev Lett* **64**, 1107 (1990).

[61] K. H. Hahn, D. A. King, and S. E. Harris, Nonlinear generation of 104.8nm radiation within an absorption window in zinc *Phys Rev Lett* **65**, 2777 (1990).

[62] K. Hakuta, L. Marmet, and B. P. Stoicheff, Electric-field-induced second-harmonic generation with reduced absorption in atomic hydrogen *Phys Rev Lett* **66**, 596 (1991).

[63] K. Hakuta, L. Marmet, and B. P. Stoicheff, Nonlinear optical generation with reduced absorption using electric-field coupling in atomic hydrogen *Phys Rev A* **45**, 5152 (1992).

[64] G. Z. Zhang, K. Hakuta, and B. P. Stoicheff, Noninear optical generation using electromagnetically induced transparency in atomic hydrogen *Phys Rev Lett* **71**, 3099 (1993).

[65] Maneesh Jain, G. Y. Yin, J. E. Field, and S. E. Harris, Observation of electromagnetically induced phase matching *Opt Lett* **18**, 998 (1993).

[66] S. P. Tewari and G. S. Agarwal, Control of phase matching and nonlinear generation in dense media by resonant fields *Phys Rev Lett* **56**, 1811 (1986).

[67] Surya P. Tewari and G. S. Agarwal, Vacuum-ultraviolet generation using electromagnetic-field-induced transparency *Phys Rev Lett* **66**, 1797 (1991).

[68] G. S. Agarwal and Surya P. Tewari, Large enhancements in nonlinear generation by external electromagnetic fields *Phys Rev Lett* **70**, 1417 (1993).

[69] Suyra P. Tewari, Nonlinear mixing of radiation in a medium having gain without population inversion *Opt Commun* **103**, 216 (1993).

[70] P. Anantha Lakshmi and S. Swain, Effect of laser linewidths on nonlinear optical processes exploiting electromagnetically induced transparency *J Mod Opt* **38**, 2031 (1991).

[71] K. M. Gheri, C. Saavedra, and D. F. Walls, Intracavity second-harmonic generation using an electromagnetically induced transparency *Phys Rev A* **4**, 48 (1993).

[72] J. Gao, C. Guo, X. Guo, G. Jin, P. Wang, J. Zhao, H. Zhang, Y. Jiang, D. Wang, and D. Jiang, Observation of light amplifiication without population inversion in sodium *Opt Commun* **93**, 323 (1992).

[73] A. Nottelmann, C. Peters, and W. Lange, Inversionless amplification of picosecond pulses due to Zeeman coherence *Phys Rev Lett* **70**, 1783 (1993).

[74] W. E. van der Veer, R. J. J. van Diest, A. Dönszelmann, and H. B. van Linden van den Heuvell, Experimental demonstration of light amplification without population inversion *Phys Rev Lett* **70**, 3243 (1993).

[75] Edward S. Fry, Xingfu Li, Dmitri Nikonov, G. G. Padmabandu, Marlan O. Scully, Arlie V. Smith, Frank K. Tittel, Ching Wang, Steve R. Wilkinson, and Shi-Yao Zhu, Atomic coherence effects within the sodium D_1 line: Lasing without inversion via population trapping *Phys Rev Lett* **70**, 3235 (1993).

[76] Olga Kocharovskaya, Anplification and lasing without inversion *Phys Rep* **219**, 175 (1992).

[77] Richard R. Moseley, *Nonlinear Optical Coherence Processes in Vapours*, First year report, University of St. Andrews, Scotland (unpublished).

[78] Paul Mandel, Lasing without inversion: a useful concept? *Contemp Phys* **34**, 235 (1993).

[79] O. Kocharovskaya, P. Mandel, and Y. V. Radeonychev, Inversionless amplifiction in a three-level medium *Phys Rev A* **45**, 1997 (1992).

[80] C. H. Keitel, O. A. Kocharovskaya, L. M. Narducci, M. O. Scully, S.-Y. Zhu, and H.M. Doss, Two mechanisms for inversionless amplification in four-level atoms with raman pumping *Phys Rev A* **48**, 3196 (1993).

[81] B. R. Mollow, Stimulated emission and absorption near resonance for driven systems *Phys Rev A* **5**, 2217 (1972).

[82] F. Y. Wu, S. Ezekiel, M. Ducloy, and B. R. Mollow, Observation of amplification in a strongly driven two-level atomic system at optical frequencies *Phys Rev Lett* **38**, 1077 (1977).

[83] M. Lewenstein, Y. Zhu, and T. W. Mossberg, Two-photon gain and lasing in strongly driven two-level atoms *Phys Rev Lett* **64**, 3131 (1990).

[84] O. A. Kocharovskaya and Ya. I. Khanin, Coherent amplification of an ultrashort pulse in a three-level medium without a population inversion *JETP Lett* **48**, 630 (1988).

[85] M. O. Scully, S.-Y. Zhu, and A. Gavrielides, Degenerate quantum-beat laser : Lasing without inversion and inversion without lasing *Phys Rev Lett* **62**, 2813 (1989).

[86] L. M. Narducci, H. M. Doss, P. Ru, M. O. Scully, S. Y. Zhu, and C. Keitel, A simple model of a laser without inversion *Opt Commun* **81**, 379 (1991).

[87] A. Imamoğlu, J. E. Field, and S. E. Harris, Lasers without inversion : A closed lifetime broadened system *Phys Rev Lett* **66**, 1154 (1991).

[88] G. S. Agarwal, Origin of gain in systems without inversion in bare or dressed states *Phys Rev A* **44**, R28 (1991).

[89] Y. Zhu, Lasing without inversion in a closed three-level system *Phys Rev A* **45**, R6149 (1992).

[90] Yifu Zhu, Oliver C. Mullins, and Min Xiao, Inversionless laser from a closed multilevel system *Phys Rev A* **47**, 602 (1993).

[91] R. Coussement, M. Van den Bergh, G. S'heeren, G. Neyems, R. Nouwen, and P. Boolchand, Nonreciprocity of gamma emission and absorption due to quantum coherence at nuclear-level crossings *Phys Rev Lett* **71**, 1824 (1993).

[92] M. O. Scully and S.-Y. Zhu, Ultra-large index of refraction via quantum interference *Opt Commun* **87**, 134 (1992).

[93] M. Fleischhauer, C. H. Keitel, M. O. Scully, Chang Su, T. Ulrich, and Shi-Yao Zhu, Resonantly enhanced refractive index without absorption via atomic coherence *Phys Rev A* **46**, 1468 (1992).

[94] Marlan O. Scully and Michael Fleischhauer, High-sensitivity magnetometer based on index-enhanced media *Phys Rev Lett* **69**, 1360 (1992).

[95] Max Born and Emil Wolf, *Principles of Optics*, 5 ed. (Pergamon Press, Oxford, 1975).

[96] W. J. Duffin, *Electricity and Magnetism*, 3rd ed. (McGraw-Hill, London, 1980).

[97] Charles M. Bowden and Jonathan P. Dowling, Near-dipole-dipole effects in dense media: Generalized Maxwell-Bloch equations *Phys Rev A* **47**, 1247 (1993).

[98] Charles M. Bowden and Jonathan P. Dowling, Erratum: Near-dipole-dipole effects in dense media: Generalized Maxwell-Bloch equations *Phys Rev A* **49**, 1514 (1994).

[99] R. Friedberg, S. R. Hartmann, and Jamal T. Manassah, Mirrorless optical bistability condition *Phys Rev A* **39**, 3444 (1989).

[100] M. E. Crenshaw, M. Scalora, and C. M. Bowden, Ultrafast intrinsic optical switching in a dense medium of two-level atoms *Phys Rev Lett* **68**, 911 (1992).

[101] R. Friedberg, S. R. Hartmann, and Jamal T. Manassah, Effect of local-field correction on a strongly pumped resonance *Phys Rev A* **40**, 2446 (1989).

[102] Jeffery J. Maki, Michelle S. Malcuit, J. E. Sipe, and Robert W. Boyd, Linear and nonlinear optical measurements of the Lorentz local field *Phys Rev Lett* **67**, 972 (1991).

Chapter 2

Theory and Numerical Modeling

2. Theory and Numerical Modeling

When an atom is subject to incident radiation the evolution of its excited state populations, and its feedback on to the field, are of prime interest. For broad-band or incoherent excitation the response of the system may be described well by a rate equation approach using the Einstein coefficients. However, if the incident radiation (light) is narrow-band (relative to the width of the atomic level) and coherent then the reaction of the atom requires a more complex description. Quantum mechanics is used and the atomic description is given in terms of the populations of the various atomic levels and the coherences set up between them. In the first part of this chapter I will summarise the possible theoretical bases of interest and then proceed in more detail with the density matrix approach which is used dominantly in later chapters. Thereafter, various simple atomic systems will be covered as examples both of the formalism and various atomic coherence effects of interest ie. sum frequency mixing, electromagnetically-induced transparency and inversionless lasing.

2.1. Descriptions of Coherent Excitation

2.1.1. Atomic Probability Amplitudes

The quantum mechanical treatment of the atom takes as its starting point the time dependent Schrödinger equation [1, 2]:

$$\mathcal{H}\Psi(\mathbf{r},t) = i\hbar\frac{\partial\Psi(\mathbf{r},t)}{\partial t} \tag{2.1}$$

Here $\Psi(\mathbf{r},t)$ is the overall wavefunction of the atom and $\mathcal{H}$ the Hamiltonian of the system. In this approach $\mathcal{H}$ is taken as the sum of the atomic Hamiltonian, $\mathcal{H}_0$, and atom-field interaction Hamiltonian, $V(t)$:

$$\mathcal{H} = \mathcal{H}_0 + V(t) \tag{2.2}$$

The majority of the effects dealt with in this work have at their base the three-level atom. This is a simplified view of an atom where only three levels have an important role in the atomic response and is a useful and popular approximation. Figure 2.1 is a cascade three level atom, which is of interest in sum frequency mixing among other phenomena, and is the one used predominantly in this work.

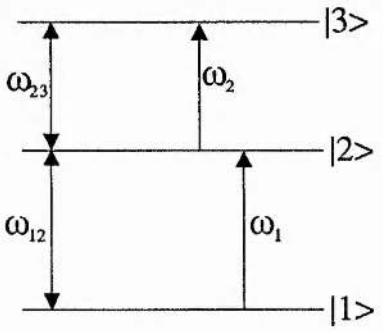

Figure 2.1: A simple cascade three-level atom

The wavefunction of the atomic system is generally expressed as a linear combination of some basis set, most usefully the unperturbed states of an isolated atom. These are the solutions of the atomic Hamiltonian and satisfy the Schrödinger equation, both time dependent and time independent. In Dirac notation [2], this is expressed, for level $|i>$ with energy ϵ_i, as:

$$\mathcal{H}_0|i> = \epsilon_i|i> \tag{2.3}$$

The total system wavefunction is by definition:

$$\Psi = \sum_i a_i|i> \tag{2.4}$$

where a_i are the probability amplitudes for the individual levels. The physical observable most closely associated with these is the probability of finding the atom in that level and is the square modulus, $|a_i|^2$.

In order to discern the evolution of the probability amplitudes for the cascade system the interaction Hamiltonian, $V(t)$, must be stated. In the dipole approximation, where only dipole allowed transitions are important, we may state it as:

$$V(t) = -e\mathbf{r}.\mathbf{E} \tag{2.5}$$

in which the two electric fields included in $\mathbf{E}$ are defined to be:

$$E_i(t) = \frac{E_i}{2}\left(\exp(i\omega_i t) + \text{c. c. }\right) \qquad i = 1, 2 \tag{2.6}$$

To proceed, equation 2.4 is substituted in equation 2.1 and the properties of $|i>$ are used to remove several terms. The system then simplifies to:

$$a_1 V(t)|1> + a_2 V(t)|2> + a_3 V(t)|3> = i\hbar\dot{a}_1|1> + i\hbar\dot{a}_2|2> + i\hbar\dot{a}_3|3> \tag{2.7}$$

To find the evolution of the three probability amplitudes in turn this equation is operated on by the appropriate bra ($< i|$) and the orthonormality of the basis set invoked. The interaction strengths of the levels with the fields are embodied in the transition matrix elements, μ_{ij}, with the definitions:

$$<1|V(t)|2> = \mu_{12}E_1 \tag{2.8a}$$

$$<2|V(t)|3> = \mu_{23}E_2 \tag{2.8b}$$

and complex conjugates thereof. We then gain equations for the rapidly-varying Schrödinger amplitudes, under the rotating-wave approximation [1, 3], for example:

$$\dot{a}_1 = i\Omega_{12}e^{i(\omega_1 - \omega_{12})t}a_2 \tag{2.9}$$

where Ω_{12} is the half-Rabi frequency for the transition, defined as:

$$\Omega_{12} = \frac{\mu_{12}E_1}{2\hbar} \tag{2.10a}$$

$$\Omega_{23} = \frac{\mu_{23}E_2}{2\hbar} \tag{2.10b}$$

However, when looking over long time scales, especially for steady-state behaviour, it is useful to convert to the interaction picture and remove the optical frequency oscillations of the amplitudes by the definitions:

$$\dot{\tilde{a}}_2 = a_2 e^{-i(\omega_1-\omega_{12})t} \tag{2.11a}$$

$$\dot{\tilde{a}}_3 = a_3 e^{-i([\omega_1+\omega_2]-[\omega_{12}+\omega_{23}])t} \tag{2.11b}$$

This then gives the completed coupled time evolution of the slowly-varying amplitudes as:

$$\dot{\tilde{a}}_1 = i\Omega_{12}\tilde{a}_2 \tag{2.12a}$$

$$\dot{\tilde{a}}_2 - i\Delta_{12}\tilde{a}_2 = i\Omega_{12}^* a_1 + i\Omega_{23}\tilde{a}_3 \tag{2.12b}$$

$$\dot{\tilde{a}}_3 - i\Delta_{13}\tilde{a}_3 = i\Omega_{23}^*\tilde{a}_2 \tag{2.12c}$$

wherein the detuning terms, Δ_{ij}, are defined as:

$$\Delta_{12} = \omega_1 - \omega_{12} \tag{2.13a}$$

$$\Delta_{13} = (\omega_1 + \omega_2) - (\omega_{12} + \omega_{23}) \tag{2.13b}$$

and decay rates may be added phenomenologically by the generalisation to complex detunings eg.:

$$\Delta_{12} \rightarrow \tilde{\Delta}_{12} = \Delta_{12} - \frac{i\Gamma_2}{2} \tag{2.14}$$

Solutions to this system are gained in different ways depending on the problem under consideration. Perturbation theory may be appropriate or linearisation with respect to some probe field may be used. Steady-state is often considered and for this the time derivatives are simply set to zero. Physically the population probabilities may be gained by the square modulus of the various amplitudes, and products of the form $a_1 a_2^*$ are associated with transition rates. Many papers use this formalism to avoid the complications of a full density matrix treatment eg. [4, 5] and it can be a relatively simple way to calculate various quantities or gain some physical insight into the response of the atom.

2.1.2. The Density Matrix

The density matrix is an alternative and very popular formalism for dealing with the quantum mechanics of the atom-radiation interaction. It deals directly with bilinear combinations of the probability amplitudes, and hence observables, with the matrix elements given by the definition [1, 2, 6]:

$$\rho_{ij} = \overline{a_j^* a_i} \tag{2.15}$$

Apart from dealing directly with the observable quantities the density matrix incorporates an ensemble average over the individual elements of the system, as denoted by the bar in equation 2.15. In this way it may handle statistical properties of the system, eg. collisions and its value is that of an average system in the ensemble. Furthermore, the mathematics may be simpler, but not always!

The classic texts referenced above introduce the density matrix in more detail and list its many properties. Of direct interest here, however, is the trace normalisation condition:

$$\mathrm{tr}(\rho) \equiv \sum_{i=1}^{n} \rho_{ii} = 1 \tag{2.16}$$

which ensures conservation of population, and the property of index reversal:

$$\rho_{ij} = \rho_{ji}^* \tag{2.17}$$

Derivation of the Density Matrix Equations

The same basis set for the atomic system, that of the unperturbed isolated atom states, is used here also and the Schrödinger equation may be re-stated in terms of the density matrix components. In this form it is called the Liouville equation [7] and is:

$$\begin{aligned} \frac{\partial \rho_{ij}}{\partial t} &= -\frac{i}{\hbar}[\mathcal{H}, \rho]_{ij} \\ &= -\frac{i}{\hbar} \sum_{k=1}^{n} (\mathcal{H}_{ik}\rho_{kj} - \rho_{ik}\mathcal{H}_{kj}) \end{aligned} \tag{2.18}$$

Decay phenomena are added by appending a term of the form $-\Gamma_{ji}\rho_{jj}$ to the diagonal elements (whose thermal equilibrium values are zero) to describe spontaneous emission out of a level, with the corresponding positive term in the receiving level, if that is within the system of study. The off-diagonal elements will also decay towards their thermal equilibrium values, usually zero, and contain a term $-\gamma_{ij}\rho_{ij}$ where γ_{ij} is generally given by:

$$\gamma_{ij} = \frac{1}{2}(\Gamma_{ii} + \Gamma_{jj}) + \gamma_{deph} \tag{2.19}$$

The final quantity in this, γ_{deph}, takes account of any further dephasing rate that acts of the system, without causing important population decay, eg. collisional effects [2, 8, 9, 10]. The Hamiltonian of the system is unchanged and may be stated, recollecting equations 2.8, as:

$$\mathcal{H} = \mathcal{H}_0 - \mu_{ij}E(t) \tag{2.20}$$

Once again we consider a cascade three-level atom and will derive the equations of motion for it. The now generalised system is shown in figure 2.2 and includes spontaneous decay back down the cascade. Due to atomic selection rules not all three transitions can be dipole allowed and hence, while 1-2 and 2-3 are dipole allowed, transition 1-3 may only be quadrupole allowed at best. Therefore, $\mu_{13} \approx 0$ as the atom only interacts strongly with fields on 1-2 and 2-3, but it is important to note that μ_{13} is not identically zero and this leads to the sum frequency mixing observed in such systems. The approximation made here is valid however, as the matrix element is in the order of $(z/130)^2$ below the dipole-allowed ones [11], where z is the atomic number of the atom.

Once again we consider two sinusoidal interacting fields. In doing so we are working in the semiclassical picture, ie. classical fields but a quantised atom. We also assume that the fields are each near resonant to one of the transitions only, a not very stringent assumption for real systems. Including propagation terms for the

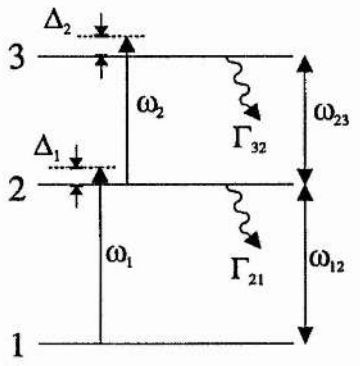

Figure 2.2: A cascade three-level system for sum frequency mixing, such as the 3S-3P-3D levels of sodium

z direction the fields are:

$$E_i(z,t) = \frac{E_i}{2}\{\exp[i(\omega_i t - k_i z)] + \text{c.c.}\} \qquad i = 1,2 \tag{2.21}$$

The Rabi frequencies are defined as in equations 2.10 and are assumed without loss of generality to be real, with real matrix elements. The optical frequency oscillations are removed by the substitutions:

$$\rho_{12} = \tilde{\rho}_{12}\exp[i(\omega_1 t - k_1 z)] \tag{2.22a}$$

$$\rho_{23} = \tilde{\rho}_{23}\exp[i(\omega_2 t - k_2 z)] \tag{2.22b}$$

$$\rho_{13} = \tilde{\rho}_{13}\exp[i\{(\omega_1+\omega_2)t - (k_1+k_2)z\}] \tag{2.22c}$$

and the remaining rapidly oscillating terms at twice the optical frequencies, or sums and differences of them are removed by invoking the rotating-wave approximation [1, 3] as they will average to zero for an intergration time of any time above a few optical cycles. The coupled equations for the evolution of the density matrix components are therefore:

$$\dot{\rho}_{11} = i\Omega_{12}(\tilde{\rho}_{21} - \tilde{\rho}_{12}) + \Gamma_{21}\rho_{22} \tag{2.23a}$$

$$\dot{\rho}_{22} = i\Omega_{12}(\tilde{\rho}_{12} - \tilde{\rho}_{21}) + i\Omega_{23}(\tilde{\rho}_{32} - \tilde{\rho}_{23}) - \Gamma_{21}\rho_{22} + \Gamma_{32}\rho_{33} \tag{2.23b}$$

$$\dot{\rho}_{33} = i\Omega_{23}(\tilde{\rho}_{23} - \tilde{\rho}_{32}) - \Gamma_{32}\rho_{33} \tag{2.23c}$$

$$\dot{\tilde{\rho}}_{12} = -i(\Delta_1 - i\gamma_{12})\tilde{\rho}_{12} + i\Omega_{12}(\rho_{22} - \rho_{11}) - i\Omega_{23}\tilde{\rho}_{13} \quad (2.23d)$$

$$\dot{\tilde{\rho}}_{23} = -i(\Delta_2 - i\gamma_{23})\tilde{\rho}_{23} + i\Omega_{23}(\rho_{33} - \rho_{22}) + i\Omega_{12}\tilde{\rho}_{13} \quad (2.23e)$$

$$\dot{\tilde{\rho}}_{13} = -i(\Delta_1 + \Delta_2 - i\gamma_{13})\tilde{\rho}_{13} + i\Omega_{12}\tilde{\rho}_{23} - i\Omega_{23}\tilde{\rho}_{12} \quad (2.23f)$$

These equations, with the complex conjugates of the latter three, describe the evolution of the atomic system through time. Once again solutions are gained under various approximations, of which, steady-state is probably the most common, whereby all the time derivatives are set to zero. Analytical solutions of the system in steady-state have been obtained [12] but are very lengthy and complicated and until simplified for a specific problem yield little physical insight. Numerical solutions allow for exact solutions without simplifying assumptions and are used extensively in this work with simplified analytical results derived as necessary to highlight the physical processes and parameters involved a specific process.

Physical Significance of the Density Matrix Components

As indicated at the head of this section the individual components of the density matrix have direct physical significance. Firstly, the diagonal elements, ρ_{ii}, are the average probability of finding an atom in state $|i>$; that is, the population of that state (eg. if there are $\mathcal{N}$ atoms in the ensemble, $\mathcal{N}\rho_{33}$ will be in the uppermost state).

The off-diagonal elements are termed coherences. They denote the strength and phase of interaction between the levels and are related to the radiating dipole of the ensemble which feeds back on the incident fields in terms of refractive index and attenuation/gain. Specifically, the induced polarisation in the medium, $P(t)$, is given by [1, 7]:

$$P(t) = \mathcal{N}\mu_{ij}\rho_{ij} \quad (2.24)$$

for an ensemble of $\mathcal{N}$ atoms. This expression for the polarisation may then be compared to the macroscopic expression for the polarisation in terms of the medium's

susceptibility, χ and the electric field:

$$\begin{aligned} P(t) &= \epsilon_0 \chi E(t) \\ &= \epsilon_0(\chi' - i\chi'')E(t) \end{aligned} \tag{2.25}$$

Doing this relates the real and imaginary components of the susceptibility to the off-diagonal density matrix element components as follows:

$$\chi' = \frac{\mathcal{N}\mu_{ij}^2}{\epsilon_0 \hbar} \frac{\Re(\tilde{\rho}_{ij})}{\Omega_r} \tag{2.26}$$

$$\chi'' = -\frac{\mathcal{N}\mu_{ij}^2}{\epsilon_0 \hbar} \frac{\Im(\tilde{\rho}_{ij})}{\Omega_r} \tag{2.27}$$

wherein, $\Omega_r = (\mu_{ij}E)/\hbar$, the full Rabi frequency of the field. Thereafter, reference to Maxwell's wave equation for electromagnetic waves reveals the physical significance of the susceptibility [7]. The real part, χ', is related to the deviation of refractive index from the background value, n, which may be stated in terms of a phase delay per unit length, Δk by:

$$\Delta k = \frac{k\chi'}{2n^2} \tag{2.28}$$

The imaginary part, χ'', gives the amplitude attenuation ($\Im(\tilde{\rho}_{ij}) < 0$), or gain ($\Im(\tilde{\rho}_{ij}) > 0$) by the function:

$$E(z) = E(0) \exp\left\{\left(-\frac{k\chi''}{2n^2}\right) z\right\} \tag{2.29}$$

2.1.3. Dressed States

A useful alternative viewpoint is of the dressed-atom [13] within which the density matrix components are expressed for a basis set satisfying the combined isolated atom and interaction Hamiltonians. This is semiclassical but incorporates many strong field effects, eg. ac Stark effect, in a fundamental way. It can provide a straightforward method of explaining resonance fluorescence pictures and is useful in electromagnetically-induced transparency.

All the above formalisms are semiclassical in nature, ie. a quantised atom and classical electric field. It is possible to quantise the radiation field as well by use

of the photon creation and annihilation operators [1, 14]. This work, however, will not use that formalism as the incident fields are fairly strong and individual photon statistics unnecessary and squeezing is not considered. However, the related concept of dressed photon-atom states is interesting and can provide a useful physical explanation of some effects [14, 15, 16, 17]. For these the Hamiltonian of the system is now taken as the sum of the isolated atom Hamiltonian, the field Hamiltonian and the interaction Hamiltonian. This naturally leads to ac Stark splitting and light shifts again and the infinite ladder of states created can explain some inversionless lasing mechanisms and phenomena such as the two-photon laser [18].

2.2. Numerical Solutions and Extensions

Several three and four level systems were studied using the density matrix equations derived as described above. All were taken under steady-state conditions, relevant for the use of continuous-wave lasers, and the methods of solution are detailed below.

2.2.1. Analytical Solutions

It is possible to gain exact analytical solutions for the density matrix equations if the system is taken as being purely homogeneously broadened. Unfortunately, Doppler broadening requires an integration which is not tractable analytically for these equations. Solutions, in the absence of Doppler broadening, are given by Brewer and Hahn [12] and are notable for their complexity. It is hard to gain physical insight without making simplifying assumptions to them. Such assumptions may involve linearising the system with respect to one or more variable, such as a probe field amplitude for instance. Symbolic algebra packages, such as Maple, can solve the simultaneous equations, removing the tedium, improving accuracy and can aid analytical work, especially under tightly restricted parameters eg. resonant fields.

Simplified analytical solutions will be obtained under various conditions later in this work to highlight physical processes and important parameters for the specific

problem.

2.2.2. Numerical Solutions

Numerical solutions are forced by Doppler broadening and the corresponding integration which is not tractable analytically. They also have the advantages of being exact, requiring no further simplifications and can be of arbitrary accuracy depending on the complexity and precision of the programming technique. Furthermore, they are very flexible and allow scans over any parameter at will which help visualise the importance, or otherwise, of them.

To proceed to numerical solutions of the density matrix system of equations 2.23 in steady-state they are first converted to a set of real equations by splitting the off-diagonal equations into their real and imaginary parts. This is done by defining two real variables, ρ_{ij}^r and ρ_{ij}^i as the real and imaginary parts of coherence $\tilde{\rho}_{ij}$ respectively:

$$\tilde{\rho}_{ij} = \rho_{ij}^r + i\rho_{ij}^i \tag{2.30}$$

and then converting the system into 9 real simultaneous equations. One degree of freedom is removed by the trace invariance condition of equation 2.16 which can be used to substitute $\rho_{11} = 1 - \rho_{22} - \rho_{33}$ for the lower level population throughout the system leaving only 8 independent variables.

The system of simultaneous equations is then most compactly stated in matrix

form ($Ax = b$) as below:

$$\begin{bmatrix} -\Gamma_{21} & \Gamma_{32} & 0 & 0 & 0 & -2\Omega_{12} & 0 & 2\Omega_{23} \\ 0 & -\Gamma_{32} & 0 & 0 & 0 & 0 & 0 & -2\Omega_{23} \\ 0 & 0 & \gamma_{12} & 0 & 0 & -\Delta_1 & -\Omega_{23} & 0 \\ 0 & 0 & 0 & \gamma_{13} & 0 & -\Omega_{23} & -\Delta_1 - \Delta_2 & \Omega_{12} \\ 0 & 0 & 0 & 0 & \gamma_{23} & 0 & \Omega_{12} & -\Delta_2 \\ -2\Omega_{12} & -\Omega_{12} & \Delta_1 & \Omega_{23} & 0 & \gamma_{12} & 0 & 0 \\ 0 & 0 & \Omega_{23} & \Delta_1 + \Delta_2 & -\Omega_{12} & 0 & \gamma_{13} & 0 \\ \Omega_{23} & -\Omega_{23} & 0 & -\Omega_{12} & \Delta_2 & 0 & 0 & \gamma_{23} \end{bmatrix} \begin{bmatrix} \rho_{22} \\ \rho_{33} \\ \rho_{12}^r \\ \rho_{13}^r \\ \rho_{23}^r \\ \rho_{12}^i \\ \rho_{13}^i \\ \rho_{23}^i \end{bmatrix} = \begin{bmatrix} 0 \\ 0 \\ 0 \\ 0 \\ 0 \\ -\Omega_{12} \\ 0 \\ 0 \end{bmatrix} \tag{2.31}$$

Numerical solution of this system was achieved using LU decomposition [19, 20] using Crout's algorithm with partial pivoting and back substitution. Due to the accumulation and magnification of round off errors in the solution iterative improvement of the solution was implemented [19] until the residual error was in the ninth significant figure.

Doppler integration could then be added to the routine. The Doppler shift of an atom moving at velocity V_z in the z direction alters the detunings of the incident fields from resonance. This is incorporated by extending the detunings to account for this as follows:

$$\Delta_{12} = \omega_1 - k_1 V_z - \omega_{12} = \Delta_{12}^0 - k_1 V_z \tag{2.32a}$$

$$\Delta_{23} = \omega_2 - k_2 V_z - \omega_{23} = \Delta_{23}^0 - k_2 v_z \tag{2.32b}$$

Thus the density matrix components are now velocity dependent and are integrated over the Maxwell-Boltzman velocity distribution, ie.:

$$\overline{\rho}_{ij} = \int_0^\infty f(V_z)\tilde{\rho}_{ij}(V_z)dV_z \tag{2.33}$$

where $f(V_z)$ is the fraction of atoms with velocity between V_z and $V_z + dV_z$:

$$f(V_z) = \frac{e^{-\left(\frac{V_z}{u}\right)^2}}{\sqrt{\pi}} \frac{dV_z}{u} \; ; \quad u \equiv \left(\frac{2k_B T}{M}\right)^{\frac{1}{2}} \tag{2.34}$$

This was implemented in C in a UNIX environment on Sun SPARC workstations with the integration carried out by Simpson's rule [20]. The main control algorithm is detailed below:

- Set Δ_{ij}^0, Ω_{12}, Ω_{23} etc.
  - Loop over the velocity from -5u to 5u in small steps
    - Calculate Δ_{ij} including Doppler shift
    - Solve equation matrix for $\tilde{\rho}_{ij}$
    - Iteratively improve solution
    - Add to integration totals: $\alpha f(V_z)\tilde{\rho}_{ij}(V_z)$
      where α is the appropriate Simpson factor (1,2 or 4)
  - End inner loop, next velocity point
- Multiply results by overall integration factor
- Save Doppler integrated data point
- End outer loop, next input parameter point

This was capable of calculating a scan of 100 data points including integration over 1000 velocity points for each data point in under two minutes on the faster workstations. (A time of up to 30 minutes was possible on the slower workstations for integrations of 6000 points, the most accurate numerical implementation used.) While not a traditional programming language for such tasks, C proved to be fast and flexible for this application.

2.2.3. Extensions

Incoherent Pumps

Incoherent pumps such as discharges, flashlamps and excitation followed by spontaneous decay were included for modeling of the inversionless laser concept. A small

amount of population generally needed to be transferred to the upper level for laser action, and incoherent means were preferred due to conceptual ease and to avoid disturbing the coherences already in the system. The terms were added phenomenologically to the Liouville equation or the derived system evolution equations in one of two ways.

Firstly, for excitation by collisions induced in a discharge or high excitation followed by spontaneous decay simple pump terms of the following form were included:

$$\begin{aligned} \dot{\rho}_{11} &= \ldots - \Pi\rho_{11} \\ \dot{\rho}_{22} &= \ldots + \Pi\rho_{22} \end{aligned}$$

where Π is the incoherent pump rate. For excitation via a thermal incoherent radiation bath (eg. [21]) transitions can be stimulated both ways and so the terms become:

$$\begin{aligned} \dot{\rho}_{11} &= \ldots + R_{12}(\rho_{22} - \rho_{11}) \\ \dot{\rho}_{22} &= \ldots - R_{12}(\rho_{22} - \rho_{11}) \end{aligned}$$

where R_{12} is related to the incoherent radiation intensity. The dephasing between the levels is raised by the action of either of these incoherent pumps and appropriate additions (eg. $R_{12}/2$) should be included in these [21].

Propagational Effects

As the incident radiation propagates through a strongly polarised medium the field amplitudes and phases will evolve due to attenuation and the refractive index experienced. This evolution can be incorporated by integrating over small path steps and updating the field amplitudes accordingly. The feedback to the fields can be approximated as follows starting from Maxwell's equations. In one dimension we have:

$$\frac{\partial^2 E}{\partial z^2} = \mu_0 \frac{\partial^2 D}{\partial t^2} \tag{2.35}$$

where $D = \epsilon_0 E + P$ as normal. The polarisation induced in the medium is, as before, calculated from the appropriate density matrix component:

$$P(t) = \mathcal{N}\mu_{ij}\tilde{\rho}_{ij}e^{-i(\omega_i t - k_i z)} \tag{2.36}$$

Substituting this into equation 2.35 and invoking the slowly varying amplitude approximation we may derive for the change in amplitude for a small length in the vapour:

$$dA_i = -ic^2 k_i \mu_0 \mathcal{N}\mu_{ij}\tilde{\rho}_{ij}dz \tag{2.37}$$

This is then used to alter the field Rabi frequency and then the system is recalculated and so on. In this way absorption can be taken into account, important in resonant sum frequency mixing, and the evolution of fields within the experimental path length followed.

2.3. N Level Rules

Various other level systems were used in this work and implemented as described above. Some of these will be described later in order to shed light on a certain problem or issue, while other systems not important in the overall thrust of this thesis will not be looked at in detail. However, after dealing with these various systems it became apparent that certain empirically derived rules could be used to write down the system matrix for many systems without reference to the Liouville equation, hence saving a full and time consuming derivation. These rules are summarised in Appendix A and are very useful if used with care and an appreciation of the nature of these systems.

2.4. Specimen Systems

As well as the cascade three-level system — described and discussed above — other three and four level systems were derived and are relevant to this work. Along with

the cascade system two others, the lambda three-level atom and raman inversionless laser, will be discussed below to demonstrate the power of these numerical models and their interpretation

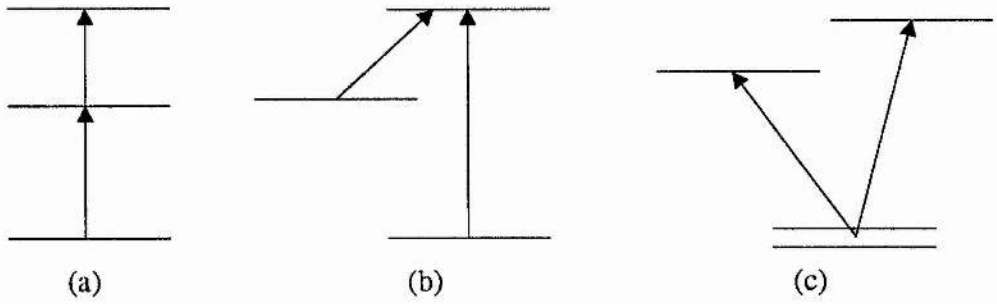

Figure 2.3: The three main atomic systems discussed: (a) the cascade and (b) the lambda configuration three-level atoms; (c) the "Raman" inversionless laser.

2.4.1. Cascade Three-level Atom

For sum frequency mixing in vapours the cascade three-level atom forms the basis of the enhancement structure. The incident lasers are tuned close to two transitions in series and the sum frequency output is produced on the return transition. Commonly the two input transitions are dipole-allowed and the return is dipole-forbidden, but allowed by a higher order process, and this forms the cascade system. The system is used throughout this work and has already been displayed (see figure 2.2) and its density matrix system equations have been derived (see equations 2.23).

The system was modelled using wavelengths and decay rates appropriate for the 3S-3P-3D level scheme in sodium. The sample output discussed below considers the case of a resonant lower laser and a scanning upper laser. Doppler broadening was included and the field strengths were relatively low, although well above the homogeneous saturation intensity levels for these transitions. The upper laser scan is chosen due to the experimental problems associated with a lower level scan ie. swiftly changing linear absorption and phase matching and the greater difficulty

with interpreting simultaneous changes in single- and two-photon resonances.

Populations

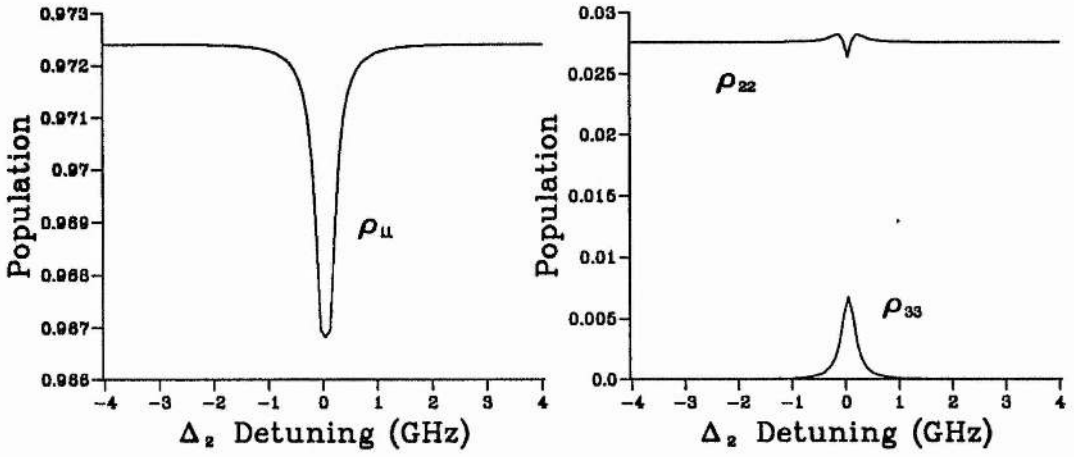

Figure 2.4: The population components of the density matrix for $\Omega_{12} = \Omega_{23} = 0.03$GHz.

The results for the populations of each of the levels are plotted in figure 2.4. Due to the steady, resonant lower laser field there is a constant low level of population transfer from level 1 to level 2 of around 3%. However, as the upper laser tunes across two-photon resonance ($\Delta_{13} = 0$) some population is excited into the uppermost level and this perturbs the others. The most notable factor in the predictions is the width of the resonant feature which is well below the Doppler width of some 2GHz. This is due to velocity selection in the excitation [4, 22]. This occurs as a velocity subset of atoms may have the correct Doppler shift to simultaneously bring both the atomic levels into single- and two-photon resonance (in this case, trivially $V_z = 0$) and a narrow resonance is observed. This effect will be discussed further in Chapter 5 as will the detailed shape of ρ_{22} which is due to an interference effect.

Coherences at the Laser Wavelengths

The feedback of the atomic system on the light at ω_1 is governed by the coherence element $\tilde{\rho}_{12}$. This is plotted in figure 2.5 and shows the fairly constant linear absorption experienced by this wave due to the negative imaginary part. Again as the upper laser tunes across two-photon resonance this is perturbed and the wave experiences some refractive index variations and a slight change in absorption.

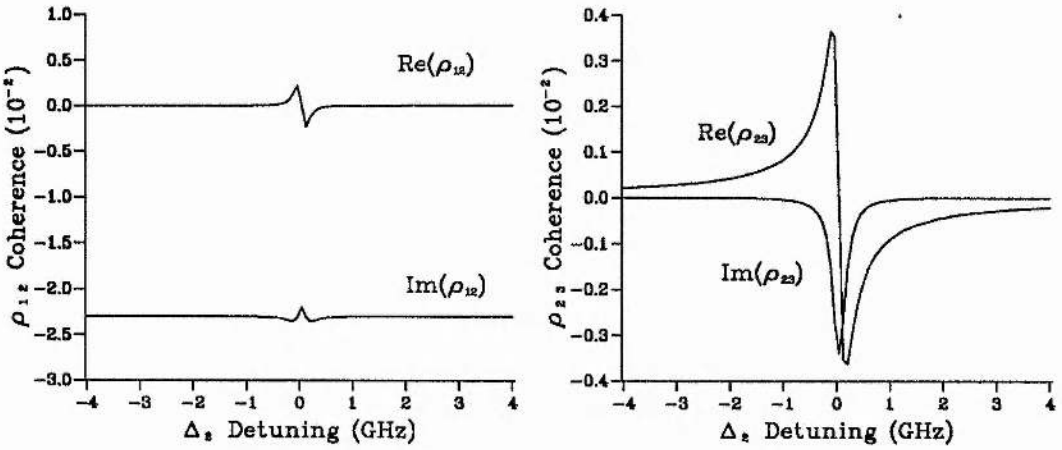

Figure 2.5: The coherence elements $\tilde{\rho}_{12}$ and $\tilde{\rho}_{23}$ for the same parameters as the previous figure.

The upper laser experiences a typical absorption and refractive index change for a wave tuning across an allowed transition sharpened by the velocity-selection mechanism. Note that the maximum absorption is an order of magnitude down on the level of that on the other field due to the lower population available in the intermediate level and the lower cross-section for two-photon absorption.

Sum Frequency Output

The usual splitting and linking of the real and imaginary parts of the coherences with refractive index and gain respectively, is not valid for $\tilde{\rho}_{13}$ as there is no input

field driving the coherence to reference against. Any polarisation produced on this transition will, if the matrix element is non-zero, lead to an output power proportional to the length of the coherence phasor, ie. $|\tilde{\rho}_{13}|^2$. The nature of $\tilde{\rho}_{13}$ is shown in figure 2.6.

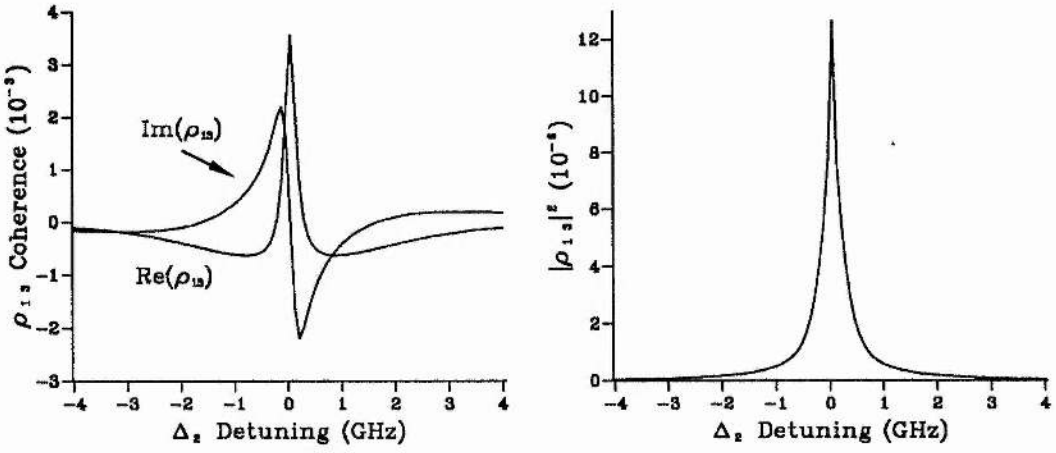

Figure 2.6: The coherence element $\tilde{\rho}_{13}$ and its square modulus for the same parameters as the previous two figures

Striking initially is the apparent swap of the functional forms of the real and imaginary parts in this coherence generated by the other two. However, the modulus behaves as may be predicted, showing a velocity-selected resonance. The Doppler broadened background is just visible as a pedestal to the main feature and enhances the flanks a little. Later chapters will deal in more detail with the features and behaviour of this coherence.

2.4.2. Lambda (Λ) Three-Level Atom

The "Lambda" configuration three-level atom is similar to the cascade system but with the top level folded down. Figure 2.7 shows it in detail. The lower levels may or may not be close together but this is only important if dealing with Doppler shifts which can cancel if ω_1 is close to ω_2. Transitions 1-3 and 2-3 are dipole allowed and

have incident waves near resonant with them, while transition 1-2 is forbidden. This system, much studied for electromagnetically-induced transparency and inversionless gain, is in its "ideal" form if level 2 is metastable and hence the population decay rate (Γ_{21}), and the coherence decay rate (γ_{12}), are both approximately zero.

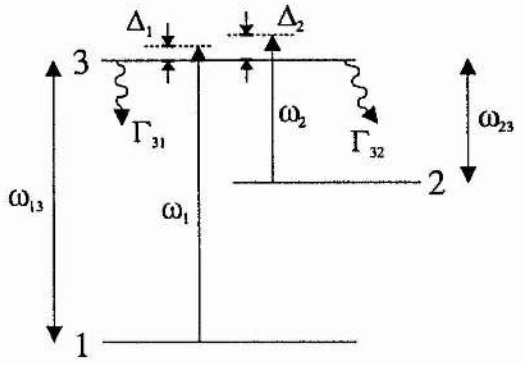

Figure 2.7: A Lambda configuration three-level atom

This system is associated with coherent population trapping, amoung other non-linear optical coherence processes, as the first observation of this phenomena was in such a system in sodium [23, 24]. The lower levels were the ground state (3S) sublevels and the upper level a 3P sublevel. In the strong field regime, ie. with field strengths greater than the saturation intensity for the various transitions it behaves in an analogous way to the cascade system and much of the mathematics and results can be taken over directly. The density matrix system equations are stated by Imamoğlu, Field and Harris [21] and include incoherent pumping terms to allow for inversionless gain. After conversion to a steady-state set of real simultaneous equations the system in matrix form is:

$$\begin{bmatrix} -R_{23} & R_{23}+\Gamma_{32} & 0 & 0 & 0 & 0 & 0 & 2\Omega_{23} \\ R_{23}-R_{13} & -R_{23}-2R_{13}-(\Gamma_{32}+\Gamma_{31}) & 0 & 0 & 0 & 0 & -2\Omega_{13} & -2\Omega_{23} \\ 0 & 0 & \gamma_{12} & 0 & 0 & \Delta_2-\Delta_1 & -\Omega_{23} & -\Omega_{13} \\ 0 & 0 & 0 & \gamma_{13} & 0 & -\Omega_{23} & -\Delta_1 & 0 \\ 0 & 0 & 0 & 0 & \gamma_{23} & \Omega_{13} & 0 & -\Delta_2 \\ 0 & 0 & \Delta_1-\Delta_2 & \Omega_{23} & -\Omega_{13} & \gamma_{12} & 0 & 0 \\ -\Omega_{13} & -2\Omega_{13} & \Omega_{23} & \Delta_1 & 0 & 0 & \gamma_{13} & 0 \\ \Omega_{23} & -\Omega_{23} & \Omega_{13} & 0 & \Delta_2 & 0 & 0 & \gamma_{23} \end{bmatrix} \begin{bmatrix} \rho_{22} \\ \rho_{33} \\ \rho_{12}^{r} \\ \rho_{13}^{r} \\ \rho_{23}^{r} \\ \rho_{12}^{i} \\ \rho_{13}^{i} \\ \rho_{23}^{i} \end{bmatrix} = \begin{bmatrix} 0 \\ -R_{13} \\ 0 \\ 0 \\ 0 \\ 0 \\ -\Omega_{13} \\ 0 \end{bmatrix} \quad (2.38)$$

where R_{13} and R_{23} are the incoherent pumping rates as defined in the paper.

Coherent population trapping is easily predicted in this system if the population of level 3 is monitored. Using a probe field of $\Omega_{13} = 0.5$MHz and a coupling field of $\Omega_{23} = 3$MHz (with spontaneous decay rates of $\Gamma_{31} = 2$MHz and $\Gamma_{32} = 5$MHz) and keeping in the homogeneously broadened domain, figure 2.8 was produced. The population of level 3 drops sharply to zero on two-photon resonance, with the peaks on either side split by $2\Omega_{23}$. This is exactly the effect observed by early workers [23, 25] and dubbed coherent population trapping. It should be noted that there is no threshold level for the coupling laser strength in a *purely* homogeneously broadened system of this kind and very narrow trapped regions are possible. Electromagnetically-induced transparency (EIT) is the same effect looked at in terms of the absorption of the probe laser instead of the upper level population. As shown on the right of figure 2.8 the coherence shows a similar sharp feature on two-photon resonance. The lineshapes consist of two homogeneously broadened resonances with their peaks separated by twice the coupling Rabi frequency (Ω_{23}). However, where they overlap instead of adding constructively the two features tend to cancel out due to a quantum mechanical interference in possible pathways.

These results were taken for the ideal case, that is for $\gamma_{12} = 0$. Only in this case will the trapping be complete and the medium completely transparent on double resonance. Numerical models allow these parameters to be easily changed and the general assumption of a very weak probe laser to be lifted. As an example figure 2.9 shows the effect of increasing γ_{12} which is the restricting parameter in this effect. As γ_{12} is increased the level of transparency lowers.

Why this is so can be appreciated by looking at the contributory terms to ρ_{13} for this system. In steady-state equation (1e) of reference [21] may be written as:

$$\rho_{13} = \frac{\frac{1}{2}i\Omega_{13}(\rho_{33} - \rho_{11}) - \frac{1}{2}i\Omega_{23}\rho_{12}}{(\frac{1}{2}\gamma_{31} - i\Delta_1)} \tag{2.39}$$

The first term in the numerator is fairly constant across two-photon resonance as the probe field only excites a small level of population into level 3 (a maximum of

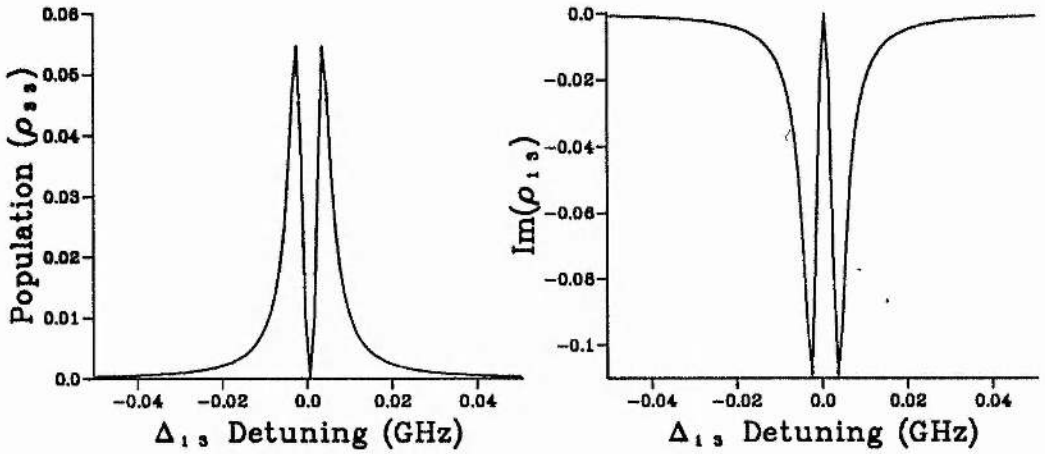

Figure 2.8: Coherent population trapping in the population of level 3 (left) and EIT in the probe absorption (right) for a lambda system.

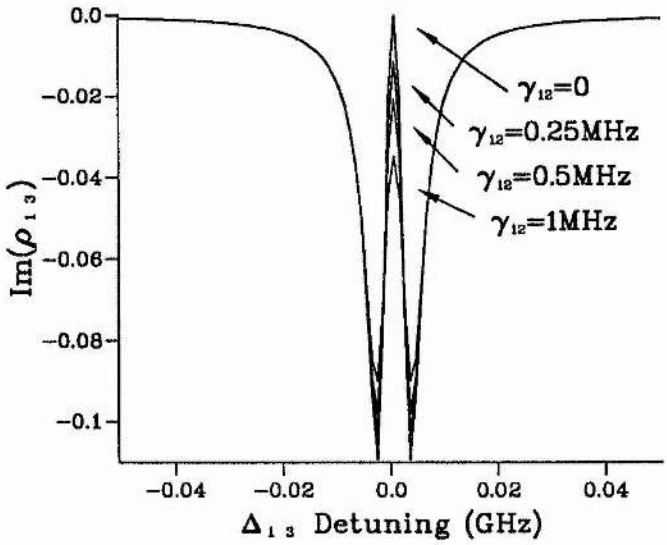

Figure 2.9: The effect of increasing γ_{12} on EIT.

6% in the above example). It is the feedback of ρ_{12}, the second term, that leads to the transparency and any additional damping on ρ_{12} will reduce its value and degrade the result. The other dephasing rates have little impact in the mechanism. A greater γ_{13} leads to a broader linewidth, within which the transparency manifests, but does not reduce it (see [26] for experimental proof of this) and γ_{23} has very little effect at all as the strong coupling laser outweighs it.

A prediction of inversionless gain may be straightforwardly produced by a non-zero incoherent pump rate R_{13} while a more detailed discussion on the mechanism and further requirements is given in reference [21] and other papers. Here, in figure 2.10, an example is given with $R_{13} = 0.7\Gamma_{31}$ and gain is clearly seen at the head of the transparency as the coherence becomes positive. The inset shows the three populations, with over 80% of the population remaining in the ground state, level 1, throughout proving the inversionless nature in the bare state basis.

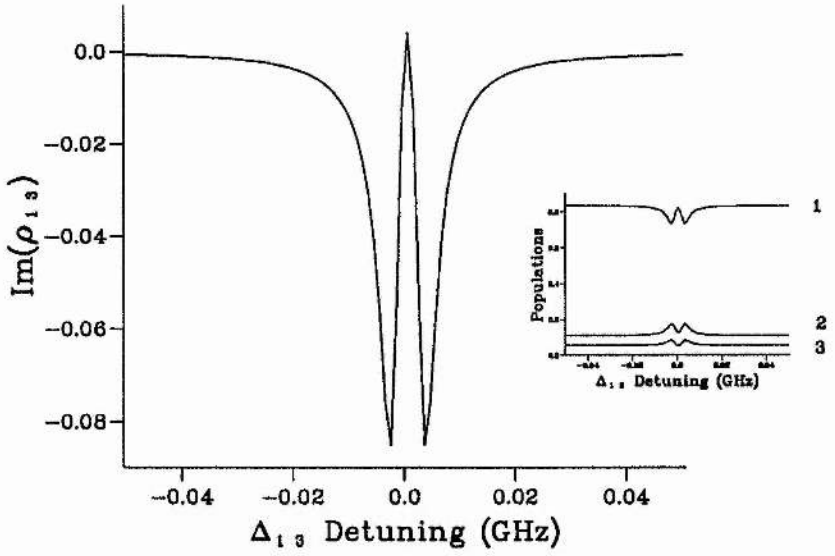

Figure 2.10: Inversionless gain in the Lambda configuration

2.4.3. Raman Inversionless Laser

The "Raman" four level inversionless laser system [27, 28] (see figure 2.11) has

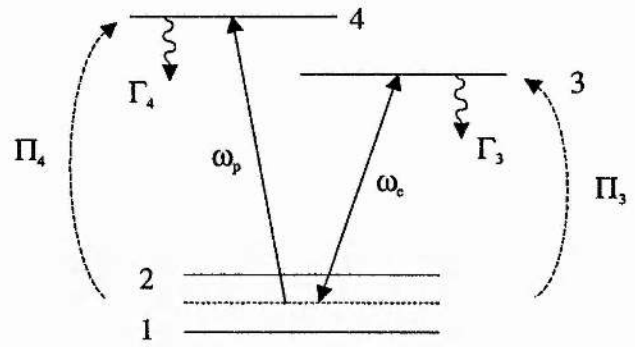

Figure 2.11: The Raman four level inversionless laser scheme.

been proposed as a useful system which combines two inversionless gain mechanisms [29] and can provide gain even when subject to Doppler broadening and collisions. The system consists of two closely spaced ground states both coupled to two upper levels. A strong coupling laser, ω_c, prepares the system and incoherent pumps provide for inversionless gain on the probe laser, ω_p, under suitable conditions. (See the cited papers for the density matrix system equations for the Raman inversionless laser. The numerical system used below was created via the rules of Appendix A.)

Previous theoretical treatments assumed generally low levels of Doppler broadening for such systems and so a model was developed, based on the 5S to 5P transitions of rubidium, to test whether inversionless gain could still be predicted under vapour cell conditions. The lower states were spaced by 3GHz, applicable to the ^{85}Rb isotope, and the pump and probe laser wavelengths chosen for the $5S_{1/2}$–$5P_{1/2}$ and $5S_{1/2}$–$5P_{3/2}$ transitions respectively. With an appropriate level of incoherent pumping and a sufficiently strong coupling laser gain could still be predicted, see figure 2.12. Here strong gain is predicted at $\pm$4GHz on either side of the ground state centre with only about 17% of the population in the upper laser level.

A numerical model such as this could be extended to deal with the evolution of the system as the laser field grows and deal with propagational effects in the medium, but that is not included in the scope of this work. However, their practicality and usefulness has been demonstrated in the examples above. Further results will be

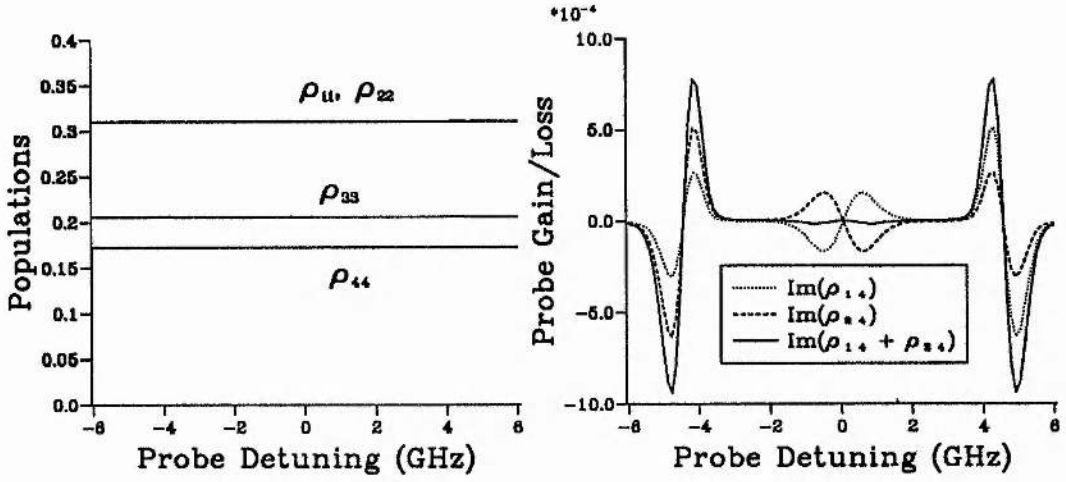

Figure 2.12: Probe gain in the Raman system for a coupling laser strength of Ω_c = 3GHz and a pump rate of Π_4 = 25MHz. (Γ_4 = 40MHz, Doppler broadening included for 600K.)

given in chapters 5–8 in the appropriate context when dealing with: interference effects in sum frequency mixing; the use of electromagnetically-induced transparency to reduce fundamental wave absorption; the local field correction for dense media; and lensing in EIT, respectively.

REFERENCES

[1] R. Loudon, *The Quantum Theory of Light, Oxford Science Publications*, 2 ed. (Oxford University Press, Oxford, 1991).

[2] Murray Sargent III, Marlan O. Scully, and Willis E. Lamb, Jr., *Laser Physics* (Addison-Wesley, Massachusetts, 1974).

[3] I. I. Rabi, N. F. Ramsey, and J. Schwinger, Use of rotating coordinates in magnetic resonance problems *Rev Mod Phys* **26**, 167 (1954).

[4] J. E. Bjorkholm and P. F. Liao, Line shape and strength of two-photon absorption in an atomic vapour with a resonant or nearly resonant intermediate state *Phys Rev A* **14**, 751 (1976).

[5] S .E. Harris, J. E. Field, and A. Imamoğlu, Nonlinear optical processes using electromagnetically induced transparency *Phys Rev Lett* **64**, 1107 (1990).

[6] E. U. Condon and G. H. Shortley, *The Theory of Atomic Spectra* (University Press, Cambridge, 1953).

[7] Amnon Yariv, *Optical Electronics*, 3 ed. (Holt-Saunders, New York, 1985).

[8] P. R. Berman, Effects of collisions on linear and non-linear spectroscopic line shapes *Phys Rep* **43**, 101 (1978).

[9] W. R. Hindmarsh and J. R. Farr, in *Collisional Broadening of Spectral Lines by Neutral Atoms*, No. 3 in *Progress in Quantum Electronics*, 1 ed., edited by J. H. Sanders and S. Stenholm (Pergamon Press, Oxford, 1972).

[10] R. Karplus and J. Schwinger, A note on saturation in microwave spectroscopy *Phys Rev* **73**, 1020 (1948).

[11] G. K. Woodgate, *Elementary Atomic Structure* (Clarendon Press, Oxford, 1980).

[12] R. G. Brewer and E. L. Hahn, Coherent two-photon processes : Transient and steady-state cases *Phys Rev A* **11**, 1641 (1975).

[13] P. R. Berman and Rainer Salomaa, Comparison between dressed-atom and bare-atom pictures in laser spectroscopy *Phys Rev A* **25**, 2667 (1982).

[14] Bruce W. Shore, *The Theory of Coherent Atomic Excitation* (Wiley, New York, 1990).

[15] Claude Cohen-Tannoudji and Serge Reynaud, Dressed-atom description of resonance fluorescence and absorption spectra of a multi-level atom in an intense laser beam *J Phys B: At Mol Phys* **10**, 345 (1977).

[16] Claude Cohen-Tannoudji and Serge Reynaud, Modification of resonance raman scattering in very intense laser fields *J Phys B: At Mol Phys* **10**, 365 (1977).

[17] B. R. Mollow, Stimulated emission and absorption near resonance for driven systems *Phys Rev A* **5**, 2217 (1972).

[18] M. Lewenstein, Y. Zhu, and T. W. Mossberg, Two-photon gain and lasing in strongly driven two-level atoms *Phys Rev Lett* **64**, 3131 (1990).

[19] William H. Press, Brian P. Flannery, Saul A. Teukolsky, and William T. Vetterling, *Numerical Recipes in C: The Art of Scientific Computing* (Cambridge University Press, Cambridge, 1988).

[20] Erwin Kreysig, *Advanced Engineering Mathematics*, 6 ed. (Wiley, New York, 1988).

[21] A. Imamoğlu, J. E. Field, and S. E. Harris, Lasers without inversion : A closed lifetime broadened system *Phys Rev Lett* **66**, 1154 (1991).

[22] Alistair J. Poustie, *Magnetic Field Induced Sum Frequency Mixing in Sodium Vapour*, PhD thesis, University of St. Andrews, 1990.

[23] G. Alzetta, L. Moi, and G. Orriols, Nonabsorption hyperfine resonances in a sodium vapour irradiated by a multimode dye-laser *Il Nuovo Cimento B* **52 B**, 209 (1979).

[24] E. Arimondo and G. Orriols, Nonabsorbing atomic coherences by coherent two-photon transitions in a three-level optical pumping. *Nouvo Cimento Lettere* **17**, 333 (1976).

[25] H. R. Gray, R. M. Whitley, and C. R. Stroud Jr, Coherent trapping of atomic populations *Opt Lett* **3**, 218 (1978).

[26] J. E. Field, K. H. Hahn, and S. E. Harris, Observation of electromagnetically induced transparency in collisionally broadened lead vapour *Phys Rev Lett* **67**, 3062 (1991).

[27] Ernst E. Fill, Marlan O. Scully, and Shi-Yao Zhu, Lasing without inversion via the lambda quantum-beat laser in the collision-dominated regime *Opt Commun* **77**, 36 (1990).

[28] L. M. Narducci, H. M. Doss, P. Ru, M. O. Scully, S. Y. Zhu, and C. Keitel, A simple model of a laser without inversion *Opt Commun* **81**, 379 (1991).

[29] C. H. Keitel, O. A. Kocharovskaya, L. M. Narducci, M. O. Scully, S.-Y. Zhu, and H.M. Doss, Two mechanisms for inversionless amplification in four-level atoms with raman pumping *Phys Rev A* **48**, 3196 (1993).

Chapter 3

Experimental Equipment and Atomic Systems

3. Experimental Equipment and Atomic Systems

This chapter details the experimental equipment assembled and used to study resonant sum frequency mixing in sodium vapour and electromagnetically-induced transparency in rubidium vapour. Modifications to one of the titanium sapphire lasers used in order to generate a mode-hop free scan are detailed. Later, the atomic systems used experimentally are described with their important parameters and the various level structures explained.

3.1. Laser Systems

This work concentrates on radiation-atom interactions with two important features. Firstly, the radiation must be coherent and powerful, thus implying the use of laser sources, and secondly the system must reach a steady-state, requiring these lasers to be continuous-wave in operation. Furthermore, the input sources were chosen to be of narrow spectral width in keeping with the assumption of monochromatic radiation and allowing sub-Doppler resolution in the vapour systems. Due to the wavelengths required by the atomic systems three tunable laser sources were used: a dye laser and two titanium sapphire lasers.

3.1.1. Pump Lasers

Continuous-wave (cw) mainframe argon-ion lasers provided the primary power source for the tunable lasers used in this work. Initially one Spectra-Physics 2030 laser [1] running at around 14W was split 50:50 to pump the two secondary lasers, and the work in Chapter 4 was carried out with this arrangement. Later, however, in order to increase the available power a second pump laser was added, a Spectra-Physics 2080 laser with BeamLock^{TM} [2]. This allowed independent pumping of the secondary lasers and greatly increased the slope efficiency of the titanium sapphire laser, its output power and the experimental flexibility.

3.1.2. Dye Laser ($\approx$ 589nm)

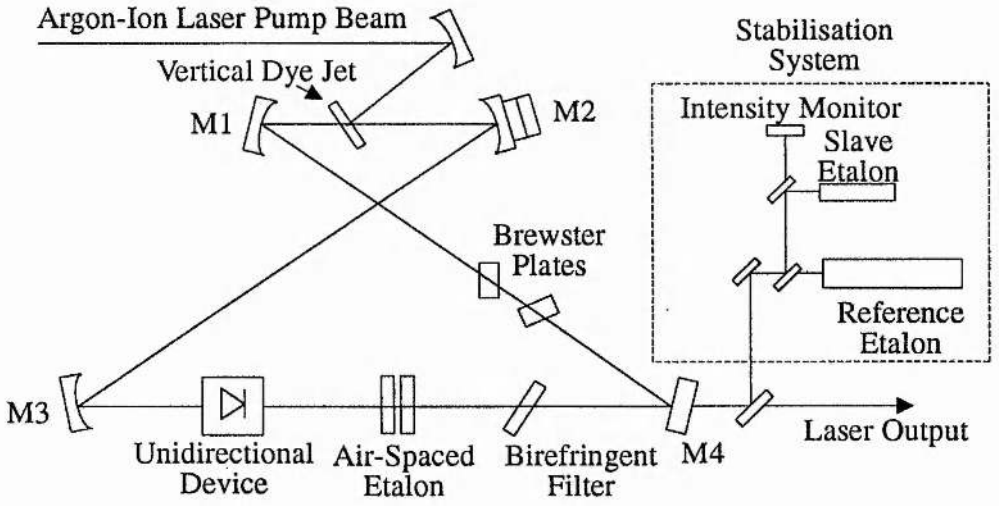

Figure 3.1: Schematic of the Spectra-Physics 380D Ring Dye Laser

A dye laser was the ideal source for the provision of tunable radiation around the orange 'D' lines of sodium, ie. the 3S-3P transition. The Spectra-Physics 380D used is a cw, frequency-stabilised, single-mode scanning system with a linewidth of approximately 1MHz and could scan up to 30GHz under the manufacturer's electronic control [3, 4]. The cavity design is a figure of 8 ring arrangement with a

unidirectional device and air-spaced etalon to ensure single-frequency operation, see figure 3.1. Rhodamine 6G dye was dissolved in ethylene glycol to provide the lasing medium and typically had an operating lifetime of around 6 weeks between dye changes. With a 7W all lines argon-ion laser pump source the dye laser produced up to 250mw at 589nm and constituted a reliable scanning source.

3.1.3. Schwartz Titanium Sapphire (750 → 820nm)

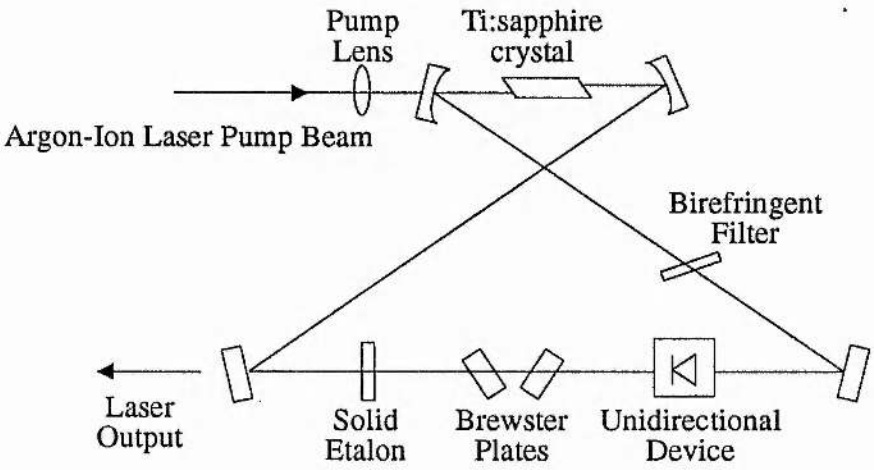

Figure 3.2: Schematic of the modified Schwartz Electro-Optic Titan-CW

The first titanium-sapphire laser (hereafter abbreviated to Ti:sapphire) used was a modified Schwartz Electro Optics Titan-CW model and very similar in concept to the dye laser. It is described in detail by Shepherd [5] and the cavity is displayed in figure 3.2. A single un-coated solid etalon of thickness about 1mm was sufficient to hold the unidirectional ring to a single longitudinal mode and galvo-mounted Brewster plates allowed the cavity length to be scanned. No commercial scanning or stabilisation system was included but the free-running linewidth was measured to be < 5MHz over short periods as long as the laser was insulated from acoustic noise [5, 6]. With an independent argon-ion laser pump the Ti:sapphire laser was capable of producing up to 1.3W of single-frequency radiation at a slope efficiency

of some 11%. (A second system including galvo mounted etalon and Brewster plates was evaluated for a period during efforts to develop a system capable of mode-hop free scans which, due to optimised output coupling and a improved crystal and optics, could extend single-frequency operation to greater than 2.4W.) The modular construction of the laser on its breadboard made modifications easy to include in the cavity and considerable effort was put into developing a scanning capability.

Scanning the Schwartz Ti:sapphire laser

Being able to scan the Ti:sapphire laser smoothly over several GHz to monitor spectral lineshapes was necessary for this work. Two elements need to be synchronised for this. Firstly the Brewster plates are tilted at the same rate in opposite directions to change the optical path length of the cavity. In this way the circulating laser mode is not deviated in spatial terms and the longitudinal mode frequencies of the cavity change linearly with angle. These modes are spaced by 250MHz in this laser and if the intra-cavity etalon remains stationary the laser will hop to a more favourable mode after around 125MHz cavity frequency shift. Therefore, it is necessary to move the peak of the etalon transmission band in precise synchrony with the cavity frequency change. The change in etalon peak position, in frequency terms, for angular changes from normal incidence is approximated by:

$$\Delta\nu = \frac{\nu\theta^2}{2n^2} \tag{3.1}$$

so the etalon angle, θ, must move as the square root of the Brewster plate angle.

Initial attempts at scanning the laser involved dead-reckoning of the voltages to be applied to the two galvos controlling the solid etalon and Brewster plates [5]. Partial success was achieved but the scan range was limited to less than 10GHz and day-to-day reliability was poor. The tolerances required on the galvanometers and electronics were simply to great and other workers report similar performances and conclusions [7]. Where the nature of the experiment would not show up the occasional 250MHz hop this method was suitable and allowed quick scanning. Im-

provements by computer generation of square root ramps, closed-loop galvanometers and more stable mounts could not significantly improve either performance or reliability. Therefore, an active feedback and lock technique was required in which the etalon was dithered over a small frequency range and an error signal was derived and used to keep the transmission peak on the cavity frequency. This has been used successfully by one group [8], however, other published systems incorporate an air-spaced thick etalon into the cavity and lock this to remove mode-hops [9, 10, 11].

Scanning by Solid Etalon Lock

Due to the expense and intra-cavity loss associated with a thick air-spaced etalon (some 50-60% in the dye laser) development of a dither and lock technique for the solid etalon was pursued. The concept followed that of Adams [7] and the Microlase MBR-110 commercial system developed from that work.

In this scheme the thin, solid etalon is dithered in angle by a small ac signal. This leads to two possible error signals which can be detected. In the first method, the intra-cavity power is modulated due to the changing etalon loss — which can be detected externally as a modulation on the laser output. When detected with a phase sensitive detector, referenced to the original dither, an error signal is produced. If the etalon is correctly centred over the cavity mode the error signal is zero and on either side it has a finite value with sense appropriate to the direction of misalignment. Alternatively, the etalon reflection is modulated as the etalon transmission frequency is changed and the product of this and the intra-cavity power may be detected by tilting the etalon a degree or so off axis and imaging the reflected beam on a photodiode. Phase sensitive detection leads to an error signal exactly as before. Either of these error signals may then be integrated and applied either as an addition to an estimated etalon tuning voltage or on their own.

Using un-coated solid etalons of various free spectral ranges between 115GHz and 225GHz both of these error signals were used to try to gain a reliable lock.

Dither was applied either directly down the galvanometer ($\leq$ 1kHz) or by a split piezo arrangement at higher frequencies. A good error signal was detected with a strong background, and locking achieved by subtraction of this. However, when scanning was attempted the background would alter and lock would be lost when the background had changed by a sufficient amount, typically after 1–2GHz. This background had a sinusoidal nature, in contrast to the square law offset observed by Adams, and was measured to have a period of about 16GHz and was thought to be due to some weak etalon in the cavity. Attempts to remove it failed and while use of 20% reflection coated solid etalons improved the error signal to background ratio they did not help sufficiently. Furthermore, attempts to sample the offset and correct for it by computer control proved unreliable and slow. Therefore, locking by the solid etalon alone was abandoned.

At this point it is interesting to note that during attempts to scan the Ti:sapphire laser in this way notable hysteresis was observed in the mode-hopping behaviour. Such hysteresis has been studied in an argon-ion laser [12] but to our knowledge has not been observed in the titanium sapphire laser. Due to the complicated cavity and many optical elements no systematic study was made of this and it is left for later detailed study.

Scanning by Air-spaced Etalon Lock

Due to the problems experienced in removing mode-hops with the solid etalon alone, an air-spaced etalon was incorporated in the laser cavity. Such etalons are spaced by a piezo-ceramic element and can be precisely scanned without changing the intracavity loss. They generally have a shorter free spectral range and so have better discrimination between adjacent cavity modes and due to their design have better stability. Unfortunately they may be expensive and may introduce substantial loss into the laser cavity, but they have been used satisfactorily in scanning dye laser systems for some time.

The air-spaced etalon used was a recovered Coherent 599 dye laser etalon of free spectral range 10GHz. The patented design of this etalon uses Brewster cut inside faces to reduce loss and the piezo scanning components are so mounted as to keep the optical path length of the cavity constant while the etalon pass band is moved. The coatings were wide-band and specified usable for Styryl-9 dye which lases up to 900nm [13]. This etalon was incorporated in the cavity and could be scanned by the application of a voltage within the range 0-900 volts. The laser output power was not lowered significantly by the introduction of the etalon, probably due to the low-loss Brewster angled faces. A 2KHz dither was applied and the error signal monitored via the modulation impressed on the laser output power. Phase sensitive detection and integration provided the feedback and a high voltage amplifier then powered the etalon. This system is shown in figure 3.3.

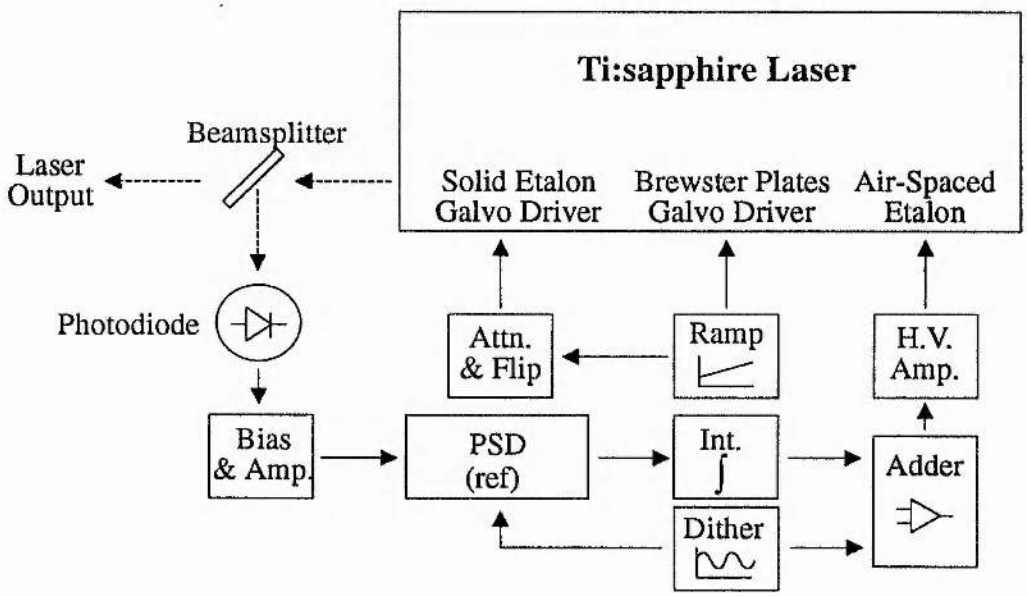

Figure 3.3: Dither-and-Feedback system for scanning the Ti:sapphire without mode-hops. (Attn & Flip = Attenuation and direction control.)

Results were good for this system, the error signal strong and the lock steady. As the etalon remained at near normal incidence in the cavity and the cavity optical

length was not altered by the dither, due to the etalon design, there was no changing offset on the error signal. The thinner solid etalon was still necessary in the cavity to prevent 10GHz hops between the air-spaced etalon modes but its specifications were relaxed and an un-coated 115GHz free spectral range device proved sufficient. Reliable scans up to 10GHz were achieved using a simple linear feedback on to the thin etalon. Further range, if required, could be achieved by more accurate synchronisation of the thin etalon via a square root circuit and improved high voltage amplifier range, which was limited to 0-200 volts in this work (sufficient for a shift of two free spectral ranges of the air-spaced etalon pass-band). This scanning capability was used for the experimental work described in chapter 5.

3.1.4. Microlase Titanium Sapphire ($\approx$ 780nm)

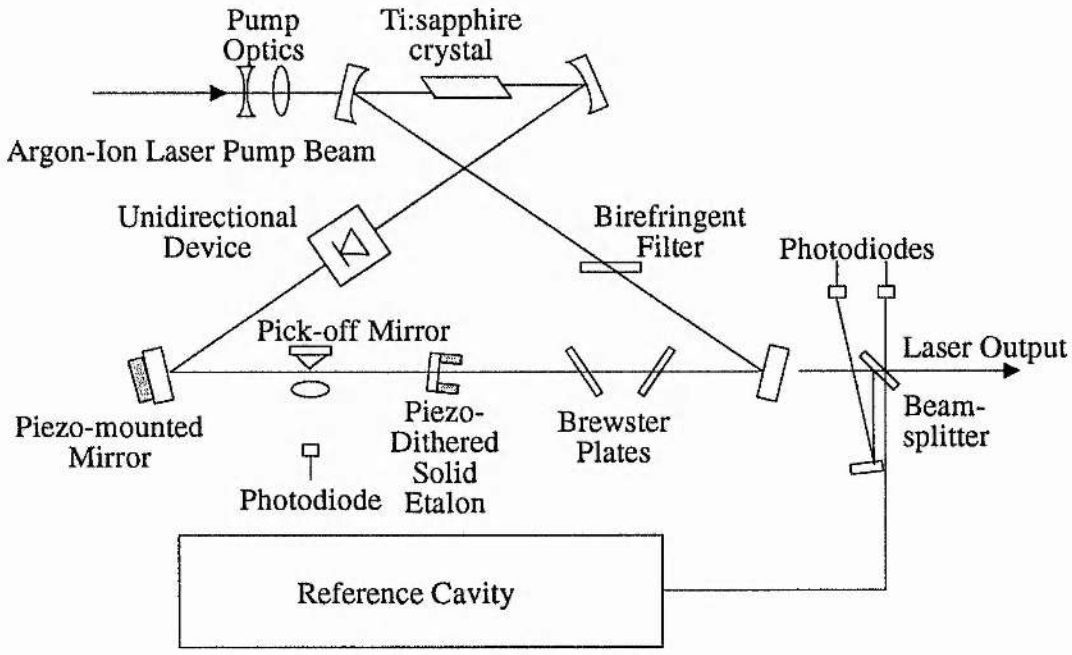

Figure 3.4: Schematic of the optical arrangement of the Microlase MBR-110.

For the later work in rubidium vapour (chapter 8) a second titanium sapphire laser was required as the two transition wavelengths both fell outside the range of

the dye laser. In order to meet future requirements, which include the possibility of rubidium beam work, the Microlase MBR-110 laser system was chosen as the specifications included high stability and frequency scanning operation. The design is, like the Schwartz system, a unidirectional ring and is shown in figure 3.4. However, the Microlase system incorporates frequency stabilisation via side-of-fringe locking in an external, temperature-controlled confocal etalon [14]. With this locking active, linewidths of $\leq$ 200kHz are specified. Furthermore, microprocessor controlled scans of the laser (up to some 30GHz) may be initiated by the control unit and mode-hop free operation is attained by the servo lock of the single solid etalon in the cavity. Excellent passive stability is gained by the monolithic block within which the resonator is housed. Output powers were strongly dependent on the state of cleanliness of the laser (which degraded over a few days) but a slope efficiency of between 12 and 20% was realised for 6–12W argon laser pump input power.

3.2. Other Experimental Equipment

3.2.1. Laser diagnostics

Single-frequency operation of the lasers was monitored using separate piezo-tuned confocal Fabry-Perot interferometers of free spectral range 1.5GHz. They were also used as a guide to detuning measurements from a given point and when the voltage ramp was removed provided 1.5GHz marker fringes as a frequency axis for laser scans. A low-finesse etalon of free spectral range 300MHz was used to monitor the scanning of the Microlase Ti:sapphire laser in the rubidium work.

In order to measure and set the absolute frequency of the laser systems a Kowalski-style travelling wavemeter was used, capable of 1 part in 10^6 accuracy. This was achieved in a double Michelson interferometer arrangement with a scanning arm. Fringe-counting compared the wavelength of the incident light with that of a polarisation-stabilised helium-neon laser and the operating wavelength range was very wide due to the use of aluminium coated reflective optics. A full descrip-

tion is given by Kane [15]. Accuracy was sufficient to place the lasers within an etalon mode of the relevant atomic transition, typically within a few GHz.

Spectroscopic means were also used to determine absolute frequency. A sodium spectroscopic cell, described below, was used to determine single or double resonance conditions in the sum frequency mixing schemes by monitoring sideways 589nm or 819nm fluorescence. Fluorescence was also monitored from the rubidium cell, principally 421nm radiation from the 6P–5S transition, which was produced via spontaneous decay from the 5D levels.

3.2.2. Signal Detection and Collection

A schematic of the whole sum frequency mixing experiment is shown in figure 3.5. The dye laser beam was chopped at a few hundred Hertz and phase sensitive detection used to raise the signal-to-noise levels. Primary sum frequency detection (at either 342nm or 330nm) was by a Hamamatsu 931B photomultiplier tube. The initial radiation fields were screened off by 1 or 2 UG11 filters, and during work on the 3S-3P-4P system an extra BG38 filter removed the residual infra-red Ti:sapphire radiation that leaked through due to a small parasitic pass band in the UG11 filters. Neutral density filters or graduated wheels were used to control input beam powers and similar filters were used to cut down the strong UV signals detected, which at times overloaded the phase sensitive detectors (Brookdeal Type 401, later Stanford Research Systems SR510).

For sum frequency mixing the beams could be introduced into the oven either unfocused or focused. For the experiments of chapter 5 the beams were always unfocused, while the description surrounding the results presented in chapter 4 specify which lens was used.

The experiments on electromagnetically-induced transparency in rubidium used a different experimental configuration, due to the requirement for counter-propagating probe and coupling laser beams. This setup is shown in figure 3.6. The coupling

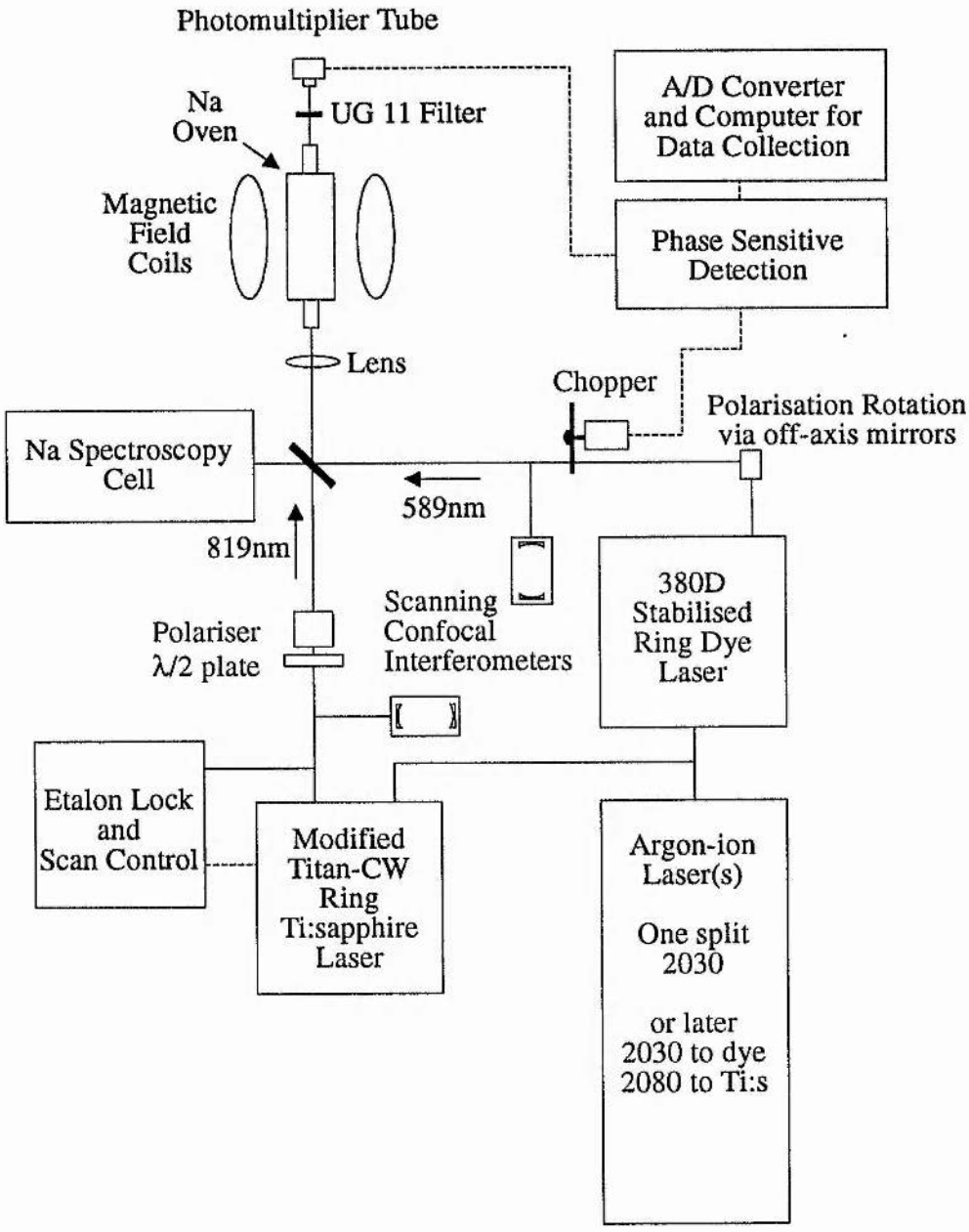

Figure 3.5: General experimental diagram for sum frequency mixing in sodium vapour

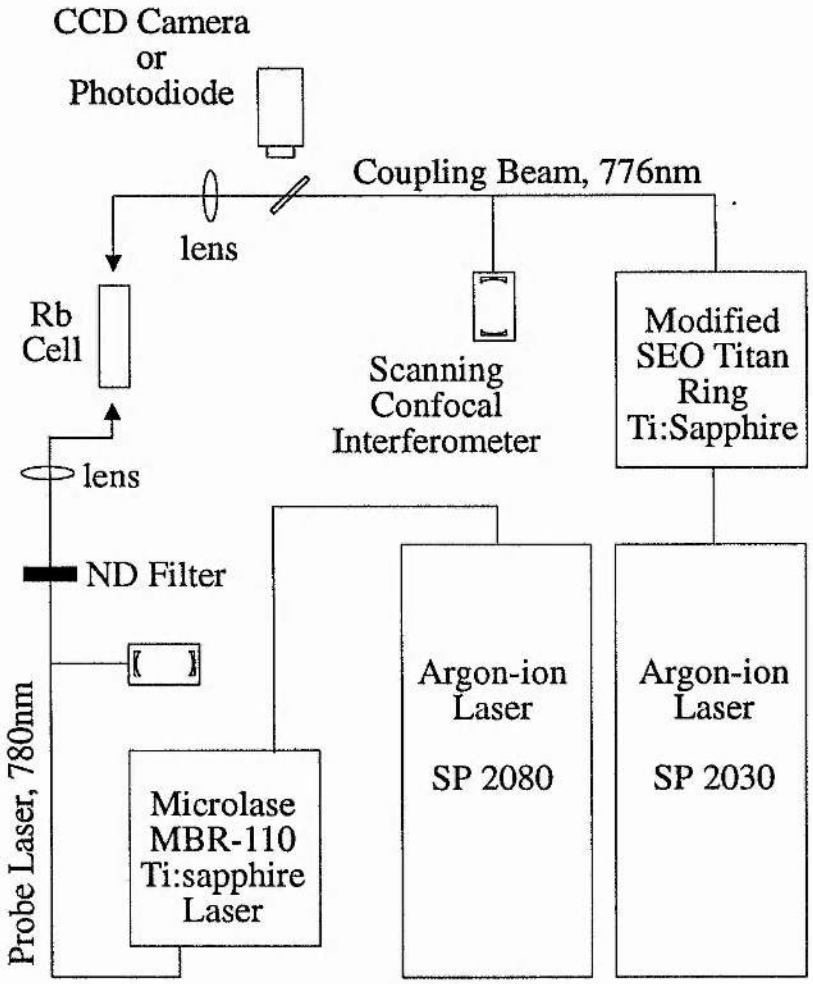

Figure 3.6: General experimental diagram for electromagnetically-induced transparency experiments in rubidium vapour

beam was focused into the vapour cell by a 50cm lens, while the probe laser was focused in from the other end by a 40cm lens. This combination of optics was chosen to give the tightest coupling laser beam waist while still retaining a confocal parameter of similar length to the 10cm long vapour region. The shorter focal length lens in the probe beam ensured that the probe beam was contained within the coupling laser beam at all times within the vapour. The probe radiation was reduced in power to the sub-milliwatt level by ND filters to avoid saturation of the initial transition. A pellicule beamsplitter after the lens sampled a portion of the transmitted probe radiation for detection, either on a wide area photodiode, or a CCD camera.

Data collection in both experiments was achieved via a 12-bit 16-channel A-to-D board (Amplicon Liveline PC30AT) fitted within a 486 PC (Elonex PC-433). Software allowed timed sampling either from a commercial program (Amplicon Dash-300) or in-house written utilities for more specific applications using provided software drivers. A multi-channel connection box was constructed to feed the individual channels to standard BNC connectors via 12V diode clamps for on-board chip protection and by variable potential dividers to cut large voltages down to the switchable operating range (maximum $\pm$12V) of the board. The board also incorporated two D-to-A output channels (used during Ti:sapphire scanning trials) and several digital in/out control lines. It proved to be a relatively cheap and flexible interface between computer and experiment.

3.3. Vapour Systems

The sodium and rubidium vapours used as the atomic media for study in this work were produced in simple ovens and cells. The oven was used when high densities of vapour were required (ie. temperatures in excess of 200^0C) and therefore mainly during SFM experiments.

The oven is shown schematically in figure 3.7 and consists of an insulated cylindrical body without any lining. Heat-pipe ovens include a wick and can produce

more uniform vapour regions[4, 16] but that was not necessary in this work where the oven was merely designed to restrict the vapour region to between the poles of the magnet. Cooling water running through flanges at the ends of the oven helped condense the sodium within the oven to reduce contamination of the oven windows, which were held out from the oven by glass tubes. However, after prolonged use at high temperatures the sodium metal within the oven would migrate to the ends where the cooled surface ensured it did not re-evaporate and thus it was effectively removed from the active region of the oven. When this occurred, simply opening the oven, under a flowing nitrogen gas environment, and scraping the metal back into the oven centre returned the metal for use. The temperature was controlled by a three-term device (FGH Controls Ltd S900-K-2-0-240) and monitored by a type K thermocouple. The vapour temperature was somewhat lower than this reading, due to heat gradients in the walls and vapour region, by up to 40 degrees at high temperatures so it was an approximate measure only.

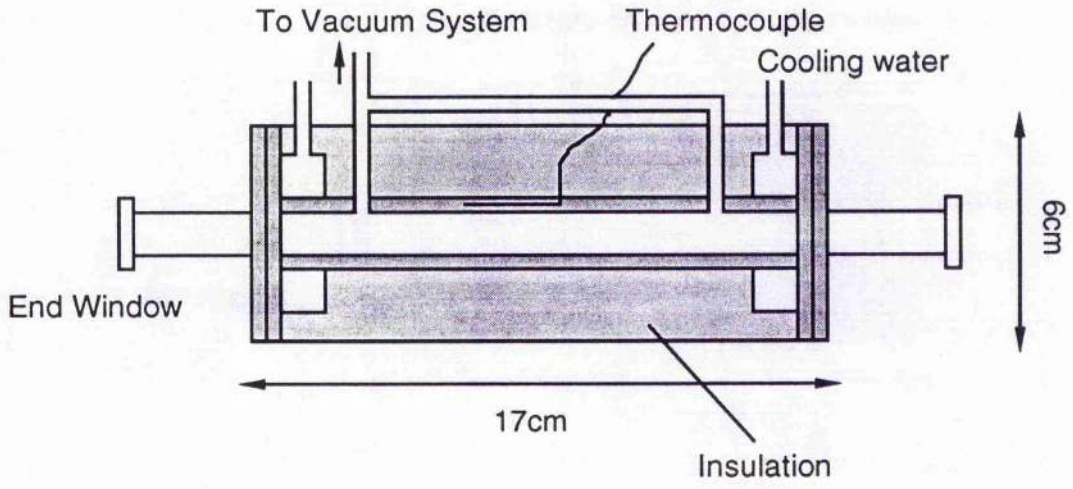

Figure 3.7: Schematic of the sodium vapour oven

Loading of the sodium metal was carried out while flowing nitrogen through the oven. The metal was cut from blocks stored under paraffin and washed in petroleum spirit before dipping in ethanol to remove the oxidised surface layer. A second rinse

in petroleum spirit then preceded loading into the oven. Once sealed the oven was pumped down and cycled a couple of times through heating and pumping to let the system outgas and remove any impurities. During normal operation a quantity of buffer gas, usually 1–2mbar argon, was added to the oven to reduce sodium–sodium collisions.

Smaller vapour cells were also used in this work. A quartz sodium cell of length 13cm and diameter 2cm [16] was used for saturated spectroscopy and for experiments out of the magnetic field. The body was heated to 190^{0}C from the mains supply using a Variac transformer to reduce the voltage to around 20 volts. The tip-off stem was kept 10–15^{0}C lower in temperature so that sodium tended to condense here and not on the end windows, and this was controlled by a Digitron 3800-K temperature controller. A static 240:15V transformer and a separate variable transformer allowed some degree of control on the current in the heating element so that the on-off cycles were slowed down.

For rubidium experiments a similar quartz cell was purchased from Opthos Instruments Inc. of length 10cm and diameter 2.5cm. This was supplied having been evacuated to 10^{-6}torr before filling with Rb and sealing. It was heated in the same jig used for the above sodium cell.

To calculate the vapour densities produced the empirical relation of Miles and Harris [17] was used. This is valid for vapour pressures around 1 torr (as typical in this work) and is:

$$N = \frac{9.66084 \times 10^{24}}{T} \exp\left[-\frac{a}{T} + d\right] \tag{3.2}$$

where N is in units of atoms/m^3, T is the Kelvin temperature and the constants a and d are given in table 3.1 for the appropriate element.

A transverse magnetic field, required for symmetry breaking in second order nonlinear processes, was produced by a Newport type A electromagnet. This had pole pieces of length 10cm which roughly matched the vapour length in the sodium oven. Fields of up to 0.4T could be produced with a calibration of 0.045T/amp

Element	*a*	*d*
Na	12423.3	17.3914
Rb	9140.07	16.0628

Table 3.1: Vapour pressure constants.

gained from Zeeman splitting measurements.

3.4. Atomic Systems: Na and Rb

The atoms used in this work were alkali metals and were chosen for their suitability for study with dye and Ti:sapphire lasers. These atoms have the advantage of having one unpaired electron in the outermost orbit and, as such, are amenable to theoretical study. However, the energy levels are not single well spaced levels due to the effects of fine and hyperfine structure removing the degeneracies of the sub-levels. In the next subsection I will summarise the relevant aspects of the coupling systems and then detail the parameters for the two elements.

3.4.1. Spin-Orbit Coupling: Fine Structure

Spin-orbit couping has been treated in many texts [18, 19] and is caused by the intrinsic spin of the electron interacting with the magnetic moment caused by the electron's orbit. Therefore, it is strongest in states of lower quantum number and only occurs where the orbit has angular momentum, ie. $L > 1$.

The two angular momenta, orbital and spin, are coupled to produce states labeled by $\mathbf{J}$ and m_J, where $\mathbf{J} = \mathbf{L} + \mathbf{S}$. Therefore, by the Clebsch-Gordon series there are discrete states for $|L - S| \leq J \leq L + S$ with degeneracy $2J + 1$ as denoted by the m_J value. Spin-orbit splitting is inversely proportional to radial distance from the nucleus and thus is large for low lying P states and, while much smaller, still important for D states. In one electron systems the J=L-S and J=L+S states are

separated by ΔE_F where ΔE_F is related to the fine structure constant, A_F by:

$$\Delta E_F = \frac{A_F}{2}(2L+1) \tag{3.3}$$

The new wavefunctions can be related to the original L, S, m_L and m_S basis by means of Clebsch-Gordon coefficients or the 3-j symbols which describe the coupling of two angular momenta [18, 20].

3.4.2. Hyperfine Structure

A further, and weaker, perturbation on the atomic Hamiltonian is caused by the finite size of the nucleus causing a nuclear magnetic moment. This can then couple to the total angular momentum, **J**, and cause further sublevel structure. In general the splittings, termed hyperfine structure, are very small, especially for levels whose wavefunction has minimal overlap with the nucleus. The ground and, to a lesser extent, the first excited states of alkali atoms, however, exhibit fairly strong coupling and have structure on the order of a few MHz to a few GHz.

The coupling of **J** to the nuclear spin, denoted by **I**, leads to a basis described by **F** and m_F, where $\mathbf{F} = \mathbf{J} + \mathbf{I}$. This basis has similarities to that of spin-orbit coupling by again being the coupling of angular momenta. In the S states, where there is no spin-orbit coupling as $L = 0$ and $J = \frac{1}{2}$, hyperfine structure can be said to directly replace fine structure and the mathematics are directly analogous with the substitution of $J \rightarrow F$, $L \rightarrow J$ and $S \rightarrow I$. Here again, the new basis is related to the original atomic basis by 3-j symbols. For states where there is spin orbit coupling ($L \geq 1$) the hyperfine structure provides further structure, on a smaller scale and the coupling of the three angular momenta can be described by means of 6-j symbols [18, 21].

For $J = \frac{1}{2}$ states the two hyperfine structure states, $F = I + \frac{1}{2}$ and $F = I - \frac{1}{2}$ states are displaced by ΔE_{HF} which is related to the hyperfine dipole constant [22], A_{HF} by:

$$\Delta E_{HF}(F) = \frac{A_{HF}}{2}[F(F+1) - I(I+1) - J(J+1)] \tag{3.4}$$

The $J = \frac{3}{2}$ state structure depends also on the quadrupole hyperfine constant, B_{HF}, and is described by:

$$\Delta E_{HF}(F) = \frac{A_{HF}}{2}\kappa + \frac{B_{HF}}{4}\frac{\frac{3}{2}\kappa(\kappa+1) - 2I(I+1)J(J+1)}{I(2I-1)J(2J-1)} \tag{3.5}$$

with $\kappa = F(F+1) - I(I+1) - J(J+1)$.

3.4.3. The Sodium Atomic Levels

Sodium exists in one stable isotope, ^{23}Na, and has been extensively used for research into the interaction of radiation and atomic systems due to the fortunate spacing of the 3S ground state and 3P excited states, the so called D lines, corresponding to a visible orange wavelength of 589nm. Figure 3.8 shows the levels relevant to this work and the wavelengths for transitions between them. The wavelengths quoted are for air assuming a refractive index of 1.0002766 [23], which is an important correction for high resolution spectroscopy. Where the levels have important fine or hyperfine structure within the Doppler width, but greater than the homogeneous linewidth, the appropriate splittings are shown in detail in figure 3.9.

Level	A_F/GHz
3P	343.7
4P	112.5
3D	-0.592

Table 3.2: The fine structure constants for sodium

The fine structure of the relevant sodium levels was measured some time ago [24] and the constants for the 3P, 3D and 4P levels are given in table 3.2. Note that the D states of sodium are inverted in their fine structure due to a relativistic effect and hence are quoted with a negative fine structure constant. Furthermore, the hyperfine structure of these levels has been the subject of several investigations, reviewed in

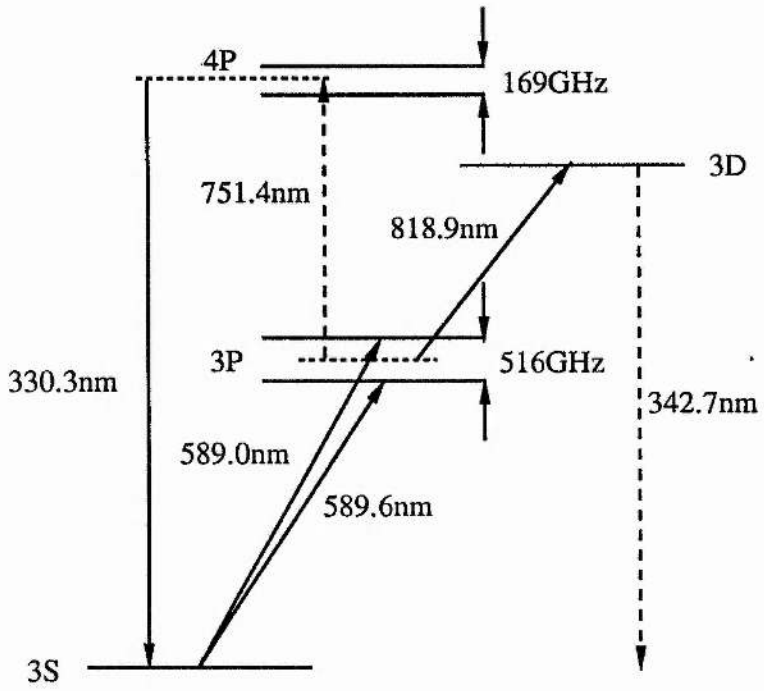

Figure 3.8: A partial energy level diagram for sodium. Selected transitions are shown and the large fine structure splitting for the 3P and 4P levels. Dipole-forbidden, quadrupole-allowed transitions are indicated by dotted arrows.

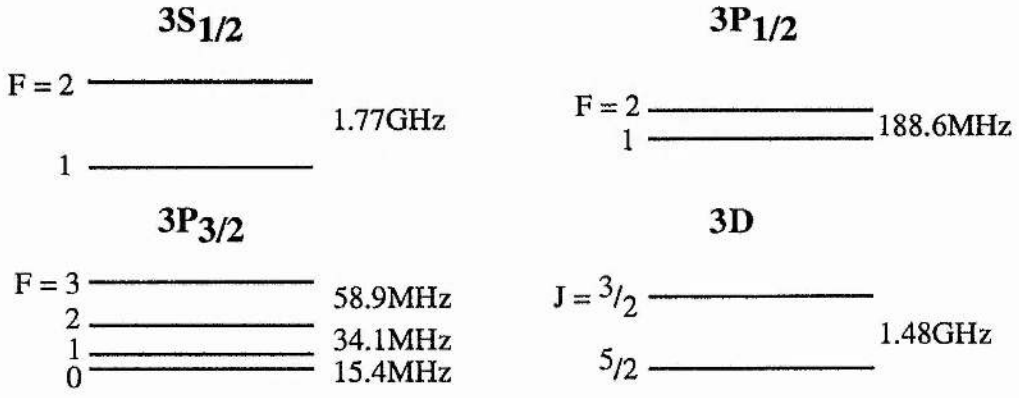

Figure 3.9: The small scale splitting of sodium atomic levels relevant to this work.

[22], and table 3.3 lists the appropriate constants and tolerances. (The 3S constant is now known to a degree of accuracy in excess of the number of significant figures displayed.) Only the 3S and 3P levels are included as they are the only levels to have significant structure. The hyperfine splitting for the 4P levels is around 8MHz and hence within the natural linewidth and the 3D levels have similar unresolved structure.

Level	A_{HF}/MHz	B_{HF}/MHz
3S	885.813	
$3P_{1/2}$	94.3 ± 0.1	
$3P_{3/2}$	18.7 ± 0.1	3.0 ± 0.2

Table 3.3: The hyperfine structure constants for sodium

Level	t_{spont}/ns	
3P	$(J = \frac{1}{2})$ 16.14	$(J = \frac{3}{2})$ 16.09
4P	$(J = \frac{1}{2})$ 107	$(J = \frac{3}{2})$ 106
3D	$(J = \frac{3}{2})$ 19.44	$(J = \frac{5}{2})$ 19.47

Table 3.4: Natural lifetimes for the sodium energy levels

The natural lifetimes of the various levels have either been measured or calculated by various means. Theodosiou [25] has undertaken calculations of extensive numbers of levels in alkali atoms and compares them to experimental data, where that exists. His results are displayed in table 3.4 and experimental values are within 10%, or much better, of these. The natural linewidths, $\Delta\nu_{\text{spont}}$ may be calculated from:

$$\Delta\nu_{\text{spont}} = \frac{1}{2\pi t_{\text{spont}}} \tag{3.6}$$

and are 10MHz, 8MHz and 1.5MHz for the 3P, 3D and 4P levels respectively.

3.4.4. The Rubidium Atomic Levels

The other alkali metal vapour used in this work was that of rubidium. This element was chosen as having several transitions ideal for study using a Ti:sapphire laser, and in the future by diode laser technology. The first excited state transitions, 5S to 5P, are 795 and 780nm — near the peak of the Ti:sapphire gain curve and readily suited to present diode lasers.

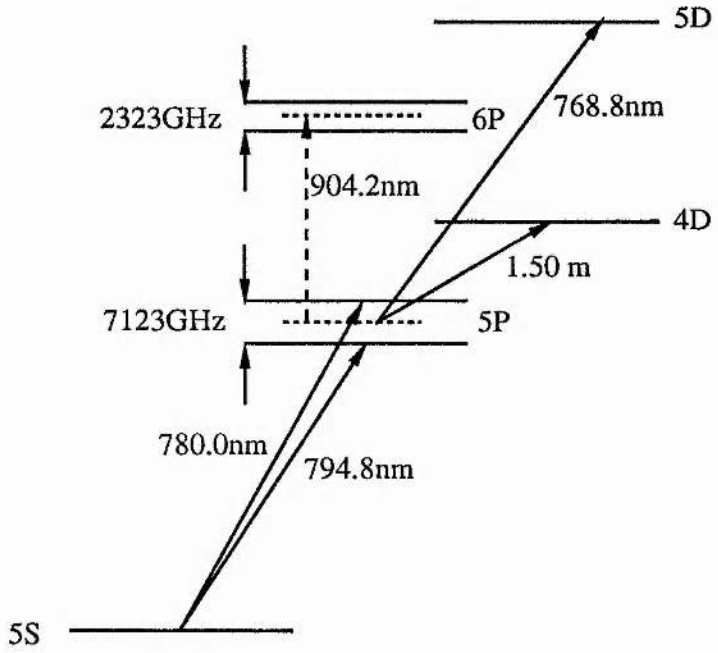

Figure 3.10: A partial energy level diagram for rubidium. Selected transitions are shown and the large fine structure splittings for the 5P and 6P levels are indicated. Dipole-forbidden, quadrupole-allowed transitions are indicated by dotted arrows.

Rubidium is two places down group one in the periodic table and , as such, is more reactive than sodium and melts at a lower temperature, 39^{0}C. It has atomic number 37 and the lone outer electron is in a 5s orbital making the energy level structure similar to sodium, but at n+2, as shown in figure 3.10. Unfortunately, from the experimenter's point of view, it exists in two stable isotopes: ^{85}Rb and ^{87}Rb. The relative abundances are 72.12% for ^{85}Rb and 27.83% for ^{87}Rb and the

nuclear spin varies between them, $I = \frac{5}{2}$ for ^{85}Rb and $I = \frac{3}{2}$ for ^{87}Rb [26].

Isotope	^{85}Rb		^{87}Rb	
Level	A_{HF}/MHz	B_{HF}/MHz	A_{HF}/MHz	B_{HF}/MHz
$5S_{1/2}$	3417.35		1011.9	
$5P_{1/2}$	120.72		406.2	
$5P_{3/2}$	25	26	84.8	12.6

Table 3.5: The hyperfine structure constants for rubidium

The difference in nuclear spin between the two isotopes and different hyperfine structure constants leads to a relatively complex sublevel structure. The fine structure constant for the 5P level is $A_F = 4.749$THz [24] and the hyperfine structure constants are tabulated in table 3.5 [22]. However, due to the smaller Doppler width in the D line transitions (approx. 500MHz) the two isotopes are resolved in their unperturbed transitions from the ground state. Figure 3.11 shows the hyperfine structure on the 5S to 5P transitions. Note the large ground state splitting, especially in ^{87}Rb.

Theodosiou [25] does not discriminate between the isotopes in his lifetime calculations and obtains values of 27.04nsec and 25.69nsec for the $5P_{1/2}$ and $5P_{3/2}$ levels respectively. The quoted experimental results indicate that these are reasonable figures and this gives a natural linewidth of around 6MHz for these transitions. The $5D_{3/2}$ and $5D_{5/2}$ levels have calculated lifetimes of 239.72nsec and 231.48nsec, respectively, implying 0.7MHz linewidths. However, the A coefficient for the 5P–5D transition is somewhat lower than that calculated from this decay rate as the 5D spontaneous decay is split between the 6P and 5P levels. From [27] the oscillator strength for the 5P–5D transition is quoted as 3.44×10^{-3} which implies [28] a decay rate on the $5D_{5/2} \rightarrow 5P_{3/2}$ transition of $A = 254 \times 10^3 s^{-1}$.

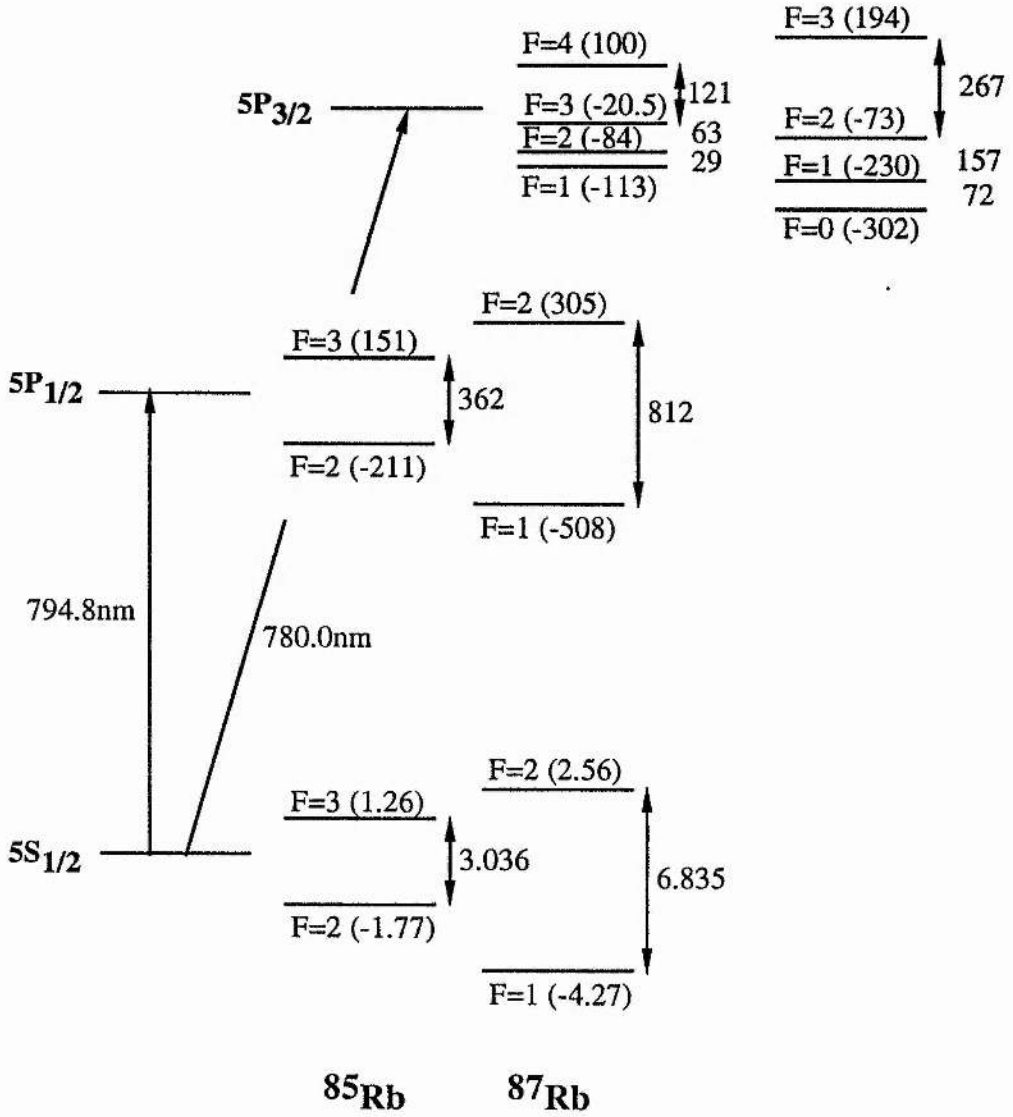

Figure 3.11: The hyperfine structure of the rubidium D lines for each isotope. Note that the unit for the ground state splitting is GHz, while MHz is used for the two 5P levels.

3.4.5. Rabi Frequencies and Matrix Elements

When dealing with the coherent interaction of laser radiation and an atomic system a key parameter is the Rabi frequency. This is defined as the rate at which the state probability amplitudes oscillate back and forth, or flop, [18, 29] in undamped systems. Within an ensemble, spontaneous emission ensures that the atoms lose relative phase and the system as a whole reaches a steady-state. However, other phenomena such as the dynamic (or ac) Stark effect are observable under such conditions and depend on the Rabi frequency for their strength. The Rabi frequency, Ω, is defined as:

$$\Omega = \frac{\mu E}{\hbar} \tag{3.7}$$

(Note that in the numerical work in this thesis a definition of $\Omega = \frac{\mu E}{2\hbar}$ is used for mathematical ease, and simply refers to half the above value.)

The definition combines the two elements for the interaction of radiation and matter — the electric field strength of the radiation, E, and the matrix element of the transition, μ. This latter parameter measures the strength of overlap of the two state wavefunctions as coupled by the relevant field interaction ie. dipole, quadrupole etc. For transitions with degenerate levels no single matrix element, and, hence, Rabi frequency is appropriate. However, a useful definition is the RMS Rabi Frequency [18]. In calculating this we relate the spontaneous emission rate, A_{ij}, for a transition of energy $\hbar\omega_{ij}$ to the matrix element (in SI units) thus:

$$|\mu_{ij}|^2 = \frac{3\pi\hbar\epsilon_0 c^3}{\omega_{ij}^3} A_{ij} \tag{3.8}$$

and hence, may deduce for the RMS Rabi frequency, in terms of the input intensity:

$$\Omega_{ij}^2 = \frac{3\lambda_{ij}^3}{8\pi^2\hbar c} A_{ij} I \tag{3.9}$$

Here, Ω_{ij} is in units of radians per second, while I is measured in Wm^{-2}.

When dealing with individual levels in degenerate systems individual Rabi frequencies may be calculated by use of angular momenta coupling coefficients. The

matrix element may be broken up into two parts:

$$\mu_{ij} = \sqrt{S(i,j)}G_q(i,j) \tag{3.10}$$

where $S(i,j)$ is the reduced matrix element and $G_q(i,j)$ contains the dependence on magnetic quantum numbers due to atomic orientation. The subscript q is the ΔM_J of the induced transition and depends on the selection rules for the system. The geometric factor, G_q, is defined in terms of a 3-j symbol as [18]:

$$G_q(JM_J, J'M_J') = (-1)^{\phi} \begin{pmatrix} J & 1 & J' \\ -M_J & q & M_J' \end{pmatrix}, \quad \phi = \max(J, J') - M_J \tag{3.11}$$

Further information on 3-j, and the related 6-j, symbols may be found in many texts, for example Weissbluth [21], Condon and Shortley [20] and Shore [18]. They describe the coupling of angular momentum systems, 2 for 3-j symbols and 3 for 6-j symbols and are necessary when combining fine and hyperfine structure, both angular momentum systems, to the orbital angular momentum L and spin S. Compact expressions that may be calculated by a straightforward computer algorithm are given by Weissbluth. Note that when in a hyperfine structure basis with F as a good quantum number the above formula is valid with the substitution $J \rightarrow F$ throughout.

The reduced matrix element may be then further reduced by one or more 6-j symbols giving the relative strengths of lines in a multiplet until the desired basis is attained. For examples of the construction under various atomic basis sets see Shore. (For the sodium D2 line see ref. [30] and for nonlinear susceptibilities see ref. [31]). The matrix elements for the sub-level transitions between the 3P and 3D levels of sodium will be calculated later, in Chapter 6.

By reference to the parameters in 3.4.4 and equation 3.9 the following conversion between intensity [Wm^{-2}] and and Rabi frequency [Hz] may be calculated for rubidium:

$$\Omega^2_{5P_{3/2} \rightarrow 5D_{5/2}} = 3.6 \times 10^9 I \tag{3.12}$$

Therefore, moderate continuous wave powers of around 750mW lightly focused to around 130μm may induce Rabi frequencies of couple of hundred MHz of pure frequency or about 1.5GHz of angular frequency, below the Doppler width but significantly in excess of the homogeneous linewidth. More discussion will be given, as relevant, in chapters 6 and 8.

3.4.6. Zeeman Splitting

During the sum frequency mixing experiments a transverse magnetic field was applied to break the intrinsic symmetry of the vapour system. This also had the effect of inducing the well known Zeeman effect on the atoms. The interaction of a static magnetic field has the effect of lifting the degeneracy of the various sublevels by inducing energy level shifts.

The application of the Zeeman effect to the relevant levels of sodium has been covered by Sinclair [4], Poustie [16] and Shepherd [5] and in various classic texts (eg. [20]) and will not be repeated here. In summary, however, the strength of the magnetic field as used in this work was sufficient to induce Zeeman shifts greatly in excess of the hyperfine structure in all levels but the ground $3S_{1/2}$ state, where only fields over 0.2T could be classed as the Paschen-Back, or strong field, case. For the 3P and 4P levels the splitting was approximately linear and very weak compared to the fine structure. The 3D levels, though, were in the intermediate regime between fine structure and Zeeman splitting and their behaviour had to be calculated from the Breit-Rabi formula in a similar manner to that of the 3S state.

When dealing with transitions between the Zeeman sublevels it is most useful to employ the m_l, m_s basis. Expressions for calculating the level admixtures at arbitrary field strengths exist [4, 5, 32] and with reference to the various selection rules may provide relative transition strengths.

REFERENCES

[1] *Model 2030 High Power Ion Laser Instruction Manual*, Spectra-Physics.

[2] *BeamLok*^{TM} *2080 Ion Laser User's Manual*, Spectra-Physics.

[3] *Model 380 D Frequency Stabilised Dye Laser Instruction Manual*, Spectra-Physics.

[4] Bruce D. Sinclair, *Second Harmonic Generation in Sodium Vapour Induced by a Magnetic Field*, PhD thesis, University of St. Andrews, 1987.

[5] Sara Shepherd, *Use and Development of a CW Titanium Sapphire Laser for Non-Linear Optics*, PhD thesis, University of St. Andrews, 1993.

[6] *Titan-CW Series Preliminary Operator's Manual*, Schwartz Electro-Optics.

[7] C. S. Adams, *Narrow Linewidth Operation of a Ti:sapphire laser: Applications in High Resolution Spectroscopy*, PhD thesis, University of Strathclyde, 1991.

[8] C. S. Adams and A. I. Ferguson, Saturated spectroscopy and two-photon absorption spectroscopy in rubidium using an actively stabilised Ti:Al_2O_3 ring laser *Opt Commun* **75**, 419 (1990).

[9] F. Biraben and P. Labastie, Balayage d'un laser a colorant continu monomode sur 150 GHz *Opt Commun* **41**, 49 (1982).

[10] S. Bourzeix, M. D. Plimmer, F. Nez, L. Julien, and F. Biraben, Efficient frequency doubling of a continuous wave titanium:sapphire laser in an external enhancement cavity *Opt Commun* **99**, 89 (1993).

[11] Joan Gambogi, Princeton University (unpublished).

[12] M. Harris, R. Loudon, T. J. Shepherd, and J. M. Vaughan, Mode-hopping hysteresis in a single-frequency laser *Opt Commun* **101**, 432 (1993).

[13] Roger Beaman, Coherent (UK) Ltd. (unpublished).

[14] *MBR-110 Ti:sapphire Laser Operators Manual*, Microlase Optical Systems.

[15] D. M. Kane, *Atomic Spectroscopy in the UV and Visible*, PhD thesis, University of St. Andrews, 1983.

[16] Alistair J. Poustie, *Magnetic Field Induced Sum Frequency Mixing in Sodium Vapour*, PhD thesis, University of St. Andrews, 1990.

[17] R. B. Miles and S. E. Harris, Optical third-harmonic generation in alkali metal vapors *IEEE J Quantum Electron* **QE-9**, 470 (1973).

[18] Bruce W. Shore, *The Theory of Coherent Atomic Excitation* (Wiley, New York, 1990).

[19] B. W. Shore and D. H. Menzel, *Principles of Atomic Spectra, Wiley Series in Pure and Applied Spectroscopy* (John Wiley and Sons, New York, 1968).

[20] E. U. Condon and G. H. Shortley, *The Theory of Atomic Spectra* (University Press, Cambridge, 1953).

[21] Mitchel Weissbluth, *Atoms and Molecules* (Academic Press, London, 1978).

[22] E. Arimondo, M. Inguscio, and P. Violino, Experimental determinations of the hyperfine structure in the alkali atoms *Rev Mod Phys* **49**, 31 (1977).

[23] *CRC Handbook of Chemistry and Physics*, 53 ed., edited by Robert C. Weast (The Chemical Rubber Co., Ohio, 1972).

[24] Charlotte E. Moore, *Atomic Energy Levels* (National Bureau of Standards, Washington, 1949), Vol. 1.

[25] Constantine E. Theodosiou, Lifetimes of alkali-metal—atom Rydberg states *Phys Rev A* **30**, 2881 (1984).

[26] John Emsley, *The Elements* (Clarendon Press, Oxford, 1989).

[27] F. Nez, F. Biraben, R. Felder, and Y. Millerioux, Optical frequency determination of the hyperfine components of the $5S_{1/2}$–$5D_{3/2}$ two-photon transitions in rubidium *Opt Commun* **102**, 432 (1993).

[28] *A Physicist's desk Reference, Physics Vade Mecum*, 2 ed., edited by Herbert L. Anderson (American Institute of Physics, New York, 1989).

[29] R. Loudon, *The Quantum Theory of Light, Oxford Science Publications*, 2 ed. (Oxford University Press, Oxford, 1991).

[30] P. M. Farrell, W. R. MacGillivray, and M. C. Standage, Quantum-electrodynamic calculation of hyperfine-state populations in atomic sodium *Phys Rev A* **37**, 4240 (1988).

[31] M. A. Yuratich and D. C. Hanna, Nonlinear atomic susceptibilities *J Phys B: At Mol Phys* **9**, 729 (1976).

[32] H. Uchiki, H. Nakatsuka, and M. Matsuoka, Optical second harmonic generation in gases in magnetic field *J Phys Soc Japan* **52**, 3010 (1983).

Chapter 4

The Consequences of Different Resonant Enhancement Schemes for Sum Frequency Mixing in Vapours

4. The Consequences of Different Resonant Enhancement Schemes for Sum Frequency Mixing in Vapours

Sum frequency mixing in vapours can provide a useful way of generating short wavelength radiation where no convenient source exists. It also can provide a good testing ground for elements of quantum electronics theory and the interaction of coherent radiation with atoms. In this chapter two possible sets of atomic levels, differing in the ordering of dipole allowed and quadrupole allowed transitions, are considered for sum frequency mixing and experimentally studied. Theoretical calculations can predict the main features observed and are compared. The most obvious changes in behaviour occur in their reaction to phase mismatch, via the incident wavelengths and the particle density, and this is studied in depth.

4.1. Introduction to Sum Frequency Mixing

Vapours have established themselves as useful nonlinear media for frequency conversion to short wavelength regions [1, 2, 3]. Conventional nonlinear crystals may have very large nonlinear coefficients but are not transparent in the deep UV, VUV and X-ray regions of the spectrum and, to date, there is no useful direct source of laser light for the shorter wavelength end of this region. Therefore, harmonic generation and sum frequency mixing (SFM) in vapours can provide a useful means of

converting light from conventional laser sources to very much shorter wavelengths for applications in this spectral area.

Due to the intrinsic symmetry of vapour systems third-order nonlinear processes are most common in vapours [3], but second-order ($\chi^{(2)}$) processes are also possible if an external means is used to break the symmetry of the system. Various methods have been used, including transverse electric or magnetic fields, high power pulsed excitation, and non-collinear beams (see Sinclair [4, 5] for a comprehensive review and references). Due to the levels involved in this work, and the desire to use continuous-wave lasers for high spectroscopic resolution, a transverse magnetic field is used in this work, as it has been in previous work in this laboratory [4, 5, 6, 7, 8, 9, 10].

One of the disadvantages of using a vapour as a nonlinear medium is the low particle density and hence, low second-order nonlinear coefficient at most wavelengths. However, the efficiency of nonlinear processes may be improved by many orders of magnitude by tuning the input lasers close to allowed atomic transitions for resonant enhancement. We may see the effect of this by considering the excitation of $\tilde{\rho}_{13}$ for a cascade three-level atom system, following the derivation in section 2.1.2. (If the two input fields ω_1 and ω_2 are tuned close to the transitions 1–2 and 2–3 then the sum frequency wave, $\omega_3 = \omega_1 + \omega_2$, will be generated with a strength proportional to $|\tilde{\rho}_{13}|$.) Consider the application of fields such that ω_1 is detuned sufficiently from level 2 for there to be inconsequential population transfer out of the ground state. Therefore, with $\rho_{11} = 1$ and $\rho_{22} \approx \rho_{33} \approx 0$ in steady-state we may write:

$$\tilde{\rho}_{13} = \frac{\Omega_{12}\Omega_{23}}{(\Delta_{12} - i\gamma_{12})(\Delta_{13} - i\gamma_{13})} \tag{4.1}$$

and, with reference to the atomic polarisation induced, infer:

$$\chi^{(2)} \propto \mathcal{N}\left(\frac{\mu_{12}\mu_{23}\mu_{13}}{(\Delta_{12} - i\gamma_{12})(\Delta_{13} - i\gamma_{13})}\right) \tag{4.2}$$

This situation is reasonable in actuality as detuning from single photon resonance removes parasitic linear absorption on the wave at ω_1 and is used experimentally.

From equation 4.2 we can see that the output is proportional to the product of the three transition matrix elements involved and inversely proportional to the detunings from single- and two-photon resonance, shown schematically in figure 4.1. This implies that for the greatest conversion efficiency the input waves should be tuned as close as possible to sequential transitions of strong matrix element. It also provides an insight as to why other wavelength generation processes (at $2\omega_1$, $2\omega_2$ and $\omega_1 - \omega_2$) are not observed — they are far from resonant enhancement.

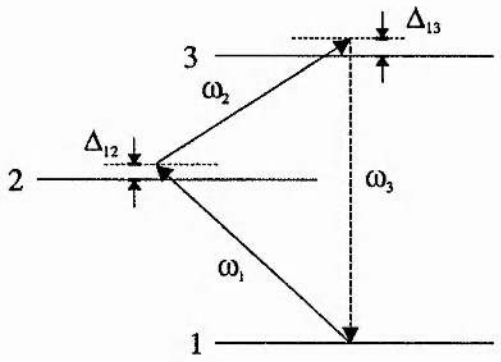

Figure 4.1: A simplified sum frequency mixing resonant enhancement system

Unfortunately, selection rules introduce a problem with the matrix elements. The strongest matrix elements correspond to dipole-allowed transitions, which by selection rules involve a parity change between the two levels [11]. Therefore if two of the transitions involve a parity swap the last transition must be between states of equal parity and involve a higher-order interaction. The next strongest interactions after electric-dipole are magnetic-dipole and electric-quadrupole and, while much weaker, the latter has been shown to lead to useful and easily detectable output [12]. (The requirement for the transverse symmetry-breaking magnetic field is also hidden within the matrix elements. For the transitions used, collinear input waves cannot lead to the excitation of a quadrupole component able to radiate in the forward direction [4, 10, 13].) Other solutions to this problem may involve non-collinear excitation or mixing parity states by an applied dc electric field.

Both the resonant-enhancement schemes considered in this work form a circuit of two dipole-allowed and one dipole-forbidden quadrupole-allowed transition. However, the ordering of these transitions is open and two different solutions are investigated here. The first uses the 3S–3P and 3P–3D dipole-allowed transitions in sodium vapour for the input waves and the sum frequency wave is generated on the quadrupole-allowed return transition. In contrast, the second route uses the 3P–4P quadrupole-allowed transition for the second input transition and generates on a dipole-allowed return (4P–3S). These resonant-enhancement schemes are shown in figure 4.2 which also introduces our shorthand labels for them: DDQ for the 3S-3P-3D system; and DQD for the 3S-3P-4P.

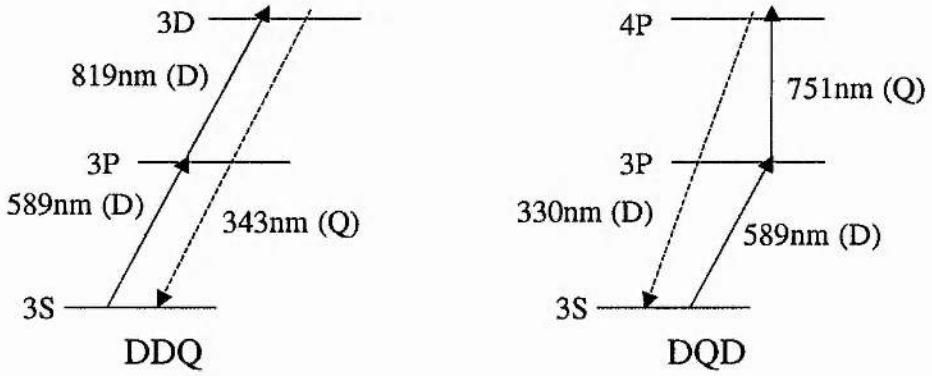

Figure 4.2: The two contrasting resonant-enhancement routes compared in this chapter, differing principally in the placing of the dipole-forbidden transition

The study in this chapter is concerned with non single-photon resonant excitation ($\Delta_{12} > \Delta\nu_{dopp}$, where $\Delta\nu_{dopp}$ is the Doppler width) on the first input wave. This removes parasitic linear absorption from this wave and eases the analysis by keeping out of the rapidly changing refractive index around resonance. Furthermore, little population transfer is induced allowing simplified perturbation solutions for the atomic suscectibility. The vapour pressure can be varied widely by changing the temperature which, as will be discussed below, allows the phase matching conditions to be changed radically. Both input lasers, as described earlier, are continuous-

wave single-frequency sources allowing spectroscopic resolution to be limited only by Doppler broadening on the Zeeman sub-levels and allowing the system to settle to steady-state.

If phase matching is neglected, the overall powers of the two routes are still not equal under similar vapour and input laser conditions as the matrix elements for the various transitions are different. The DQD route has a matrix element product of about 1/25 of that for the DDQ route which fundamentally reduces powers on this route. Furthermore, as the sum frequency wave is produced on a dipole-allowed transition it is vulnerable to re-absorption which will further reduce and limit output on this route. This work, though, concerns itself with the detailed changes in behaviour between the two routes, principally in the phase matching behaviour, as opposed to comparing their maximum powers, as they are taken as typical, rather than specific, examples of their transition systems. The results have wide relevance in the design of frequency converters to shorter wavelengths than those produced here (which could be done using modern nonlinear crystals) and give an interesting insight into the feedback of the atomic transition scheme on the parametric process, dictating that the choice of such transition circuits cannot be arbitrary.

4.2. Phase Matching in Vapours

The principle difference in operation between the two resonant enhancement schemes considered in this chapter manifests in their susceptibility to phase mismatch. The refractive index conditions experienced by the three waves in the process differs substantially between the two routes and causes some suprising results to be obtained. Before considering the experimental results, the factors governing phase matching in vapours are reviewed. Thereafter, the different theoretical calculations of the predicted output variations are summarised and some results displayed to show the effects of important parameters. The depth of the study was necessary to adequately

explain the observations and the work considerably extends the previous study of phase matching in vapour phase sum frequency mixing of Poustie and Dunn [8, 9].

As well as conservation of energy, which dictates the relation: $\omega_3 = \omega_1 + \omega_2$, conservation of momentum must also be satisfied in the nonlinear process. The momentum of a photon is given by $\hbar\mathbf{k}_i$, where $\mathbf{k}_i$ is the appropriate wavevector for the photon, and hence we have the following condition:

$$\mathbf{k}_3 = \mathbf{k}_1 + \mathbf{k}_2 \tag{4.3}$$

for efficient generation. If this condition is not satisfied the waves experience phase slippage and, for a plane wave in the absense of pump depletion, the power generated in the sum frequency wave follows the expression [14]:

$$P_3 \propto \mathcal{N}^2 l^2 \frac{\sin^2\left(\frac{\Delta k l}{2}\right)}{\left(\frac{\Delta k l}{2}\right)^2} \tag{4.4}$$

where l is the vapour length, $\mathcal{N}$ the particle density and the phase mismatch, Δk, is defined, for collinear beams, as:

$$\begin{aligned} \Delta k &= k_3 - k_1 - k_2 \\ &= 2\pi\left(\frac{n_3}{\lambda_3} - \frac{n_1}{\lambda_1} - \frac{n_2}{\lambda_2}\right) \end{aligned} \tag{4.5}$$

Within the above equation the shorthand n_i refers to the refractive index experienced by the wave at ω_i in the vapour.

4.2.1. Methods of Phase Mismatch Control

There are various methods of phase mismatch control open to the experimenter. Poustie [8] reviews these and they are briefly summarised below. The first, atomic dispersion is not strictly speaking a control mechanism, it is the original spanner in the works that the others try to re-dress.

Atomic Dispersion

In the region of an atomic transition the refractive index of the vapour is altered by the atomic polarisation induced in response to the propagating wave. A good approximation for the refractive index experienced by a non-resonant wave with wavelength λ, is the Sellmeier equation [3]:

$$n(\lambda) = 1 + \frac{\mathcal{N} r_e}{2\pi} \sum_j \frac{f_{ij}\alpha_i}{\frac{1}{\lambda_{ij}^2} - \frac{1}{\lambda^2}} \tag{4.6}$$

The sum proceeds over all atomic states of relevance with f_{ij} the oscillator strength of the transition, α_i the fractional population of the lower level, λ_{ij} the transition wavelength and $r_e = 2.818 \times 10^{-15}$m, the classical electron radius.

Therefore, the waves will experience differing refractive indices due to their tuning, and close tuning to a transition is likely to lead to a substantial phase mismatch. Furthermore, the dependence on $\mathcal{N}$ implies that at low particle densities the phase mismatch will be minimal but it shall increase linearly as the density rises.

Buffer Gas Compensation

The addition of a substantial quantity of buffer gas can compensate for a phase mismatch if $\Delta k < 0$ without it [15]. This is because the refractive index of an inert gas at the wavelengths of interest is always positive. Generally the quantities of buffer gas required are fairly high and can lead to significant collisional dephasing of the sum frequency coherence. Changing the vapour temperature or wavelengths involved implies changing the buffer gas pressure to match, which compels precise control of the partial pressure of the two gases, a difficult experimental requirement. However, where wavelengths are fixed this method can be used profitably.

Non-collinear Beams

If Δk is originally negative, once again, non-collinear input beams can compensate [12]. Since momentum is a vector quantity the two input wavevectors can be intro-

duced to the medium at an appropriate angle to remove Δk. Unfortunately, this also shortens the interaction length over which the crossing beams overlap within the vapour. For the continuous-wave laser sources used here, often focused, the reduction in path length would outweigh any benefits from non-collinear phase matching [8].

Periodic Phase Matching

If the sum frequency process is induced by a transverse field, reversing this field just before the sum frequency wave back-coverts, ie. at each coherence length, can lead to a continual growth in the output wave [16]. Experimentally, reversing the field repeatedly in a short region can be hard to realise and a fixed electrode geometry can only compensate for a fixed phase mismatch.

Intensity Dependent Refractive Index

The nonlinear refractive index, given by $n = n_0 + n_2 I$, can be used to change the refractive index of the vapour. Unfortunately, the intensity required is generally very high (in the order of several hundred MWcm^{-2}) and quite outside the realms of the continuous-wave powers used here.

Therefore, in all experiments an appreciation of the effects of atomic dispersion is paramount as the latter two methods above may be ruled out completely for many experiments and the other two can only compensate for a fixed negative Δk. Atomic dispersion, on the other hand, is always present and changing with wavelengths and vapour pressure throughout all experiments. This work will concentrate on its effects. If necessary one of the control mechanisms can then be added to a wave mixing process to improve its efficiency if control of atomic dispersion is not possible.

4.2.2. Atomic Dispersion on the DDQ route

The wavelengths used in the DDQ route are 589, 819 and 343nm. Of these, there is a significant refractive index deviation only on the 589nm input wave. The 819nm wave is near resonant with a dipole allowed transition but there is little population in the lower (3P) level and, therefore, little dispersion associated with it. The 343nm wave is resonant with a transition with population in its lower state but that transition is only quadrupole allowed and as such, has a very weak matrix element which makes refractive index contributions minimal (approximately 2 or 3 orders of magnitude lower).

The refractive index contribution around the 589nm area was calculated using the Sellemeier equation, integrated for inhomogeneous broadening, and the per atom phase mismatch it produces on the wave at ω_1 is shown in figure 4.3. It shows the two strong resonances corresponding to the fine structure components of the 3P level and the crossover between them. This crossover is useful and allows the experimenter to set the contribution to the phase mismatch to be positive, negative or zero by tuning the laser around the doublet. Contributions from other dipole-allowed transitions in the vapour are negligible for wavelengths this close to these strong lines.

Therefore, in the DDQ route the total phase mismatch has only one major contribution and may be approximated by $\Delta k \approx -\Delta k_1$, where $\Delta k_1 = 2\pi(n_1 - 1)/\lambda_1$, as the other two waves experience a refractive index of essentially unity. Control of this may be exercised by the tuning of the dye laser and altering the particle density of the vapour.

4.2.3. Atomic Dispersion on the DQD route

The DQD scheme, however, has two main sources of relevant atomic dispersion. Firstly, the 589nm wave experiences the influence of the 3S–3P transition as detailed in the previous subsection. However, now the output, 330nm, wave is resonant with a dipole-allowed transition to the ground state and sustains a fairly strong

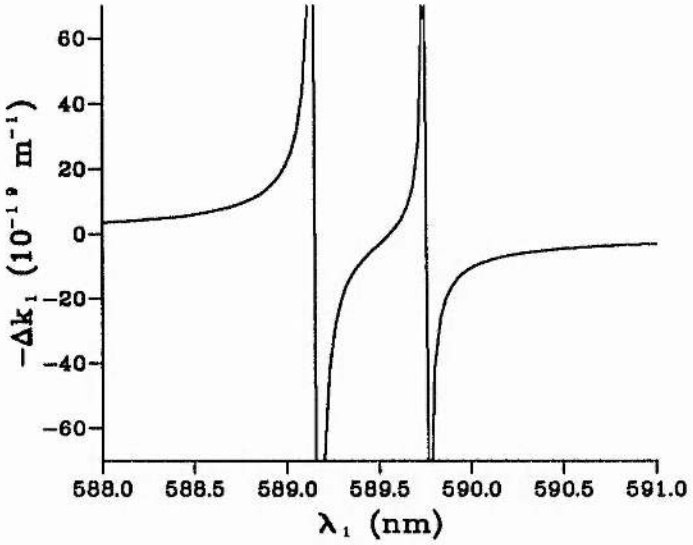

Figure 4.3: The per atom phase mismatch, $-\Delta k_1/\mathcal{N}$, contribution from the dye laser wave due to the 3S-3P transitions in sodium. (Wavelength axis is for vacuum values.)

refractive index perturbation also. The 4P level is split by fine coupling into two sublevels, the $4P_{1/2}$ and the $4P_{3/2}$ which are separated by 168GHz. Due to this wide separation they can be considered independently and we use the $4P_{1/2}$ level in the work below. The per atom contribution to the overall phase mismatch from this transition, Δk_3, is shown in figure 4.4 for an applied transverse magnetic field of 0.27T. This was calculated including the positions of all the Zeeman sub-levels involved in the transition and Doppler broadening. It consists of two close Zeeman split sublevel clusters which lead to the overall asymmetric double resonance shape. The overall magnitude of the refractive index change is smaller than that for the 3S-3P transition due to the lower oscillator strength for the transition and the much shorter range of the abscissa axis should be noted. The asymmetry caused by the two closely spaced contributions leads to important effects and should be appreciated. The wave at 751nm experiences very little refractive index as it is resonant with a dipole-forbidden transition with minimal lower level population.

Whereas for the DDQ scheme the phase mismatch is set by the dye laser tuning

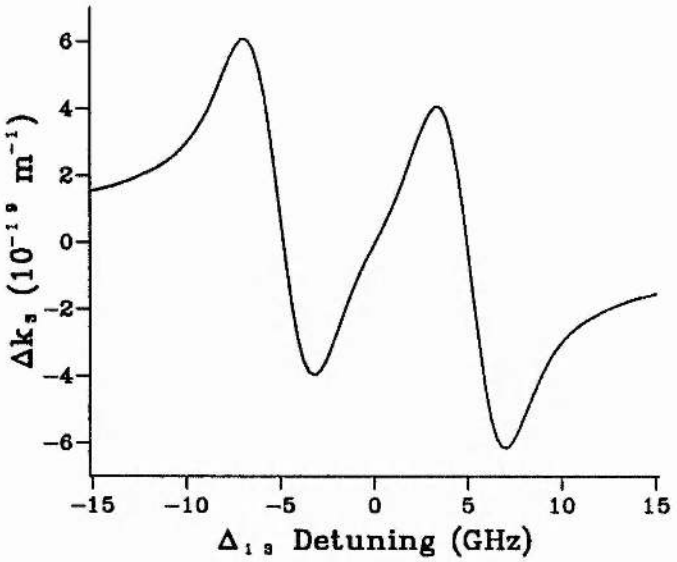

Figure 4.4: The per atom phase mismatch contribution from the output wave due to the 4P-3S transition in sodium. (Δ_{12} constant.)

relative to the 3S–3P transition which varies very little during a scan across two-photon resonance, the DQD phase mismatch varies swiftly during a scan over two-photon resonance due to the output transition contribution. During such a scan the phase mismatch will be modulated due to Δk_3 and will sit on a fairly steady offset determined by Δk_1. As I shall show later the relative magnitudes of these two can lead to radical effects, but for now, consider the two regimes shown in figure 4.5. Both traces show the total per atom phase mismatch, $\Delta k/\mathcal{N} = (1/\mathcal{N})(\Delta k_3 - \Delta k_1)$, for a scan across two-photon resonance but for different dye laser wavelengths as shown above each graph. In the left-hand trace the offset on the modulation is sufficient that phase matching is never achieved at appreciable vapour densities, while on the right-hand, phase matching is achieved on one sub-component only. Once the vapour density is sufficient that the modulation in Δk is over a few phase match minima this phase match point will give one subcomponent a distinct advantage in conversion efficiency and will lead to a severe distortion in the output lineshape.

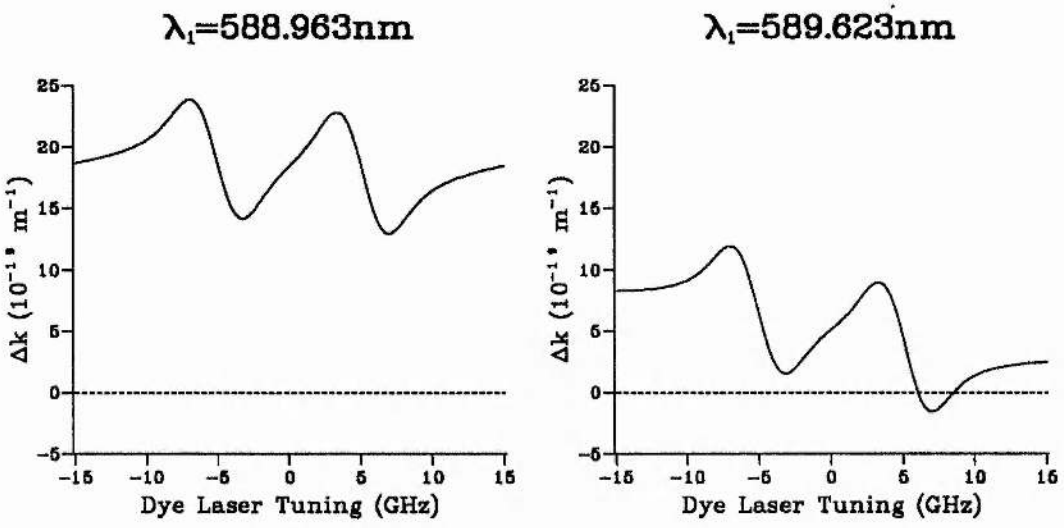

Figure 4.5: Two sample areas of operation for the DQD route. On the left, phase mismatch is not achieved at reasonable densities, while on the right, it is always, but only for parts of one subcomponent. (Wavelengths quoted, here and throughout this chapter are vacuum values.)

4.3. Phase Match Behaviour Calculations

Three useful phase match behaviour calculations used later will be reviewed here. They become progressively more general starting with the assumption of plane waves and then extending to gaussian beams with equal confocal parameters and focii and ending with two arbitrary gaussian beams.

4.3.1. Plane Wave

By the integration of plane waves propagating in a medium of constant phase mismatch, Δk, the behaviour of the sum frequency power with particle density, $\mathcal{N}$, or interaction length, l, is [14]:

$$P_3 \propto P_1 P_2 \mathcal{N}^2 l^2 \frac{\sin^2\left(\frac{\Delta k l}{2}\right)}{\left(\frac{\Delta k l}{2}\right)^2} \tag{4.7}$$

In this, P_1 and P_2 are the powers of the two input waves. For a vapour with readily changeable particle density it can be more useful to re-express this in terms of the per atom phase mismatch denoted by $\Delta k'$, where $\Delta k' = \Delta k/\mathcal{N}$, and we have:

$$P_3 \propto P_1 P_2 \left(\frac{2}{\Delta k'}\right)^2 \sin^2\left(\frac{\mathcal{N}\Delta k' l}{2}\right) \tag{4.8}$$

This removes the "hidden" dependence of Δk on $\mathcal{N}$. Thus at low particle densities, ie. when $\mathcal{N}\Delta k' l/2 \ll \pi$, we can simplify equation 4.8 to:

$$P_3 \propto P_1 P_2 \mathcal{N}^2 l^2 \tag{4.9}$$

In this condition the rise of P_3 will then be proportional to the square of the particle density and, later, after the first phase matching maxima the power will experience sine squared oscillations. This behaviour is shown in figure 4.6 against increasing temperature with the particle density following equation 3.2. The functional form is the same for both $\Delta k > 0$ and $\Delta k < 0$ and the oscillations merely start at lower temperatures for regions of greater $|\Delta k'|$.

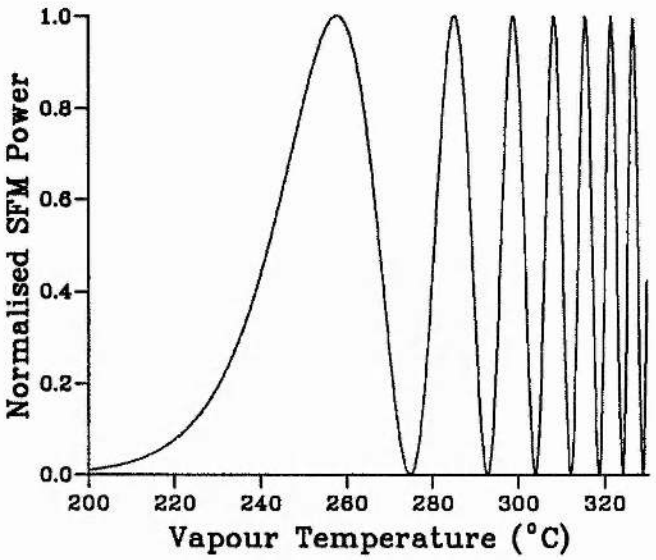

Figure 4.6: Plane wave phase matching behaviour for increasing temperature for $\lambda_1 = 588.6$nm in the DDQ route.

4.3.2. Identical Focused Gaussian Beams

If the input waves are focused into the vapour cell such that the confocal parameter is approximately equal to or less than the vapour length the assumption of plane waves is no longer valid. The focused gaussian beams alter the behaviour of the process in two main ways. Firstly, due to the propagation in and out of the focus a certain non-collinear element is introduced to the originally collinear input beams which leads to the optimum confocal parameter to length ratio to be 1:2.84 [17]. Secondly, a wave propagating through a focus is phase retarded in comparison to an unfocused wave by π radians. In the SFM process this translates to a phase slippage within the sum frequency beam where there was none before. If both the input beams propagate completely through a focus they are both retarded by π radians. The sum frequency wave will then be generated after the focus with a 2π phase lag compared to the plane wave case, assuming no phase mismatch ($\Delta k = 0$) in that case. The SFM wave generated before the focus will accumulate only a π lag from propagation through the focus and will therefore have a π *lead* compared to the wave generated after the focus.

It is due to this that the behaviour is no longer symmetrical for Δk positive or negative. If $\Delta k > 0$ the first maximum is reduced in size as it takes less input wave phase mismatch to add on to the sum frequency slippage and reach the first minima and for $\Delta k < 0$ the first maximum is increased as it takes additional mismatch to offset the π lead and reach the first minima. The maximum power is produced for Δk negative in a strongly focused situation.

The formal theory of phase matching for second harmonic generation and sum frequency mixing was presented by Boyd and Kleinman [17]. Their expression for the sum frequency power, simplified for a medium with no absorption or double refraction (relevant for off-resonant processes in a vapour), is:

$$P_3 \propto P_1 P_2 l h(\sigma, \xi, \mu) \tag{4.10}$$

where the function $h(\sigma, \xi, \mu)$ contains the phase matching information. The three parameters are: $\sigma = -(1/2)b\Delta k$, the phase mismatch*; $\xi = l/b$, the focal strength; and $\mu = (l-2f)/l$, relating to the focal position, f. Using these, $h(\sigma, \xi, \mu)$ is defined as:

$$h(\sigma, \xi, \mu) = \left(\frac{\pi^2}{\xi}\right) \left| \frac{1}{2\pi} \int_{-\xi(1-\mu)}^{\xi(1+\mu)} \frac{\exp[i\sigma\tau]}{1+i\tau} d\tau \right|^2 \tag{4.11}$$

This is best converted to separate real and imaginary parts for numerical evaluation as follows:

$$h(\sigma, \xi, \mu) = \left(\frac{1}{4\xi}\right) \left| \int_{-\xi(1-\mu)}^{\xi(1+\mu)} \frac{\cos\sigma\tau + \tau\sin\sigma\tau}{1+\tau^2} d\tau + i \int_{-\xi(1-\mu)}^{\xi(1+\mu)} \frac{\sin\sigma\tau - \tau\cos\sigma\tau}{1+\tau^2} d\tau \right|^2 \tag{4.12}$$

Examples of focused phase matching behaviour are given in figure 4.7 using the above analysis. Plane wave behaviour is overlaid on the same graphs and equivalent axis scales are used. They clearly show the advantage to be gained in output power by focusing and how negative Δk leads to greater powers in the first maxima. (The focusing parameter used is $\xi = 3$ which is roughly that obtained by use of a 20cm lens in the experiment.)

*A minus sign has been introduced here due to the different definition of Δk in [17]

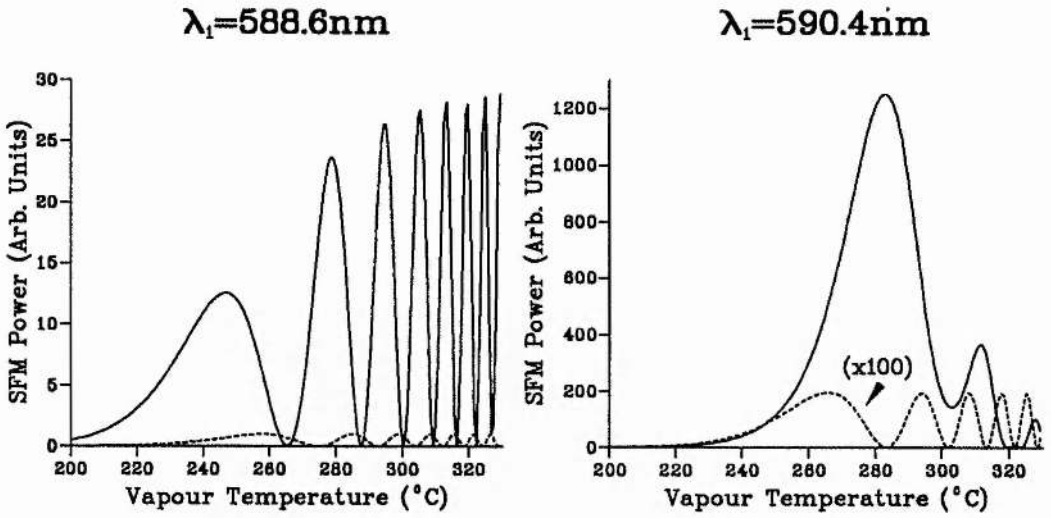

Figure 4.7: Focused phase matching behaviour with increasing particle density for $\lambda_1 = 588.6\text{nm}$ ($\Delta k > 0$) and $\lambda_1 = 590.4\text{nm}$ ($\Delta k < 0$) in the DDQ route for focusing parameters of: $\xi = 0.1$ (dotted line) to approximate plane waves; and $\xi = 3$ (solid line) for focusing.

4.3.3. Arbitrary Focused Gaussian Beams

Phase matching behaviour is calculated for beams of different confocal parameters by Guha and Falk [18] but the most general approach is by Lago, Hilber and Wallenstein [19, 20] who consider wave mixing with an arbitrary number of different gaussian beams in an arbitrary gas density distribution.

The full theory is, unsurprisingly, very involved but if the optimisation parameter considered is the density of the gas the behaviour of the process with phase mismatch may be described by the dimensionless function, $G^{(n)}$, where:

$$G^{(n)} = (b_1 \Delta k)^2 F^{(n)} \tag{4.13}$$

The superscript n refers to the number of input waves and allows results to be gained for different order processes. Here $n = 2$ and we assume a top-hat density distribution of the form:

$$\mathcal{N}(z) = \begin{cases} \mathcal{N} & \text{for } |z| \leq \frac{l}{2} \\ 0 & \text{for } |z| \geq \frac{l}{2} \end{cases} \tag{4.14}$$

where the origin of the z axis is taken at the centre of the oven of length l. Other density distributions were considered and a 0 to π sine curve implemented, but the results only differed slightly and so will not be discussed here. Using the vapour distribution as above and simplifying the functions for second-order sum frequency mixing the function $F^{(2)}$ may be expressed as:

$$F^{(2)} = \frac{4k_3}{b_2}\left(\frac{2}{b_1}\right)^2 \int_0^\infty r' \left| \int_{-\frac{l}{b_1}}^{\frac{l}{b_1}} \frac{1}{a(u,\epsilon_1')} \exp[-r'^2 q(u,\epsilon_1')] \exp\left[-i\frac{b_1 \Delta k}{2} u\right] du \right|^2 dr' \tag{4.15}$$

where

$$\begin{aligned} a(u,\epsilon_1') &= [1 - i(\epsilon_1 - \epsilon_1')h(u)](1 + i\epsilon_1)(1 + i\epsilon_2) \\ q(u,\epsilon_1') &= \frac{k_3}{b_1} \frac{[\overline{b_1 k_1}(1 + i\epsilon_2) + \overline{b_2 k_2}(1 + i\epsilon_1)]}{a(u,\epsilon_1')} \\ h(u) &= \frac{\overline{b_1 k_1}}{1 + i\epsilon_1} + \frac{\overline{b_2 k_2}}{1 + i\epsilon_2} \end{aligned}$$

Normalised confocal parameters and wavevectors have been used, with the definitions $\overline{b_j} = b_1/b_j$ and $\overline{k_j} = k_j/k_3$, and furthermore, the following other definitions are incorporated:

$$\epsilon_1 = u - \frac{2z_{0,1}}{b_1} \quad ; \quad \epsilon_1' = \frac{l}{b_1}\left[1 - \frac{2z_{0,1}}{l}\right]$$
$$\epsilon_2 = \overline{b_2}(\epsilon_1 - 2\overline{\Delta z_2}) \quad ; \quad \overline{\Delta z_2} = \frac{z_{0,2} - z_{0,1}}{b_1}$$

Finally, the focal positions for the two gaussian input beams are $z_{0,1}$ and $z_{0,2}$. The function is then evaluated numerically by integrating over the vapour path (u) and then the beam profile radius (r').

This theory then allows us to calculate how unequal confocal parameters affect the phase matching behaviour. For our single-lens experiment the confocal parameters for the two beams are not equal and no attempt was made to match them. For a 20cm lens the confocal parameters were $b_1 = 3.6$cm and $b_2 = 2.5$cm and these values are used in figure 4.8 to predict the output. Also shown in the same graph are the curves for equal confocal parameters and it can be seen that the mismatch does not significantly alter the functional profile or the magnitude.

The focal position is approximately the same for the two beams but may be easily moved within the oven by changing the distance of the lens from the oven window. This proved to be a very important parameter and the effect of moving the focal position within the 10cm vapour region is shown in figure 4.9 for the same wavelengths as previously. When the focus is not central the minima tend to be less pronounced as the vapour is no longer distributed symmetrically about the focus and complete cancellation is impossible. The phase shift on going through the focus is partly moved outside the vapour region and so both curves tend to a similar form as the difference between positive and negative phase mismatch is reduced.

An advantage of this formalism for phase match calculations is the integration over the beam profile. The integration may easily be removed and the output beam profile displayed. Figure 4.10 shows the beam profile at the output window of the oven and it can be seen to be of gaussian-like form. No ring structures or unusual beam profiles were produced for sum frequency mixing calculations under

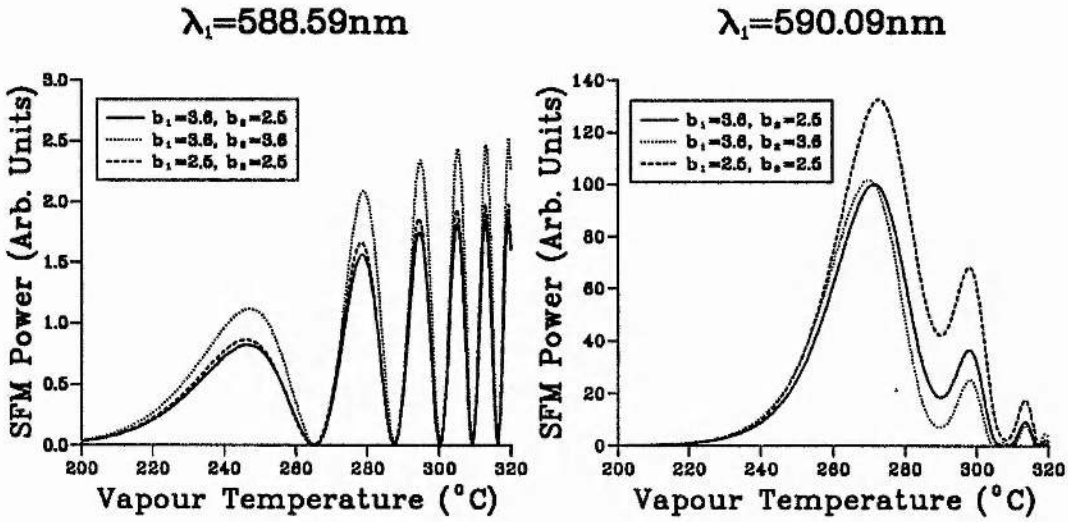

Figure 4.8: Theoretical calculations for phase matching behaviour at $\lambda_1 = 588.59$nm ($\Delta k > 0$) and $\lambda_1 = 590.09$nm ($\Delta k < 0$) using the confocal parameters displayed in the legend.

any conditions tried, however, such profiles may be found in difference frequency mixing [20].

4.4. Initial Experiments

To begin with, before looking at the phase matching behaviour in detail, the conventional, low particle density behaviour of the sum frequency schemes are presented. Output lineshapes for both routes are predicted and compared to observations. Thereafter, the maximum conversion efficiency measured — and the conditions required for achieving it — is stated.

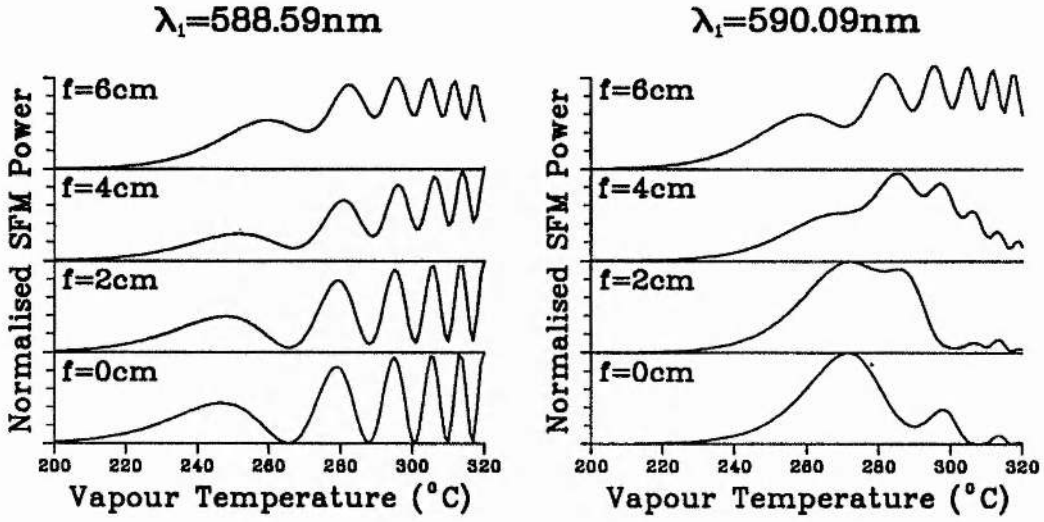

Figure 4.9: Phase matching behaviour with changing focal position, f, in the oven, relative to the oven centre. The confocal parameters $b_1 = 3.6$cm and $b_2 = 2.5$cm were used and all the curves are normalised to unit height to show the changing form.

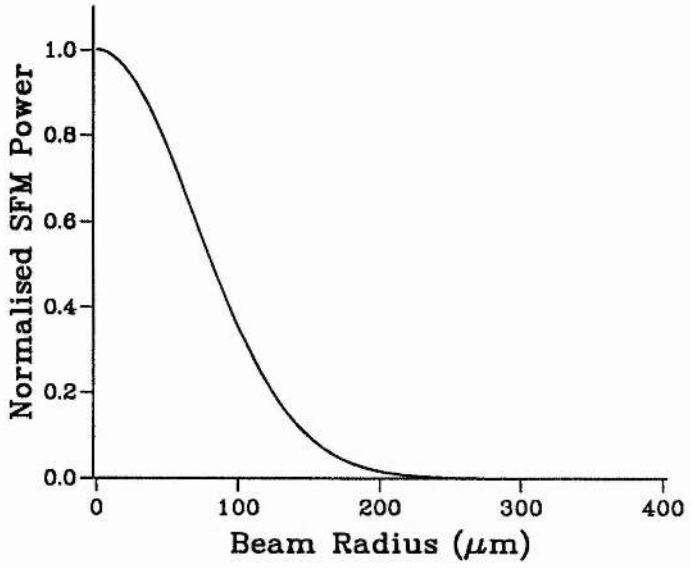

Figure 4.10: The theoretical output sum frequency mixing beam profile against the beam radius at the oven end for $\lambda_1 = 590.09$nm, at a vapour temperature of 300^{0}C and confocal parameters as above.

4.4.1. Low Power Behaviour

At low vapour temperature, transverse magnetic field, and laser powers the non single-photon resonant sum frequency output power varies as follows [4, 8]:

$$P_3 \propto P_1 P_2 \mathcal{N}^2 B^2 \tag{4.16}$$

This expression is true for both routes and was experimentally verified. The experimental dependence on input laser powers is shown in figure 4.11 for the DQD route and can be seen to be linear against either laser power. The rise of SFM power with the square of the particle density constitutes figure 4.12, measured here on the DDQ route, at temperatures below the onset of significant phase mismatch. The rise of the output power with transverse field (figure 4.13) was measured at the centre of the lineshape and clearly shows the quadratic rise until the line profile starts to split into two components [4].

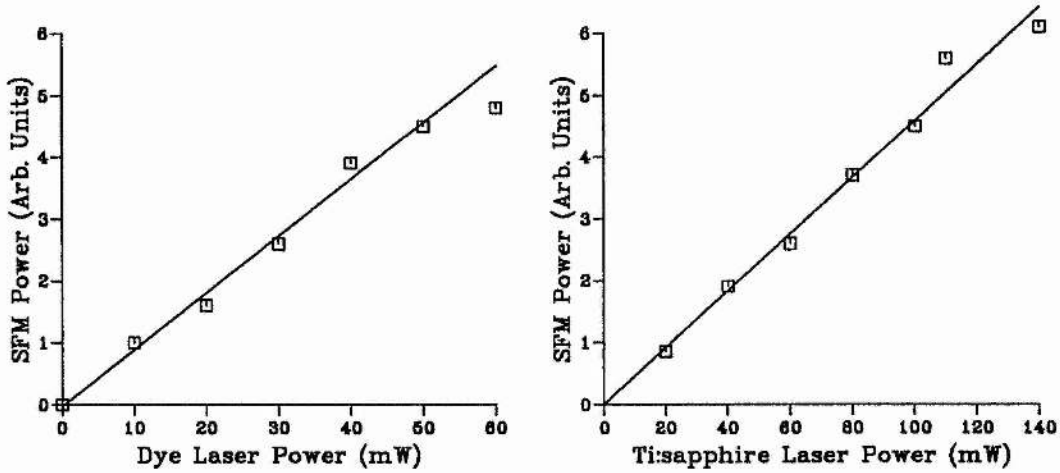

Figure 4.11: The output sum frequency power variation with input laser powers, measured on the DQD route.

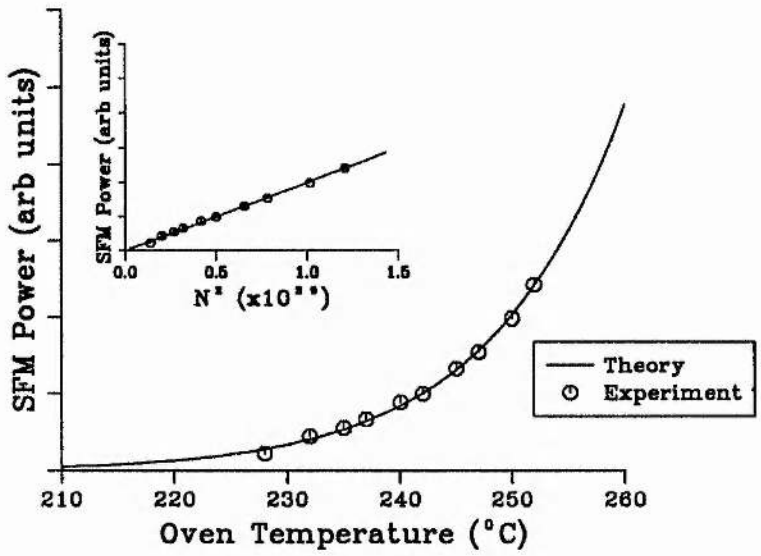

Figure 4.12: The output sum frequency power variation with particle density (or equivalently vapour temperature), measured on the DDQ route.

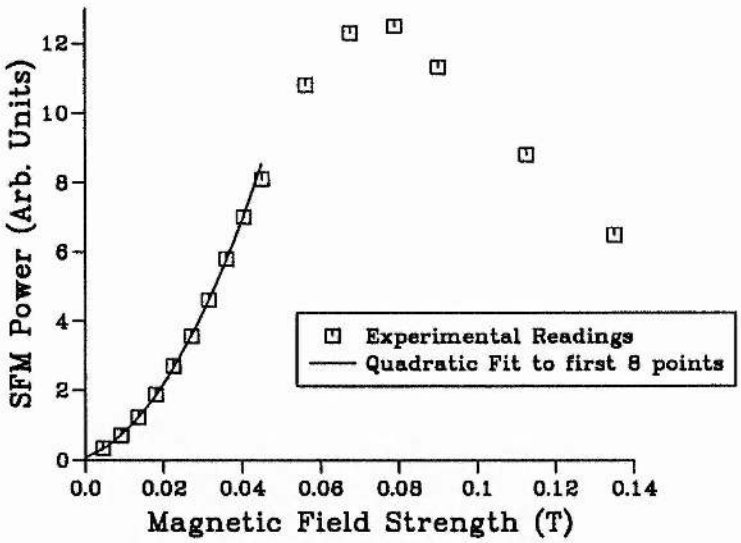

Figure 4.13: The output sum frequency power variation with transverse magnetic field strength. Measured at the centre of the DDQ line-profile and fitted with a quadratic for the first 8 experimental points.

4.4.2. Lineshapes

The lineshapes of the two routes, when detuned from the intermediate level, may be calculated by an integral perturbation solution to the density matrix. The formalism is quite complex as it must incorporate the effects of the magnetic field on the level energies and transition strengths. Once again, an integration over the Doppler profile is required and a knowledge of the operative selection rules is needed. Theory for second harmonic generation is given by Uchiki [13], and separately by Sinclair [4], and this has been generalised for sum frequency mixing by Shepherd [10]. Due to the complexity of the final result it is not stated here and the reader is directed to the cited works.

The theoretical expressions were evaluated by computer and the results for increasing magnetic field strengths on the DDQ route are given in figure 4.14. They are very similar to those for second harmonic generation unless the dye laser is tuned quite close to one of the 3P levels when different routes can be selectively enhanced and the trace may become quite asymmetrical. The lineshape was observed by scanning the dye laser and the experimental results for the same magnetic fields as the theory are displayed in figure 4.15. The agreement is very good and the use of single-frequency sources rewarded. It should be noted that the DDQ lineshape at high magnetic fields is not merely two Doppler broadened lines but two clusters of closely spaced sublevel transitions. Furthermore, the DDQ lineshape is observed to be unaffected by any phase mismatch as scanning across two-photon resonance does not change Δk significantly.

For the DQD route the theoretical calculations followed a similar line but with the different transitions (3S–3P–$4P_{1/2}$) involved. However, observation of the basic lineshape proved to be quite difficult due to phase matching modulations which will be discussed in detail later. However, at low temperatures an approximation to the lineshape could be gained before the signal levels became too low to detect. A comparison of theory and experiment is shown in figure 4.16 for three magnetic field

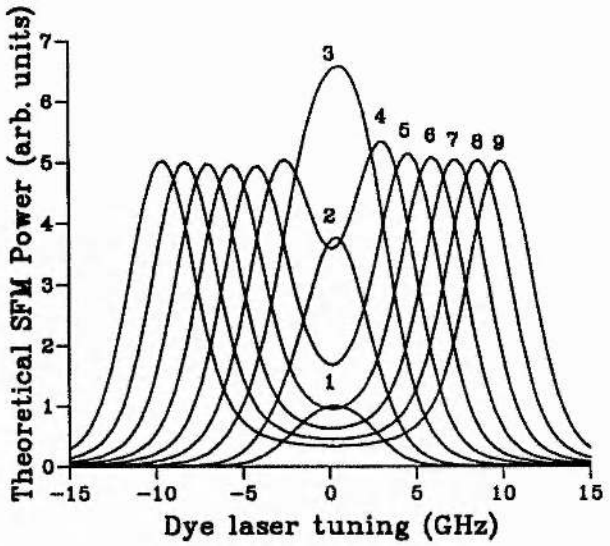

Figure 4.14: Theoretically predicted SFM output lineshapes for the DDQ route at 0.0225, 0.045, 0.09, 0.135, 0.18, 0.225, 0.27, 0.315 and 0.36 Tesla magnetic fields, labeled 1 to 9 in order.

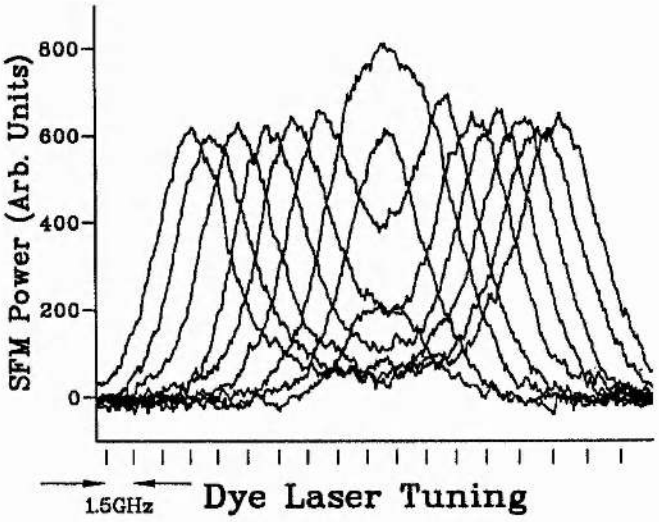

Figure 4.15: Experimentally observed SFM output lineshapes for the DDQ route for the same magnetic fields as the theoretical traces. Confocal marks of frequency separation 1.5GHz are shown below the figure to provide a frequency scale.

strengths and shows reasonable agreement.

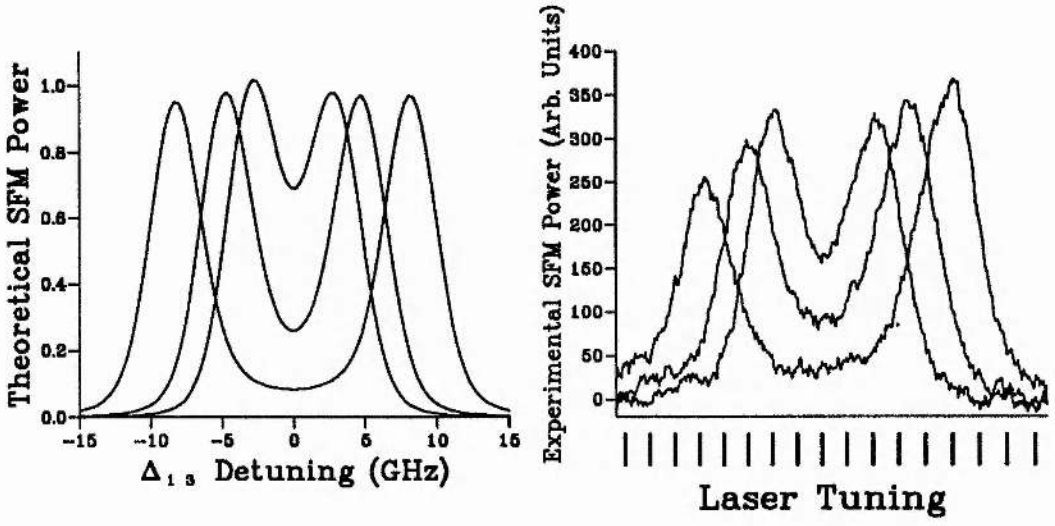

Figure 4.16: On the left theory, and on the right experiment for the DQD route lineshapes at 0.18, 0.27 and 0.45 Tesla magnetic fields. Confocal markers of 1.5GHz separation are shown under the experimental trace.

4.4.3. Maximum Output Conditions

For maximum efficiency of conversion to the sum frequency wave the dye laser should be tuned on to resonance with the 3S-3P transition to gain single-photon enhancement as well as two-photon enhancement. For the DDQ route, with the stronger transition matrix elements, some effort was expended to maximise the conversion efficiency and the conditions for maximum conversion are detailed below. The efficiency of the DQD scheme was typically around two orders of magnitude below the other one for three reasons. Firstly the matrix element product was around 1/25 of the other route. Secondly the output was generated on a dipole-allowed transition, and hence, was subject to re-absorption. This is a common problem in four-wave sum frequency mixing and limits the output at some balance between generation and absorption. Lastly phase mismatch effects were harder to

control and the tolerance on the correct tuning, when close to resonance, was very tight.

For the DDQ scheme the maximum output power detected was 17μW for cw input powers of 140 and 300mW on the dye and Ti:sapphire lasers, respectively. This was measured using a calibrated UV-100 photodiode and was sufficient for a deep blue spot to be visible to the naked eye when imaged on a card (figure 4.17). From the focusing and vapour length the estimated effective non-linearity was around 0.5pmV^{-1}. This is greater than some nonlinear crystals, eg. KDP, despite use of the quadrupole transition. The conditions for this conversion were however quite tight. The vapour temperature was 230–240^{0}C and a 20cm focusing lens was used. The dye laser was strongly absorbed on resonance and could not penetrate the entire oven length. This parasitic absorption reduced the interaction length and, therefore, the efficiency. However, use of a strong magnetic field (approx. 0.27 Tesla) split the sub-components of the transition apart by more than the Doppler width and by tuning the lasers within the components the maximum power was observed. A compromise between absorption and close detuning appeared to be struck at the best points.

Chapter 6 will propose a method for removing this parasitic absorption on resonance and further improving this efficiency by using electromagnetically-induced transparency.

4.5. The Dipole-Dipole-Quadrupole Scheme

The two routes differ in maximum conversion efficiencies, but more interestingly in terms of the role of phase mismatching. A theoretical model was developed, which explains well the effects of each transition. Separate sections are used for reporting on the study of the two routes due to the rather different approach taken due to the different circumstances.

The behaviour of the DDQ route with phase mismatch was studied by raising

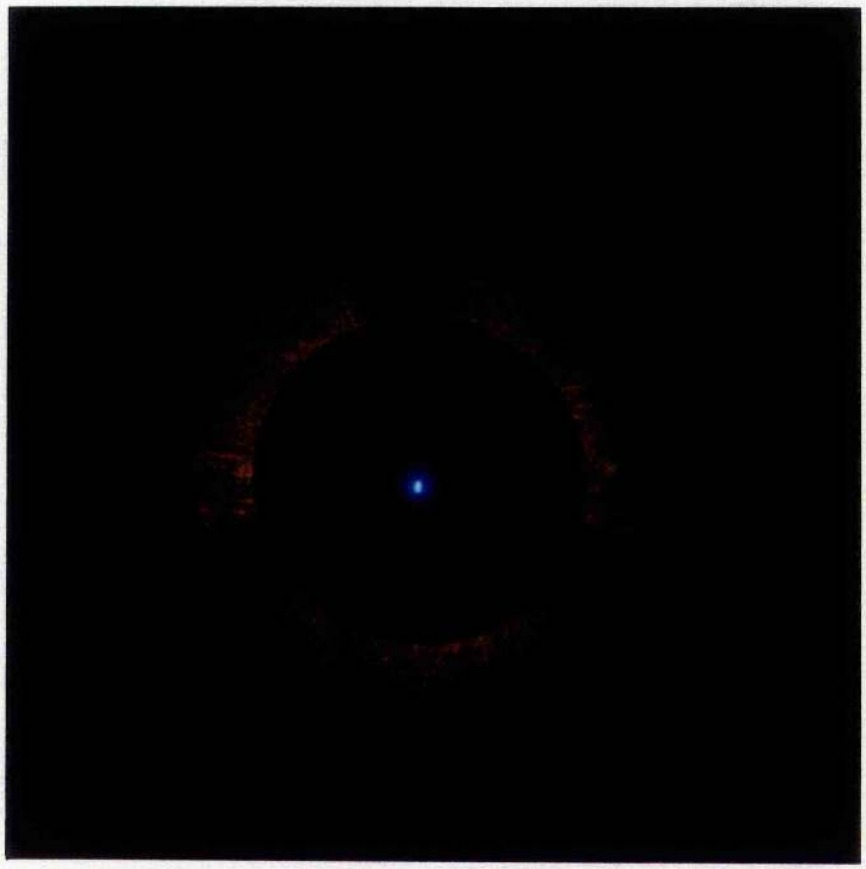

Figure 4.17: The blue flourescence induced on a card by the 342nm output wave imaged at the end of the oven.

the oven temperature and following the output power variation. The Ti:sapphire laser was continually scanned back and forth in a swift dead-reckoned scan so that the maximum output power was always registered, countering the problem of laser drift on this unstabilised system. Unfocused and focused beams were studied and the deviations from theoretically predicted behaviour analysed.

4.5.1. Plane Wave Behaviour

When unfocused the near-collimated laser output beams were a good approximation to plane waves. By tuning the dye laser wavelength to various points around the 3P levels Δk could be chosen in sign and as the oven temperature was increased $|\Delta k|$ would increase at a rate determined by the per atom phase mismatch contribution. Figure 4.18 shows two such results with the experimental points overlaid by the theoretical fit for a positive (left) and negative (right) phase mismatch region. The oscillations have very good contrast with well defined minima and are quite regular. The value of the per atom contribution to $|\Delta k|$ was increased experimentally and the oscillations were seen to set in at lower temperatures and more would be seen in a given high temperature range. The slight fall off in maximum amplitude at high temperatures could be due to dephasing effects with high particle densities, absorption from sodium dimers [8] or uneven vapour densities at high temperatures where only a degree or two separates the peaks and troughs.

The $\Delta k = 0$ point at 589.555nm (vacuum) between the two 3P sublevels was also experimentally investigated, and the result shown in figure 4.19. The rise in power with temperature is unbroken and continued to the maximum temperature allowed for our apparatus. This point is potentially very useful for vapour-phase sum frequency mixing and allows the use of dense, high temperature gases giving good conversion efficiency with low input and output wave attenuation. Such doublet structures give the near-ideal situation of close resonant enhancement and precise phase mismatch control. The maximum conversion efficiency reached would be

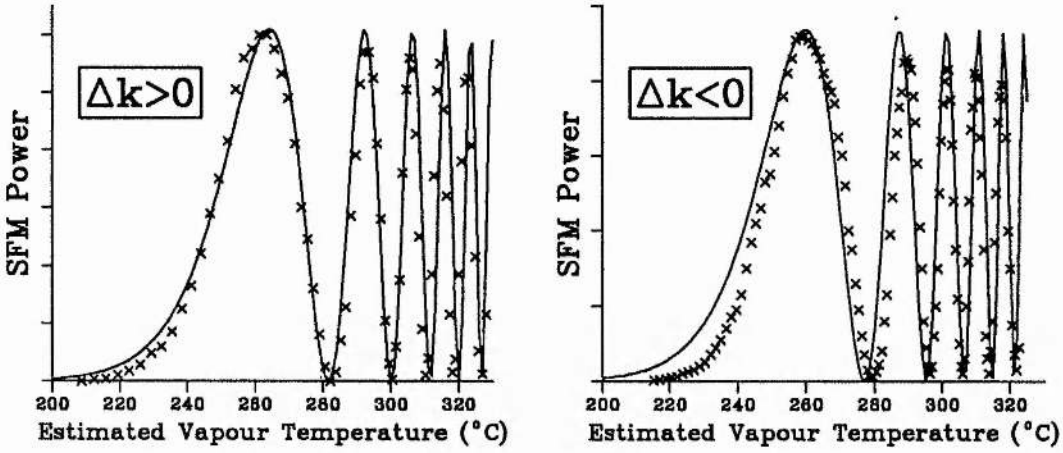

Figure 4.18: Experimentally observed plane wave phase matching behaviour for the DDQ route. The solid line is the theoretical predictions and the crosses the experimental points. (Due to the poor correspondance between indicated temperature and vapour temperature in the apparatus, the experimental results on the left hand trace were fitted to the peak and dip positions by a smooth temperature offset curve. The same curve was used on the right hand trace with good matching of the oscillations.)

determined by: dephasing effects, especially on the output coherence; the accuracy of tuning to the $\Delta k = 0$ point; and the parasitic effects of the rising sodium dimer density.

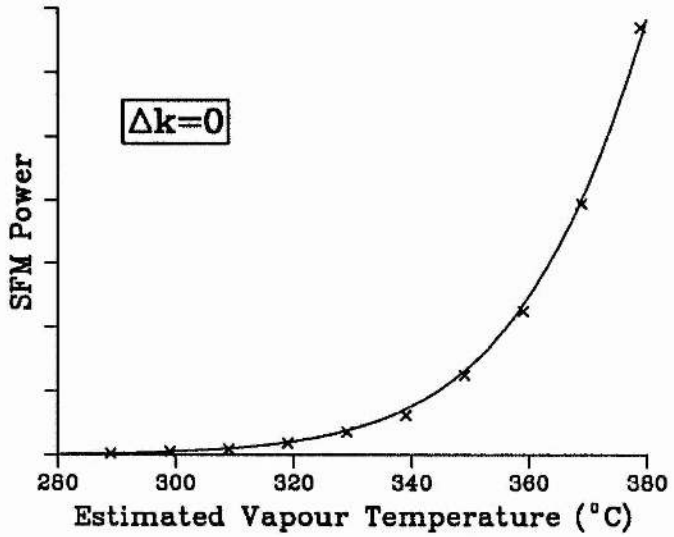

Figure 4.19: Experimentally observed steady rise in SFM power at the $\Delta k = 0$ point between the 3P levels, $\lambda_1 = 589.55$nm.

4.5.2. Focused Input Beams

As predicted theoretically focusing the beams into the vapour oven radically altered the phase matching behaviour. Various lenses were used from a 40cm lens ($b_1 =$ 14cm, $b_2 = 10$cm) for a weak focus to a 20cm lens ($b_1 = 3.6$cm, $b_2 = 2.5$cm) for a tighter focus. Most results will be presented for the latter as the effects were more notable for this lens and the powers were higher due to the proximity of the focusing parameters to the ideal 2.84 as quoted in [17].

Figure 4.20 shows the measured output power variation with temperature in a positive (left) and negative (right) phase mismatch region. These should be compared to the theoretical predictions in figure 4.8 and show the main features expected. The first peak is shifted, compared to the plane wave position (see [10] for an experimental proof of this), as expected, and is small for $\Delta k > 0$ and large for

$\Delta k < 0$.

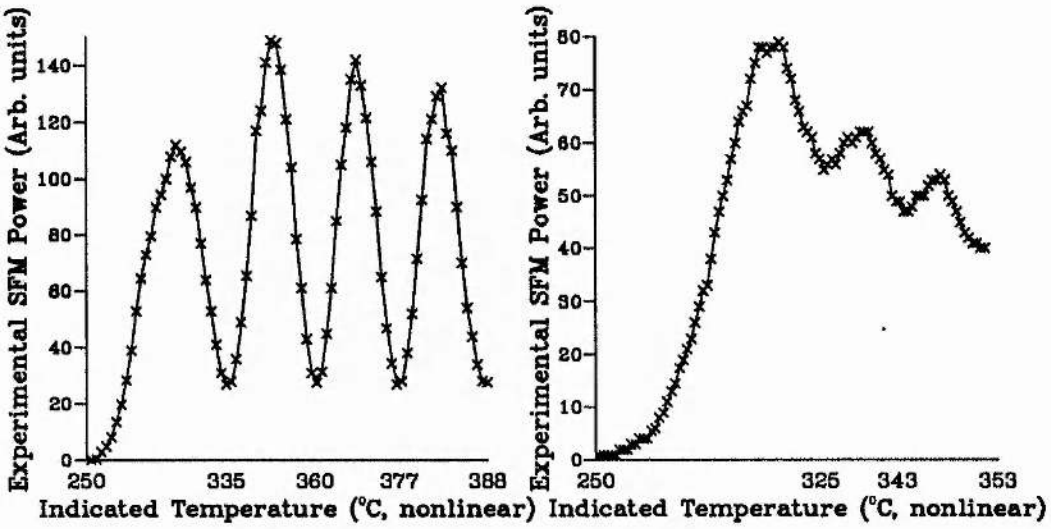

Figure 4.20: Experimentally observed phase match behaviour for input beams focused with a 20cm lens.

Functionally the fit is quite good for positive phase mismatch, with just the minima not being of as good contrast as expected, but poorer for the negative mismatch case. This regime showed very radical changes with the experimental parameters while the positive mismatch variations did not change significantly from the form shown in the previous figure. The five most important parameters governing the behaviour were found empirically to be: the sign of Δk, the strength of focusing, the position of the focus, the vapour uniformity and, to a lesser extent, the collinearity of the beams. The difference between the confocal parameters of the two beams could not be controlled in the single-lens experiment and from theory presented earlier should have little functional effect. Beam distortions could also be present but deliberate astigmatism introduced on the dye laser beam had little effect, nor did spatial filtering. Of the five main parameters listed above, the first two matched well between theory and experiment. Less strong focusing produced outputs comparable to relevant theory and the differences pointed out for the sign of Δk above are again

as predicted.

The process, however, proved to be very sensitive to changes in the focal position. As the lens was moved relative to the oven window the focal position was moved in the vapour and four traces taken at various positions are shown in figure 4.21 for a negative mismatch region, as the effects were stronger here. The predicted extremes are close to observations with regular oscillations of low contrast. When moved about the oven centre the output power variations show some strong similarities to theory (cf. figure 4.9) but are never an exact match. Inaccuracies in measuring the focal position are likely but not on the scale of more than a centimetre's tolerance, suggesting some vapour asymmetry in the apparatus. This would act very like an offset in focal position as the process would not be the same on either side of the focus and exact cancellation could not occur.

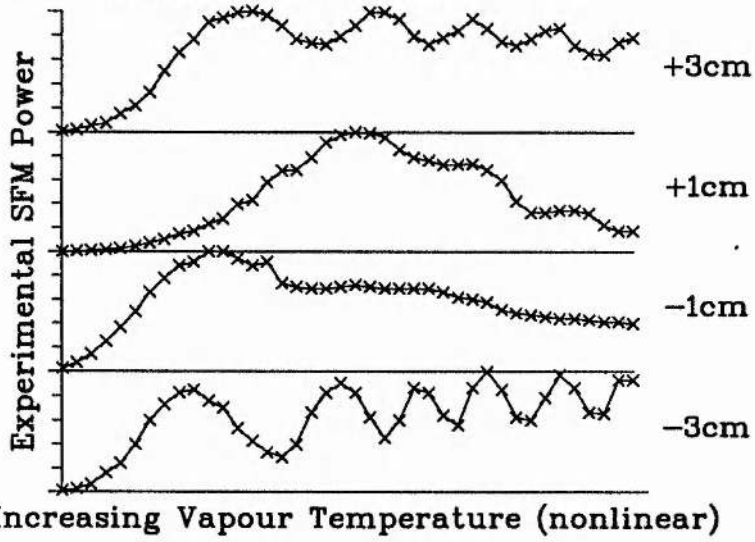

Figure 4.21: Experimentally observed output power behaviour with increasing temperature for $\lambda_1 = 590.10$nm, a 20cm lens and focal position offsets from the oven centre as shown.

Vapour uniformity could also be suspect in the radial direction as well. This was implied by observations of sample portions of the output beam using a pinhole. When this was done different portions of the beam acted as if experiencing different

phase mismatches, with maxima and minima occurring displaced in temperature for different points. The traces did, however, have good contrast oscillations and looked similar to theoretical predictions for focused behaviour, but for a focusing parameter a bit less than the one expected. Integration of these different regions over the whole output beam, giving the total output power, would explain the poor contrast oscillations and the deviations between theory and experiment. None of the theories considered above took into account possible Δk variations in a radial direction and so could not predict the results of this. However, the unfocused phase matching traces appeared immune to such problems and so the problem is unlikely to be completely due to a radial change in vapour density. It is as if there is a radial effect overlooked in the calculations or being introduced in the experiment giving this mix of different Δk values seen in the output beam.

The most striking way of observing these radial effects was to look at the output beam profile using a CCD camera to record the sum frequency beam profile at different temperatures. The fundamental input waves were filtered off and the results for the sum frequency beam is shown are figure 4.22, with cross-sections shown in figure 4.23. At low temperatures, before the first phase match peak, the beam profile consists of one gaussian-like feature as expected and predicted (cf. figure 4.10). However, at high temperatures, above the first phase match peak, a broken ring was seen to move outwards from the central maximum and die away. As the temperature continued to rise, a subsequent second ring appeared and expanded. By changing the alignment of the beams the ring geometry could be changed to a fringe pattern in the plane of the misalignment and back again. Therefore, we concluded that the problem was not due to non-collinearity and the beams were well aligned for the most radially symmetric situation. The incorporation of the effects of this radial change in phase mismatch into theory is not attempted here but the results displayed suggest that very careful consideration must be paid to the vapour conditions if theory is to predict accurately observations under conditions of appreciable focusing.

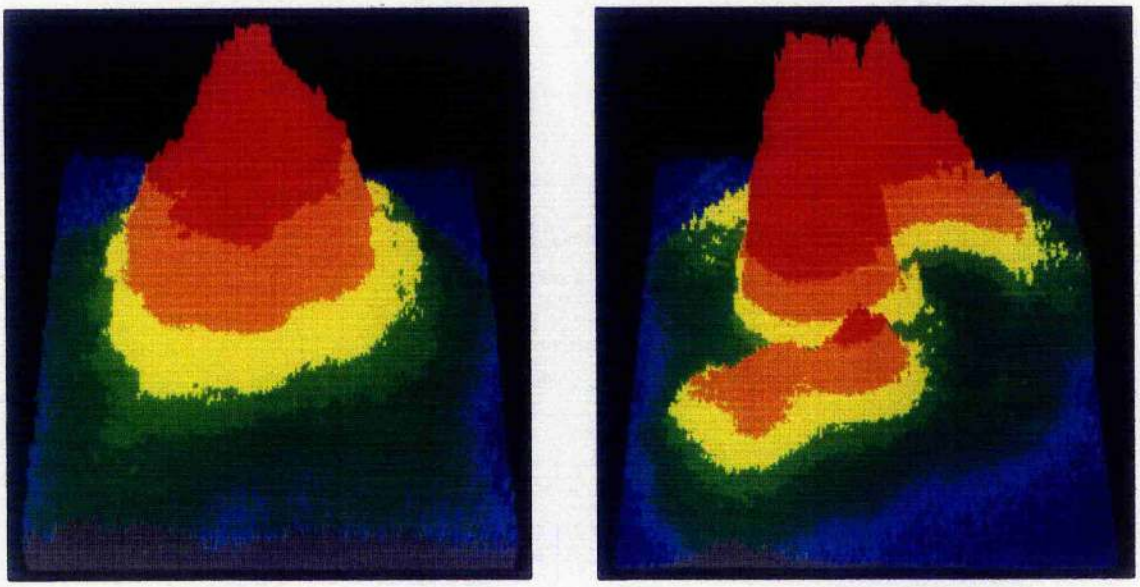

Figure 4.22: The SFM output beam profile for focused input waves at low (left) and high (right) temperatures clearly showning the beam breakup due to phase mismatching effects.

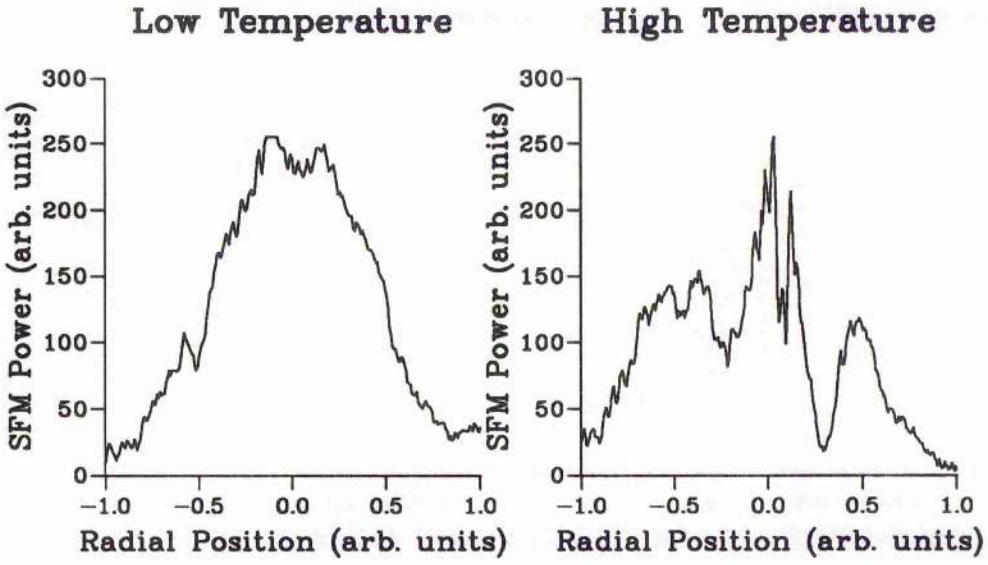

Figure 4.23: Cross-sections through the SFM beam profiles for low temperatures on the left, and high temperatures on the right.

4.6. The Dipole-Quadrupole-Dipole Scheme

As discussed above, the DQD route contains two transitions that significantly contribute to the phase mismatching. This results in considerably "distorted" lineshapes being observed as the phase mismatch must change during a scan of either laser. Theory is developed which gives a good qualitative description of the presented experimental results.

4.6.1. Lineshape Alterations due to Phase Mismatching

While in the DDQ route it is possible to set the phase mismatch by the coarse tuning of the dye laser alone, this it not the case for the DQD route. Now, as discussed previously, the scan across two-photon resonance introduces a second significant variation in phase mismatch. As it would be experimentally difficult to set the Ti:sapphire laser accurately to a given phase mismatch due to the swift change across resonance the results discussed here will be for scans across two-photon resonance. Moreover, no difference between results taken in this route for increasing temperature and the previous route would be expected.

When the two-photon detuning is scanned across resonance, by a scan of either laser (but in this work the dye laser), the Zeeman split lineshape would be expected to be observed. However, due to phase mismatching — and the rapid change of this — what is observed is the lineshape modulated strongly by phase matching changes. In order to predict the output a numerical model was developed. This takes the SFM lineshape, as calculated from detailed theory (see subsection 4.4.2) and modulates the lineshape with the result of a phase matching prediction for the relevant Δk at each detuning point. The phase mismatch theory used was that of Boyd and Kleinman [17] (see subsection 4.3.2) for a focusing parameter of $\xi = 3$ and is close enough to gain a good insight into the expected result.

The controlling parameters are the temperature of the vapour and the tuning of the dye laser. This second parameter is critical to the behaviour of the output. If

the offset provided by the nearly static Δk_1 is small (ie. $\lambda_1 \sim 589.5$nm) then phase matching will occur at one or more points during the scan. If, on the other hand, the tuning of the dye laser is such that the offset from Δk_1 outweighs the modulation from Δk_3 then phase matching is never achieved and the maximum output power is limited. Figures 4.24, 4.25 and 4.26 display results of these calculations for the indicated dye laser wavelengths. In the first two, the offset from Δk_1 is sufficient so that perfect phase matching is never achieved in a scan. The peaks can be seen to

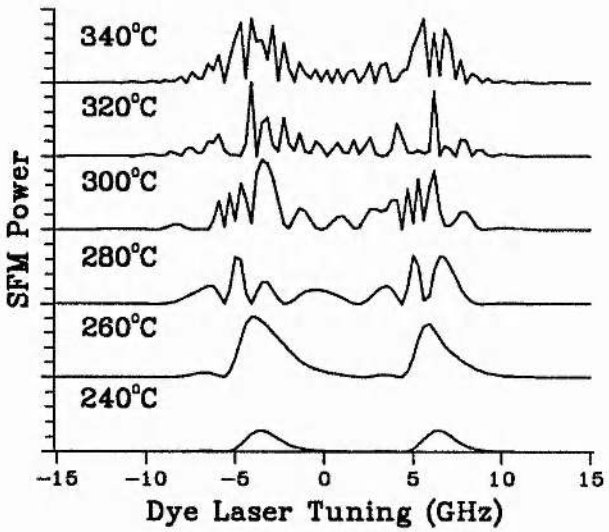

Figure 4.24: Theoretically predicted modulated output lineshapes at the vapour temperatures quoted for a dye laser tuning of $\lambda_1 = 588.963$nm.

be a mass of phase match oscillations at high temperatures and distorted at lower ones. Also the differences in positive and negative phase match behaviour can be seen. For figure 4.24 the phase mismatch is positive and as seen previously for this case (see figure 4.7) the results tend to a steady level at higher temperatures. For figure 4.25 the mismatch is smaller but negative and hence at this dye laser tuning maximum power is recorded at intermediate temperatures and drops off at high order oscillations (cf. figure 4.7).

However, the most intriguing result is for a dye laser tuning of $\lambda_1 = 589.623$nm (figure 4.26). The appropriate Δk was shown in figure 4.5 and achieves perfect phase

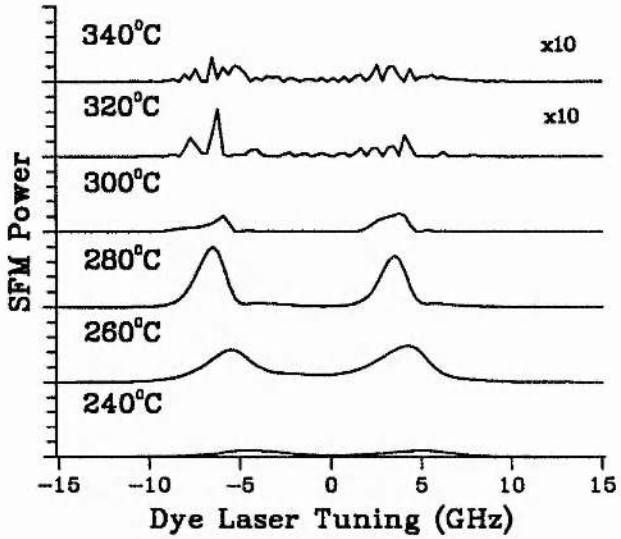

Figure 4.25: Theoretically predicted modulated output lineshapes at the vapour temperatures quoted for a dye laser tuning of $\lambda_1 = 589.363$nm.

matching on one subcomponent in two places. The predicted lineshapes are now very one sided and an increase in strength with the particle density is seen at the phase matched points. The other, non-phase matched, subcomponent is dominated completely by the phase matched one and drops out of view at higher temperatures. At this tuning then we would expect to see only one main line at high temperatures.

4.6.2. Experimental Observations

Lineshapes were recorded for the DQD route under various vapour temperatures, magnetic fields and dye laser tunings. All showed distortions which changed with each parameter. A 20cm focusing lens was used in the experiment, which produced a confocal parameter to match the theoretical predictions.

Figures 4.27 and 4.28 show the lineshape variations as the temperature was increased for dye laser tunings of $\lambda_1 = 588.963$nm and $\lambda_1 = 589.363$nm, corresponding to the predictions in figures 4.24 and 4.25 respectively. The traces are shown normalised here so that the detail can be seen but the overall peak power variation

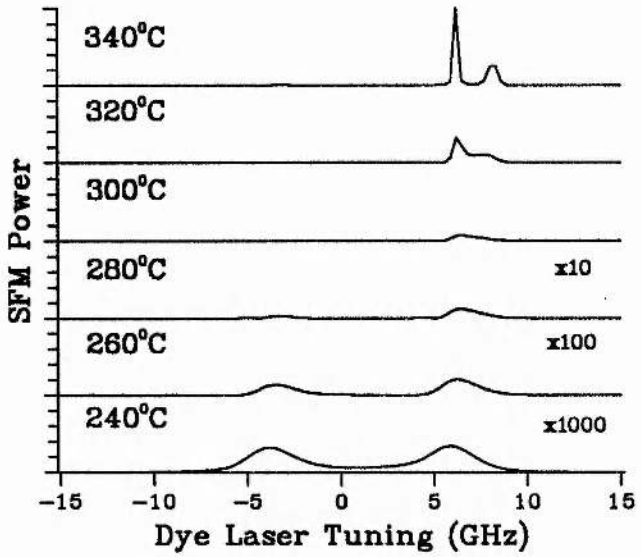

Figure 4.26: Theoretically predicted modulated output lineshape at the vapour temperatures quoted for a dye laser tuning of $\lambda_1 = 589.623$nm.

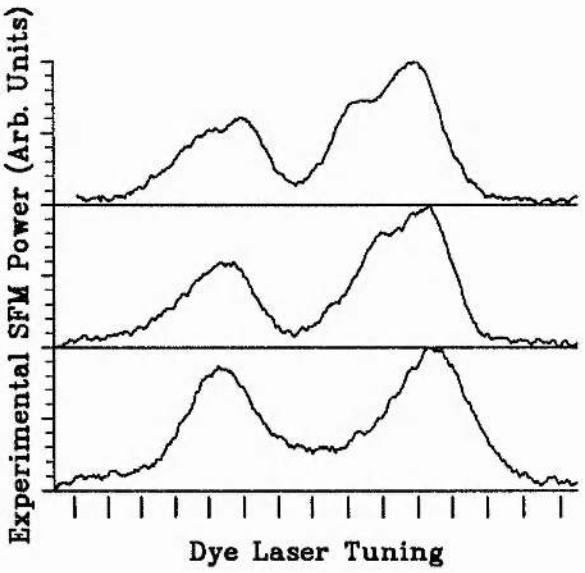

Figure 4.27: Experimentally observed SFM output power for a scan across two-photon resonance via a dye laser scan of 21GHz about $\lambda_1 = 588.963$nm at three increasing vapour temperatures (from bottom to top) for a magnetic field of 0.27 Tesla. A 1.5GHz confocal marker provides the frequency scale along the base. Amplitudes have been normalised for ease of viewing.

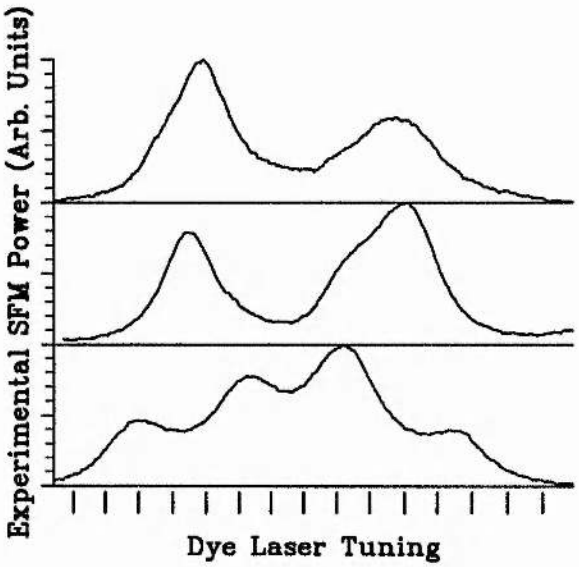

Figure 4.28: Experimentally observed SFM output power for a dye laser tuning of $\lambda_1 = 589.363$nm. Other parameters as before.

with temperature for fixed laser tunings was also observed. This showed a very flat output power trace (only a gentle 10–20% deviation) for the first tuning, figure 4.27, (a $\Delta k > 0$ region), which is as expected for the smoothed out oscillations at the high temperature end of such a phase mismatch region (cf. figure 4.8). For the second tuning (figure 4.28) the output power went through a distinct maximum at about the vapour temperature of the second trace in the figure and dropped swiftly on either side, the other two traces in the figure being around 20% of the peak amplitude of the central one. This is, once more, as expected as the region is a $\Delta k < 0$ area which accords maximum power on the first phase match peak and drops thereafter (cf. 4.8). Both figures show distortions to the lineshapes, changing with temperature, but do not show any swift oscillations during tuning, thought to be due to the same blurring effects as discussed for the DQD route. (Focusing was used throughout these experiments due to the lower efficiency of the DQD route.) The detail in the lineshapes does not match the predictions very closely — there is no breakup of each resonance into multiple phase matching components and the 4 peak shape of the first trace in figure 4.28 is unexpected — but the broad sim-

ilarities in the peak amplitude variations and the fact of distortions indicate some agreement. More accurate predictions of the phase mismatch and the conditions in the vapour cell would be needed to gain a better experimental fit.

However, at the tuning for one line to dominate strongly, $\lambda_1 = 589.623$nm, this is exactly what is observed. As the temperature is increased the higher frequency peak grows until it dominates in the output, as shown in figure 4.29. This should be compared to the theoretical prediction of figure 4.26. A good test of the theory is that at a tuning slightly down in wavelength the other peak should dominate as the offset is sufficient to bring the modulation mostly below $\Delta k = 0$ with only the top of the left hand resonance clipping it. This is precisely what is seen in figure 4.30 for a dye laser tuning of $\lambda_1 = 589.54$nm. Maximum power observed from the DQD route is of course achieved here due to phase matching but the output lineshape is radically different to that predicted without including the effects of the phase match variations during the scan.

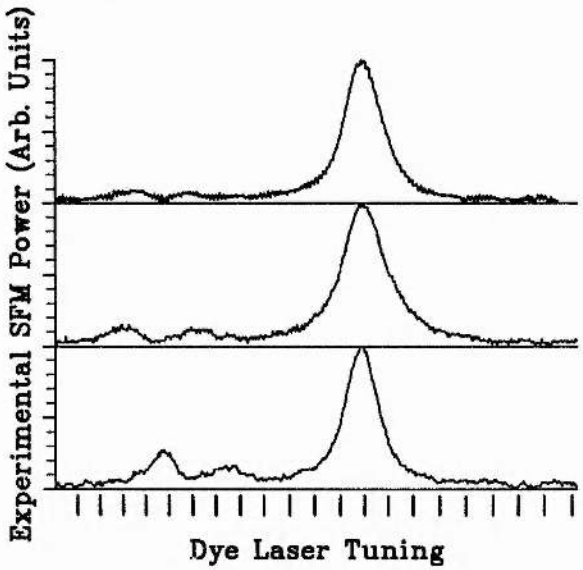

Figure 4.29: Experimentally observed SFM output lineshape for a dye laser tuning of $\lambda_1 = 589.623$nm. Other parameters as the previous two figures.

These results give excellent confirmation of the physical concept involved. While close detail is not matched, the blurring effects observed in the DDQ route can

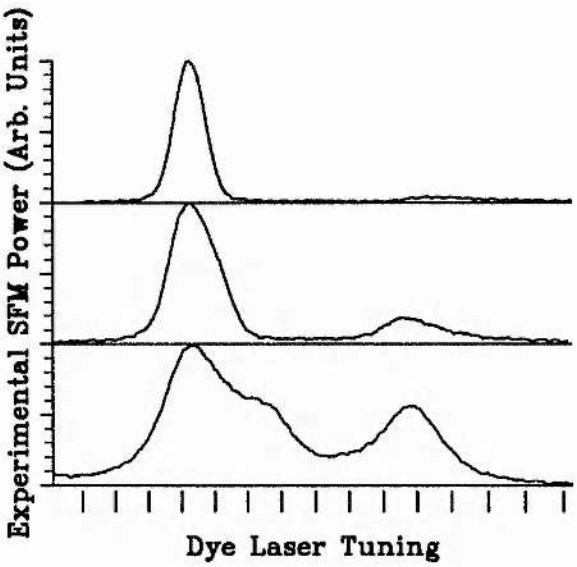

Figure 4.30: Experimentally observed SFM output lineshape for a dye laser tuning of $\lambda_1 = 589.54$nm. Other parameters as the previous three figures.

account for this. However, the most radical observation, that of one line dominating to the exclusion of the other at higher temperatures for certain dye laser wavelengths, is predicted well by phase matching theory and the conditions for the selection of either line matched between theory and experiment. This selection of either line is remarkably strong and quite straightforward to achieve. The importance of including the change of phase mismatching effects across two- photon resonance is underlined by these results.

Changing the magnetic field changed both the spacing of the resonances in the output lineshape and the distortions. This is to be expected as the shape of the phase mismatch modulation will be altered due to the increased Zeeman splitting. Also observed was output from the 3S–3P–$4P_{3/2}$ level scheme when the Ti:sapphire laser was tuned to come into two-photon resonance with this new upper level. The lineshapes and affects were broadly similar to those observed on the 3S–3P–$4P_{1/2}$ route, which has been considered throughout this chapter, including the dominance of one peak when the dye laser wavelength was tuned close to the crossover in atomic dispersion between the 3P sublevels.

The physical background to the modulations of the DQD lineshapes has been detailed here. In the future a better fit between theoretical and experimental results could be pursued. Some consideration should be given to the exact form of the phase matching modulation including the different subcomponent strengths which were assumed equal here. However, the most important advance would be a method of predicting the blurring features seen for both the DDQ and DQD routes. This may require an accurate vapour density map of the oven and input beam characteristics and is beyond the scope of this work.

4.7. Final Remarks

In this chapter I have described experiments on two different resonant enhancement schemes in sodium vapour for $\chi^{(2)}$ sum frequency mixing differing in their phase matching behaviour due to the placing of the dipole-forbidden transition. The 3S–3P–3D level scheme is shown to be well suited to a study of phase matching in vapours under different conditions and is able to be phase matched by tuning the dye laser to a crossover point in the atomic dispersion of the vapour. The 3S-3P-4P level scheme is shown to have strong distortions on its output lineshapes and these are explained by the phase matching modulation that occurs during a scan across resonance. It is possible to select either of the two lines to be phase matched independently, thus completely altering the observed lineshape.

An Acknowledgement

The work described in this chapter was conducted in close cooperation with another PhD student, now Dr. Sara Shepherd. More details and the full theory for the calculation of the unperturbed lineshapes can be gained from her thesis, [10].

REFERENCES

[1] N. Bloembergen, *Nonlinear Optics* (Benjamin, New York, 1965).

[2] Y. R. Shen, *The Principles of Nonlinear Optics* (Wiley, New York, 1984).

[3] D. C. Hanna, M. A. Yuratich, and D. Cotter, *Nonlinear Optics of Free Atoms and Molecules* (Springer Verlag, Berlin, 1979).

[4] Bruce D. Sinclair, *Second Harmonic Generation in Sodium Vapour Induced by a Magnetic Field*, PhD thesis, University of St. Andrews, 1987.

[5] B. D. Sinclair and M. H. Dunn, Continuous-wave second-harmonic generation in sodium vapour *Phys Rev A* **34**, 3989 (1986).

[6] M. H. Dunn, Continuous-wave, single-frequency, second harmonic generation in sodium vapour *Opt Commun* **45**, 346 (1983).

[7] B. D. Sinclair and M. H. Dunn, Magnetic field gradients and particle density effects in second-harmonic generation in sodium vapour *J. Mod. Opt.* **35**, 517 (1988).

[8] Alistair J. Poustie, *Magnetic Field Induced Sum Frequency Mixing in Sodium Vapour*, PhD thesis, University of St. Andrews, 1990.

[9] A. J. Poustie and M. H. Dunn, Magnetic field induced sum frequency mixing in sodium vapour *Phys Rev A* **47**, 1365 (1993).

[10] Sara Shepherd, *Use and Development of a CW Titanium Sapphire Laser for Non-Linear Optics*, PhD thesis, University of St. Andrews, 1993.

[11] *A Physicist's desk Reference, Physics Vade Mecum*, 2 ed., edited by Herbert L. Anderson (American Institute of Physics, New York, 1989).

[12] D. S. Bethune, R. W. Smith, and Y. R. Shen, Optical quadrupole sum-frequency generation in sodium vapour *Phys Rev Lett* **37**, 431 (1976).

[13] M. Matsuoka, H. Nakatsuka, H. Uchiki, and M. Mitsunaga, Optical second-harmonic generation in gases : "Rotation" of quadrupole moment in magnetic field *Phys Rev Lett* **38**, 894 (1977).

[14] Amnon Yariv, *Optical Electronics*, 3 ed. (Holt-Saunders, New York, 1985).

[15] R. B. Miles and S. E. Harris, Optical third-harmonic generation in alkali metal vapors *IEEE J Quantum Electron* **QE-9**, 470 (1973).

[16] D. P. Shelton and A. D. Buckingham, Optical second-harmonic generation in gases with a low-power laser *Phys Rev A* **26**, 2787 (1982).

[17] G. D. Boyd and D. A. Kleinman, Parametric interaction of focused gaussian light beams *J App Phys* **39**, 3597 (1968).

[18] Shekhar Guha and Joel Falk, The effects of focusing in the three-level parametric upconverter *J Appl Phys* **51**, 50 (1980).

[19] A. Lago, G. Hilber, and R. Wallenstein, Optical-frequency conversion in gaseous media *Phys Rev A* **36**, 3827 (1987).

[20] G. Hilber, D. J. Brink, A. Lago, and R. Wallenstein, Optical-frequency conversion in gases using gaussian laser beams with different confocal parameters *Phys Rev A* **38**, 6231 (1988).

Chapter 5

Route Interference in Resonant Sum Frequency Mixing

5. Route Interference in Resonant Sum Frequency Mixing

This chapter considers sum frequency mixing (SFM) in vapours with close single and two-photon resonances. Theory is presented to show that there are two possible routes of excitation of the output coherence and that they can be controlled in relative strength by the relative input laser powers. Furthermore, these routes can, under the appropriate conditions, interfere destructively. Resonant excitation of the upper level is considered, and experimentally monitored; in this case the two routes do not interfere and cannot be changed in relative strength. Experimental SFM results are presented and the features that were observed are shown to agree with the theoretical predictions. A cancellation of 94% of the SFM output power is measured under the conditions of strongest destructive interference found.

5.1. Resonant Sum Frequency Mixing

Having dealt in the previous chapter with some of the aspects of sum frequency mixing in vapours with a near resonant intermediate level I will now consider the case where the single-photon detuning, Δ_{12}, is very small, typically less than the Doppler width. When the intermediate level is brought into resonance in this way the efficiency of the wave mixing process should increase over the non-resonant case according to equation 4.2, but the assumptions used in deriving this equation are broken. Therefore, this theoretical approach is no longer valid and a full density

matrix approach is required if the efficiency of the process is to be calculated.

Sum frequency mixing with close single and two-photon resonances has not been discussed in detail, to our knowledge, except for the work of Poustie and Dunn [1, 2]. In that work resonant sum frequency mixing in sodium vapour on the 3S–3P–4D level scheme was studied using two continuous-wave dye lasers for the experiment. The background theory consisted of numerical solutions of the density matrix system but a full exploration of the parameters involved was not undertaken. Some numerical results showed a Doppler broadened lineshape for the ρ_{13} coherence that drives the sum frequency wave, and others a narrow lorentzian shape. No explanation was given for this change or for the intermediate case where a lorentzian hole was seen in a broader resonance. The experiments were carried out at low laser powers and the change in lineshapes with different laser powers was not explored.

This work will show that these experiments were inadvertently carried out in one extreme of sum frequency mixing conditions and that very different lineshapes can be seen if the relative laser strengths are varied. The wide Doppler broadened profile and the narrow Lorentzian lines that are predicted are identified separately with the two excitation pathways for ρ_{13} and I will discuss how the relative strengths of these may vary and show that they can interfere and lead to a cancellation of the output under a critical parameter set.

5.2. Excitation of Population

Previous work in the interaction of two resonant fields in a cascade three-level atomic scheme was often concerned with the excitation of population to the uppermost level. Two important applications required this calculation: sub-Doppler spectroscopy (performed by monitoring fluorescence from the uppermost level); and multiphoton ionisation yields (requiring maximum population in the pre-ionisation excited state). From this interest, two processes yielding sub-Doppler spectroscopic information from the uppermost level were developed. These are discussed below and shown in

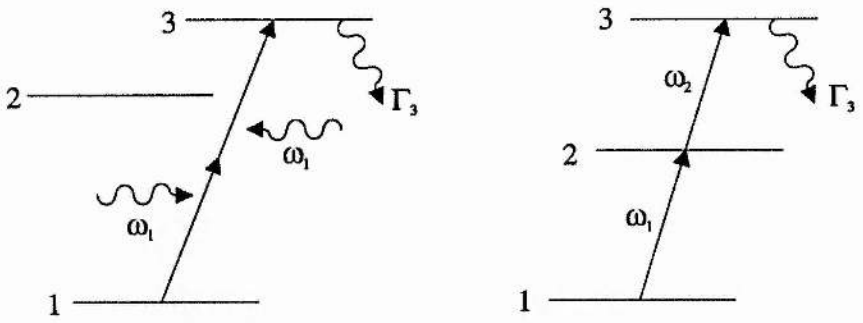

Figure 5.1: On the left two-photon Doppler-free spectroscopy with counter-propagating, equal-frequency laser beams and on the right sub-Doppler spectroscopy using a resonant intermediate level and velocity-selection.

figure 5.1.

Doppler-free two-photon spectroscopy (see any laser spectroscopy text eg. [3]) uses two counter-propagating equal frequency light beams to excite atoms via a two-photon transition. The Doppler shifts of two oppositely travelling photons impinging on the atom cancel and sharp, Doppler-free resonances are observed. Unfortunately, the transition rate can be low if there is no intermediate level situated conveniently to resonantly enhance the process [4, 5].

However, a second technique can be applied using two unequal frequency lasers and tuning the first laser directly onto single-photon resonance. A second laser then excites these atoms to the third level. This simultaneously produces the highest possible transition rate and also gives Doppler-free information [6]. Bjorkholm and Liao first presented theory and results using this second technique and were able to gain high resolution spectroscopic information with very low input intensities and particle densities. The mechanism for sub-Doppler excitation here is different to conventional two-photon spectroscopy and either co- or counter-propagating beams may be used. The mechanism for this process relies on the first laser exciting a well defined velocity group of atoms to the intermediate level — those with the correct Doppler shift to be within the homogeneous linewidth. This small velocity

subset may then be excited in a second step to the upper level when the second laser frequency is such that their Doppler shift brings them into homogeneous resonance with the uppermost level also. This velocity-selection relies on a sufficient number of atoms being in the correct velocity group and therefore is only observed for close resonant tuning of the lower laser.

5.2.1. Population Excitation Routes

The latter sub-Doppler technique is of interest here as it uses the same input laser conditions that resonant sum frequency mixing does. While we are interested in the excitation of ρ_{13} for this end, the excitation of the population, described by ρ_{33}, is also instructive. Previous work has concentrated on ρ_{33} due to the spectroscopy or ionisation applications considered.

The lineshape of excitation to the upper level consists of two distinct features [6, 7]. One is a Doppler broadened feature and the other a narrow Doppler-free feature from velocity-selection. The origin of these two features and their different resonance conditions lie in two different routes for the excitation of population. Berman [7, 8] displays density matrix perturbation chains highlighting this. The first route is direct two-photon excitation following the chain:

$$\rho_{11} \overset{\Omega_{12}}{\rightarrow} \left\{ \begin{array}{c} \tilde{\rho}_{12} \\ \tilde{\rho}_{21} \end{array} \right\} \overset{\Omega_{23}}{\rightarrow} \left\{ \begin{array}{c} \tilde{\rho}_{13} \\ \tilde{\rho}_{31} \end{array} \right\} \overset{\Omega_{12}}{\rightarrow} \left\{ \begin{array}{c} \tilde{\rho}_{23} \\ \tilde{\rho}_{32} \end{array} \right\} \overset{\Omega_{23}}{\rightarrow} \rho_{33} \tag{5.1}$$

The process is resonantly enhanced by the close resonance with the intermediate level but does not lead to any population transfer in to or out of this level. It leads to a Doppler broadened lineshape and has the two-photon resonance condition: $\Delta_2 = -\Delta_1$, in the absence of any frequency-pulling effects [6]. It dominates for off-resonant and nearly-resonant excitation and will be referred to as two-photon (TP) excitation hereafter. The second route is a two-step process involving the creation

of a population in level 2 by the route:

$$\rho_{11} \overset{\Omega_{12}}{\rightarrow} \left\{ \begin{array}{c} \tilde{\rho}_{12} \\ \tilde{\rho}_{21} \end{array} \right\} \overset{\Omega_{12}}{\rightarrow} \rho_{22} \overset{\Omega_{23}}{\rightarrow} \left\{ \begin{array}{c} \tilde{\rho}_{23} \\ \tilde{\rho}_{32} \end{array} \right\} \overset{\Omega_{23}}{\rightarrow} \rho_{33} \tag{5.2}$$

Due to the velocity-selection of population to level 2 this route is Doppler-free and has the two-photon resonance condition: $\Delta_2 = (k_2/k_1)\Delta_1$, where k_1 and k_2 are the wavevectors of the two input fields. A straightforward hole-burning argument for this resonance condition is as follows. For a given lower laser detuning, Δ_1, there will be some velocity, V_z, such that atoms moving at that velocity are Doppler-shifted on to exact resonance, ie. $\Delta_1 - k_1 V_z = 0$. These atoms may be excited by exact resonance to the upper level if the condition $\Delta_1 + \Delta_2 - (k_1 + k_2)V_z = 0$ is satisfied. Substitution of V_z from the first equation into this yields the appropriate resonant condition for the upper field tuning. This route dominates when the number of atoms within the velocity subgroup for the selection process is appreciable, ie. Δ_1 is within a Doppler width of resonance. Due to the introduction of population to level 2 this pathway is known as two-step (TS) excitation. Note that both routes use both fields twice, merely using them in a different order, and, therefore, have strength proportional to $(\Omega_{12}\Omega_{23})^2$.

The fact that two distinct routes were involved in the transfer of population between two levels via a resonant or near-resonant intermediate level was first formally stated by Shen [9] for the case of resonance Raman scattering versus hot luminescence. In this work he states that under steady-state conditions the two routes may be differentiated by different linewidths but cannot be separated. Berman [7, 8] considers the routes as they are affected differently by collisions but states, similarly, that without collisional perturbations the formal split is academic under steady-state conditions. Only in their time dependencies can they be separated. Consider the sudden removal of the lower laser field: the two-step route will decay away as the level 2 population relaxes to the ground state, while the two-photon route will depend on the decay of $\tilde{\rho}_{13}$. This difficulty of separation is encapsulated by the

Schrödinger atom calculation for the upper level population. From second order perturbation theory the population of level 3 is [6]:

$$|a_3|^2 = \left| \frac{\Omega_{12}\Omega_{23}}{\tilde{\Delta}_{12}\tilde{\Delta}_{13}} \right|^2 \tag{5.3}$$

using the notation and definitions of section 2.1.1. Integration over the Maxwellian velocity distribution, via the detunings, leads to *both* features and the resulting total lineshape. A set of examples is shown in figure 5.2. With the lower field on resonance the narrow velocity-selected route dominates in the lineshape. As the lower field is detuned the strength of this feature is reduced and the Doppler broadened line becomes visible and in turn dominates at large intermediate detunings.

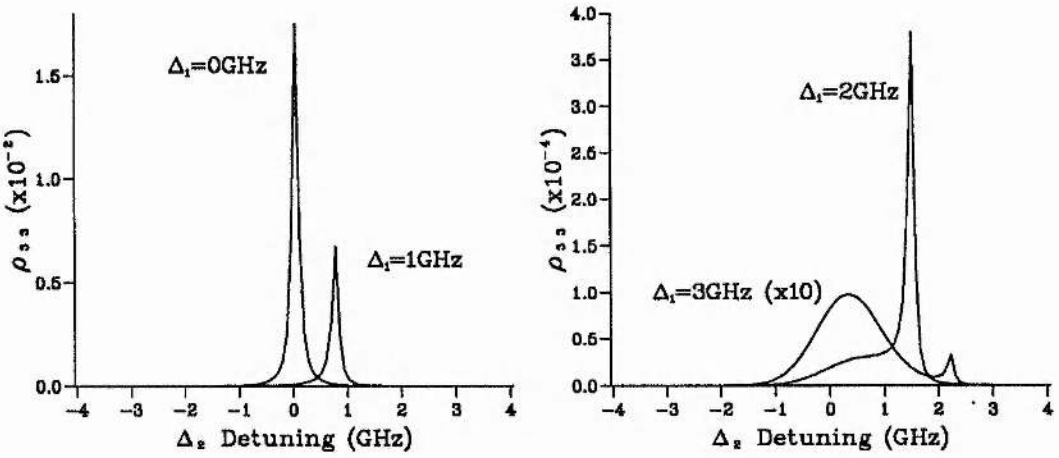

Figure 5.2: Excitation to level 3 calculated for different intermediate level detunings of $\Delta_1 = 0, 1, 2, 3$GHz as indicated on the figure, using a simplified density matrix system.

5.3. Excitation of ρ_{13}

A similar analysis with perturbation chains may be carried out for the excitation of ρ_{13}. It is found that there are again two routes. One is a two-photon (TP) route

and one is a two-step (TS) process. The TP chain has merely two links:

$$\rho_{11} \overset{\Omega_{12}}{\rightarrow} \left\{ \begin{array}{c} \tilde{\rho}_{12} \\ \tilde{\rho}_{21} \end{array} \right\} \overset{\Omega_{23}}{\rightarrow} \left\{ \begin{array}{c} \tilde{\rho}_{13} \\ \tilde{\rho}_{31} \end{array} \right\} \tag{5.4}$$

while the TS chain has four:

$$\rho_{11} \overset{\Omega_{12}}{\rightarrow} \left\{ \begin{array}{c} \tilde{\rho}_{12} \\ \tilde{\rho}_{21} \end{array} \right\} \overset{\Omega_{23}}{\rightarrow} \rho_{22} \overset{\Omega_{12}}{\rightarrow} \left\{ \begin{array}{c} \tilde{\rho}_{23} \\ \tilde{\rho}_{32} \end{array} \right\} \overset{\Omega_{12}}{\rightarrow} \left\{ \begin{array}{c} \tilde{\rho}_{13} \\ \tilde{\rho}_{31} \end{array} \right\} \tag{5.5}$$

This analysis shows immediately that the two routes may now be separated by control of the input field amplitudes. The TS path is of order $\Omega_{12}^3\Omega_{23}$, while the TP path is of order $\Omega_{12}\Omega_{23}$. Therefore, at high values of Ω_{12} the narrow TS route will dominate in the output and a velocity-selected sub-Doppler SFM line-profile will be observed, while at low values a Doppler broadened SFM profile will be generated. This is in stark contrast to the population case where both routes were symmetrical in their use of the fields and the TS route always dominated on resonance.

5.3.1. Simplified Density Matrix Analysis

To gain a more quantitative view we must refer to the density matrix equations for the three level cascade system of chapter 2. Under steady-state conditions equation 2.23f for the slowly varying SFM driving coherence $\tilde{\rho}_{13}$ may be written:

$$\tilde{\rho}_{13} = \frac{\Omega_{12}\tilde{\rho}_{23} - \Omega_{23}\tilde{\rho}_{12}}{(\Delta_1 + \Delta_2 - i\gamma_{13})} \tag{5.6}$$

The first term in the numerator is identifiable as the last link in the TS chain and the second term the end of the TP chain. Substituting for the coherences, to first order, back down the perturbation chain this becomes:

$$\tilde{\rho}_{13} = \frac{\Omega_{12}\Omega_{23}(\rho_{33} - \rho_{22})}{(\Delta_1 + \Delta_2 - i\gamma_{13})(\Delta_2 - i\gamma_{23})} - \frac{\Omega_{12}\Omega_{23}(\rho_{22} - \rho_{11})}{(\Delta_1 + \Delta_2 - i\gamma_{13})(\Delta_1 - i\gamma_{12})} \tag{5.7}$$

neglecting the higher order terms for $\tilde{\rho}_{13}$. Assuming the applied fields are of low strength (which in a Doppler broadened medium is easily satisfied) the populations may be approximated by $\rho_{11} \approx 1$, $\rho_{22} \approx 0$ and $\rho_{33} \approx 0$. Incorporating this and

substituting down the rest of the TS chain, using $\Im\{\}$ to denote the imaginary part, we finally have:

$$\begin{aligned}\tilde{\rho}_{13} &= -\frac{2\Omega_{12}^3\Omega_{23}}{\Gamma_{21}(\Delta_1+\Delta_2-i\gamma_{13})(\Delta_2-i\gamma_{23})}\Im\left\{\frac{1}{(\Delta_1-i\gamma_{12})}\right\} \\ &\quad +\frac{\Omega_{12}\Omega_{23}}{(\Delta_1+\Delta_2-i\gamma_{13})(\Delta_1-i\gamma_{12})} \end{aligned} \tag{5.8}$$

The TS path is described by the first term on the right hand side with the predicted field dependence. Doppler integration will lead to velocity-selection and note that it is inversely proportional to the spontaneous decay rate of level 2. The TP path, on the other hand, is purely dependent on coherence decay rates, ie. γ_{12} and γ_{13}.

5.3.2. Interference of the Two Routes

The second difference between the behaviour of the routes in SFM as opposed to population movements is now obvious from equation 5.8. The two terms on the right hand side are of opposite sign indicating that the routes may interfere destructively. As a detuning scan is performed the two routes will change in phase and magnitude but on simultaneous single and two-photon resonance they are exactly in anti-phase and can cancel out completely if they are of appropriate strengths. Since the strengths can be adjusted by the relative input wave powers, it will be possible to null any SFM output by adjusting these when tuned directly on resonance at both the middle and upper levels. This is a most surprising and interesting result. One view is to compare it to Fano interference or electromagnetically-induced transparency. In both of these processes two paths to the same end interfere. For the former the two paths are, direct ionisation and ionisation via a short-lived autoionising level. It is the same idea here with the interference between the TP and TS routes to ρ_{13}.

To look at this in detail the two terms from equation 5.8 were separately integrated over the Maxwellian velocity distribution and the resulting real and imaginary parts of each are displayed in figure 5.3. The field strengths are chosen to illustrate

near cancellation and the lower field is taken as resonant. This figure illustrates the

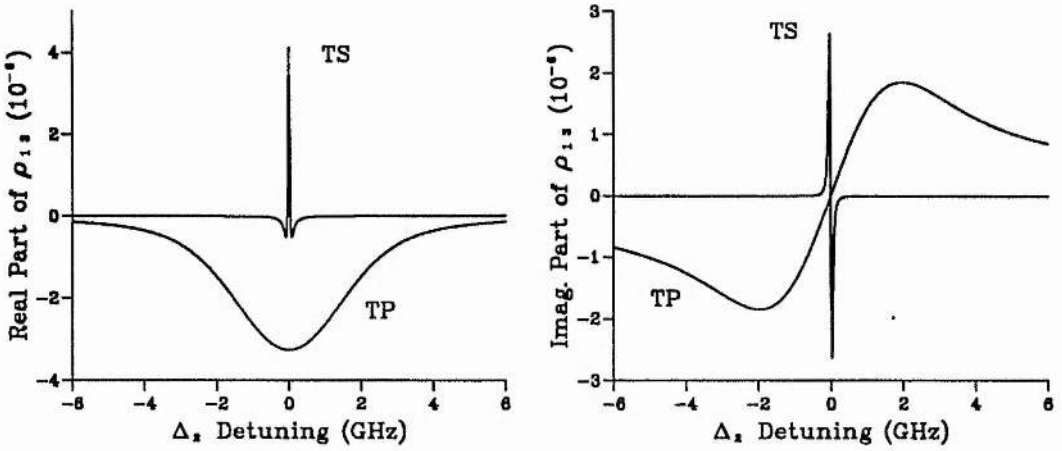

Figure 5.3: Separate solutions of the TP and TS terms split into real (left) and imaginary (right) parts. Integration over the Doppler shift was for 500K and the other parameters used were: $\Omega_{12} = \Omega_{23} = 0.001$GHz, $\Gamma_{32} = \Gamma_{21} = 0.05$GHz, $\gamma_{12} = \gamma_{23} = 0.025$GHz, $\gamma_{13} = 0.01$GHz and $\Delta_1 = 0$.

different broadening conditions for the two routes and opposing phases. Perhaps a better view is in the complex plane using phasors. The two phasor lobes mapped out by each of the two terms is shown in figure 5.4 for the same parameters. (The corresponding total SFM output is shown in an inset.) Two individual phasors, one for an upper level tuning of exact resonance (labelled "0") and the other for 100MHz detuning (labelled "100") are displayed within the figure. These show that, starting on resonance, the two routes are in anti-phase and as the upper laser is tuned off resonance the TP phasor rotates slowly in a clockwise direction while the TS phasor rotates much more rapidly and in an anti-clockwise direction. The difference in rotation rates is due to the difference in linewidths and at arbitrary detuning points a vector addition between the two phasors is necessary to produce the resultant output, shown by a dotted phasor lobe.

This method of visualisation is helpful when $\Delta_1 \neq 0$. For detunings around

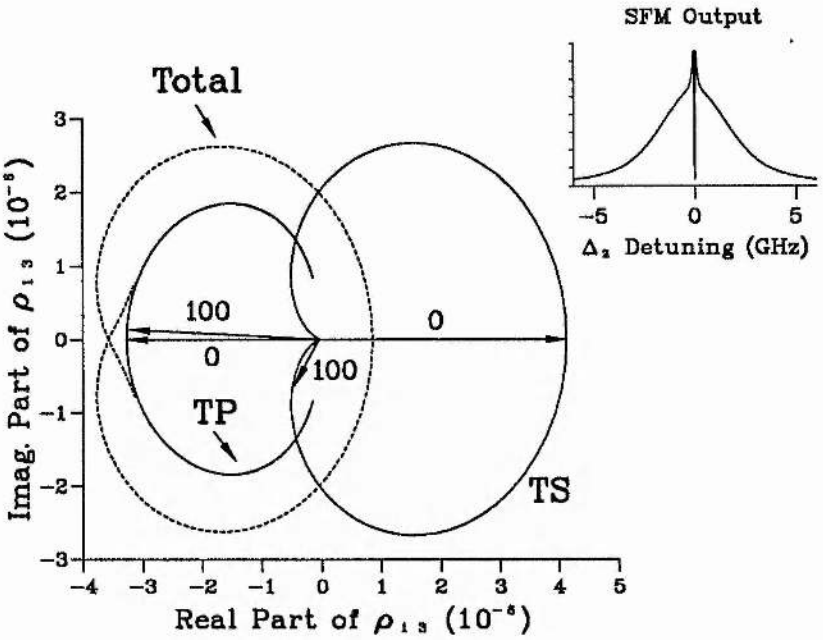

Figure 5.4: The locus of points swept out by the phasors for the TP and TS routes, and the resulting total, for the same parameters as the previous figure. Phasor arrows are displayed for $\Delta_2 = 0$ and $\Delta_2 = 100$MHz.

the Doppler width the routes combine with a dispersive-like feature. Figure 5.5 shows the calculations for the two terms when $\Delta_1 = 2$GHz, with other parameters unchanged. Both routes have moved their resonance position in different directions, as described earlier, and the TS route has dropped markedly in strength relative to the TP route. This is due to the smaller number of atoms in the correct velocity group for the selective excitation. The total SFM lineshape is an inset in figure

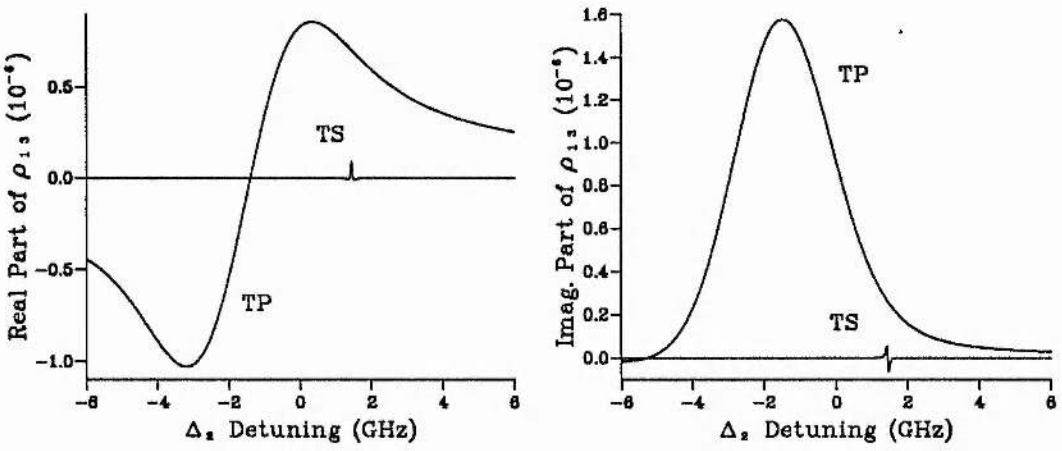

Figure 5.5: Solutions for the TS and TP routes with parameters as before, except $\Delta_1 = 2$GHz

5.6 which shows the phasor lobes for this situation. The TS lobe is as before but much smaller while the TP lobe has been rotated about the origin due to the phase offset from the intermediate level detuning. The total phasor follows the TP route until the point when the TS phasor grows quickly. The vector addition then doubles briefly back on itself before being extended and the total magnitude undergoes a brief dip and then peak on the falling edge of the TP route. At intermediate level detunings higher than this the TP route can have fallen almost to zero before the TS route becomes important and so the combination is trivial and almost scalar in manner.

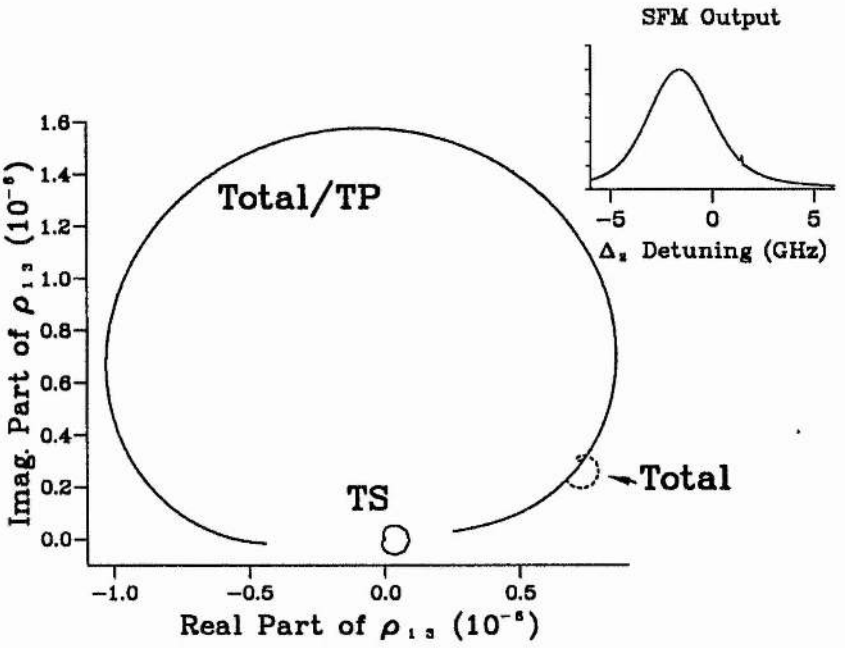

Figure 5.6: The locus of points swept out by the phasors for the TP and TS routes, and the resulting total, for the same parameters as the previous figure.

5.3.3. Full Numerical Model

To accurately predict the experimental situation and test the assumptions used in deriving the simplified equations full numerical solutions were sought. The field strengths used were raised to above the saturation level for the individual transitions, as they are in the experiment, but the essential features of the simplified calculations remain.

Results from the model display the profile of $|\tilde{\rho}_{13}|^2$ (which predicts the SFM lineshape) as Δ_2 is changed to simulate an upper laser scan. First, the upper field strength, Ω_{23} is systematically raised as the other parameters are held constant as shown in figure 5.7. The lower field was set to resonance so both routes peak at $\Delta_2 = 0$. To begin with, at very low values of Ω_{23}, the profile is a single, narrow resonance due to the TS route alone. As Ω_{23} is increased, and the broader TP route grows in strength, wings appear on the edge of the peak, and sharp dips flank the TS feature. These are caused by the phasor flipping from the TS phase to the TP

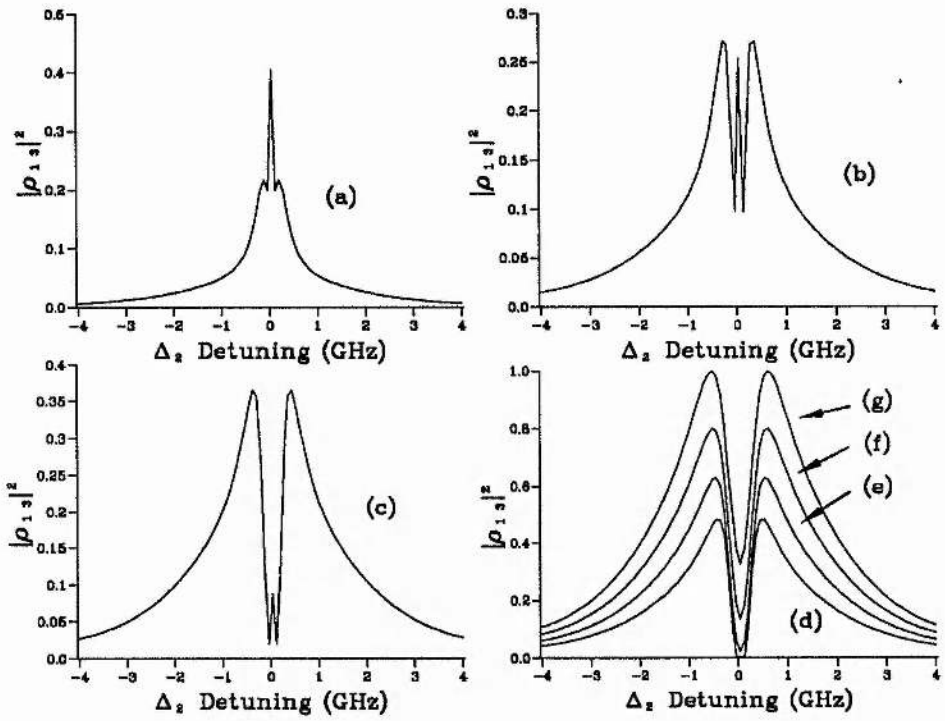

Figure 5.7: Full numerical solutions for $|\tilde{\rho}_{13}|^2$ including Doppler broadening plotted against Δ_2 for $\Omega_{12} = 0.02$GHz and $\Omega_{23} = 0.04, 0.06, 0.08, 0.10, 0.12, 0.14, 0.16$GHz (traces (a) to (g) respectively).

phase and passing close to the origin as is does so. Eventually, at a critical point, the two routes cancel completely on resonance (trace (d)) and then as the TP route continues to grow the TS route appears as a dip in the Doppler broadened profile. Eventually when $\Omega_{23} \gg \Omega_{12}$ the lineshape is a pure Doppler profile.

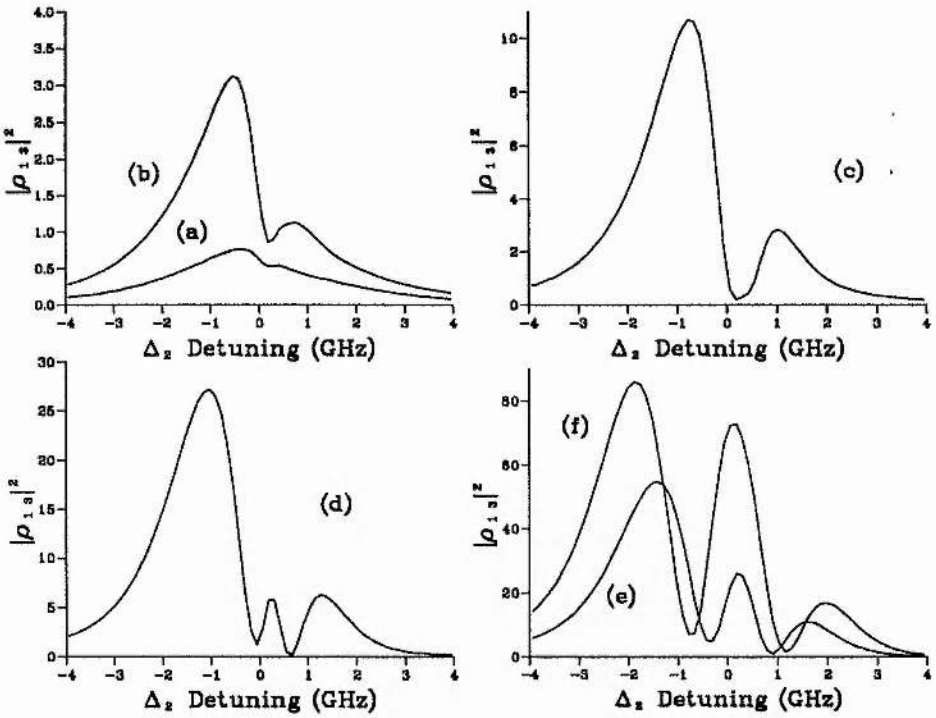

Figure 5.8: Full numerical solutions for $|\tilde{\rho}_{13}|^2$ including Doppler broadening plotted against Δ_2 for $\Omega_{23} = 0.2$GHz and $\Omega_{12} = 0.0125, 0.025, 0.05, 0.1, 0.2, 0.4$GHz (traces (a) to (f) respectively) with $\Delta_1 = 0.25$GHz.

The features are essentially the same in reverse order if Ω_{23} is held steady and Ω_{12} rises, figure 5.8. Here the lower level is just to one side of resonance to show that the features are not restricted to exact resonance. Distinct power broadening of the TS route is noticeable as the lower field power level rises but the dips surrounding this route remain. Note that the closest cancellation point is on one side of the TS route in trace (d). This is because the TS route is offset from resonance and the total SFM phasor swings very close to zero as it returns to the TP path on one side.

If the intermediate level detuning, Δ_1, is altered in isolation the changes are complicated. Both the resonances move relative to the origin and each other and, more dramatically, the TS route strength varies strongly due to the Maxwellian distribution of velocities determining the atoms available for selective excitation. Figure 5.9 shows five such traces. To begin with only the TP Doppler line is visible (trace (a)) as the lower laser is detuned significantly. In trace (b) the TS route is seen as a small distortion on one flank, rising to a dispersive feature in (c) and (d). Finally, in (e) it becomes strong enough to be a distinct dip in the profile. This agrees with the predictions made above: that at sufficient detunings (typically, $\Delta_1 >$ Doppler width) the two routes seem additive in the profile and no interference effects are visible in the output, becoming similar to the upper state population predictions.

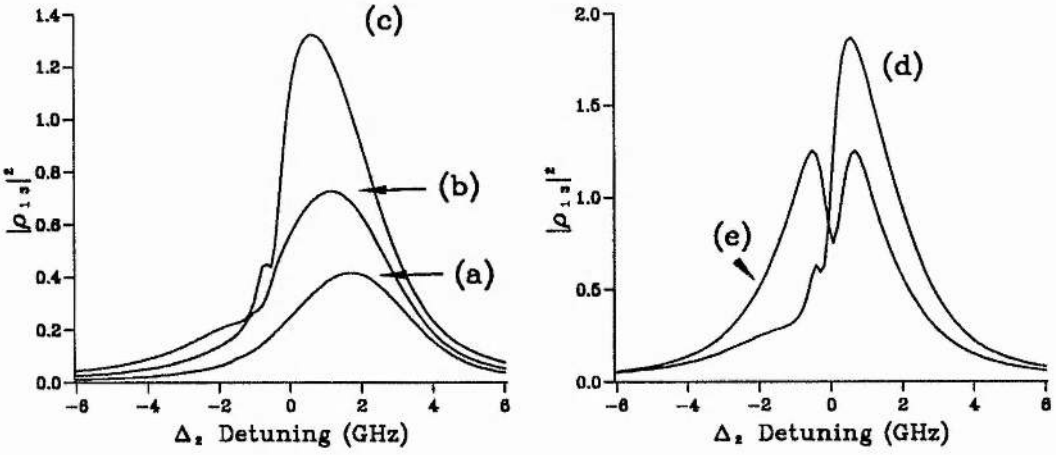

Figure 5.9: Full numerical solutions for $|\tilde{\rho}_{13}|^2$ including Doppler broadening plotted against Δ_2 for $\Omega_{12} = 0.02$GHz, $\Omega_{23} = 0.2$GHz and $\Delta_1 = -2, -1.5, -1, -0.5, 0$GHz (traces (a) to (e) respectively).

5.4. Experimental Excitation to the 3D Levels

The experimental work to study the interference between the two routes for excitation of the SFM coherence consists of two parts. A study of the excitation to the upper (3D) levels was undertaken at the laser powers relevant to the SFM experiment because previous experiments concentrated on low laser powers to reduce power broadening [6]. These profiles then provide an ideal background to present the SFM results against and the novel features of the SFM output are highlighted.

The majority of the experimental work was carried out using the $3P_{1/2}$ level as the resonant intermediate state as then selection rules only allow excitation to the $3D_{3/2}$ upper state. Due to velocity-selection and the ratio of wavevectors involved, the structure of the levels are not displayed at their base splitting. Table 5.1 summarises the level structures, their relevant display parameters (from [6]) and the resulting prediction for the observed splitting. Using the $3P_{1/2}$ level the structures of the 3S and $3P_{1/2}$ levels are seen in the output. If, though, the $3P_{3/2}$ level is used as a resonant intermediate, the structures of the 3S and 3D states are imaged as the $3D_{5/2}$ level can now be excited and the intermediate level hyperfine structure is smaller and, therefore, unresolved.

Level	*3S*	*3P$_{1/2}$*	*3D*
Fine/Hyperfine Structure	1.77GHz	188MHz	1.48GHz
Observation Factor	k_2/k_1	$(1+(k_2/k_1))$	1
Predicted Observation	1.27GHz	323MHz	1.48GHz

Table 5.1: Velocity-selection observation factors for the 3S-3P-3D levels.

5.4.1. 819nm Fluorescence

Excitation to the 3D levels can be probed by monitoring the 819nm spontaneous decay from the 3D to the 3P levels. Unfortunately, this fluorescence is at the same

wavelength as one of the exciting lasers but phase sensitive detection rendered reasonable signal to noise ratios possible for a side detector. Bjorkholm and Liao [6] studied excitation to the 4D levels in sodium in a similar way but at much reduced laser powers due to their emphasis on high resolution spectroscopy. The stronger lasers used here produced appreciable power broadening and the results are comparable to those of Poustie [1] for fluorescence monitored during SFM using the 4D level.

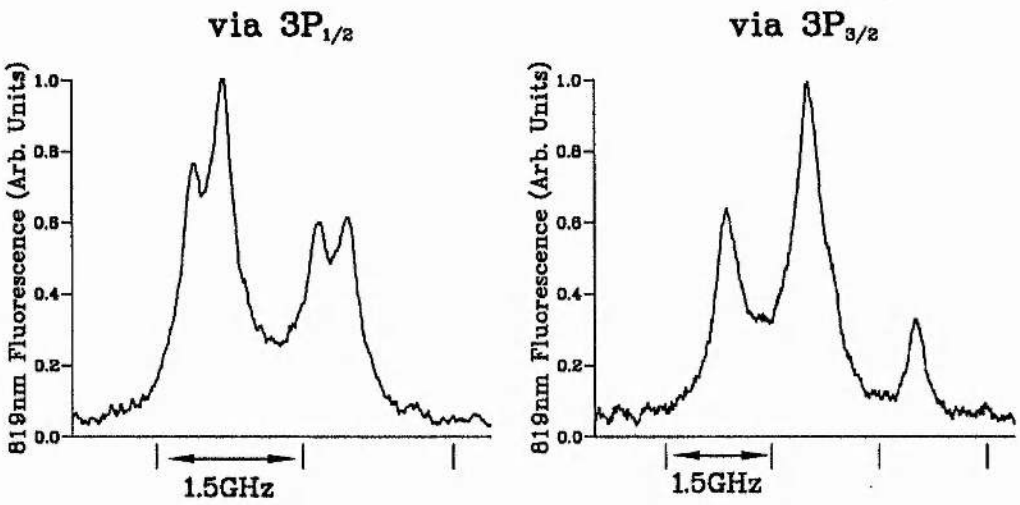

Figure 5.10: Sideways 819nm fluorescence from the decay of the 3D level with the $3P_{1/2}$ (left) and $3P_{3/2}$ (right) level as intermediate resonance. Laser powers were 90mW (dye) and 100mW (Ti:sapphire). A marker determined by a 1.5GHz confocal Fabry-Perot interferometer gives a horizontal frequency tuning axis scale for the Ti:sapphire laser scan in this, and all subsequent, experimental figures. No magnetic field was applied.

With the dye laser on resonance with the $3P_{1/2}$ level the fluorescence observed for a Ti:sapphire laser scan across the 3D level is shown in figure 5.10 (left hand trace). There are four distinct peaks which are (left to right):

$3S_{1/2}$		$3P_{1/2}$		3D
F=2	→	F=1	→	$3D_{3/2}$
F=2	→	F=2	→	$3D_{3/2}$
F=1	→	F=1	→	$3D_{3/2}$
F=1	→	F=2	→	$3D_{3/2}$

with the smaller splitting corresponding to the intermediate level hyperfine structure and the spacing of the two pairs from the larger ground state hyperfine splitting. Note that despite the narrow homogeneous linewidth (< 10MHz) the lines are not well resolved. This is due to the power broadening of the lasers which will be investigated in more detail in the next section. Notable also is the sub-Doppler lorentzian nature of the lines due to velocity-selection. With the Ti:sapphire laser power raised a couple of orders of magnitude above the dye laser power (and even focused) no evidence of a Doppler profile was seen on resonance, as predicted previously and confirming that the two routes have equal dependencies on the input fields.

Using the $3P_{3/2}$ level as the resonant intermediate state, figure 5.10 (right hand trace), the fluorescence profile should contain four resonances but now, due to the different sources, the central two are unresolved. The three peaks are (left to right):

$3S_{1/2}$		3P		3D
F=2	→	$3P_{3/2}$	→	$3D_{5/2}$
F=1	→	$3P_{3/2}$	→	$3D_{5/2}$
F=2	→	$3P_{3/2}$	→	$3D_{3/2}$
F=1	→	$3P_{3/2}$	→	$3D_{3/2}$

The profile shows similar power broadening and velocity-selection to the previous case.

5.4.2. 343nm anti-Stokes Raman Process

The second signal probing excitation to the upper level was observed at 343nm at the end of the oven. The line profile exactly matched that of the 819nm fluorescence

(checked with simultaneous recordings) but the signal-to-noise ratio was much better and so the parameter range could be explored more widely.

This signal is thought not to be due to sum frequency mixing, even though it occurred at the same output wavelength, for three reasons. As there was no transverse magnetic field applied the $\chi^{(2)}$ sum frequency process is disallowed due to symmetry arguments. Notwithstanding, there has been some experiments demonstrating second order processes without external symmetry breaking [10, 11, 12]. However, all of these experiments used high peak power pulsed laser systems and the mechanism allowing the process is thought to require these high powers. A sensitive continuous-wave experiment designed to test this confirmed this view, detecting no parametric output [13]. Another mechanism using arbitrary beam profiles has been considered by Bethune [14] but the input beams used here were close approximations to gaussians. Therefore, neither of these mechanisms is likely to be operating in the vapour and the signal cannot be from a $\chi^{(2)}$ process. Furthermore, no phase matching power oscillations were seen with increasing oven temperature confirming this. Finally, the line profiles match those predicted for excitation of population to the upper level ie. purely velocity-selective on resonance, no interference features, no change in route strengths with laser powers etc.

There are two possible remaining sources for the UV signal. Quadrupole fluorescence (3D-3S) is one. However, the output was quite strong (similar in strength to the SFM signal at very low magnetic fields) and quite directional. It was detectable up to 1m away from the oven end and was significantly stronger when detected at the end of the oven or cell than when the photomultiplier tube was situated at a side port. Therefore, it is concluded to be due to a $\chi^{(3)}$ anti-Stokes Raman process. The mechanism is thought to be that during the excitation to the 3D level the atom is dephased, probably due to a collision, and the atomic orientation is lost. Then the final excitation step by the Ti:sapphire laser beam can set up one of the quadrupole moments able to radiate in the forward direction. Without a dephasing step for input parallel linear polarisations, in the absence of a magnetic field, selection rules

do not allow these quadrupole moments to be coherently set up [15, 16]. The Raman process must rely on a quadrupole transition for resonant enhancement but there is a precedent for this in potassium vapour [17, 18]. In these experiments the process was Stokes generation by single-photon excitation on the quadrupole transition and then subsequent coherent relaxation to the P level. The efficiency was measured as being fairly high due to the low parasitic absorption associated with the quadrupole transition.

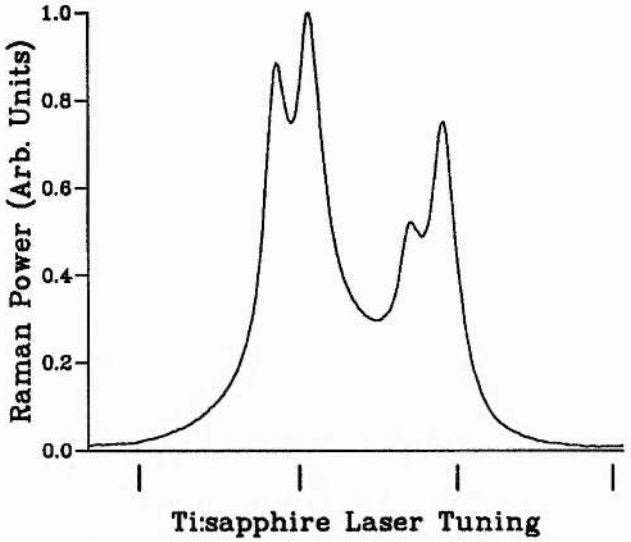

Figure 5.11: The lineshape of the anti-Stokes Raman process with the $3P_{1/2}$ resonant intermediate state. (Vapour temperature $\approx 180^0$C, laser powers both $\approx$ 20mW.)

The basic on-resonance lineshape is shown in figure 5.11. It is very similar to the fluorescence previously displayed but the better signal-to-noise ratio is obvious. This allowed a clearer investigation of the lineshape with different laser powers and intermediate level detunings. The change in signal strength with each of the lasers in turn is displayed in figure 5.12. The signal is linearly dependent on the dye power throughout its range but saturates with strong Ti:sapphire laser powers. A possible mechanism for this is based on the fact that for a given dye laser power there is only a certain number of atoms excited out of the ground state. Therefore, as the Ti:sapphire laser power is raised it will reach a point where the majority of these

atoms are being excited on to the 3D level and saturation occurs.

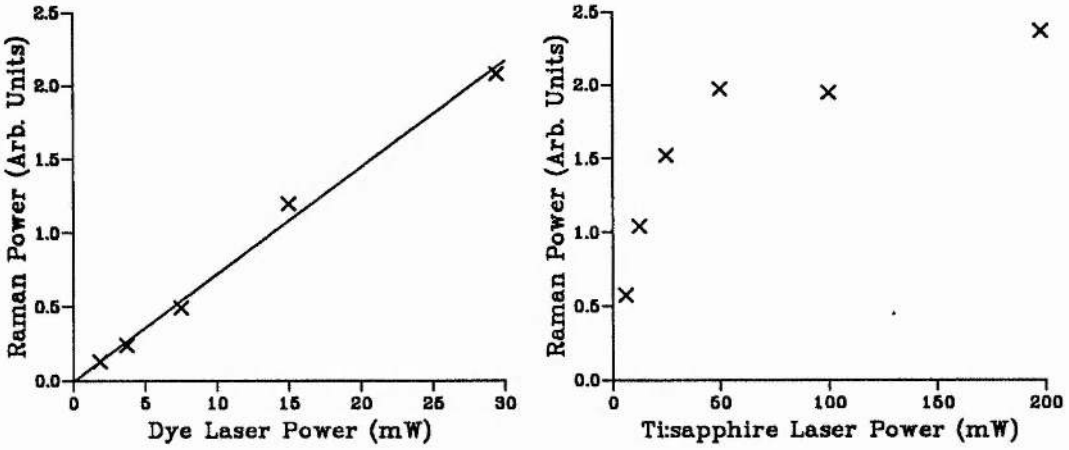

Figure 5.12: Variation of the peak Raman signal strength with: (left) the dye laser power (Ti:sapphire 190mW); and (right) the Ti:sapphire laser power (dye 30mw).

The effects of raising the laser powers on the lineshape are shown in figures 5.13 and 5.14. The lineshapes are normalised to equal height for the broadening effects to be clearly seen. As expected, the lineshapes merely power broaden and no wings from a repressed Doppler broadened TP route come through. The line broadens more with the Ti:sapphire laser power as the Ti:sapphire laser power was relatively high during the results taken for different dye laser powers, and thus causes the dominant broadening on the lineshape.

As the dye laser is detuned from intermediate level resonance the TS and TP routes can be separately seen. It is not until the lower laser has been tuned around 4GHz from resonance that the peak of the Doppler profile shows through clearly. Output powers are held down on intermediate level resonance due to the parasitic linear absorption of the the dye laser on the first transition step lowering the interaction length. This helps the detuned traces to be observed without having dropped excessively in output strength by comparison. Figure 5.15 shows four successive 1.5GHz moves of the dye laser.

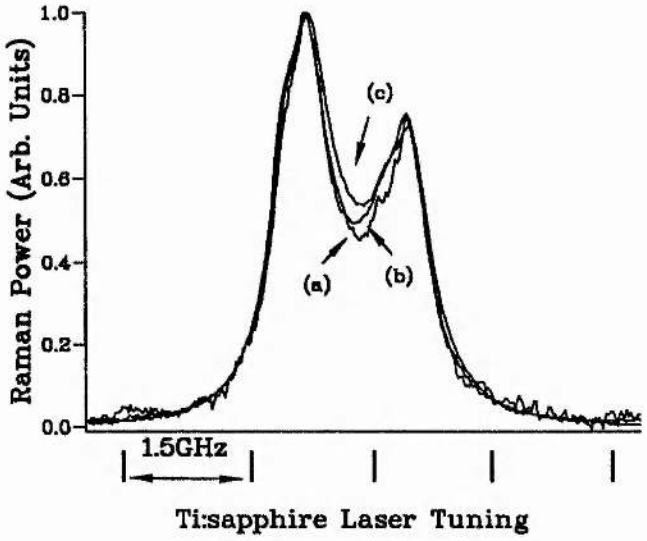

Figure 5.13: Normalised Raman signal lineshapes for dye laser powers of (a) 1.9mW, (b) 7.5mW and (c) 29.5mW with a Ti:sapphire laser power of 190mW.

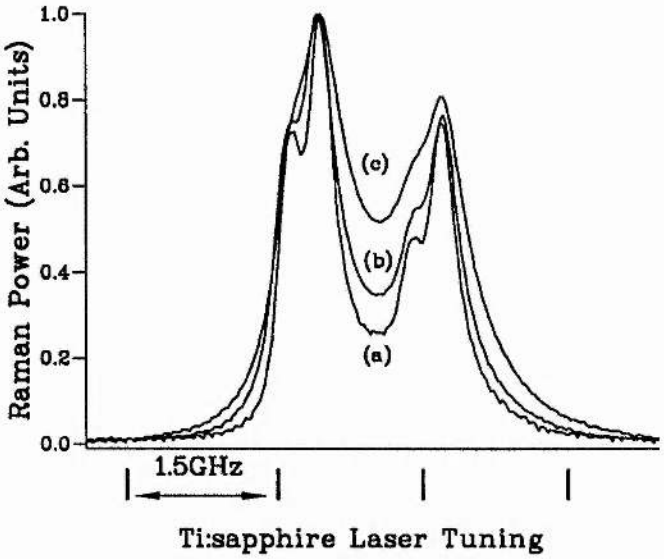

Figure 5.14: Normalised Raman signal lineshapes for a dye laser power of 29mW and Ti:sapphire laser powers of (a) 12.5mW, (b) 50mW and (c) 200mW.

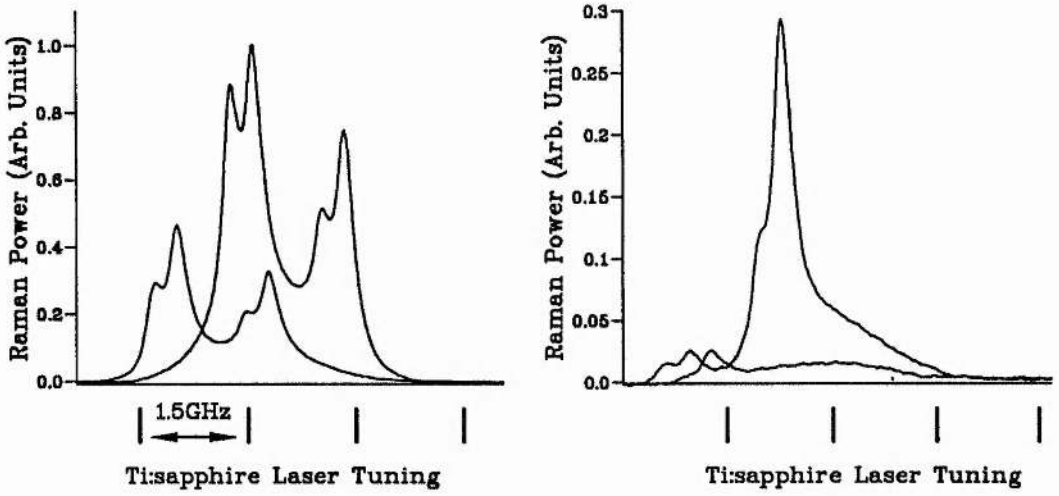

Figure 5.15: Four Raman signal lineshapes as the dye laser is detuned by successive 1.5GHz intervals, starting with the larger trace in the left set of axes and ending with the smaller trace in the right set.

While the use of this Raman signal is useful in this work, it is also quite novel. This is believed to be the first continuous-wave and high-resolution observation of a quadrupole enhanced Raman process in vapours.

5.5. Experimental Resonant SFM

The SFM output was separated from the Raman output by the application of a transverse magnetic field. If the lasers were tuned about 8GHz to one side of the intermediate resonance and the temperature raised clear phase matching oscillations were seen (where none are seen without the field) proving the output to be mainly sum frequency in origin. The $3P_{1/2}$ level was used as the resonant intermediate state throughout the SFM work as the Raman signal was stronger with the larger amount of possible routes and smaller hyperfine spacings encountered if the $3P_{3/2}$ state was involved. The oven temperature was raised to approximately 230^0C (from about 180^0C used to observe the Raman route) which also strengthened the second order process.

The velocity-selected lineshapes expected for the SFM output should be similar to those observed for the fluorescence or Raman signal. However, the magnetic field applied, 0.013–0.018 Tesla typically, will split the levels to some extent. This field should still leave two clusters of routes split by about 1.3GHz due to the ground state hyperfine splitting which is not yet significantly altered. By empirically tuning the dye laser around resonance it is easily possible to get one cluster to dominate in the output, leaving somewhat clearer experimental traces. This was used for several of the traces below to aid clarity (but figures 5.19 and 5.21 show all the routes roughly equal in magnitude). The mechanism for this selection of one cluster is a combination of differing resonant enhancements and optical pumping of the population within the ground state manifold.

A possible parasitic modulation on the lineshapes could occur due to phase matching. All scans are presented for the tuning of the Ti:sapphire laser which should change the phase matching conditions least. Results presented in Chapter 2 show that an upper laser scan does perturb the refractive index on both input waves to some extend, but to a far lesser extent than for a lower laser scan. (Lower laser scans were taken and show no clear lineshape features at all.) Phase matching features are not obvious on the lineshapes presented. The lasers were unfocused thus clear oscillations would be expected rather than blurred modulations. However, in order to minimise wrongful conclusions the results are presented for several upper laser powers. The refractive index should not be altered as this is changed (as the power levels are too low for strong field effects such as Autler-Townes splitting to manifest) and they help show evolution of the relative route strengths aiding interpretation.

5.5.1. Observation of Changing Route Strengths

Whereas, on, or near, resonance for the fluorescence or Raman signals purely velocity-selected lines were observed, the SFM output had an obvious Doppler broadened

component at higher Ti:sapphire laser powers. This is as predicted in the theory earlier for the TP route becoming stronger as Ω_{23} is increased.

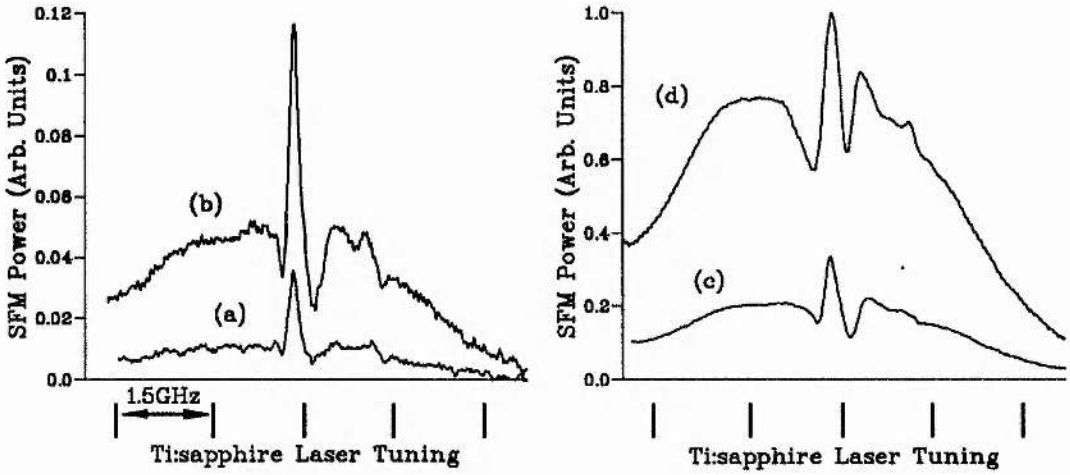

Figure 5.16: Experimental SFM output observed against a Ti:sapphire scan at 8mW dye laser power and (a) 3mW, (b) 12.5mW, (c) 50mW and (d) 200mW Ti:sapphire laser power. Vapour temperature $\approx 230^0$C, magnetic field of 0.013T. (A 1.5GHz confocal marker is shown below this, and all following experimental figures.)

Figure 5.16 shows the growth of the TP route as predicted. In (a), at the lowest Ti:sapphire laser power, a single, narrow, resonance is visible (with the much smaller second route cluster about 1.3GHz to the right). As the Ti:sapphire power is progressively quadrupled (implying a doubling of the Rabi frequency) the wings grow due to the Dopper broadened TP route. At the same time the sides of the velocity-selected feature show sharp dips as predicted by the theory for the SFM phasor swapping from one dominant route to the other. This figure indeed, shows both the main results of this chapter: that the two routes, TS and TP, for excitation of the SFM coherence can change in relative strength by alteration of the input laser powers; and that they have different phases, as shown by the dips flanking the TS feature.

The same sort of progression can be seen with the dye laser tuned slightly out

to one side in figure 5.17. Here the dye laser power is double that of the previous figure and the TS route remains a stronger feature. Comparing these results with those presented earlier for the effect of stronger upper laser powers on the Raman route, the difference in route dependencies are obvious. Before, the lines merely power broadened with no wings coming through — in strong contrast to these traces which clearly show the two routes changing in relative strength.

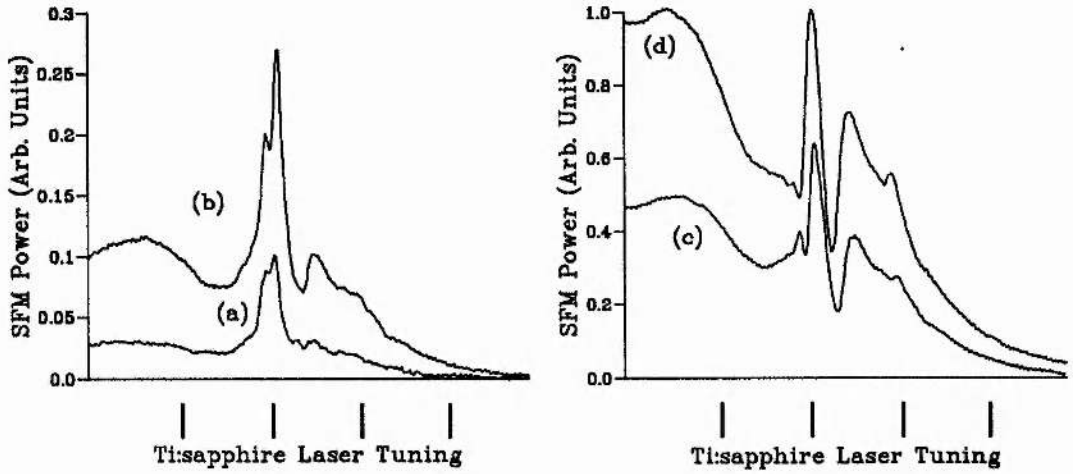

Figure 5.17: Experimental SFM output observed against a Ti:sapphire scan at 16mW dye power and (a) 3.2mW, (b) 12.5mW, (c) 50mW and (d) 100mW Ti:sapphire power. Other parameters as in the preceding figure except the dye laser tuning which has been moved by less than 1GHz. The horizontal axis markers are separated by a Ti:sapphire laser tuning of 1.5GHz.

5.5.2. Interference Between the Two Routes

Strong cancellation was observed between the routes under tight empirically defined conditions. Due to the level structures and available powers the best cancellations observed were for part of a Zeeman cluster to one side of a strong velocity-selected route. If the dye laser power was lessened to try to bring the main route into

cancellation the signal strength was lowered such that detection was compromised and there was not sufficient Ti:sapphire laser power to compensate.

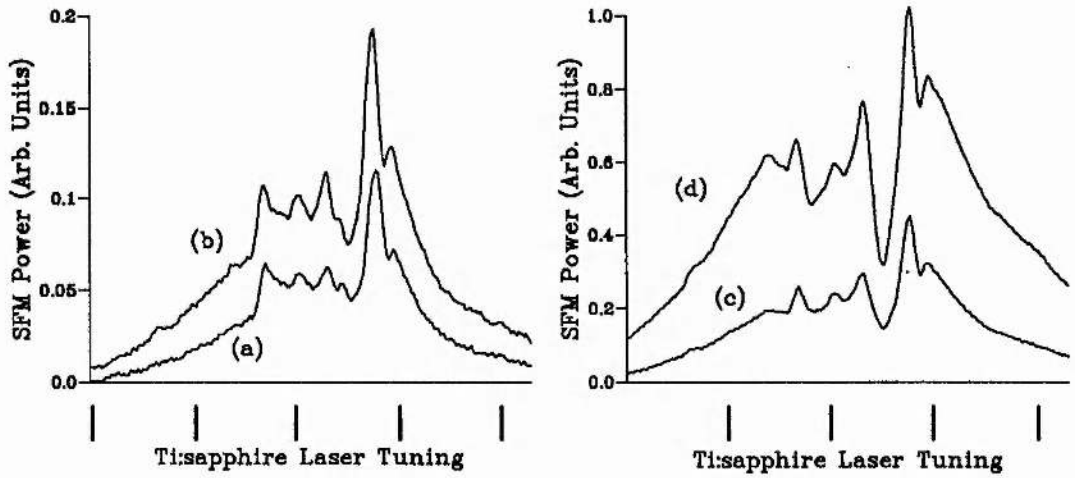

Figure 5.18: Experimental SFM output with resonant dye laser tuning and laser powers of 20mW (dye) and (a) 20mW, (b) 40mW, (c) 80mW and (d) 160mW (Ti:sapphire). Vapour temperature as before, magnetic field 0.018 Tesla.

With the dye laser tuned such that all the routes are similarly visible, strong interference is seen in figure 5.18. At the highest Ti:sapphire power (trace (d)) a clear interference dip is seen to the left of the strongest velocity-selected resonance. This is shown to be due to a TS pathway as the laser power is dropped. In trace (b) and (a) a small peak can be seen emerging where the cancellation was before as the TS route strengthens compared to the TP route at lower upper laser powers. Therefore, at low Ω_{23}, with the TS route in dominance, this peak outweights the TP route at its maximum but as the TP route rises in relative strength, through traces (c) and (d), the two reach a balance of near equal strengths leading to the minima seen.

A clearer cancellation is found with the dye laser tuned to select one ground state cluster as before. In figure 5.19, trace (a), a very strong cancellation is seen to the right of the left-hand route cluster. As the Ti:sapphire power is lowered through

traces (b) and (c) this dip is seen first to flatten out at the base as the TS route just over-balances the TP route and then a clear small TS resonance is seen in the base as it gains further relative strength. As the Ti:sapphire laser was further reduced in power this peak rose to become a clear TS resonance.

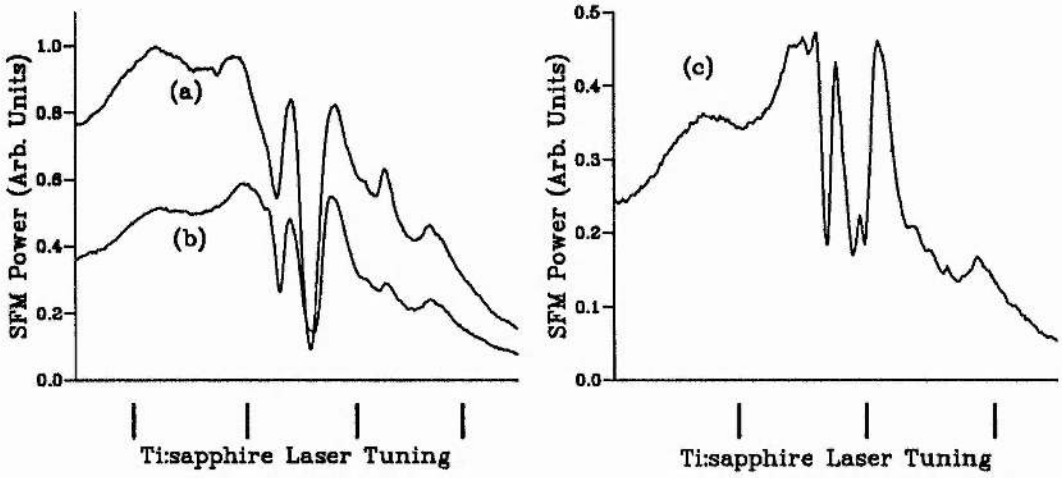

Figure 5.19: Experimental SFM output showing a strong cancellation for a dye laser power of 80mW and Ti:sapphire powers of (a) 160mW, (b) 80mW and (c) 40mW. Vapour temperature as before, magnetic field 0.013 Tesla.

The maximum cancellation seen in the above trace corresponds to a ratio of the signal at the dip to the maximum in the trace of 94%. The ideal of total cancellation is not reached due to several possible reasons. Probably most significant is the changing value of Ω_{12} in the oven due to linear absorption of the dye laser. Thus the output is from a set of different conditions experienced at different points in the oven and total cancellation at one position along the beam is sabotaged by incomplete cancellation at another due to a reduced Ω_{12}. Also the Raman signal provides a low background to the SFM traces as it is dominated rather than removed. As it is at the same frequency, separation is not possible here. Lastly it is possible that the optimum laser power for cancellation was not found, or was out of the possible range. Notwithstanding, figure 5.19 shows a very striking reduction in SFM power

due to the opposing route phases.

5.5.3. The Effects of Detuning

As noted above, during the theoretical section, detuning leads to complex changes in the output lineshape. In the vapour cell the effects are even more complicated due to optical pumping, linear absorption and phase matching. All of these will change the relative magnitude of the lineshapes taken at different dye laser tunings and optical pumping will cause changes in the relative magnitude of features within the trace. Two experimental sets are presented here. The first, figure 5.20, shows the variation with 750MHz steps of the dye laser under similar vapour conditions to figures 5.16, 5.17 and 5.19; while the second, figure 5.21, is for 375MHz detunings from the situation of figure 5.18.

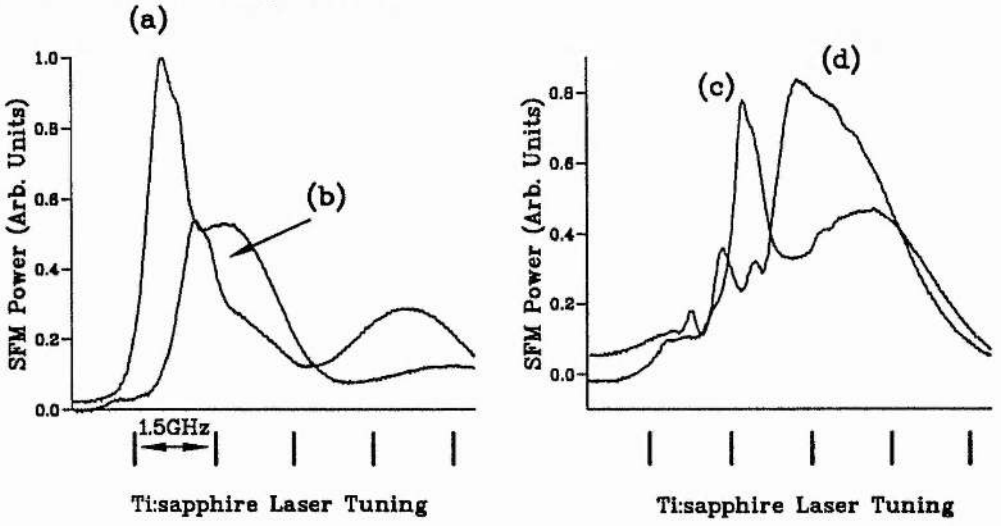

Figure 5.20: Experimental SFM output profiles for successive moves of 750MHz towards resonance of the dye laser. (Dye laser power 8mW, Ti:sapphire laser power 50mW, magnetic field 0.013T)

Both of the figures clearly show the separation of the two routes at larger detunings. They also show their opposite movements with the intermediate detuning whereby they come together from opposite directions to meet on resonance. For

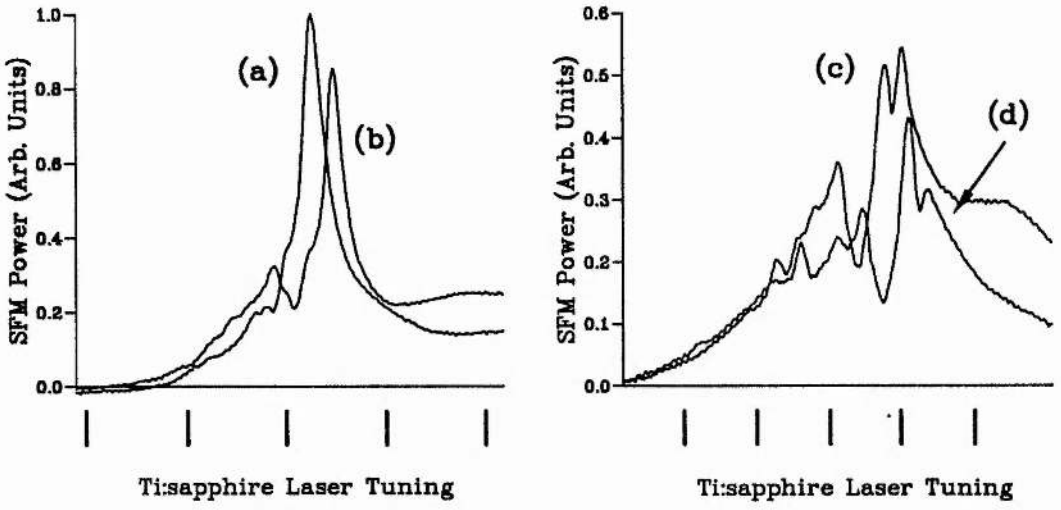

Figure 5.21: Experimental SFM output profiles for successive moves of 375MHz towards resonance. (Dye laser power 20mW, Ti:sapphire laser power 80mW, magnetic field 0.018T)

detunings of around 1.5GHz and more from resonance no interference features are observed and the routes are essentially separate. At large detunings both routes can be observed independently. As the detuning is reduced below 1GHz strong interference features can be seen with the characteristic dips surrounding the TS features becoming clear. Small changes in the detuning around the resonant point change the relative route strengths by the number of atoms available to be velocity selected and this leads to quite major changes in the observed spectra. Due to the combination of several effects contributing to the changes near resonance and the number of levels involved no quantitative analysis was undertaken of these lineshapes.

5.6. Discussion

While the above experimental results serve to give a good demonstration of how the TP and TS routes combine in a resonant SFM process, the large numbers of levels involved with fine, hyperfine and Zeeman splittings complicate the experimental

results. It would be desirable to conduct further work in a "cleaner" three-level atom which would allow a better fit between theory and experiment. Such a system could be found in an atom with no nuclear spin, or where the level structure is of such size that the levels are spaced by more than the Doppler width. An approach from the other direction would be to include the level structure into the numerical model and add the effects of propagation (absorption and phase matching). However this would lead to a horrific numerical problem which, even on the computers at present, would be unwieldy and take an inordinate amount of time to compute.

This interference in excitation pathways should be fundamental to *resonant* SFM. The theory could be generalised to include the solid and liquid phases of matter and similar results are expected. For instance, in a crystalline solid the TS route will become site-selective within the inhomogeneous lattice broadening. Very strong absorption will require the use of lightly doped or thin samples for experimental tests but it is anticipated that the general features would prevail.

As mentioned before, this phenomena has some parallels with other quantum interference effects, such as electromagnetically-induced transparency (EIT) or Fano interference as they all rely on two routes to the end state interfering. However, this interference does not require an initial threshold input value to be reached for its observation. EIT requires that the inhomogeneous broadening be overcome before its benefits are apparent, which in a solid is likely to imply damaging light intensities. Route interference in SFM could be demonstrated without high intensities as it is the balance of light powers that is important and the corresponding balance in route strengths. Therefore it could provide a platform for the observation of atomic coherence effects in a solid medium.

The point of cancellation between the two routes is not confined to low field strengths although the above analytical theory assumed it. By solving the exact numerical system over a range of field strengths the cancellation point was seen to persist as high as the fields were taken, which was above the point of Autler-Townes splitting becoming greater than the Doppler width. Figure 5.22 shows the

calculated value of $|\tilde{\rho}_{13}|$ for both fields resonant over a matrix of field strengths. The cancellation point is seen as a valley in the produced surface and extends over the whole range of the figure. Therefore, the cancellation will have to be considered in any resonant SFM process — using pulsed or cw lasers — as the conversion efficiency will be lessened if the routes balance in anti-phase.

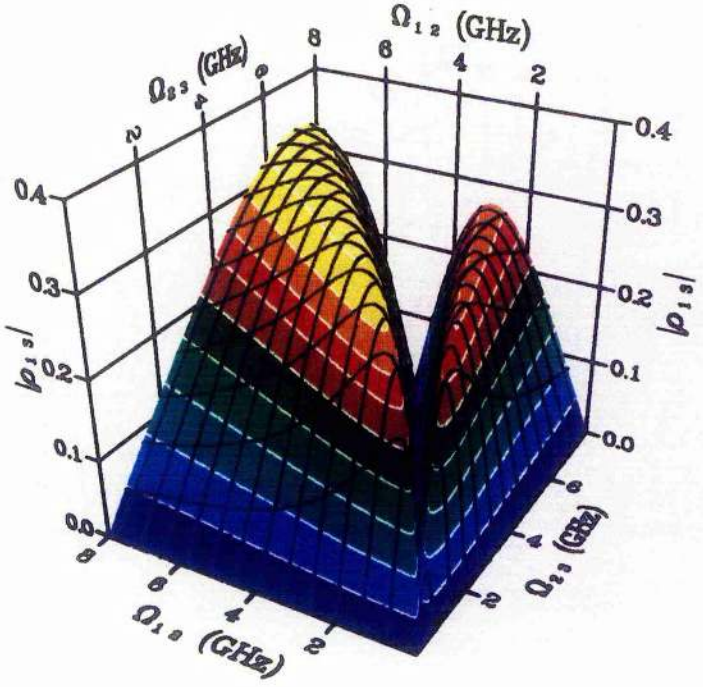

Figure 5.22: Calculated value of $|\tilde{\rho}_{13}|$ for $\Delta_1 = \Delta_2 = 0$ over the range of Rabi frequencies as shown. Doppler integration included.

This SFM "death valley" serves as a useful delineation of two regimes of SFM operation. The high Ω_{12} side is where the TS route dominates, with velocity-selected lineshapes, as described by Poustie [1]. The high Ω_{23} side, however, is where EIT can greatly increase the efficiency of the SFM process by reducing the parasitic absorption on the wave at ω_1 if Ω_{23} is above a certain threshold. Theory and predictions for this effect and its implications are presented in the next chapter.

REFERENCES

[1] Alistair J. Poustie, *Magnetic Field Induced Sum Frequency Mixing in Sodium Vapour*, PhD thesis, University of St. Andrews, 1990.

[2] A. J. Poustie and M. H. Dunn, Magnetic field induced sum frequency mixing in sodium vapour *Phys Rev A* **47**, 1365 (1993).

[3] Marc D. Levenson, *Introduction to Nonlinear Laser Spectoscopy* (Academic Press, London, 1982).

[4] J. E. Bjorkholm and P. F. Liao, Resonant enhancement of two-photon absorption in sodium vapour *Phys Rev Lett* **33**, 128 (1974).

[5] R. Salomaa and S. Stenholm, Two-photon spectroscopy II. Effects of residual Doppler broadening. *J Phys B* **9**, 1221 (1976).

[6] J. E. Bjorkholm and P. F. Liao, Line shape and strength of two-photon absorption in an atomic vapour with a resonant or nearly resonant intermediate state *Phys Rev A* **14**, 751 (1976).

[7] P. R. Berman, Effects of collisions on linear and non-linear spectroscopic line shapes *Phys Rep* **43**, 101 (1978).

[8] Paul R. Berman, Theory of collisional effects in Doppler-free spectroscopy *Phys Rev A* **13**, 2191 (1976).

[9] Y. R. Shen, Distinction between resonance Raman scattering and hot luminescence *Phys Rev B* **9**, 622 (1974).

[10] T. Mossberg, A. Flusberg, and S. R. Hartmann, Optical second-harmonic generation in atomic thallium vapour *Opt Commun* **25**, 121 (1978).

[11] D. S. Bethune, Optical second harmonic generation in atomic vapours with focused beams *Phys Rev A* **23**, 3139 (1981).

[12] D. S. Bethune, Erratum: Optical second-harmonic generation in atomic vapours with focused beams *Phys Rev A* **25**, 2845(E) (1982).

[13] V. Mizrahi and D. P. Shelton, Observations of second-harmonic generation in isotropic vapours tested at low power *Phys Rev A* **33**, 1396 (1986).

[14] D. S. Bethune, Quadrupole second-harmonic generation for a focused beam of arbitrary transverse structure and polarization *Opt Lett* **6**, 287 (1981).

[15] B. D. Sinclair and M. H. Dunn, Continuous-wave second-harmonic generation in sodium vapour *Phys Rev A* **34**, 3989 (1986).

[16] M. Matsuoka, H. Nakatsuka, H. Uchiki, and M. Mitsunaga, Optical second-harmonic generation in gases : "Rotation" of quadrupole moment in magnetic field *Phys Rev Lett* **38**, 894 (1977).

[17] David Cotter and Michael A. Yuratich, Stimulated multipole Raman scattering between opposite-parity states of atomic potassium *Opt Commun* **29**, 307 (1979).

[18] S. G. Dinev, G. B. Hadjichristov, and I. L. Stefanov, Efficient red stimulated emission enhanced by quadrupole Raman scattering *Opt Commun* **74**, 176 (1989).

Chapter 6

Enhanced Conversion Efficiency by Electromagnetically-Induced Transparency

6. Enhanced Conversion Efficiency by Electromagnetically-Induced Transparency

In this chapter I present the theoretical basis for the enhancement of a second-order sum frequency mixing process by using electromagnetically-induced transparency to reduce a parasitic fundamental wave absorption. Simplified dressed susceptibilities are derived and evaluated and the enhancement realisable discerned by consideration of Maxwell's equations. Exact solutions of the three-level cascade atom by a numerical model confirm the conclusions of the simplified analysis. Possibilities for experimental realisation are discussed and potential problems highlighted.

6.1. Introduction

With both input waves resonant with allowed transitions the sum frequency mixing process is expected to be at its highest efficiency, if the interference effects detailed in the previous chapter are avoided. Indeed in the experimental study in chapter 4 this was the case and efficiencies rivaling those of a conventional nonlinear crystalline solid were observed. However, the conversion under those conditions was affected by two factors: linear absorption and phase mismatching. Of these, the most problematic is the parasitic linear absorption of the first input wave, as careful tuning should be able to eliminate any phase mismatch. This wave is resonant with

a dipole-allowed transition from the ground state, and as such, suffers considerable attenuation. In the sodium oven temperatures of around 230°C were sufficient to totally absorb the 589 nm input wave in a fraction of the 10cm oven length. This limited the interaction length for the nonlinear process and capped the output. (See also Poustie, reference [1], for a similar verdict.)

The use of electromagnetically-induced transparency (EIT) [2, 3] to reduce parasitic absorption in a wave mixing process was proposed by Harris et al. [4]. The authors considered a four-wave sum frequency process and the relevant parasitic absorption was the re-absorption of the generated output wave. This was reduced by use of a strong coupling laser on the final upward transition as shown in figure 6.1. Demonstration of the concept followed from researchers in Toronto [5, 6, 7] using atomic hydrogen and a dc electric field to create the transparency. Recently, the predicted phase matching properties inherent in the process have also been observed [8].

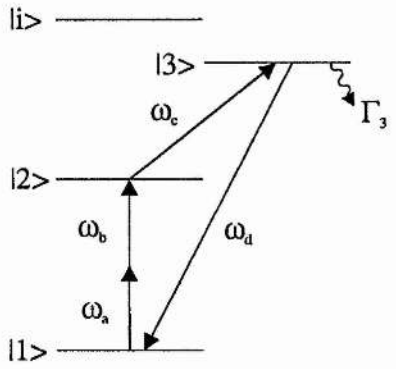

Figure 6.1: The use of EIT four-wave mixing proposed at Stanford utilises ω_c to create transparency on the output wave, ω_d.

All of these works used EIT to reduce absorption on an *output* wave. Can the process be extended to reduce absorption on *input* waves with similar results? What of energy conservation in the nonlinear process — the input waves must be

attenuated in production of the output. Also, can EIT work advantageously using one of the two input waves in the $\chi^{(2)}$ process as the coupling laser? The hydrogen work [5, 6] used theory couched in $\chi^{(2)}$ formalism, but it is an external dc field that produced the necessary dressing of the atom.

6.2. Density Matrix Theory

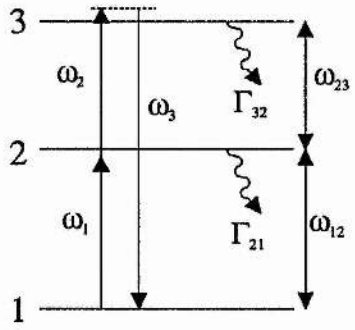

Figure 6.2: The cascade three-level atom for second-order resonant sum frequency mixing

The system considered in this chapter is, once again, the cascade three level atom, as shown in figure 6.2. The strong absorption that limits the process acts on the field at ω_1, which is resonant with the 1–2 transition. The field at ω_2 is taken to be the coupling field to induce transparency on the former wave, while still retaining its role as the second wave in the three-wave mixing process. It is necessary to calculate how the linear susceptibility on ω_1 varies with Ω_{23} and to find out how the second-order susceptibility is correspondingly affected. To do this a density matrix analysis is followed.

6.2.1. Inclusion of the Sum Frequency Wave

The generation and feedback of the sum frequency wave, ω_3, must now be incorporated explicitly into the density matrix system. This is necessary for derivation of

the susceptibilities relating to it and allows for the full numerical system later on to include any feedback that the build up of this field may have on the atom. The transition 1–3 is still dipole-forbidden and so the transition matrix element μ_{13}, and the corresponding Rabi frequency Ω_{13}, are much smaller than those for the other transitions.

Unfortunately, adding the third wave to the system introduces some complications which must be considered. Earlier I assumed that the Rabi frequencies, Ω_{12} and Ω_{23} were real. This leads to no loss of generality as any phase factor between them could be easily included in the definitions of the slowly-varying coherences (equations 2.22). However, the Rabi frequency relating to the sum frequency wave, Ω_{13} must be retained as complex. This allows generation at the correct phase and is necessary for self-consistency. (The complex conjugate, where it appears in the equations will be denoted as Ω_{31}.) Since the wave is generated by the wave-mixing process, as opposed to being an externally sourced probe field, we may say, by definition, that $\omega_3 = \omega_1 + \omega_2$. Furthermore, in this analysis I shall assume near phase matching by the criterion:

$$\Delta k = k_3 - k_1 - k_2 \ll \frac{1}{z} \tag{6.1}$$

This is justified as the enhancement process guarantees phase matching on resonance, as shall be shown later. If the assumption is not made then the terms involving Ω_{13}, or its complex conjugate, incorporate a factor of the from $e^{\pm i\Delta kz}$. This allows for conversion and back-conversion depending on the phase mismatch and should be included for the general case of non-resonant fields but leads to unnecessary complications here.

With the above assumptions taken into consideration the equations for the off-diagonal coherence elements of the density matrix (equations 2.23d-f) may be extended to:

$$\dot{\tilde{\rho}}_{12} = -i\tilde{\Delta}_{12}\tilde{\rho}_{12} + i\Omega_{12}(\rho_{22} - \rho_{11}) + i\Omega_{13}\tilde{\rho}_{32} - i\Omega_{32}\tilde{\rho}_{13} \tag{6.2a}$$

$$\dot{\tilde{\rho}}_{23} = -i\tilde{\Delta}_{23}\tilde{\rho}_{23} + i\Omega_{23}(\rho_{33} - \rho_{22}) + i\Omega_{21}\tilde{\rho}_{13} - i\Omega_{13}\tilde{\rho}_{21} \quad (6.2b)$$

$$\dot{\tilde{\rho}}_{13} = -i\tilde{\Delta}_{13}\tilde{\rho}_{13} + i\Omega_{13}(\rho_{33} - \rho_{11}) + i\Omega_{12}\tilde{\rho}_{23} - i\Omega_{23}\tilde{\rho}_{12} \quad (6.2c)$$

The complex detunings, $\tilde{\Delta}_{ij}$, included in these for brevity have been defined as:

$$\tilde{\Delta}_{12} = \Delta_1 - i\gamma_{12} \quad (6.3a)$$

$$\tilde{\Delta}_{23} = \Delta_2 - i\gamma_{23} \quad (6.3b)$$

$$\tilde{\Delta}_{13} = \Delta_1 + \Delta_2 - i\gamma_{13} \quad (6.3c)$$

6.2.2. Derivation of the Susceptibilities

The linear and nonlinear susceptibilities produced in the atom are derived by comparing the macroscopic and microscopic expressions for the polarisation induced in the atom. In macroscopic terms the volume polarisation produced is [6]:

$$P(\omega_i) = \epsilon_0\chi^{(1)}(\omega_i)E_i + \frac{1}{2}\epsilon_0\chi^{(2)}(\omega_i)E_jE_k \quad (6.4)$$

where E_i is the field of interest and E_j and E_k are the other two fields. The single atom polarisation, the microscopic view, is defined as:

$$\begin{aligned} <\mu> &= \mathrm{Tr}[\rho\mu] \\ &= \mu_{21}\tilde{\rho}_{12}\exp[i(\omega_1 t - k_1 z)] + \mu_{32}\tilde{\rho}_{23}\exp[i(\omega_2 t - k_2 z)] \\ &\quad \mu_{31}\tilde{\rho}_{13}\exp\{i[(\omega_1+\omega_2)t - (k_1+k_2)z]\} + \text{c.c.} \end{aligned} \quad (6.5)$$

and the volume polarisation at frequency ω_i may be then expressed in terms of this and the particle number density, $\mathcal{N}$, as:

$$P(\omega_i) = \mathcal{N} <\mu(\omega_i)> \quad (6.6)$$

where $<\mu(\omega_i)>$ consists of the terms of $<\mu>$ oscillating at frequency ω_i.

Several assumptions must be made to gain physically reasonable, but usefully simple, solutions. Firstly, steady-state conditions are assumed and the time derivatives set to zero in the coherence equations. Next, as the field at ω_2 is the strong field

that dresses the atom to be transparent at ω_1, it is assumed that $\Omega_{23} \gg \Omega_{12}, \Omega_{13}$. Also, since $\mu_{13} \ll \mu_{12}$ as 1–3 is not a dipole-allowed transition and the generation of ω_3 is being considered, the further relation of $\Omega_{12} \gg \Omega_{13}$ holds. These restrictions allow the relevant coherences to be expressed as:

$$\tilde{\rho}_{12} \approx \frac{\tilde{\Delta}_{13}\Omega_{12}(\rho_{22}-\rho_{11}) - \Omega_{32}\Omega_{13}(\rho_{33}-\rho_{11}) + \xi_2\Omega_{32}(\rho_{33}-\rho_{22})}{\tilde{\Delta}_{12}\tilde{\Delta}_{13} - |\Omega_{23}|^2} \tag{6.7a}$$

$$\tilde{\rho}_{13} \approx \frac{\tilde{\Delta}_{12}\Omega_{13}(\rho_{33}-\rho_{11}) - \Omega_{12}\Omega_{23}(\rho_{33}-\rho_{11}) + \xi_3\Omega_{23}(\rho_{33}-\rho_{22})}{\tilde{\Delta}_{12}\tilde{\Delta}_{13} - |\Omega_{23}|^2} \tag{6.7b}$$

using the definitions:

$$\xi_2 = \Omega_{13}\frac{\tilde{\Delta}_{13}}{\tilde{\Delta}_{23}^*} - \frac{\Omega_{12}\Omega_{23}}{\tilde{\Delta}_{23}}$$

$$\xi_3 = \Omega_{12}\frac{\tilde{\Delta}_{12}}{\tilde{\Delta}_{23}} - \frac{\Omega_{13}\Omega_{32}}{\tilde{\Delta}_{23}^*}$$

A further assumption of low population transfer is made, reasonable as Ω_{12} is assumed weak in comparison to Ω_{23}. This is tested later in the numerical work, but previous analysis that does not assume a small probe frequency for EIT [9] shows that the main features survive when Ω_{12} is non-vanishing. In doing this we say that $\rho_{11} \approx 1$ and $\rho_{22} \approx \rho_{33} \approx 0$. Substituting this into equations 6.7 and then comparing the resulting microscopic and macroscopic polarisations leads to the following dressed susceptibilities:

$$\chi^{(2)}(\omega_3) = \frac{2\mathcal{N}\mu_{31}\mu_{12}\mu_{23}}{\epsilon_0\hbar^2}\frac{1}{\tilde{\Delta}_{12}\tilde{\Delta}_{13} - |\Omega_{23}|^2} \tag{6.8a}$$

$$\chi^{(1)}(\omega_3) = -\frac{\mathcal{N}\mu_{31}\mu_{13}}{\epsilon_0\hbar}\frac{\tilde{\Delta}_{12}}{\tilde{\Delta}_{12}\tilde{\Delta}_{13} - |\Omega_{23}|^2} \tag{6.8b}$$

$$\chi^{(1)}(\omega_1) = -\frac{\mathcal{N}\mu_{21}\mu_{12}}{\epsilon_0\hbar}\frac{\tilde{\Delta}_{13}}{\tilde{\Delta}_{12}\tilde{\Delta}_{13} - |\Omega_{23}|^2} \tag{6.8c}$$

These susceptibilities show the effects of EIT and Autler-Townes splitting. The $|\Omega_{23}|^2$ term in the denominator leads to two resonances split by $2\Omega_{23}$ which are the two Autler-Townes, or ac Stark, components. However, the numerator in both the linear susceptibilities describes the effects of EIT that manifest between these components. For resonant fields the linear absorption on ω_1 is proportional to $\gamma_{13}/|\Omega_{23}|^2$.

Therefore, if γ_{13} is low then a high transparency is seen. In contrast the second-order susceptibility has no such numerator term and the effect of Autler-Townes spitting is observed unaffected by EIT. Figure 6.3 shows the susceptibilities at several values of the upper field strength for a scan of the lower, probe, laser frequency. The sharp transparency between the dressed components in the linear absorption case is clear, while the second-order susceptibility retains a significant fraction of its doubly resonantly enhanced value.

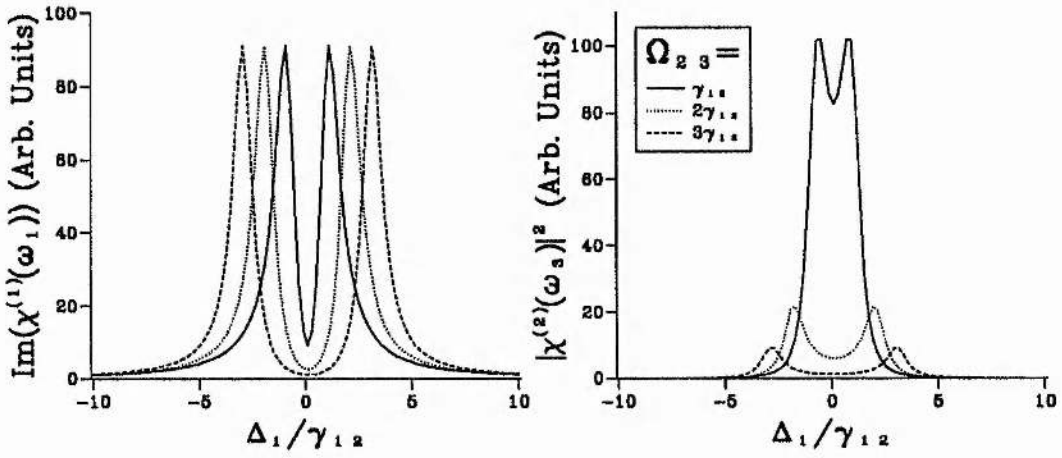

Figure 6.3: Left, $\Im[\chi^{(1)}(\omega_1)]$ and right, $|\chi^{(2)}(\Omega_3)|^2$ calculated from the simplified susceptibility expressions under homogeneously broadened conditions. Ω_{23} and Δ_1 are scaled against the 1–2 dephasing rate, γ_{12} and $\gamma_{13} = \gamma_{12}/10$.

This marked difference between absorption and emission is the basis on which EIT is able to enhance nonlinear processes [4]. It arises due to the difference in paths for the two processes. The absorption process has two main paths. Firstly, direct absorption on the transition 1–2 and, secondly, two-photon absorption to 3 and then back to 2 via stimulated emission. These two paths interfere, creating the transparency [10]. (An alternative but equivalent, view is that of coherent population trapping [2, 11, 12].) However, the emission is unburdened with alternative paths and therefore sees no interference between the dressed components. It is important

to note that the efficacy of the transparency mechanism on the 1–2 transition is controlled by the dephasing rate γ_{13} — ie. the coherence decay on the return, 1–3, transition and not the dephasing rate of either input transition. This is due to the feedback of the $\tilde{\rho}_{13}$ coherence which is vital for the EIT process.

6.2.3. Energy Conservation

It may seem at first that if the linear absorption of ω_1 drops to zero then there is no removal of energy from this wave for the nonlinear process. This is not so as there is a nonlinear absorption term in the $\tilde{\rho}_{12}$ coherence that ensures input wave depletion and it is unaffected by EIT. To illustrate this, the expression for $\tilde{\rho}_{12}$ can be simplified by the removal of higher order terms to:

$$\tilde{\rho}_{12} \approx \frac{\tilde{\Delta}_{13}\Omega_{12}(\rho_{22}-\rho_{11}) - \Omega_{32}\Omega_{13}(\rho_{33}-\rho_{11})}{\tilde{\Delta}_{12}\tilde{\Delta}_{13} - |\Omega_{23}|^2} \tag{6.9}$$

The two terms in the numerator are, respectively, the linear absorption and the depletion of the input wave for the nonlinear process. The former is affected by EIT but the latter splits by the ac Stark effect in the same way the nonlinear susceptibility does and has no interference between the components. Due to the low value of Ω_{13} this term is usually dominated by the linear absorption term which the EIT combats.

Having made this distinction between the parasitic linear and energy conserving nonlinear absorption it should be noted that in reality reduction of the linear absorption will not be absolute. Some linear absorption will remain as $\gamma_{13} \neq 0$ in any laboratory system. However, as this term is the dephasing rate on a quadrupole-allowed transition it should be fairly low in reality, and lead to good transparency.

6.2.4. Inhomogeneous Broadening

To predict the conditions in the vapour cell Doppler broadening must be taken into account. The susceptibility expressions, equations 6.8, were integrated over the Maxwellian velocity distribution numerically and the results are shown in figure 6.4.

The inhomogeneous broadening tends to smear out the response of the atom to the field until Ω_{23} is raised to a level rivalling the Doppler width. At this point very similar phenomena are seen to the homogeneously broadened situation. The linear susceptibility shows transparency between the Autler-Townes components, while the nonlinear susceptibility is additive between them.

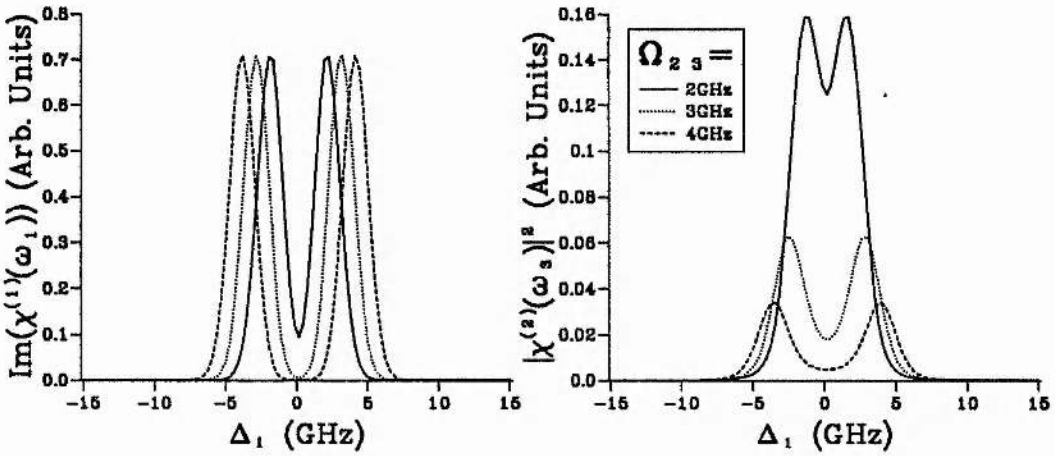

Figure 6.4: Left, $\Im[\chi^{(1)}(\omega_1)]$ and right, $|\chi^{(2)}(\omega_3)|^2$ integrated for Doppler broadening at 400K with $\gamma_{12} = 0.01$GHz and $\gamma_{13} = 0.005$GHz. (The transition wavelengths used were those for the 3S–3P–3D level scheme in sodium vapour with co-propagating lasers.)

Figure 6.5 shows the real part of the linear susceptibility, $\chi^{(1)}(\omega_1)$. This shows that on single and two-photon resonance perfect phase matching will be achieved. (The plot of $\chi^{(1)}(\omega_3)$ is equivalent.) This justifies the assumption made earlier of near phase matching as long as the fields are taken as resonant. This crossing of the atomic dispersion has been used experimentally to phase match a nonlinear process [8] but it should be noted that the steep slope of the refractive index leads to very strong dispersion. This dispersion can mean at high vapour densities the process will phase match only over a very narrow frequency bandwidth. Furthermore, the group velocity of pulses introduced into the medium can be strongly reduced [13].

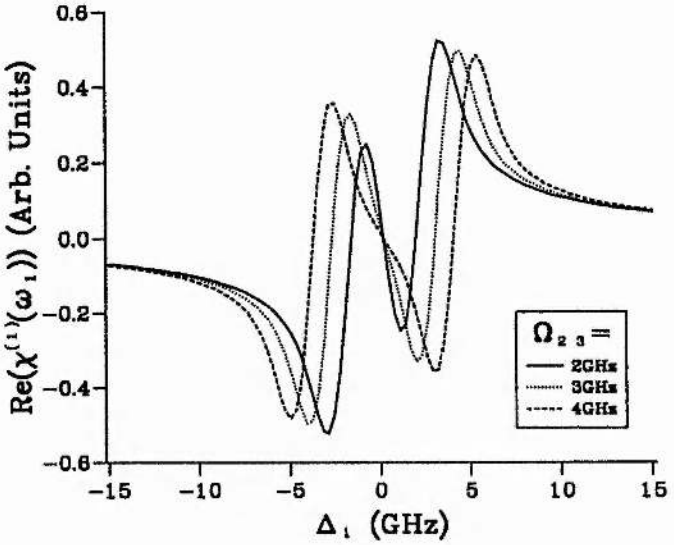

Figure 6.5: The real part of $\chi^{(1)}(\omega_1)$ for the same parameters as the previous figure including Doppler broadening.

In order to show that the effects described above are not a feature of the simplification of the system the lower laser absorption, $\Im[\tilde{\rho}_{12}]$, and the SFM output, $|\tilde{\rho}_{13}|$, were calculated from the full numerical system including Doppler broadening. Their dependence on the upper laser strength, Ω_{23}, is shown in figure 6.6 for resonant fields. At high upper field strengths (greater than about 3GHz) the lower laser absorption has dropped almost to zero, while the SFM output retains a significant proportion of its maximum value. The sharp features seen for $\Omega_{23} < 0.5$GHz are from route interference as discussed in chapter 5.

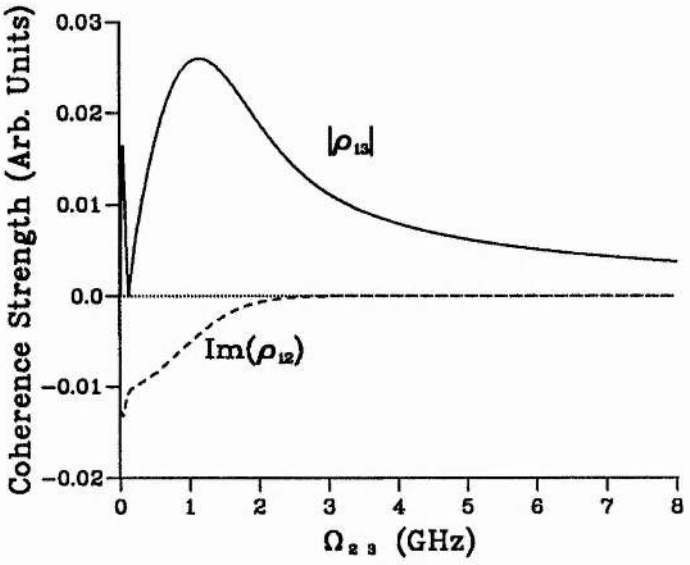

Figure 6.6: The SFM output (from $|\tilde{\rho}_{13}|$ and the lower laser absorption (from $\Im[\tilde{\rho}_{12}]$) for resonant fields against increasing Ω_{23}, the upper laser strength, calculated from the full numerical model.

6.3. Enhancement of the Nonlinear Process

In order to show how these dressed susceptibilities affect the conversion efficiency of the nonlinear process the evolution of the sum frequency field, $E_3(z)$, must be calculated including propagational effects. This is done using Maxwell's equations. The starting point is the generalised wave equation:

$$\nabla \times \nabla \times \mathbf{E} = -\mu_0 \frac{\partial^2 \mathbf{D}}{\partial t^2} \tag{6.10}$$

where

$$\mathbf{D} = \epsilon_0 \mathbf{E} + \mathbf{P} \tag{6.11}$$

Restricting the analysis to one dimension, propagation in the z direction, we can express the sum frequency polarisation as:

$$P_3(z) = \epsilon_0 \chi^{(1)}(\omega_3) E_3(z) + P_{NL} \tag{6.12}$$

with the nonlinear polarisation, P_{NL} defined as before:

$$P_{NL} = \frac{1}{2} \epsilon_0 \chi^{(2)}(\omega_3) E_1(z) E_2(z) \tag{6.13}$$

Therefore, substituting these and keeping in one dimensional space we gain:

$$\frac{\partial^2 E_3(z)}{\partial z^2} - \mu_0\epsilon_0\left[1+\chi^{(1)}(\omega_3)\right]\frac{\partial^2 E_3(z)}{\partial t^2} = \mu_0\frac{\partial^2 P_{NL}}{\partial t^2} \tag{6.14}$$

To solve this a sinusoidal trial solution for $E_3(z,t)$ is used and by invoking the slowly varying amplitude approximation [14] to remove the second-order differential with respect to z this expression may be simplified to:

$$\frac{dE_3(z)}{dz} + \frac{1}{2i}\frac{\omega_3}{c}\chi^{(1)}(\omega_3)E_3(z) = -\frac{1}{8i}\frac{\omega_3}{c}\chi^{(2)}(\omega_3)E_1(z)E_2(z) \tag{6.15}$$

At this point the specific conditions the solution is being sought under have to be considered. Absorption on ω_1 is of importance and so $E_1(z)$ is taken to be of the form:

$$E_1(z) = E_1^0\exp\left\{-\left(\frac{k_1}{2}\right)\Im[\chi^{(1)}(\omega_1)]z\right\} \tag{6.16}$$

while ω_2 is assumed not be be attenuated by a significant amount ($E_2(z) = E_2^0$). Further, due to the nature of the real part of the linear susceptibility for resonant fields phase matching is assumed. Lastly, the sum frequency field will build up from zero so the boundary condition $E_3(z=0) = 0$ is appropriate. Including all this the evolution of the sum frequency field amplitude can solved for, giving:

$$\begin{aligned} E_3(z) &= \frac{i}{4}\frac{\omega_3\chi^{(2)}(\omega_3)E_1^0E_2^0}{\{\omega_3\Im[\chi^{(1)}(\omega_3)] - \omega_1\Im[\chi^{(1)}(\omega_1)]\}} \\ &\quad\times\left\{\exp\left(-\frac{\omega_1}{2c}\Im\left[\chi^{(1)}(\omega_1)\right]z\right) - \exp\left(-\frac{\omega_3}{2c}\Im\left[\chi^{(1)}(\omega_3)\right]z\right)\right\} \end{aligned} \tag{6.17}$$

In the limit of $\Im\left[\chi^{(1)}(\omega_1)\right] \to 0$ this reduces to equation (10) of reference [6] showing the enhancement achievable from reduction of the output wave absorption. However, as $\mu_{13} \ll \mu_{12}$ the absorption of the output wave is unimportant here and the limit, $\Im\left[\chi^{(1)}(\omega_3)\right] \to 0$, is relevant. This gives:

$$E_3(z) = \frac{i}{4}\frac{\omega_3\chi^{(2)}(\omega_3)E_1^0E_2^0}{\omega_1\Im[\chi^{(1)}(\omega_1)]}\left\{1-\exp\left(-\frac{\omega_1}{2c}\Im\left[\chi^{(1)}(\omega_1)\right]z\right)\right\} \tag{6.18}$$

Therefore, as Ω_{23} is increased the generation of E_3 is effected in two ways. Firstly, the efficiency ratio $\chi^{(2)}(\omega_3)/\Im[\chi^{(1)}(\omega_1)]$ increases since the reduction in absorption

is greater than the reduction in the nonlinear susceptibility. Secondly, the useful interaction length increases as the exponential term decreases. The maximum enhancement achievable is found if the vapour length, z, is kept longer than the absorption length of ω_1 under all values of Ω_{23}. If this is the case then:

$$P_3 \propto |E_3(z \to \infty)|^2 \propto \left| \frac{\chi^{(2)}(\omega_3)}{\Im\left[\chi^{(1)}(\omega_1)\right]} E_1^0 E_2^0 \right|^2 \tag{6.19}$$

Thus the ratio $\chi^{(2)}(\omega_3)/\Im\left[\chi^{(1)}(\omega_1)\right]$ gives the enhancement in the nonlinear process and is displayed in figure 6.7.

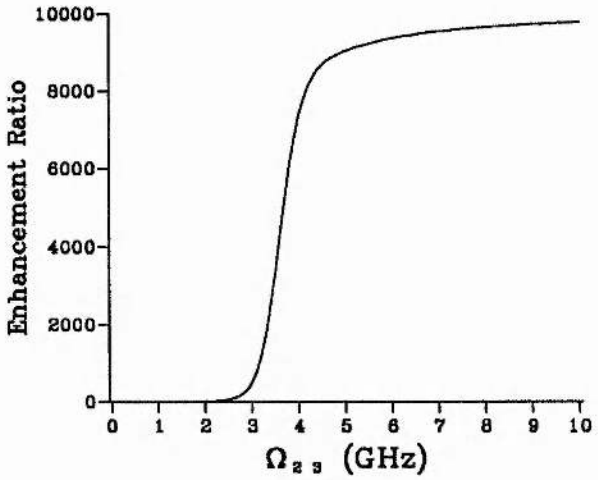

Figure 6.7: The enhancement ratio, $\left|\chi^{(2)}(\omega_3)/\Im\left[\chi^{(1)}(\omega_1)\right]\right|^2$, calculated for resonant fields with Doppler broadening at 400K and $\gamma_{12} = 0.01$GHz and $\gamma_{13} = 0.005$GHz.

This graph shows a clear step occurring when the upper laser Rabi strength becomes greater than the Doppler width (about 2GHz here) and saturating at about three times the Doppler width. Therefore, the enhancement of the nonlinear process does not occur until the inhomogeneous broadening is overcome by the upper, coupling laser. This step is not mirrored for the homogeneous case as the EIT process has no threshold for a purely homogeneously broadened system. The shape of the step is the same as that for enhancement of the nonlinear process through reduction of the output laser absorption [4, 6, 8] — which is unsurprising as so much of the mathematics and physics is unchanged. Experimentally the realisation of the en-

hancement of the conversion efficiency is produced by applying the relevant power to the upper transition and then increasing the $\mathcal{N}z$ product of the vapour. This latter adjustment stems from taking the limit of $z \to \infty$ in the above expression so as to maintain complete absorption of the probe laser. The adjustment in particle density that is required mirrors closely the enhancement ratio curve. As the easiest way to realise this in the laboratory will be simply to increase the vapour temperature, a careful check on the Doppler width (which scales with the square root of the temperature) will have to be kept and Ω_{23} may have to be slightly further increased to overcome a significant increase in this. It is worth noting that second-order nonlinear processes that are near-resonant with the intermediate level, but not close enough to be significantly absorbed, will benefit from the phase matching induced by the strong upper laser in the same way as for the four-wave mixing process demonstrated at Stanford [8].

The maximum enhancement in the output power, shown by the height of the step, is under these conditions, about four orders of magnitude. This is a huge, and potentially very useful, increase. This factor is governed by the same parameters noted by Harris, Field and Imamoğlu [4]: the square of the ratio of the Doppler width to the dephasing γ_{13}. (This was checked by numerical studies.) The dephasing rate γ_{13} controls the efficacy of EIT on the lower laser and, therefore, has this direct effect on the possible enhancement. Both the nonlinear medium and any buffer gas will have to be chosen so as to minimise any increase in this dephasing rate at the higher $\mathcal{N}z$ products. It may be that because of this it will be more effective to increase the interaction length (by multiple passing of the interacting waves) than to merely increase the particle density.

While this analysis has been undertaken using parameters relevant to sodium, the enhancement will occur in a similar way for equivalent atomic systems. If, however, the Doppler width is less than the homogeneous broadening in the system the enhancement in the conversion efficiency will require a larger Ω_{23} to combat this than just the value required to overcome the Doppler width [4].

6.4. Numerical Models

Since the analytical theory makes several assumptions, including a vanishingly small lower laser intensity, a numerical model was developed as a check of the predictions. The full density matrix system was solved, and integrated over the Doppler width at each point. Once the solution was gained the absorption or gain for each field was calculated for a small vapour path length and the values corrected. The system was re-solved and this repeated for propagation over a specified vapour length. The loss or gain on each field was calculated from the differential expression 2.37 which was derived via Maxwell's equations and the slowly-varying amplitude approximation.

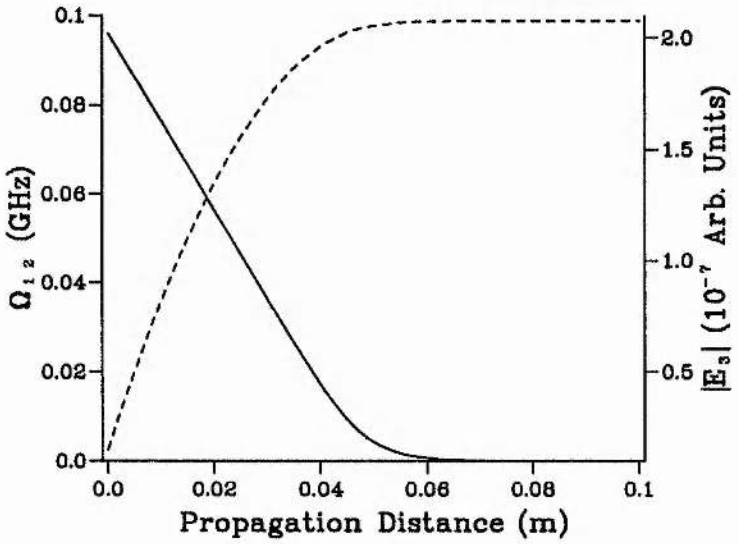

Figure 6.8: Numerical calculations of the evolution of Ω_{12} (solid line, left vertical axis) and the sum frequency wave amplitude (dashed line, right vertical axis) for initial inputs of $\Omega_{12} = 0.1$GHz and $\Omega_{23} = 1$GHz. (For resonant fields with vapour temperature 450K, $\gamma_{12} = 25$MHz and $\gamma_{13} = 7.5$MHz.)

With this model the evolution of the fields could be traced for propagation through the vapour cell. The conventional, low field case is shown in figure 6.8 with an upper field laser power of $\Omega_{23} = 1$GHz. Under the vapour conditions chosen the lower laser is completely absorbed in about 6cm and the SFM frequency

output amplitude saturated as no further conversion can take place. This situation is similar to that which the maximum conversion on the 3S-3P-4D [1] and the 3S-3P-3D (Chapter 4) schemes in sodium encountered. However, if the upper laser strength is increased to $\Omega_{23} = 8$GHz the induced Autler-Townes splitting exceeds the Doppler width and enhancement is possible. Both the vapour path length and particle density were increased to realise the increase in conversion efficiency and the result is shown in figure 6.9. Now the lower laser retains about a third of its original value even after 2m of propagation clearly demonstrating the significant increase in transparency. The sum frequency field amplitude rises to over 200 times the value previously and is still rising. Allowing for the increase in the upper laser strength of a factor of 8 there is still a factor of around 28 increase in conversion introduced by the EIT here. This will correspond to an output power of nearly three orders of magnitude more than for the low field case, again allowing for the upper laser power increase. This is achieved even though the lower laser strength is non-vanishing, indeed it is significantly greater than the saturation intensity for the lower transition [1]. This is in agreement with other work indicating that a strong lower, or probe, laser does not destroy the transparency effect [9].

The numerical model also allows the evolution of the upper field amplitude to be traced to see if there is significant absorption on it, especially in light of the stronger lower field. Figure 6.10 shows that for neither case is reduction of the upper laser a significant feature.

6.5. Towards Experimental Realisation

To evaluate the possibility of experimental realisation of the enhancement on the 3S–3P–3D level scheme in sodium vapour an estimate of the required coupling laser power is required. With reference to the earlier calculation of the link between Rabi frequency and laser intensity in section 3.4.5 and the parameters for the $3P_{3/2}$–$3D_{5/2}$ transition the required laser intensity for a Rabi frequency of 4GHz, sufficient to see

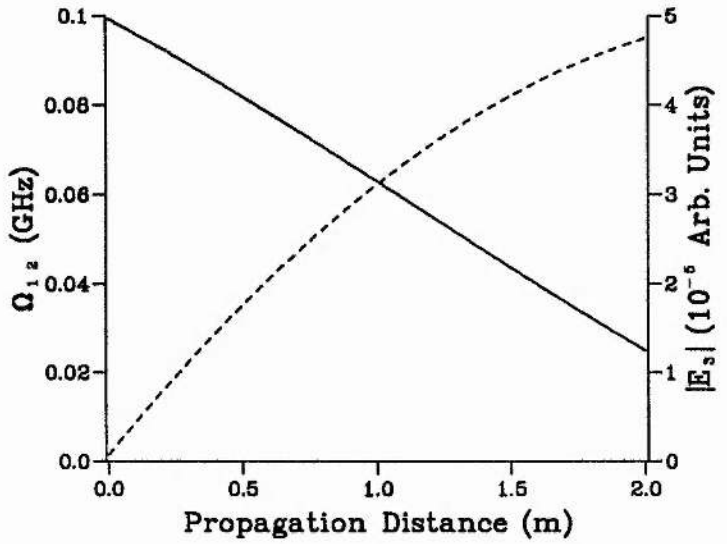

Figure 6.9: Numerical calculations of the evolution of Ω_{12} (solid line, left vertical axis) and the sum frequency wave amplitude (dashed line, right vertical axis) for initial inputs of $\Omega_{12} = 0.1$GHz and $\Omega_{23} = 8$GHz. (For resonant fields with vapour temperature 500K, $\gamma_{12} = 25$MHz and $\gamma_{13} = 7.5$MHz.)

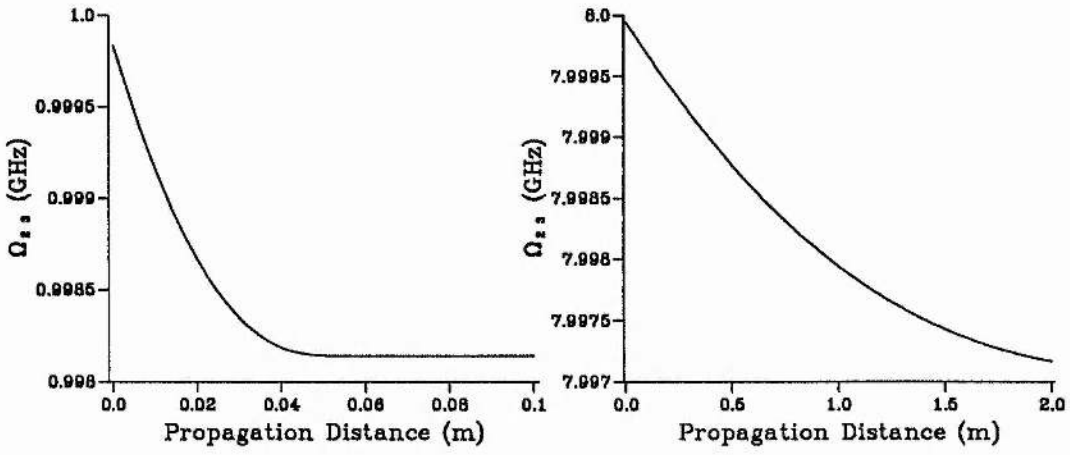

Figure 6.10: Evolution of Ω_{23} corresponding to the calculations of (left) figure 6.8, the low field case, and (right) figure 6.9, the high field case.

the enhancement, is 18.6MWm^{-2}. With continuous-wave lasers of output power approximately 1W a focal spot of radius 130μm is required to create this intensity. This is within experimental possibility and several attempts were made, without success, to observe EIT in the sodium system. While the calculated intensity to Rabi frequency conversion was accurate for experiments in sodium beams using clean three-level systems [15, 16], and also within the correct realm for the rubidium work in chapter 8, it was not accurate here. An experiment using pulsed dye lasers of linewidth about 2GHz [17], thereby coupling several hyperfine and fine structure levels, required intensities of the order of 10^{10}Wm^{-2} to observe a few GHz of splitting, a figure very much in excess of that predicted by calculations. It is thought, that if using a broad linewidth source with very little inhomogeneous broadening can be likened to using a narrow linewidth source with strong inhomogeneous broadening, then the intensities required in this experiment may be similar. The mechanism for this low splitting is unclear. It may be due to the large amount of structure in the atom helping to dephase coherences or setting up interfering ones, but what is clear is that an increase in coupling laser field intensity, possibly by 2 or more orders of magnitude, is required.

There are, therefore, two possible ways to proceed in the sodium vapour system. Keeping with continuous-wave lasers a resonant enhancement cavity could provide a much stronger circulating field. The cavity could be an external ring, frequency locked to the laser input, or the laser cavity itself with a secondary waist introduced. Intra-cavity powers in the Ti:sapphire laser can exceed 20W and at this power level a waist radius of 29μm would give 7.5GWm^{-2}. However, this method would require a very low loss sodium vapour cell, the lower laser to be coupled in to the cavity, and the sum frequency coupled out. Confocal parameters would be fairly short and the experiment would take careful design to be successful. A second possibility is to consider pulsed laser systems and utilise the high peak power available in a short pulse. If a peak power of 100W was available the waist could be increased to 65μm for the same intensity, a much more attractive value for a reasonable vapour

path length. Production of this power could be attained at the required frequency through amplifying a single-frequency Ti:sapphire ring laser [18]. Alternatively, gain switching a Ti:sapphire laser [19], possibly injection seeded to hold single-frequency operation [20], is feasible. Pulse lengths would not need to be very short for this sort of power, 50–100ns being reasonable. Injection-seeded, Q-switched lasers have been utilised successfully in EIT experiments to date [2, 3, 7, 8] and the power requirements in sodium suggest the use of similar sources in this system.

6.5.1. Consideration of Level Structure

One problem that realisation in a sodium system must address is the problem of the fine and hyperfine level structure. This could disturb the experiment due to the different matrix elements between the sub-levels and, more seriously, could disturb the coherences in the atom. A very brief discussion of these is given below.

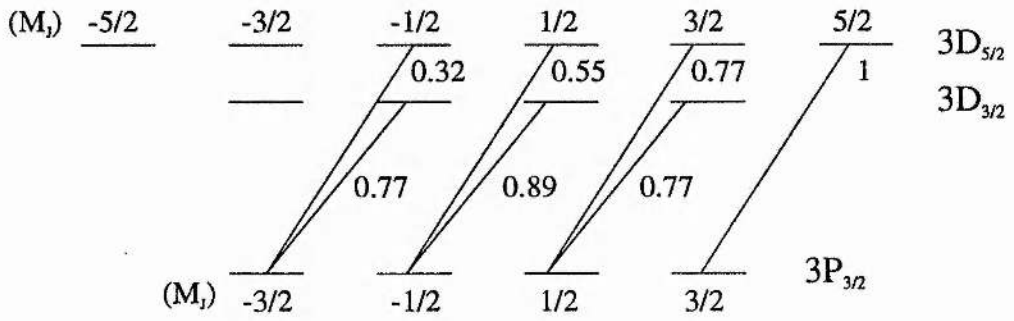

Figure 6.11: The relative strengths of the matrix elements coupling the m_J sublevels of the sodium $3P_{3/2}$ to 3D transition for $\sigma+$ polarisation. The values have been normalised to the strongest.

The calculation of the Rabi frequency above used the formula for the rms Rabi frequency for a degenerate transition. In reality each degenerate sub-level will interact with a different Rabi frequency and complicate the outcome. The relative strengths of the various sub-levels can be calculated by a 3-j symbol, as indicated

in section 3.4.4. As an example the relative strengths of the m_J sublevel transitions of the $3P_{3/2}$–3D transition, assuming a selection rule of $\Delta m_J = +1$, have been calculated and are shown in figure 6.11. These show that the Rabi frequency can vary significantly within the sublevels of one transition. Shore [21, 22] considers the effect of magnetic sublevel degeneracy on Rabi oscillations and concludes that some combinations of polarisations and ΔJ transitions give very poor observation of splitting effects while others give good observation. The recommended transitions are $J \rightarrow J$ with circular polarisation and $J \rightarrow J \pm 1$ with linear polarisation (in the absence of a magnetic field). Figure 6.11 clearly shows this as the selection rule applied was applicable to circular polarisation and the transitions to the $3D_{3/2}$ end state have a much smaller spread of Rabi frequencies than those to the $3D_{5/2}$ end state.

A second possible, and more subtle, problem concerns the possibility of coherences set up between the sublevels and their possible effect on the EIT process. One view is that no important coherences will be set up and that once the Rabi frequency exceeds the sub-level splitting the structure will be broken down. This is termed the optical Back-Goudsmit regime [23] and is equivalent to the Paschen-Back effect in Zeeman structure. However, without detailed multi-level modelling involving coherent interactions the effect of the structure is uncertain and it may tend to dampen or destroy the important optical coherences.

A further problem could be caused by optical pumping. This may be very complicated to calculate in detail as sudden reversals are possible in a short frequency range [24]. Most optical pumping studies are concerned with the effects of a single laser. A second laser could cause strong perturbations on the expected optical pumping behaviour and lead to a reduction in the number of atoms available for the nonlinear process.

6.5.2. Future Suggested Systems

The ideal system for observing the enhancement of the nonlinear process would be a clean three level atom. The absence of nuclear spin would be desirable to remove the complications of hyperfine structure and fine structure outwith the Doppler width. Recent studies in atomic lead at Stanford [3, 8, 25] have shown it to be amenable to study and very high transparency windows have been demonstrated.

However, a recent demonstration of continuous-wave EIT using counter-propagating lasers in a cell containing rubidium vapour has opened up another possibility [26]. This experiment used the 5S–5P–5D level scheme in rubidium that has the advantage that the two input wavelengths required are very similar: 780nm and 776nm. Therefore, in a counter-propagating experimental arrangement the residual Doppler width for interactions between these waves is very small. The researchers were able to demonstrate a transparency on the order of 60% using a 25mW diode laser for coupling the upper transition.

Using two Ti:sapphire lasers this experiment has recently been repeated in our laboratory and is discussed in detail in chapter 8. Using a continuous-wave coupling laser of 300mW, focused to a 135μm radius spot, in excess of 70% transparency has been seen. With this preliminary result an experiment may be proposed to enhance sum frequency mixing on this cascade scheme in rubidium. The EIT coupling laser must be introduced in a counter-propagating manner to keep the power requirements low, in an experimental scheme shown in the schematic figure 6.12. It is envisaged that this experiment could demonstrate the concept by increasing transparency on the 780nm laser and allowing a longer interaction length.

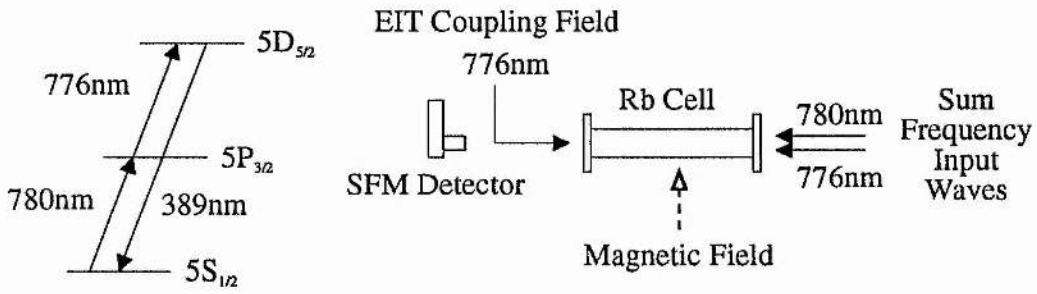

Figure 6.12: Left, the cascade system in rubidium for counter-propagating continuous-wave EIT and the proposed SFM experimental scheme.

REFERENCES

[1] Alistair J. Poustie, *Magnetic Field Induced Sum Frequency Mixing in Sodium Vapour*, PhD thesis, University of St. Andrews, 1990.

[2] K.-J. Boller, A. Imamoğlu, and S. E. Harris, Observation of electromagnetically induced transparency *Phys Rev Lett* **66**, 2593 (1991).

[3] J. E. Field, K. H. Hahn, and S. E. Harris, Observation of electromagnetically induced transparency in collisionally broadened lead vapour *Phys Rev Lett* **67**, 3062 (1991).

[4] S .E. Harris, J. E. Field, and A. Imamoğlu, Nonlinear optical processes using electromagnetically induced transparency *Phys Rev Lett* **64**, 1107 (1990).

[5] K. Hakuta, L. Marmet, and B. P. Stoicheff, Electric-field-induced second-harmonic generation with reduced absorption in atomic hydrogen *Phys Rev Lett* **66**, 596 (1991).

[6] K. Hakuta, L. Marmet, and B. P. Stoicheff, Nonlinear optical generation with reduced absorption using electric-field coupling in atomic hydrogen *Phys Rev A* **45**, 5152 (1992).

[7] G. Z. Zhang, K. Hakuta, and B. P. Stoicheff, Noninear optical generation using electromagnetically induced transparency in atomic hydrogen *Phys Rev Lett* **71**, 3099 (1993).

[8] Maneesh Jain, G. Y. Yin, J. E. Field, and S. E. Harris, Observation of electromagnetically induced phase matching *Opt Lett* **18**, 998 (1993).

[9] A. D. Wilson-Gordon and H. Friedmann, Enhanced index of refraction: a comparison between two- and three-level systems *Opt Commun* **94**, 239 (1992).

[10] Marlan O. Scully, From lasers and masers to phaseonium and phasers *Phys Rep* **219**, 191 (1992).

[11] G. Alzetta, L. Moi, and G. Orriols, Nonabsorption hyperfine resonances in a sodium vapour irradiated by a multimode dye-laser *Il Nuovo Cimento B* **52 B**, 209 (1979).

[12] H. R. Gray, R. M. Whitley, and C. R. Stroud Jr, Coherent trapping of atomic populations *Opt Lett* **3**, 218 (1978).

[13] S. E. Harris, J. E. Field, and A. Kasapi, Dispersive properties of electromagnetically induced transparency *Phys Rev A* **46**, R29 (1992).

[14] Amnon Yariv, *Optical Electronics*, 3 ed. (Holt-Saunders, New York, 1985).

[15] H. R. Gray and C. R. Stroud Jr., Autler-Townes effect in double optical resonance *Opt Commun* **25**, 359 (1978).

[16] P. R. Hemmer, B. W. Peuse, F. Y. Wu, J. E. Thomas, and S. Ezekiel, Precision atomic-beam studies of atom-field interactions *Opt Lett* **6**, 531 (1981).

[17] S. E. Moody and Melissa Lambropoulos, ac stark effect in multiphoton ionization *Phys Rev A* **15**, 1497 (1977).

[18] Patrick Georges, Frederick Estable, Francois Salin, Jean Philippe Poizat, Philippe Grangier, and Alain Brun, High-efficiency multipass Ti:sapphire amplifiers for a continuous-wave single-mode laser *Opt Lett* **16**, 144 (1991).

[19] Glen A. Rines and Peter F. Moulton, Performance of gain-switched Ti:Al_2O_3 unstable-resonator lasers *Opt Lett* **15**, 434 (1990).

[20] T. D. Raymond and A. V. Smith, Injection-seeded titanium-doped-sapphire laser *Opt Lett* **16**, 33 (1991).

[21] Bruce W. Shore, Effects of magnetic sublevel degeneracy on Rabi oscillations *Phys Rev A* **17**, 1739 (1978).

[22] Bruce W. Shore and Michael A. Johnson, Effects of hyperfine structure on coherent excitation *Phys Rev A* **23**, 1608 (1981).

[23] Wojciech Gawlik, Hyperfine interaction versus strong laser field — optical Back-Goudsmit (Paschen-Back) effect *Am J Phys* **59**, 707 (1991).

[24] Y. Nafcha, D. Albeck, and M. Rosenbluh, Reversal of the direction of population transfer between Zeeman sublevels in optical pumping *Phys Rev Lett* **67**, 2279 (1991).

[25] A. Kasapi, G. Y. Yin, M. Jain, A. Merriman, and S. E. Harris, in *International Conference on Quantum Electronics Technical Digest* (Optical Society of America, Washington DC, 1994), Vol. 10.

[26] Yong Qing Li, Shaozheng Jin, and Min Xiao, in *International Conference on Quantum Electronics Technical Digest* (Optical Society of America, Washington DC, 1994), Vol. 10.

Chapter 7

The Local Field Effect in Coherent Three-Level Atom Processes

7. The Local Field Effect in Coherent Three-Level Atom Processes

The optical Bloch equations for a three-level cascade atom are generalised for high particle densities by inclusion of the local field correction. This leads to two new sets of terms: a dynamic Lorentz shift, as seen in the two-level atom; and coherence cross-couplings, unique to the three-level atom. The effect of the correction is studied numerically with reference to two case studies: a self-broadened EIT scheme; and SFM at very high densities without self-broadening.

7.1. The Local Field Correction

A standard approximation made when relating the macroscopic properties of a gaseous medium to the microscopic response of the individual particles is that the electric field experienced by the atom is equal to the injected macroscopic electric field. This is not strictly accurate as each atom will interact with the surrounding atoms and, therefore, its response will be altered by the polarisation of these atoms feeding back. This problem is most commonly associated with solids where the proximity of a large number of close atoms significantly alters the individual response. However, in dense gases there may be sufficient feedback from the surrounding atoms to render the approximation invalid in this situation as well.

In order to gain a better description of the system the concept of the local field, E_L, experienced by the atom is introduced. To calculate the value of this a test

charge is considered within a macroscopic, but small, spherical surface. The atoms outside this surface act as a homogeneous distribution and their response can be shown to be $P/3\epsilon_0$ [1, 2]. The contribution from the atoms inside the surface cancel out for a cubic lattice and hence the local field can be related to the macroscopic electric field, E, by:

$$E_L = E + \frac{P}{3\epsilon_0} \tag{7.1}$$

This is the classical Lorentz-Lorenz relation* and is assumed approximately correct for homogeneous gaseous or liquid media, as well as the cubic lattice of the formal calculation. Hence, calculations of the atomic response that assume $E_L \approx E$, which include all the work previously carried out and stated in this thesis, are internally inconsistent at high densities. In this context high densities implies 10–100 or more atoms within a cubic wavelength of the considered atom [3]. Under these conditions the absorption length of a resonance transition is less than one wavelength of the incident radiation and such densities have been rarely used in the laboratory, explaining the lack of consideration of the local field correction in previous works. However, if EIT is used to greatly increase the penetration depth at high densities the potential now exists for high vapour densities to be used for nonlinear optics and other studies. For this reason the inclusion of the local field correction in the general theoretical system used, the three level atom, is important, and its feedback on EIT especially pressing to evaluate.

In conventional low-density calculations the volume polarisation can be stated with regards to the macroscopic susceptibility, $\chi(E)$, as:

$$P = \epsilon_0 \chi(E) E \tag{7.2}$$

This can also be written in terms of the microscopic polarisability of the atom, $\alpha(E)$,

*This statement of the Lorentz-Lorenz equation is in SI units, in keeping with the rest of this thesis. It is common to see it stated in CGS e.s.u. units as $E_L = E + (4\pi/3)P$, due to the conversion $\epsilon_0 \rightarrow 1/4\pi$.

and number density, $\mathcal{N}$ as:

$$P = \mathcal{N}\alpha(E)E \tag{7.3}$$

Therefore, the relation between the microscopic and macroscopic quantities can be discerned by equating these as:

$$\chi(E) = \frac{\mathcal{N}\alpha(E)}{\epsilon_0} \tag{7.4}$$

However, under high-density conditions the polarisation equations become:

$$P = \epsilon_0 \chi_{NDD} E \tag{7.5}$$

$$P = \mathcal{N}\alpha(E_L)E_L \tag{7.6}$$

and using the Lorentz-Lorenz expression (7.1) the Clausius-Mossotti relation is derived:

$$\chi_{NDD} = \frac{\frac{\mathcal{N}\alpha(E_L)}{\epsilon_0}}{1 - \frac{\mathcal{N}\alpha(E_L)}{3\epsilon_0}} = \frac{\chi(E_L)}{1 - \frac{\chi(E_L)}{3}} \tag{7.7}$$

This expression indicates that under high-density conditions the atomic response, via the atomic polarisability, is nonlinearly related to the volume susceptibility. A plethora of novel effects result from this including: linear and nonlinear resonance line shifts [4, 5]; intrinsic optical bistability [6, 7]; and ultrafast optical switching [8]. Recently, of most relevance for atomic coherence effects, inversionless lasing was predicted to be enhanced by up to two orders of magnitude at critical densities [3]. This theory treated a three-level atom but was simplified by linearising the system with respect to a very weak probe and injecting the atoms into the interaction region with coherences already established. Therefore, it did not include the intrinsic nonlinearity of the response and the coherence cross-couplings that arise from the full treatment given here.

7.2. The Two-Level Atom

The local field correction has been incorporated into the Bloch equations for a two-level atom by several authors [4, 5, 7, 9, 10]. However, only in the last of these

references was a formal derivation presented proving the validity of the Lorentz-Lorenz equation for arbitrary time-dependent fields in a nonlinear medium. Converting the work presented in these publications to the notation used in this thesis the generalised optical Bloch equations for a two-level atom, including the local field correction, can be stated as:

$$\dot{\rho}_{11} = i\Omega_{12}(\tilde{\rho}_{21} - \tilde{\rho}_{12}) + \Gamma_{21}\rho_{22} \tag{7.8a}$$

$$\dot{\rho}_{22} = i\Omega_{12}(\tilde{\rho}_{12} - \tilde{\rho}_{21}) - \Gamma_{21}\rho_{22} \tag{7.8b}$$

$$\dot{\tilde{\rho}}_{12} = -i(\Delta_1 - \underline{C_1(\rho_{22} - \rho_{11})} - i\gamma_{12})\tilde{\rho}_{12} + i\Omega_{12}(\rho_{22} - \rho_{11}) \tag{7.8c}$$

The only difference in these equations from the low-density approximation is the underlined term in equation 7.8c with the local field correction parameter, C_1, defined as:

$$C_1 = \frac{\mathcal{N}\mu_{12}^2}{6\hbar\epsilon_0} \tag{7.9}$$

This term manifests as an extra detuning contribution causing a spectral red-shift, termed the Lorentz shift. Due to the dependence on the population inversion it is sometimes called the dynamic Lorentz shift and leads to the proposals of intrinsic optical bistability cited above. In general it leads to a frequency shift of C_1 in the wings of the line with less shift in the centre due to population transfer and, therefore, overall a general distortion related to the probe field strength. If the resonance is only weakly probed and population transfer is low then we may say that $\rho_{11} \approx 1$ and $\rho_{22} \approx 0$ and approximate the shift to a constant value of C_1. This is, in turn, dubbed the static Lorentz shift [4].

7.3. The Three-Level Atom

The process for including the local field effect into the Bloch equations for the three-level atom is analogous to that for the two-level atom but the results are somewhat more complex. The system that will be considered here is the cascade three level

atom but similar results can be straightforwardly discerned for the other three-level atom configurations, the Lambda (Λ) and Vee (V) configurations.

Derivation proceeds from the Liouville equation, as in section 2.1.2, with the same definitions until immediately preceeding the substitution of the slowly varying coherences $\tilde{\rho}_{ij}$. At this point, as an example, the equation for $\dot{\rho}_{12}$ is:

$$\dot{\rho}_{12} = i\omega_{12}\rho_{12} - \gamma_{12}\rho_{12} + i\frac{\mu_{12}E_1(z,t)}{2\hbar}(\rho_{22} - \rho_{11}) - i\frac{\mu_{32}E_2(z,t)}{2\hbar}\rho_{13} \tag{7.10}$$

Now the local field correction can be included by the substitution:

$$E_i(z,t) \rightarrow E_i(z,t) + P/3\epsilon_0$$

with the volume polarisation expressed as:

$$P = \mathcal{N}(\mu_{12}\rho_{12} + \mu_{23}\rho_{23} + \mu_{13}\rho_{13} + \text{c.c.}) \tag{7.11}$$

in keeping with equation 2.24. In substituting this, cross-couplings between the coherences will arise due to the polarisation contribution. To simplify the expression the slowly varying coherence elements $\tilde{\rho}_{ij}$ are substituted for using equations 2.22 and, invoking the rotating wave approximation, all remaining terms oscillating at optical frequencies are removed. This includes terms at the sum or difference of the injected frequencies. (These frequencies are in the optical range as the fields were assumed sufficiently different to couple to only one transition.) Once this is worked through the generalised equations are gained, and are:

$$\dot{\rho}_{11} = i\Omega_{12}(\tilde{\rho}_{21} - \tilde{\rho}_{12}) + \Gamma_{21}\rho_{22} \tag{7.12a}$$

$$\dot{\rho}_{22} = i\Omega_{12}(\tilde{\rho}_{12} - \tilde{\rho}_{21}) + i\Omega_{23}(\tilde{\rho}_{32} - \tilde{\rho}_{23}) - \Gamma_{21}\rho_{22} + \Gamma_{32}\rho_{33} \tag{7.12b}$$

$$\dot{\rho}_{33} = i\Omega_{23}(\tilde{\rho}_{23} - \tilde{\rho}_{32}) - \Gamma_{32}\rho_{33} \tag{7.12c}$$

$$\dot{\tilde{\rho}}_{12} = -i(\Delta_1 - C_1(\rho_{22} - \rho_{11}) - i\gamma_{12})\tilde{\rho}_{12} + i\Omega_{12}(\rho_{22} - \rho_{11}) - i\Omega_{23}\tilde{\rho}_{13} - iC_2\tilde{\rho}_{32}\tilde{\rho}_{13} \tag{7.12d}$$

$$\dot{\tilde{\rho}}_{23} = -i(\Delta_2 - C_2(\rho_{33} - \rho_{22}) - i\gamma_{23})\tilde{\rho}_{23} + i\Omega_{23}(\rho_{33} - \rho_{22}) + i\Omega_{21}\tilde{\rho}_{13} + iC_1\tilde{\rho}_{21}\tilde{\rho}_{13} \tag{7.12e}$$

$$\dot{\tilde{\rho}}_{13} = -i(\Delta_1 + \Delta_2 - C_3(\rho_{33} - \rho_{11}) - i\gamma_{13})\tilde{\rho}_{13} + i\Omega_{12}\tilde{\rho}_{23} - i\Omega_{23}\tilde{\rho}_{12} + i(C_1 - C_2)\tilde{\rho}_{12}\tilde{\rho}_{23} \quad (7.12f)$$

with the three local field parameters:

$$C_1 = \frac{\mathcal{N}\mu_{12}^2}{6\hbar\epsilon_0} \quad (7.13a)$$

$$C_2 = \frac{\mathcal{N}\mu_{23}^2}{6\hbar\epsilon_0} \quad (7.13b)$$

$$C_3 = \frac{\mathcal{N}\mu_{13}^2}{6\hbar\epsilon_0} \quad (7.13c)$$

In comparison to the standard low-density system, equations 2.23, two new sets of terms can be seen to have arisen. Firstly, as per the two-level atom [4, 9] the dynamic Lorentz shift term appears in each of the three coherence equations. Secondly, each coherence equation also contains a nonlinear term containing a product of the other two coherences. These cross-coupling terms are not mirrored in the two-level system and are a consequence of the more complex three-level atom. The equations presented here are now valid for all particle densities because at low densities $C_i \rightarrow 0$, and the original system is recovered.

7.4. Discussion

These equations open the way for many nonlinear phenomena to be extended into the high density regime. Close analysis of the system may lead to the proposal of novel phenomena, as was the case for the two-level atom, and the effect of the local field on current research topics can be evaluated. Two example systems will be examined briefly below but the opportunities provided by these equations are wider ranging than just these. Already the enhancement of inversionless gain has been predicted [3] under a simplified three-level atom system and other novel effects may emerge.

Very recently, after this analysis was carried out, the author received word that research carried out in parallel by Manka, Dowling, Bowden and Fleischhauer [11]

had uncovered a novel density dependent, or piezophotonic, switching between absorption and amplification in a three-level inversionless laser system. This work incorporates in full the inclusion of the local field correction into a Lambda three-level atom but, interestingly, adopts a different approach to that detailed above. The approach used by these workers was developed to allow for analytical solutions, as the nonlinear system of equations, presented above, preclude them. In their work the low-density equations for the system were derived and presented in terms of the unknown local field and an expression for the low-density susceptibility, $\chi^0(E_L)$, derived. The local field was then substituted for via the expression:

$$E_L = \frac{E}{1 - \frac{1}{3}\chi^0(|E_L|^2)} \tag{7.14}$$

which is derived from the Lorentz-Lorenz equation and the microscopic susceptibility. In a self-consistent manner this was then used in the Clausius-Mossotti relation, equation 7.7, to gain the corrected susceptibility and the solution was checked for uniqueness and stability. This work indicates some of the potential for novel effects in the high density situation and provides an interesting counterpoint to the numerical approach used here.

The densities required for the local field correction to be important are generally larger than those used for most laboratory experiments on the interaction of coherent radiation and atomic systems but are by no means unfeasible. As an example, the particle density such that $\mathcal{N}\lambda^3 = 100$ for $\lambda = 589$nm, appropriate for the 3S–3P transition in sodium, is $\mathcal{N} \approx 5 \times 10^{20}\text{m}^{-3}$. This would be achieved at a vapour temperature of about 322^{0}C (595K) and implies a static Lorentz shift of about 40MHz on this transition. Inhomogeneous broadening would tend to wash this effect out and for an static Lorentz shift of about 1GHz, on the order of this broadening, a temperature of 450^{0}C would be needed, a density of $1.7 \times 10^{22}\text{m}^{-3}$. Neither of these densities or temperatures are experimentally difficult to achieve, indeed much higher ones are possible using heat pipes, high temperature ovens or possibly soon, atom traps.

7.4.1. Self-Broadening

The traditional enemy of the observation of local field effects in gaseous media is self-broadening. Also called resonance-broadening, this collisional broadening mechanism acts on dipole-allowed transitions to the ground state and arises from impacts with ground state atoms of the same element. The theory is reviewed by Lewis [12] and tested in various experiments (eg. see [13] and references therein). The self-broadening linewidth is proportional to the particle density and the oscillator strength of the transition and, as the oscillator strength is proportional to the transition matrix element squared, therefore, scales in the same way as the local field parameter. Their relative magnitudes depend on the degeneracies involved and the exact theoretical treatment used, but a good approximation for the ratio of the self-broadened collisional linewidth, γ_{sb}, and the local field parameter is [5]:

$$\frac{\gamma_{sb}}{C_i} = 3\sqrt{\frac{g_i}{g_j}} \tag{7.15}$$

where g_i and g_j are the degeneracies of the initial and final levels, respectively. Therefore, for most transitions self-broadening is in excess of the static Lorentz shift and can obscure local field effects [6].

This, though, does not mean that the local field correction should be ignored. For EIT experiments in a cascade system where level 1 is the ground state, the transition 1–2 will be strongly self-broadened. However, the transparency produced depends for its depth on the dephasing rate γ_{13} which, due to the dipole-forbidden nature of transition 1–3, will not be significantly affected [14]. Therefore, the effect of the local field correction on the narrow transparency region can come through unimpeded and is important to assess. A homogeneously self-broadened EIT system of this nature will be considered numerically below.

Furthermore, the link between self-broadening and the local field parameter can be broken through design of the experimental system. One way to do this is to consider a high temperature beam system capable of rapid injection of atoms into the interaction region. Due to the collimated atomic velocities the collision rate will

be low and the effect of the local field correction could be observed easily [3]. The second numerical example presented in this chapter will consider this situation.

7.4.2. Numerical Solutions

Due to the introduction of the coherence cross-coupling terms and the dynamic Lorentz shift the density matrix system is now nonlinear. A steady-state is no longer certain and the system cannot be solved by a single-step method. A simple numerical iteration was derived to solve for the steady-state of the system and proved remarkably effective.

This method was based on the Euler, or Euler-Cauchy, method [15] for solving first-order differential equations. If ρ_{ij}^n denotes the numerical value calculated for the density matrix element $\tilde{\rho}_{ij}$ after n steps, then the next approximation, ρ_{ij}^{n+1}, is calculated from:

$$\rho_{ij}^{n+1} = \rho_{ij}^n + \frac{d\rho_{ij}^n}{dt}\delta t \tag{7.16}$$

where δt is a small step factor. The value of $\frac{d\rho_{ij}^n}{dt}$ is that of the right-hand side of the appropriate equation from 7.12a $\rightarrow$ f with the previous iterative solutions ρ_{ij}^n inserted. (It should be noted that to avoid complex algebra the program actually worked with the nine real equations rather than the six complex ones.) As a method of calculating the time dependence of the system this would be fairly crude, but for finding the steady-state it proved very effective. As long as the step factor δt was sufficiently small the system converged to a stable solution. The values used to initiate the iteration, ρ_{ij}^0, were the steady-state solutions of the system with the local field correction removed. Thus the initial values were not arbitrary.

For each numerical solution presented the iteration convergence was checked. Figure 7.1 shows the convergence of the routine for an example given later in figure 7.2. The evolution was of the form of a damped oscillation whose period changed with the parameters of the problem, notably the strength of the local field correction and the detunings. For small local field corrections the iteration converged smoothly

without oscillation, but even for strong corrections with many oscillations the steady state would be found by the method eventually. There is scope for the improvement of this method in order to ensue swift convergence using a refined numerical method, possibly of second or fourth order, eg. improved Euler or Runge-Kutta methods [15].

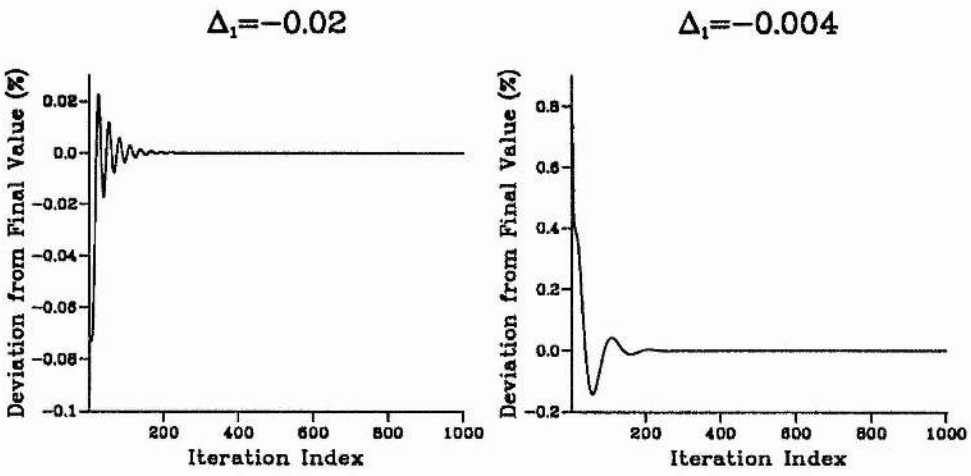

Figure 7.1: Convergence of two Δ_1 detuning points from the $C_1 = 0.4\Gamma$ curve in figure 7.2.

7.5. Application 1: Homogeneously Broadened EIT

The application of the local field correction to EIT is an important study as several experimental studies in EIT are being undertaken at various laboratories. The hallmark of EIT is the ability take a strong resonance line absorption and produce a highly transparent window in it. In this way experimental studies at high vapour densities can be made — indeed are encouraged — as the enhancement in nonlinear processes, as discussed in the previous chapter, require high densities for the realisation of the higher conversion efficiency.

For study here the cascade system was solved for parameters displaying EIT under homogeneously broadened conditions. The linewidth of the 1–2 transition,

resonant with the probe laser frequency, was taken as being dominantly set by self-broadening. This was approximated in the numerical system by setting:

$$\gamma_{12} = \Gamma_{12}/2 + 3.2C_1 \tag{7.17}$$

where the $3.2C_1$ term allows for a broadening of just over three times the local field correction. This broadening ratio was chosen as being relevant for a $J = \frac{1}{2} \rightarrow J' = \frac{1}{2}$ transition†. The EIT feature is unaffected by this broad linewidth as its efficacy is controlled by the quadrupole return transition, 1–3, which is not strongly self-broadened. Therefore, a useful EIT window will be seen, as was the case experimentally in reference [14] under strongly self-broadened conditions. Furthermore, the approximation, $C_3 \approx 0$ is made due to the low matrix element on the 1–3 transition, compared to the two dipole transitions.

Four sets of lineshape curves are shown in figure 7.2 as the particle density is increased giving rise to an increasing local field correction parameter and self-broadened linewidth. It is immediately obvious that the EIT feature remains relatively unaffected by the local field correction. Its position, governed by the two-photon detuning, is not changed due to C_3 being insignificant, and importantly the depth is unaltered. The residual absorption on an incomplete transparency at low densities will scale linearly with increasing $\mathcal{N}$. What does change is the 1–2 linewidth, via self-broadening, and the position of the absorption maximum. This shifts to lower frequencies via the Lorentz shift, as expected.

Therefore, the effect of the local field correction at these levels appears to reduce to a mere Lorentz shift on the absorption profile. Confirmation of this can be sought in two ways. Firstly, the system was solved with changing upper field detunings with no local field correction. Figure 7.3 shows these results and it can be clearly seen

†The use of 3.2, as opposed to 3.0 which would be implied from equation 7.15, is somewhat historical in this work. It is retained as it merely additionally broadens the lineshapes slightly and the results with either value are highly similar. As noted in section 7.4.1 there is a range of values for this constant and 3.2 is within this range.

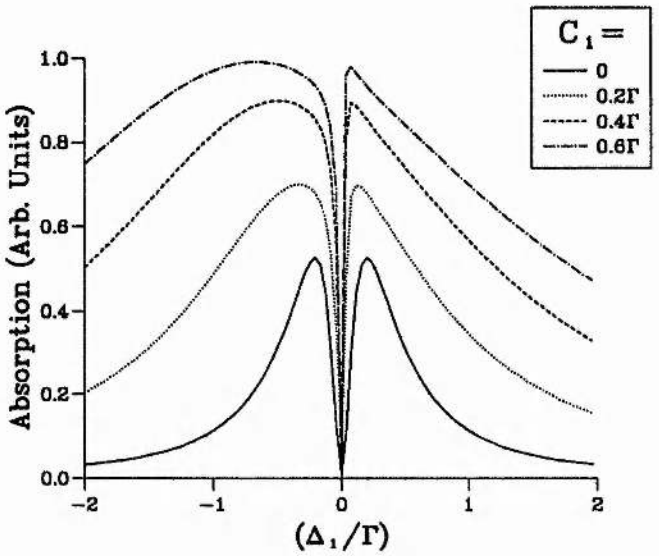

Figure 7.2: Numerical solutions for the probe absorption, from $-\mathcal{N}\Im(\tilde{\rho}_{12})$, with the field strength parameters $\Omega_{12} = 0.02\Gamma$ and $\Omega_{23} = 0.2\Gamma$ and upper field detuning $\Delta_2 = 0$. The rise in particle density is indicated by the increasing local field parameters in the legend, while the $C_1 = 0$ trace is shown artificially large for the shape to be evident. (Other parameters are: $\Gamma_{12} = \Gamma$, $\Gamma_{23} = 0.6\Gamma$, $\gamma_{12} = \Gamma_{12}/2 + 3.2C_1$, $\gamma_{23} = \Gamma_{23}/2$ and $\gamma_{13} = 0$.)

that the shape of the curves are identical to those in the figure 7.2 apart from a displacement. Thus the local field correction is not changing the shape of the curves. The second, more quantitative, check was made by solving the numerical

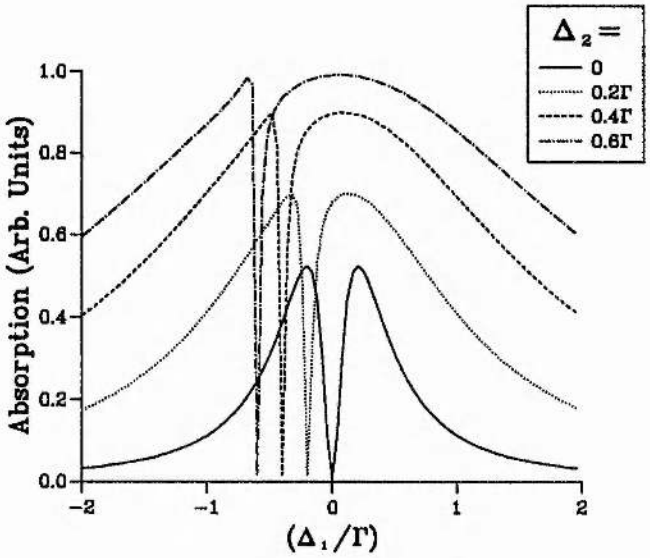

Figure 7.3: The probe absorption, from $-\mathcal{N}\Im(\tilde{\rho}_{12})$, with the same parameters as figure 7.2 except that $C_{1,2} = 0$ and the upper field detunings are varied as shown in the legend.

system with the coherence cross-coupling terms removed, but the dynamic Lorentz shift terms retained. The difference between this result and the complete system with all the terms is shown in figure 7.4. The low deviation between the two curves is quantified and is at least 2 orders of magnitude below the maximum magnitude of the absorption. Taking the approximations one step further we may replace the dynamic Lorentz shift term with the static Lorentz shift by setting:

$$C_1(\rho_{22} - \rho_{11}) \approx -C_1 \tag{7.18}$$

With this, the system is once again linear in the density matrix elements and can be solved for its steady-state without the need for an iterative approach. The deviation of this linear approximation from the full solution is also shown in figure 7.4. As can

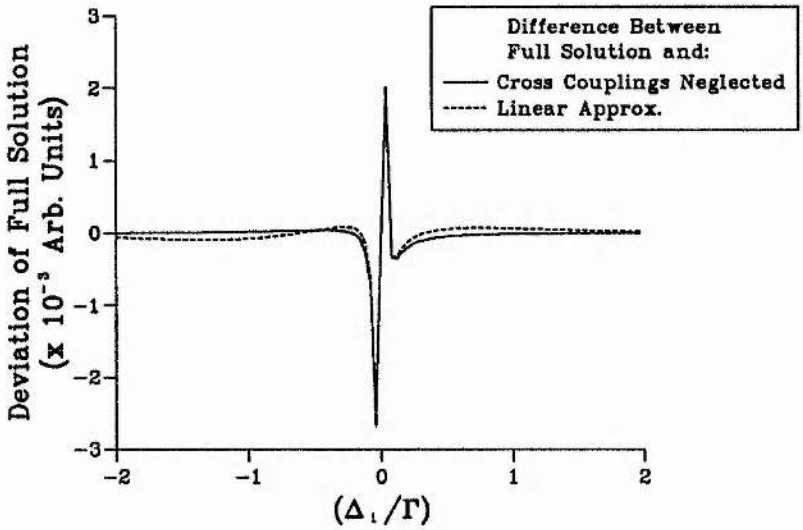

Figure 7.4: The difference between the full solution for the absorption and that without the coherence cross-coupling terms (solid line); and that of the linear approximation via the static Lorentz shift (dashed line). The curve is for $C_1 = 0.4\Gamma$ and other parameters are as for figure 7.2.

be seen it is very close to the solution without the coherence cross-coupling terms deviating only where some population transfer occurs.

Thus at these sort of densities, ie. where the local field correction parameter is less than, or on the order of, the homogeneous linewidth, the local field correction effect is merely that of the dynamic Lorentz shift. If the probe laser is sufficiently weak for there to be negligible population transfer this can be approximated in turn by the static Lorentz shift. Therefore experiments in EIT under these conditions of not excessive particle densities, which are reasonable, will not be troubled by the local field correction. If the experiment utilises tunable laser sources the experimenter will be able to counteract the shift of the transparency window from line centre via the upper field detuning and indeed, unless an absolute frequency reference is checked, may never notice it.

7.6. Application 2: High Density SFM

Once the local field correction parameters become much greater than the homogeneous linewidth there is the potential for the coherence cross-coupling terms to have a significant effect on the atomic response. This is the region considered in references [3, 11] but requires that the link between self-broadening and the local field shift is severed. This could be done by careful experimental design avoiding the use of a vapour cell. Specifically, a high temperature beam giving rapid injection of atoms into the interaction region could reduce collisional effects due to the collimation of atomic velocities and allow observation of local field correction phenomena, if they prove useful, without strong self-broadening.

The combination of the coherence cross-coupling and dynamic Lorentz shift terms will, I believe, give rise to many effects in the various three-level atom geometries. Strong line distortions [16] and even line reversal [11] may be contemplated. Due to the wide range of possible applications only a flavour of possible effects will be discussed below with reference to sum frequency mixing. However, a more general study could be undertaken using the generalised equations as a starting point under various sets of parameters. Doppler shifts and broadening can be numerically included, if required, to the system. (This was done but as self-broadening is on a par with, or even dominates, Doppler broadening at high enough densities for a shift to be significant with respect to the Doppler width no results are presented here.)

The choice of looking at a sum frequency mixing system is not arbitrary. It provides a scheme whereby it is possible to probe the very dense vapour situations that would be encountered under these high particle densities. This is because the sum frequency radiation is generated on a dipole-forbidden but quadrupole-allowed transition with low associated re-absorption and it would, therefore, be able to escape the interaction zone. The laser resonant with the lower transition would be heavily absorbed, limiting the interaction length, but the high vapour densities would give efficient conversion within that length, supplying a detectable output.

Phase matching effects would have to be taken into account in a full treatment either by trying to avoid them, eg. by tuning the upper laser with its low associated atomic dispersion, or by including them in the calculation of the predicted response.

In this study we neglect self-broadening, invoking an experimental design as detailed in reference [3]. However, we do allow for some dephasing on the 1–3 transition to block EIT effects at the field strengths used. This is reasonable as the field strengths are fairly low and a system for good SFM output would not have a metastable top level (as the matrix element μ_{13} must be non-zero) thus leading to some dephasing even without strong collisional effects.

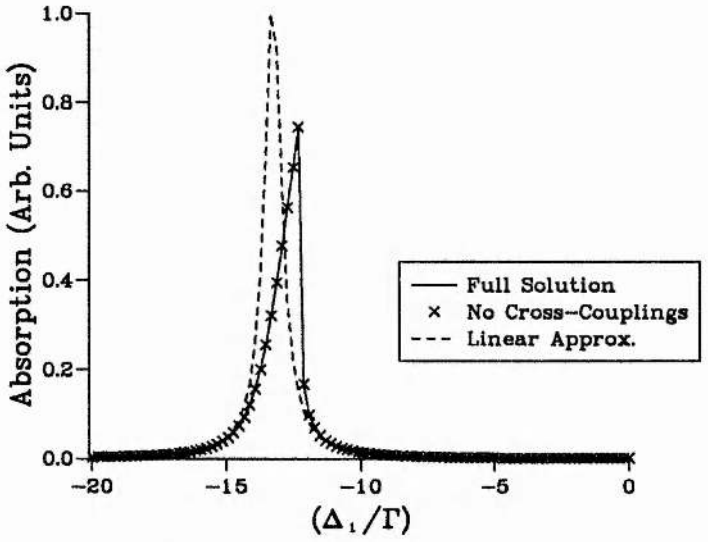

Figure 7.5: The lower field absorption, from $-\mathcal{N}\Im(\tilde{\rho}_{12})$, calculated as indicated in the legend for $C_1 = 10\Gamma$ with $\Omega_{12} = 0.2\Gamma$. Other parameters as in the previous figures except self-broadening is neglected, $\gamma_{13} = \Gamma$ and $\Omega_{23} = 0$.

As an initial example it is noted that the absorption profile experienced by the laser resonant with the lower transition is heavily altered by the local field correction. In figure 7.5 the lineshape of this absorption is displayed for $C_1 = 10\Gamma$, calculated by the full numerical solution and the two approximations discussed above. It is now notable that the static Lorentz shift approximation (labelled the "Linear Approx.") is invalid in this regime. The line has moved so that the resonance is close to

$\Delta_1 = -10\Gamma$ but the shape is now highly asymetrical. The very sharp high frequency edge of this curve is mirrored in the curves for ρ_{11} and ρ_{22} and is entirely due to the dynamic Lorentz shift term ($C_1(\rho_{22} - \rho_{11})\tilde{\rho}_{12}$ in equation 7.12). The cross-coupling terms are essentially removed by having no upper laser field in this calculation but even with this added, as for the next graph below, they have little effect. The sharp high-frequency edge to the absorption suggests the bistability that is discussed in connection with the dynamic Lorentz shift [6, 7], and this result implies that the coherence cross-coupling terms will not remove the possibility of bistability in these systems.

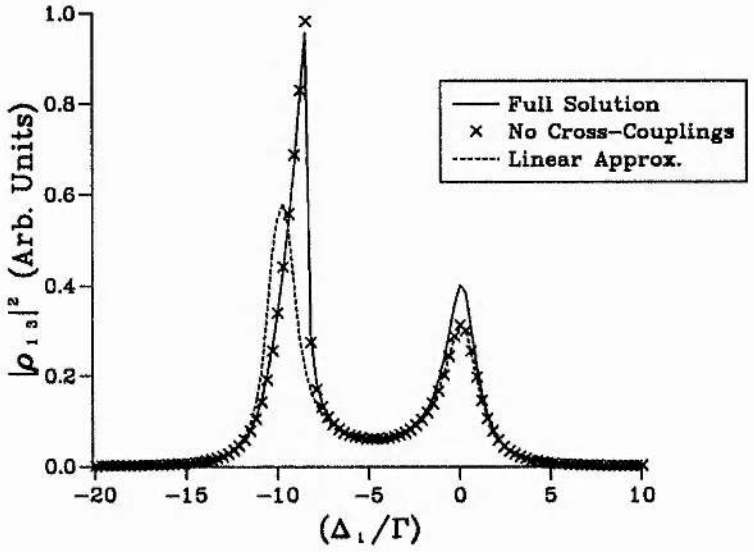

Figure 7.6: The SFM output power, from $|\tilde{\rho}_{13}|^2$, calculated as indicated in the legend for $\Omega_{12} = \Omega_{23} = 0.2\Gamma$, $C_1 = 10\Gamma$, $\Delta_2 = 0$ and other parameters as before.

However, it is not the case that the coherence cross-coupling terms can always be ignored. The next result, figure 7.6, adds an equal strength field on the upper transition, 2–3, to the lower one and displays the square modulus of the 1–3 transition coherence, which is proportional to the SFM output. The two peaks in the profile originate from the two routes of generation of the upper state coherence, as discussed in chapter 5. At $\Delta_1 = -10\Gamma$ is the two-step route via the middle level. It displays the line asymmetry seen above for the absorption, which is mainly

dependent on the dynamic Lorentz shift term and is a little depressed by the coherence cross-coupings. However the two-photon route, at $\Delta_1 = 0$, is enhanced by the coherence cross-couplings. Reference to equation 7.12 shows why the two react differently. In steady-state we can write:

$$\tilde{\rho}_{13} = \frac{\Omega_{12}\tilde{\rho}_{23} - \Omega_{23}\tilde{\rho}_{12} + (C_1 - C_2)\tilde{\rho}_{12}\tilde{\rho}_{23}}{\Delta_1 + \Delta_2 - i\gamma_{13}} \tag{7.19}$$

Again recalling from section 5.3.1 that the first term in the numerator is the end link of the two-step route and that the second term is the end link for the two-photon route, the sign difference between these two terms explains their difference reactions to the local field correction of the last numerator term. The local field term will be significant when either $\tilde{\rho}_{12}$ or $\tilde{\rho}_{23}$ are large, as they will be separately when each of the two routes come through. Thus the local field correction cross-coupling term interacts with both, but here constructively with the two-photon route. This constructive interaction is due to the choice of $C_2 = 1.25C_1$ which was made via the ratio of the matrix elements on the 3S–3P and 3P–3D transitions in sodium as studied for sum frequency mixing in this work. If other transitions were chosen this term could change in phase if $C_1 > C_2$, or be removed if equal matrix elements were appropriate.

Further study on the three-level atom is left for later analysis of a particular scheme when likely experimental conditions are known or when the removal of self-broadening has been accomplished by some experimental means allowing the local field correction to be observed relatively unhindered. Such a study could then proceed from the generalised equations in a straightforward manner. It is anticipated that several novel and interesting optical features in the response of a three-level atom in a dense gas will be uncovered by such studies.

REFERENCES

[1] Max Born and Emil Wolf, *Principles of Optics*, 5 ed. (Pergamon Press, Oxford, 1975).

[2] W. J. Duffin, *Electricity and Magnetism*, 3rd ed. (McGraw-Hill, London, 1980).

[3] Jonathan P. Dowling and Charles M. Bowden, Near dipole-dipole effects in lasing without inversion: An enhancement of gain and absorptionless index of refraction *Phys Rev Lett* **70**, 1421 (1993).

[4] R. Friedberg, S. R. Hartmann, and Jamal T. Manassah, Effect of local-field correction on a strongly pumped resonance *Phys Rev A* **40**, 2446 (1989).

[5] Jeffery J. Maki, Michelle S. Malcuit, J. E. Sipe, and Robert W. Boyd, Linear and nonlinear optical measurements of the Lorentz local field *Phys Rev Lett* **67**, 972 (1991).

[6] R. Friedberg, S. R. Hartmann, and Jamal T. Manassah, Mirrorless optical bistability condition *Phys Rev A* **39**, 3444 (1989).

[7] Ramarao Inguva and Charles M. Bowden, Spatial and temporal evolution of the first-order phase transition in intrinsic optical bistability *Phys Rev A* **41**, 1670 (1990).

[8] M. E. Crenshaw, M. Scalora, and C. M. Bowden, Ultrafast intrinsic optical switching in a dense medium of two-level atoms *Phys Rev Lett* **68**, 911 (1992).

[9] Charles M. Bowden and Jonathan P. Dowling, Near-dipole-dipole effects in dense media: Generalized Maxwell-Bloch equations *Phys Rev A* **47**, 1247 (1993).

[10] Charles M. Bowden and Jonathan P. Dowling, Erratum: Near-dipole-dipole effects in dense media: Generalized Maxwell-Bloch equations *Phys Rev A* **49**, 1514 (1994).

[11] Aaron S. Manka, Jonathan P. Dowling, Charles M. Bowden, and Michael Fleischhauer, Piezophotonic switching due to local field effects in a coherently prepared medium of three-level atoms *Phys Rev Lett* **73**, 1789 (1994).

[12] E. L. Lewis, Collisional relaxation of atomic excited states, line broadening and interatomic interactions *Phys Rep* **58**, 1 (1980).

[13] J. Huennekens and A. Gallagher, Self-broadening of the sodium resonance lines and excitation tranfer between the $3P_{\frac{3}{2}}$ and $3P_{\frac{1}{2}}$ levels *Phys Rev A* **27**, 1851 (1983).

[14] J. E. Field, K. H. Hahn, and S. E. Harris, Observation of electromagnetically induced transparency in collisionally broadened lead vapour *Phys Rev Lett* **67**, 3062 (1991).

[15] Erwin Kreysig, *Advanced Engineering Mathematics*, 6 ed. (Wiley, New York, 1988).

[16] V. G. Arkhipkin, A.K. Popov, and A.S. Aleksandrovsky, to be presented at EQEC'94 as QTuG14 (unpublished).

Chapter 8

Sub-Doppler Electromagnetically-Induced Transparency and Lensing

8. Sub-Doppler Electromagnetically-Induced Transparency and Lensing

In this chapter experiments on EIT using a cascade level scheme in rubidium vapour are described. A counter-propagating experimental geometry is used to lower the power requirements on the coupling laser. Spatial consequences of the EIT situation are highlighted in theory and observation with the discovery of induced lensing on the probe laser. This, and its implications, are discussed in detail.

8.1. Sub-Doppler EIT

8.1.1. Introduction

As noted in previous chapters, in order to observe electromagnetically-induced transparency in an inhomogeneously broadened medium the coupling laser must induce Autler-Townes splitting in excess of the inhomogeneous linewidth. With continuous-wave lasers, optical wavelength transitions and gas temperatures in excess of room temperature, this criterion is difficult to satisfy. However, the linewidth that must be overcome is not the Doppler width of the probe transition but the linewidth of two-photon transitions from one end of the atomic system to the other ie. in the cascade scheme, two-photon transitions from the ground to the uppermost state. The reason for this is that the transparency occurs at the point of two-photon res-

onance. So if the coupling laser is detuned by some Doppler shift, and, if the probe laser is detuned to track with it, then the probe field will always see low absorption and a well defined EIT feature is observed. In practise this requires, firstly, that the two transitions have similar wavelength so that the Doppler shifts are of the similar size. Futhermore, it requires that the experimental geometry will constrain the shifts to track in the appropriate direction. Therefore, in a cascade system the lasers must be counter-propagated so that a shift up in the coupling laser frequency is matched by an equal shift down in the probe laser frequency to maintain that important two-photon resonance condition. On the other hand, in the lambda (Λ) or vee (V) schemes the lasers must be co-propagated so that the shifts are in the same sense.

This principle was used to great effect by Li, Jin and Xiao [1] to observe EIT in a cell of rubidium, via both cascade and lambda schemes, using continuous-wave diode lasers. The were able to achieve a 60% reduction in absorption with only 25mW of power in the coupling laser beam. Earlier work by Buell and Fink [2] showed sub-Doppler features in a vee-type scheme, again using cw diode lasers, but the laser powers were only capable of inducing marginal Autler-Townes splitting.

8.1.2. Continuous-wave EIT in Rb Vapour

This work extends these earlier experiments in two ways. Firstly by using a Ti:sapphire laser to provide the coupling radiation, stronger Autler-Townes splitting may be induced with powers of up to 1 Watt available in this work. Secondly, results are presented on the observation of induced lensing of the probe beam within the EIT feature. This lensing is caused by the spatial variation of the coupling laser beam giving rise to a refractive index profile in the vapour which is then experienced by the weak probe laser. We have dubbed this phenomena "electromagnetically-induced focusing" (EIF), and it will be discussed in detail later in this chapter. At this stage the experimental application of EIT to sum frequency mixing is not discussed but

left for further work.

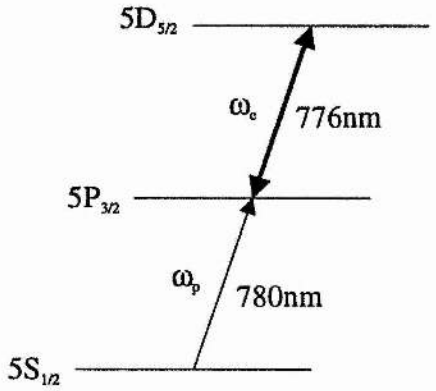

Figure 8.1: A partial energy level diagram of rubidium, showing the levels used in this chapter.

The cascade scheme used for these EIT experiments in rubidium vapour is shown in figure 8.1. It was chosen due to the close coincidence between the lower and upper transition wavelengths, 780 and 776nm, in order to lower the power requirements on the coupling laser by cancellation of Doppler shifts, as described above. This cancellation of shifts via a counter-propagating geometry in this scheme is remarkably effective. Figure 8.2 shows two numerical calculations from the density matrix for the imaginary part of the off-diagonal element $\tilde{\rho}_{12}$, which is proportional to the probe laser absorption. They both use the same field strengths but one is for co-propagating lasers and the other for counter-propagating lasers. Only in the latter is the sharp EIT window seen within the Doppler broadened absorption curve, as the Rabi frequency is much less that this Doppler linewidth.

8.2. EIT: Experimental Results

The experimental setup for the observation of EIT in rubidium vapour is given in chapter 3. The probe radiation was supplied by the Microlase MBR-110 laser due

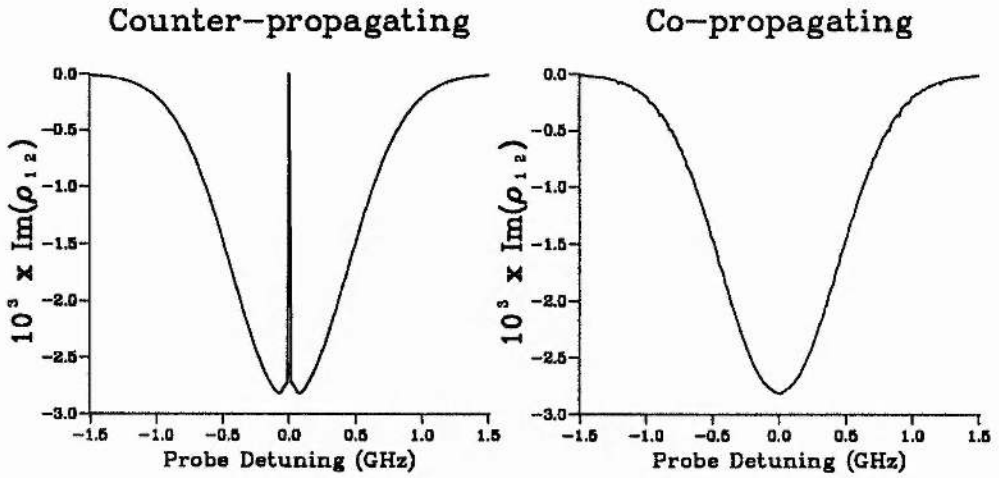

Figure 8.2: Numerical solutions for the imaginary part of $\tilde{\rho}_{12}$, including Doppler broadening with the wavevectors aligned as indicated. ($\Omega_{12} = 0.001$MHz and $\Omega_{23} = 0.05$MHz, Vapour Temperature 310K, $\gamma_{13} = 0$.)

to the built-in scanning capability of this laser. To avoid saturation of the lower transition, and effects such as self-focusing, the probe laser was attenuated by ND filters of factor at least 3. This limited the probe power to the sub-milliwatt level. This was then focused into the cell by a 40cm lens giving a waist size of approximately 80μm. The coupling radiation was introduced from the opposite end of the cell and focused by a 50cm lens giving around a 130μm waist. Absorption of the probe radiation could be detected at room temperature and complete attenuation of the probe radiation, without the coupling field, was achieved for temperatures in excess of approximately 50^0C.

Due to the two isotopes in natural rubidium vapour, and the hyperfine structure therein, there are 4 main Doppler broadened features in the probe absorption curve. From low to high frequency they are:

^{87}Rb: $5S_{1/2}$ (F=2) $\rightarrow$ $5P_{3/2}$ (F'=3,2,1)

^{85}Rb: $5S_{1/2}$ (F=3) $\rightarrow$ $5P_{3/2}$ (F'=4,3,2)

^{85}Rb: $5S_{1/2}$ (F=2) $\rightarrow$ $5P_{3/2}$ (F'=3,2,1)

^{87}Rb: $5S_{1/2}$ (F=1) $\rightarrow$ $5P_{3/2}$ (F'=2,1,0)

These four lines are clearly shown, Doppler broadened, in figure 8.3, which shows both co-propagating and counter-propagating absorption traces with the EIT coupling field present. The co-propagating lines are essentially identical to the absorption features seen with the coupling field blocked. The difference in strength between the sub-level transitions is traceable to the different matrix elements, isotope abundances involved and optical pumping. None of the lines are free from optical pumping, under the linear polarisations used here, or with circular polarisation due to the effects of Doppler broadening. Varying the laser polarisations between linear and circular produced no major differences in the observations. (In a beam of rubidium atoms, this would not be the case and a non-optical-pumping three-level atom could be probed by circular polarisation as: $5S_{1/2}$ (F=3, m_f=3) $\rightarrow$ $5P_{3/2}$ (F=4, m_f=4) $\rightarrow$ $5D_{5/2}$ (F=5, m_f=5).)

In the counter-propagating geometry the sub-Doppler EIT features are obvious on each line. The upper laser tuning was selected for near resonance on the two left-hand transitions. Therefore, as the upper transition resonance frequency shifts for the two right-hand transition lines the EIT features are seen off to one side. It is immediately obvious that the transparency is not complete: 60 to 70% in these traces. This was the maximum achieved in this work, although the transparency continued to rise up to the maximum available intensity from the coupling laser so there is reason to believe it is not the maximum possible in this level scheme. There are three principle reasons for the incomplete transparency observed here:

1. γ_{13}: In this system the dephasing rate of the coherence controlling the EIT will not be zero. It should be low, however, being a dipole-forbidden transition. Possible contributions to it come from the spontaneous decay of the 5D level

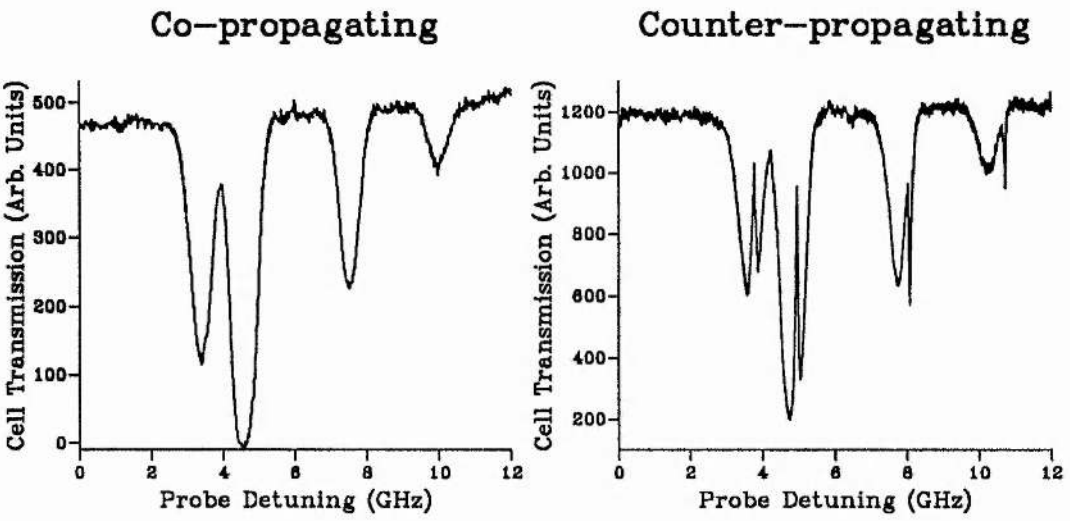

Figure 8.3: Traces of the cell transmission as seen by the probe laser beam as it is tuned across the $5S_{1/2} \rightarrow 5P_{3/2}$ transition in rubidium. (Oven temperature for both $\approx 45^0$C; upper laser power 300mW; lower laser power $<$ 1mW, but not identical in the two traces)

(with a linewidth of about 1MHz) and collisions in the heated vapour. Again, however, as there is no added buffer gas this should not be excessive. Therefore, while this is undoubtedly a contribution, it is unlikely to be the principle limiting factor.

2. *Hyperfine structure*: In this system there is significant structure from the split hyperfine sublevels with splittings in the uppermost level of up to 29MHz. With the induced Autler-Townes splitting being on the order of 300MHz this structure is not dominated, especially in the ^{87}Rb atoms, and indeed distinct structure can be seen within the EIT feature in the ^{87}Rb, $5S_{1/2}$ (F=2) sublevel transition (eg. see figure 8.5). Furthermore, each magnetic sublevel (characterised by the quantum number, m_f) will have a different Rabi frequency via the appropriate angular momentum coupling coefficients, or 3-j symbols (see sections 3.4.5 and 6.5.1). Thus each sub-level will split by a different amount and the contributions, weighted by their population and individual absorption

coefficient, will tend to reduce the clarity of the EIT window. It is thought that this is the largest contribution to the non-ideal nature of the observations.

3. *Spatial Effects*: In order to see EIT it is important that the probe radiation be kept within the coupling radiation at all times within the cell. This was attempted via the focusing lenses adopted. However, if the two beams were not ideally overlapped some absorption would occur on the unprotected part of the probe beam. Also towards the edges of the coupling beam the Gaussian profile of the intensity distribution means that the Rabi splitting will be somewhat less than at the centre and some absorption would also take place here. This is complicated by the electromagnetically-induced focusing, and especially, defocusing that will be discussed later. Due to this, mode matching of the two beams cannot be guaranteed throughout the frequencies scanned.

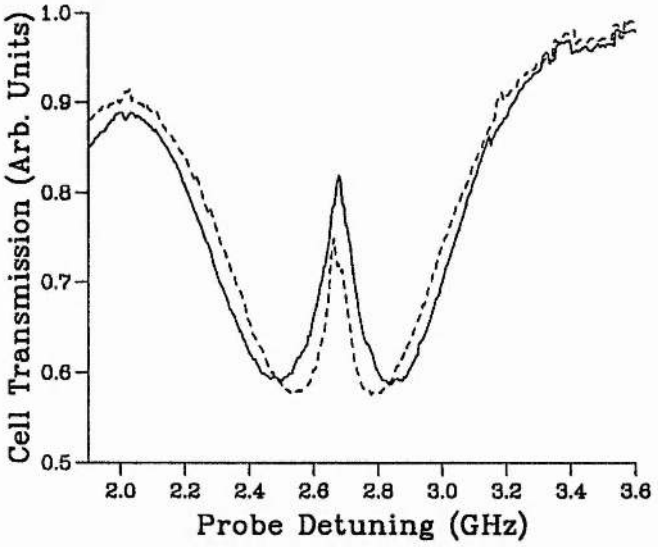

Figure 8.4: Two probe absorption traces for scans across the ^{85}Rb, $5S_{1/2}$ (F=3) $\rightarrow$ $5P_{3/2}$ transition with coupling laser powers of 780mW (solid line) and 170mW (dashed line). (Vapour temperature $\approx 43^0$C.)

Changing the coupling laser power altered the splitting observed, as expected. This is shown in the two traces of figure 8.4. The splitting at the higher power is

obvious, not only at the EIT feature itself, but also on the outer edges of the absorption feature. The splittings, measured from this trace are 366MHz and 252MHz for the two curves presented and if zero detuning is assumed the induced Rabi frequencies are just these values. These are not dissimilar to the estimate of the rms Rabi frequency via the calculated intensity and matrix element, see section 3.4.5, of 230MHz and 107MHz. The discrepancy may be due to the focal waist being smaller than expected or in the multiple Rabi frequencies induced on the transition.

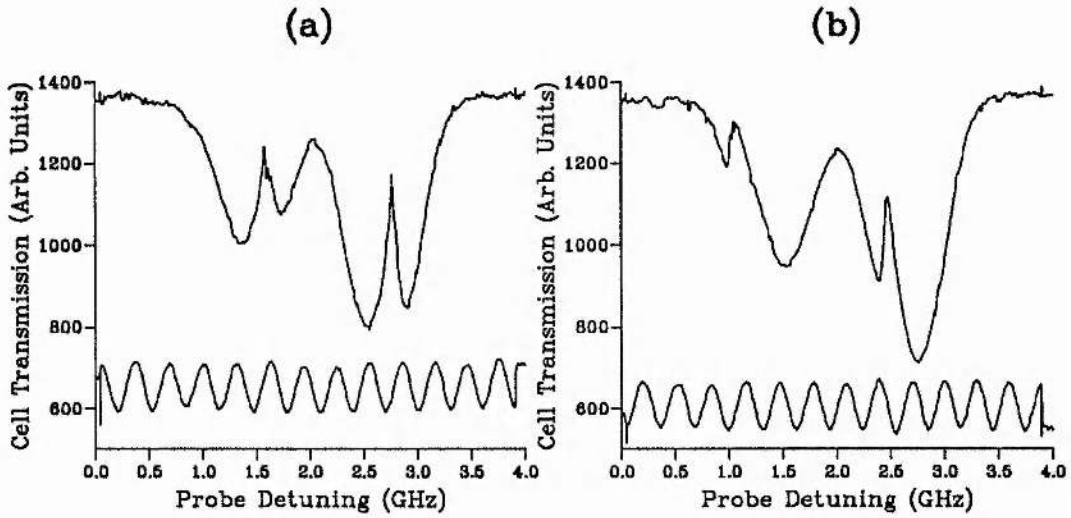

Figure 8.5: Two probe absorption curves for different coupling laser detunings. A 300MHz confocal marker trace is shown below the figures for an accurate frequency reference. (Oven temperature 43^{0}C, 780mW coupling laser power, $<$ 1mW probe laser power.)

As the upper laser frequency was changed slightly, the EIT feature moved across the Doppler broadened absorption lines as would be expected. Two traces, one with the tuning on each side of the optimum, are given in figure 8.5 of this behaviour. Note that when the EIT window is tuned away from the line centre the outside edge of the feature becomes much sharper than the inner edge. This is mirrored in numerical predictions. Also the structure in the ^{87}Rb, $5S_{1/2}$ (F=2) line is visible

in trace (a). This appeared to consist of 3 to 4 individual lines and is thought to be due to the larger hyperfine structure splitting for this isotope, and the multiple Rabi frequencies between the near-degenerate levels.

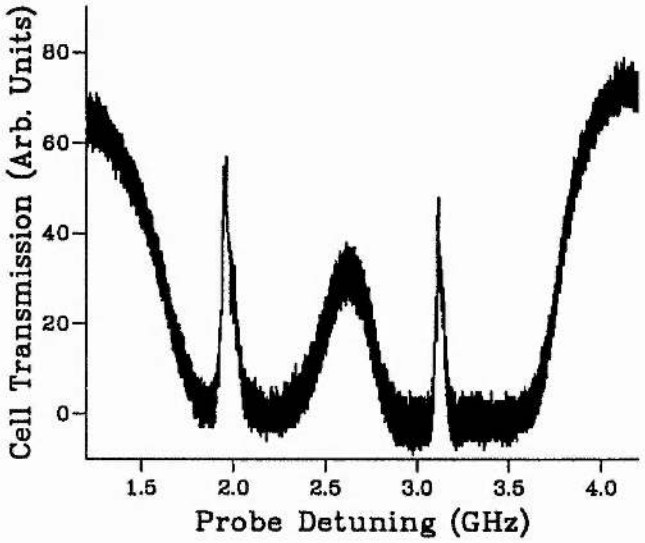

Figure 8.6: Cell transmission as experienced by the probe laser with total absorption of the probe outside of the EIT window. (Oven temperature 45°C, probe laser power $\approx 25\mu$W, coupling laser power 600mW)

At higher temperatures, or lower probe powers, the cell could be made opaque to the probe radiation on the absorption features, without the coupling laser present. Figure 8.6 shows the effect of EIT in this case. The EIT window is clearly seen within the "flat-top" of the absorption trace due to complete attenuation of the probe beam. This result is important for the enhancement of nonlinear processes, in that it is a clear demonstration that the interaction length can be increased by the effect of EIT. During the work, presented below, on electromagnetically-induced focusing, this is the sort of transmission characteristic that was encountered with the probe laser beam being completely absorbed outside the EIT window.

Various safeguarding experiments were conducted to verify that the process observed was EIT as expected. The counter-propagating results, shown in figure 8.3, checked that the reduction in absorption was not due to some velocity-selecting opti-

cal pumping process but was due to a coherent effect. Furthermore, the probe power was varied and the EIT feature was seen to be unchanged by this, at the lower limit of probe powers. At higher probe powers, $>$ 1mW, self-focusing and defocusing were seen surrounding the probe absorption features. The low threshold for this is on a par with results in sodium vapour [3]. It is possible that the self-focusing threshold within the EIT profile is anomalously low [4] but by reducing the probe power until no further changes were seen should avoid this region.

There are two further experimental points worthy of note. Firstly it was noted when using the CCD array that the probe beam initially contained a dark spot which was pump power dependent but insensitive to both laser frequencies. This was traced to a thermal effect in the probe laser ND filter which was absorbing the majority of the power from both beams. The solution was to use reflective ND filters and move the position of these attenuators to near the probe laser output port so that the coupling laser beam had diverged further and the beam overlap was not necessarily so close. Secondly, due to the induced lensing in the medium it was important to use a large-area photodiode to detect the probe transmission or misleading results could be attained due to the probe beam expanding beyond the edge of the photodiode or being distorted in its path by the coupling laser beam position and the associated lensing.

8.3. Electromagnetically-Induced Focusing

When the photodiode was replaced by a CCD camera, strong changes in the probe laser beam spot size were seen by this as the probe laser was tuned through the narrow EIT region. These changes in spot size were quite dramatic and two beam profiles are shown in figure 8.7 to show the range of spot sizes seen. Both focusing and defocusing were observed at separate probe laser frequencies, as well as rapid variations between the two regimes. After considering the possibility of self-focusing, which was ruled out by the lack of dependance on the probe laser power, a novel

mechanism for this lensing is proposed and is detailed below in this section.

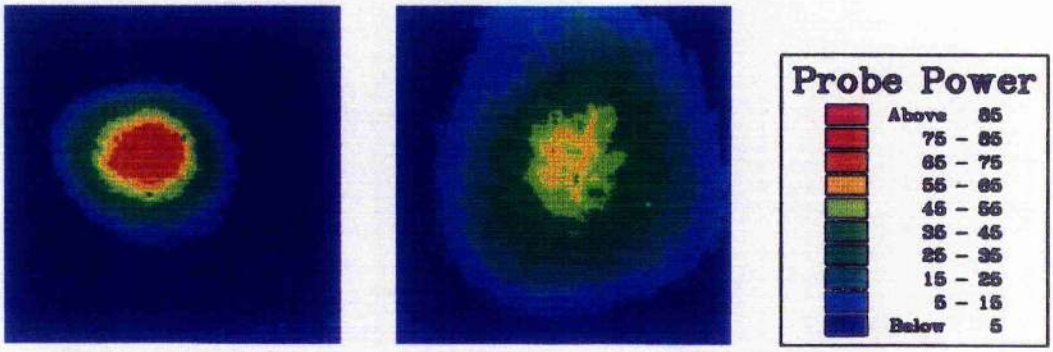

Figure 8.7: Two false colour projections of the probe laser beam as received on the CCD array during the EIT window. The left one shows clear focusing, while the right hand one is defocused relative to the unperturbed waist size.

8.3.1. Explanation of the Lensing Mechanism

The mechanism for this observed lensing is believed to be a form of cross-focusing in nature. The coupling laser beam has a radial intensity profile, assumed to be Gaussian-like in nature. Therefore, at different points across this profile the coupling laser beam will induce different Autler-Townes splitting on the rubidium system, corresponding to the beam intensity at that particular point. This leads to a spatial variation in refractive index, via the different Rabi frequencies, which is then experienced by the probe laser beam. Thus as the probe laser is tuned through the transparency the spatial properties of the beam propagation will be altered and a range of spot sizes is observed on a detector placed after the oven.

In order to predict the properties of the induced lens the refractive index variation with different coupling laser intensities must be estimated. This was done by solving the density matrix equations for a cascade three-level system with the appropriate atomic parameters for the rubidium atom. The upper laser Rabi frequency was taken to be 300MHz at the beam centre, a value close to the experimental one, and, therefore, the Rabi frequency induced at the $1/e^2$ point at the edge of the coupling

laser beam is 120MHz. The real part of the probe laser susceptibility, proportional to the refractive index, constitutes the two curves shown in figure 8.8. The difference

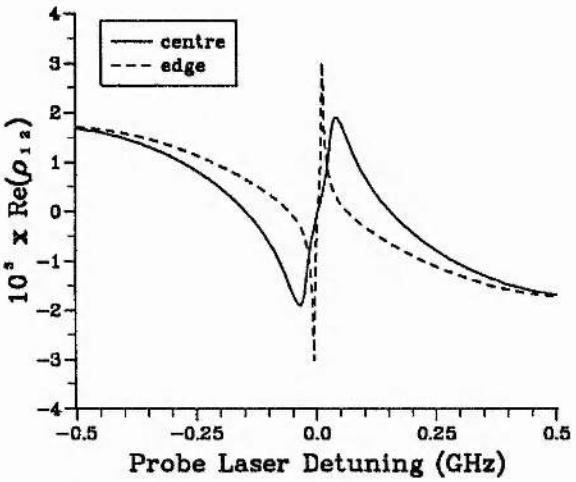

Figure 8.8: The real part of the susceptibility, proportional to the refractive index, experienced by the probe laser for an upper laser Rabi frequency of 300MHz (solid line) and 120MHz (dashed line). (Probe laser Rabi frequency 2MHz, Doppler integrated for a temperature of 40^0C.)

in Autler-Townes splitting is obvious around the centre, as are the areas where the two curves deviate from one another. This graph does not show probe detunings outside of one half a GHz of line centre, as the two curves do not deviate significantly from each other outside this frequency range. Therefore, the induced focusing effect will only occur within this region, which is that immediately surrounding the EIT feature.

To show the changes in the lensing as the probe laser tunes, the two curves in figure 8.8 were subtracted from one another. This curve is shown in figure 8.9, overlaid with the absorption prediction from the imaginary part of the probe laser susceptibility. It is normalised by the maximum deviation of the real part of the susceptibility induced by the centre of the coupling laser beam. Where the curve is positive the refractive index experienced by the probe at the edge of the coupling laser beam is in excess of that experienced at the centre. Therefore, the lens is a

diverging one with a negative focal length. On the other hand, at tunings where the curve becomes negative the probe beam will see a converging lens.

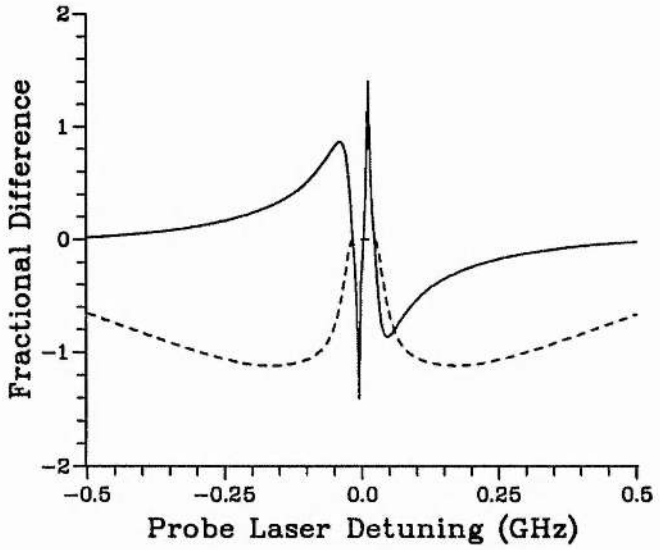

Figure 8.9: The lensing action produced calculated as the difference between the refractive index seen by the probe at the edge of the coupling laser beam and that seen at the centre (from figure 8.7). The curve is normalised to the maximum refractive index deviation from unity seen at the centre of the coupling laser beam. Overlaid is the calculated absorption of the probe for the centre of the laser beams from the imaginary part of the susceptibility (dashed line).

Figure 8.9 shows that there are four distinct lensing regions. As the probe laser is tuned up in frequency through the EIT feature it will initially be defocused, but will become progressively less diverged and subsequently focused as the absorption reduces. Across the point of maximum transparency the probe laser will then defocus again before becoming focused as the transparency drops off again. Thus around the transparency the probe laser sees rapidly changing lensing characteristics controlled by its detuning. Note that the resonance point of maximum transparency is a point of neutral lensing behaviour. Also it is worthwhile noting that during the "flat-top" of maximum transparency, as shown by the dashed line in figure 8.9, the lensing behaviour swings from one extreme to the other. Therefore, the whole range of

lensing can be induced during a non-dissipative region — for both the probe and coupling lasers.

The plot also allows a check that the refractive index variations will be sufficient to produce a lens with a measurable strength. From the plot at the points of maximum lensing action, the refractive index variation between the centre and the edge of the coupling beam is approximately the same as the maximum deviation of the refractive index from unity shown in figure 8.8 (which the figure 8.9 curve is normalised to). Since the cell is essentially opaque outside the EIT window the maximum value of the imaginary part of the linear susceptibility, χ'', is such that:

$$\frac{k\chi''}{2n^2}z > 2$$

This is implied from equation 2.29 for the amplitude attenuation caused by the linear susceptibility. For a general absorption feature the maximum value of the real part of the susceptibility, χ', is half that of the imaginary part [5] so we may say:

$$\Delta kz = \frac{k\chi'}{2n^2}z \geq 1$$

The quantity Δkz is the phase delay caused by the linear susceptibility and since it is greater than 1 we may say that there is a significant phase advantage at the centre or edge, depending which is favoured. Therefore, a reasonable quantity of lensing is expected.

It would be preferable to calculate in detail the lensing action expected in the medium. However, this calculation must take into account several elements and is, therefore, left for further work. Among the points that must be addressed are:

- *The exact beam waist sizes.* Since the beam waists are not matched the probe laser beam does not experience the full available lens induced in the medium. However, as it is 80μm (compared to the 130μm coupling beam) it will experience a reasonable lens. Further work would have to accurately measure the two beam sizes if a quantitative agreement was being sought.

- *The longitudinal coupling laser beam profile.* As the coupling laser is focused into the cell the beam waist varies along the cell length, and thus so will the induced lens. Also as the probe laser is similarly focused a plane wave treatment of this will yield inaccurate results.

- *The induced lens profile.* The lens profile may be expected to be Gaussian, following the coupling laser profile. At the lensing extremes it is thought, indeed, to be this but around the probe frequency points where the lens changes from being converging to diverging (and vice versa, except the central crossover) it is not. Around these areas due to the changing splitting at the various points on the coupling beam radius, the lens may be converging from the centre to some radius and, thereafter, diverging (and vice versa). Thus the lens profile is not straightforward and may lead to unusual, non-Gaussian, outputs.

- *The refractive index in the experiment.* Since the absorption does not return completely to zero in the rubidium experiments, as it does in the model, the refractive index variations cannot be assumed to be identical to the numerical model. A closer approximation must be made, either by including something of the rubidium structure or maybe by including a high γ_{13} dephasing rate to fit the experimental transmission results better.

8.3.2. Experimental Observation of Electromagnetically-Induced Lensing

The lensing action on the probe beam was observed by use of a CCD camera placed 55cm from middle of the cell. The probe beam was split from the coupling laser via a pellicule membrane to avoid distortions from the beamsplitter and imaged directly on to the CCD array without intervening optics (except flat ND filters to reduce the intensity to avoid damaging the array). The images from the camera were recorded onto standard VHS video cassette for later analysis. This allowed the experimental scans to be performed at a rate of 2GHz/min giving around one hundred frames of the EIT feature recorded for later systematic study.

Quantitative results were taken by connecting a PC with a Frame Grabber board to the video player and digitising selected frames. In order to reference the frames back to the probe laser scan, the selected frames were numerically integrated over their whole area to give the probe transmission at that time. The ten frames digitised cover a probe frequency range of about 110MHz, each video frame corresponding to about 1.4MHz tuning.

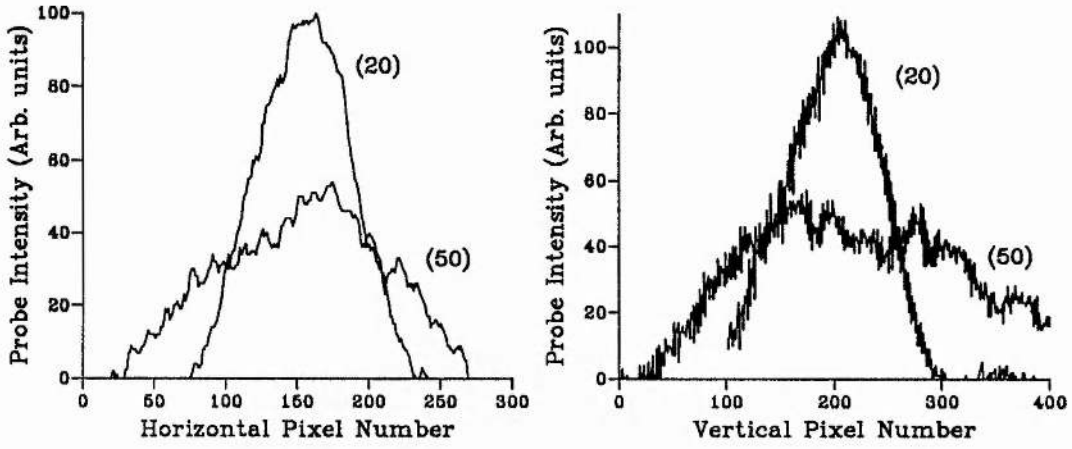

Figure 8.10: Horizontal (left) and vertical (right) cross-sections through two of the frames digitised of the probe laser — frames 20 and 50 — as marked.

Cross sections of two digitised images are shown in figure 8.10. These frames show the maximum difference in probe radius observed, a factor of just over 2. The focused beam, frame 20, has a particularly clean monotonic profile, in common with the other focused spots observed. The diverged spot is less clean, especially in the vertical plane, but does not have strong structure either.

For more quantitative results all the digitised images were analysed for their waist sizes at the $1/e^2$ intensity point. (This assumes a Gaussian profile which was a close approximation except for frames 30 and 40, which showed a double peaked profile in the vertical plane, but which were still Gaussian-like in the horizontal plane.) These waist sizes, with an appropriate error estimate, are presented in figure 8.11 below

the numerically integrated intensity values for each analysed frame.

It should be noted initially that the coupling laser was not exactly on resonance for this set of readings, as evidenced by the somewhat asymmetrical transparency feature in figure 8.11 (a), cf. figure 8.5. However, as the probe laser is tuned the variation in spot sizes is regular, and matched between horizontal and vertical dimensions. Initially focused, although this is not at the start of the transparency window but about a third of the way up it, the probe beam then defocuses before re-focusing with the digitised frame showing maximum transparency (frame 55) being very close to a point of neutral lensing. The defocusing action is measured to be slightly less strong than the focusing action and the induced lens appears to be slightly astigmatic, assumedly mirroring the coupling laser beam profile. However, the lensing effect is clear and these results contain the main thrust of the work in this chapter: that the probe laser undergoes clear lensing action during the transparency. It is interesting that the maximum transparency occurs at a point of neutral lensing, as predicted, but not on the converging-to-diverging crossing, as predicted in figure 8.9, but on the later diverging-to-converging crossing. A possible explanation of this is the detuning of the upper laser, which is slightly to the high frequency side of resonance, evidenced by the shape of the window shown by the integrated intensity points.

8.4. Discussion of EIF

The control of one laser beam by another has been demonstrated previously by Tam and Happer [6]. However, this experiment was concerned with the deflection of the path of one beam by another, non-intersecting, beam and was underpinned by an optical pumping mechanism. This work is fundamentally different as the process is not governed by optical pumping, but rather by coherent effects in a three-level atom, and the main effect is one of lensing rather than beam pointing modification. Furthermore, in the process described by Tam and Happer both beams suffered

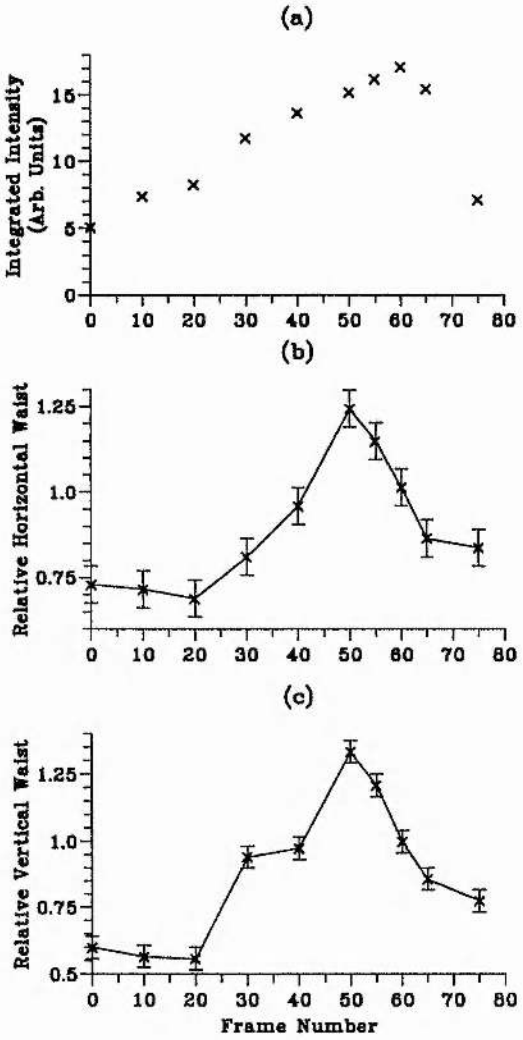

Figure 8.11: For selected images of the probe on the CCD camera during the EIT feature: (a) integrated intensity; (b) horizontal waist and (c) vertical waist sizes. The waist sizes are normalised to the off-resonance probe waist. The frame number is proportional to the upward scan of the probe laser with 1 frame corresponding to about 1.4MHz. (Vapour temperature 68°C, ^{85}Rb, $5S_{1/2}$ (F=3) $\rightarrow$ $5P_{3/2}$ transition.)

significant absorption, which is not the case for beams participating in EIF.

It is important to stress that EIF is not a self-induced effect. The possibility of self-focusing in EIT has been advanced with unusually low thresholds [4] and this would be a self-induced process, catalysed by the coupling laser. EIF however, depends fundamentally on the spatial properties of the coupling laser and in no way on the probe laser power. It will occur for arbitrarily small probe laser powers as long as the probe beam interacts with a significant proportion of the changing coupling laser radial beam profile. Furthermore, while self-focusing effects rely on some absorption of the probe laser (to saturate the refractive index) to promote the mechanism, EIF is conceptually non-dissipative on both probe and coupling lasers. A future experimental priority is to demonstrate the focusing mechanism with negligible probe absorption as predicted in the numerical work above. If this is successful there is the possibility of beam trapping on the probe, in a similar manner to self-trapped filaments [3], under circumstances where the probe should propagate without absorption or diffraction.

8.4.1. Implications and Applications

Electromagnetically-induced focusing, as described above, has important implications for experimental and device design in the areas of EIT, inversionless lasing, phasonium and the enhancement of nonlinear processes by EIT. All of these consider the use of a coupling laser and Autler-Townes splitting to some extent or another. The only exception are some inversionless lasing concepts where the coherent dressing is done prior to injection within the lasing cavity, eg. the degenerate quantum beat laser [7]. The optical design of affected experiments must take into account the EIF effect in the dressed medium and design the mode-matching of the probe and coupling laser beams with this in mind. It may be that EIF in inversionless lasers becomes the analogue of thermal lensing in contemporary solid-state laser sources.

The phasonium concept [8] is particularly susceptible to EIF. At the point of

maximum refractive index, and minimum absorption, the EIF lens is likely to be about its strongest. There is scope for theoretical and experimental work to discern which, if any, of the various atomic schemes for phasonium generation is least vulnerable to EIF.

There are, however, two ways to avoid, or minimise the effects of EIF if they are not desired. Firstly, the coupling laser radial profile can be made as invariant as possible, possibly by creating a beam profile of the "top-hat" kind often associated with excimer laser outputs. Secondly, the probe beam can be confined to a small area relative to the overall coupling laser profile. If the area is small enough there will not be a significant refractive index modulation within it as the coupling laser intensity will be essentially constant over the area.

It is interesting to speculate on applications for the lensing in its own right. Since the control of lensing is exerted by one laser on the other, some control signal on the coupling laser can be converted to the probe laser. Modulation of the coupling laser, in intensity or frequency, will give a rapidly varying lens on the probe laser and if aligned to give beam deflections, a switching application may be envisaged. The shortest time scale for such processes are likely to be on the order of the atomic decay rates, probably tens of nanoseconds. Where a smoothly varying lensing action is required on one beam, EIF can deliver that by smooth scanning of either beam frequency. Other speculations could include the effect of different coupling laser modes, eg. doughnut modes etc, and their lensing, or possibly guiding, properties. In ideal EIT conditions all of these applications would be essentially non-absorbtive on either beam. Whatever the application or implication, EIF is an intrinsic property of EIT and is likely to receive further attention in many forthcoming works in this area of atomic coherence processes in vapours.

REFERENCES

[1] Yong Qing Li, Shaozheng Jin, and Min Xiao, in *International Conference on Quantum Electronics Technical Digest* (Optical Society of America, Washington DC, 1994), Vol. 10.

[2] Walter F. Buell and Manfred Fink, in *Quantum Electronics and Laser Science Conference Technical Digest* (Optical Society of America, Washington DC, 1993), Vol. 3.

[3] J. E. Bjorkholm and A. Ashkin, cw self-focusing and self-trapping of light in sodium vapour *Phys Rev Lett* **32**, 129 (1974).

[4] B. Matisov and L. Windholz, to be presented at EQEC'94 as QTuG37 (unpublished).

[5] R. Loudon, *The Quantum Theory of Light, Oxford Science Publications*, 2 ed. (Oxford University Press, Oxford, 1991).

[6] A. C. Tam and W. Happer, Long-rage interactions between cw self-focused laser bemas in an atomic vapour *Phys Rev Lett* **38**, 278 (1977).

[7] M. O. Scully, S.-Y. Zhu, and A. Gavrielides, Degenerate quantum-beat laser : Lasing without inversion and inversion without lasing *Phys Rev Lett* **62**, 2813 (1989).

[8] M. Fleischhauer, C. H. Keitel, M. O. Scully, Chang Su, T. Ulrich, and Shi-Yao Zhu, Resonantly enhanced refractive index without absorption via atomic coherence *Phys Rev A* **46**, 1468 (1992).

Chapter 9

Conclusions

9. Conclusions

Set in the context of the current widespread interest in quantum interference and nonlinear optics, this work provides a significant contribution in the worldwide research effort. While various individual conclusions were drawn within the preceding chapters at appropriate points, a collected summary of these is presented here in conclusion.

Numerical models of the density matrix equations for three and four level atomic systems were implemented and used both to predict, and explain, coherent excitation effects, with the emphasis on the manifestation of quantum interference. Steady-state conditions were assumed throughout, in keeping with the use of the continuous-wave lasers that were employed in the experimental tests of these predictions. Inhomogeneous Doppler broadening was added to the systems, as appropriate, and the calculations proved efficient and accurate. Empirical rules for the generation of the main system matrix of the simultaneous equations for the density matrix were discerned for near-arbitrary level numbers and field linkages.

An experimental study of near-resonant, magnetic-field-induced sum frequency mixing on the 3S–3P–3D system of levels in sodium vapour was undertaken to take advantage of the particularly strong transition matrix elements between these levels. Continuous-wave lasers were used for this, and throughout the work presented in this thesis, in order to have high spectroscopic resolution and to avoid temporal effects. Conversion efficiencies implying a nonlinearity of around 0.5pmV^{-1} were observed, on a par with some nonlinear crystals but not as high as had been predicted

by Poustie [1]. The high parasitic absorption on the 3S–3P transition limited the conversion efficiency and tunability was low. Therefore, the main application for such wave mixing is in fundamental studies of laser-atom interactions and in the generation of deep UV and VUV light where no convenient laser source exists and conventional nonlinear crystals are absorbtive.

This system, however, did allow a detailed exploration of the phase matching properties of the parametric process. Focal strength and position were varied and the results matched predictions in a qualitative manner. An unexpected effect, that of a radial phase mismatching variation, was observed and isolated as the principle cause of deviations between theory and experiment. A second atomic level scheme, that of 3S–3P–4P was studied in contrast to the other route. The placing of the quadrupole-allowed transition changed between the two routes and in the latter there were two major sources of refractive index from atomic resonance lines, one of which changed rapidly across the line profile. In combination with the other, static, contribution various distortions on the lineshapes were observed and explained, including the dominance of one Zeeman component over the other.

This research was then extended to doubly-resonant sum frequency mixing. Two main excitation paths for the output coherence were identified and the parameters for their relative control were isolated. These were: the detuning from the intermediate level (also the control parameter for the two paths for population excitation); and the relative input field strengths (which did not affect the population excitation routes). Interference between the two excitation pathways was predicted with cancellation of the sum frequency output possible at various field strength and detuning parameters. Experimental studies on the $3S_{1/2}$–$3P_{1/2}$–$3D_{3/2}$ level scheme in sodium led to the observation of the two routes, their relative control and interference as predicted. A cancellation of 94% in the output due to this interference was observed. A Raman process at the same output frequency was separated from the SFM signal and provided a useful monitor of the population excitation routes along with the fluorescence from the uppermost level.

The theory for doubly-resonant SFM was extended into the strong field NLO regime with the consideration of the effects of EIT produced by a strong upper laser in the sum frequency mixing process. The theoretical treatment showed that an interference in absorption pathways could significantly reduce the fundamental wave absorption on the lower input transition, while the sum frequency process retained a useful conversion efficiency. An increase in the $\mathcal{N}L$ product of the vapour, allied with the reduction in parasitic absorption, could combine to give a predicted enhancement in the wave mixing process of 3–4 orders of magnitude. Possibilities for the observation of this enhancement were discussed.

A further theoretical extension concerned the high particle density regime, with the inclusion of the local-field correction into the density matrix equations for a three-level atom. This generalisation of the equations led to two new sets of terms, one the dynamic Lorentz shift (present in the generalised two-level atom equations) and the other set, nonlinear coherence cross-couplings. Two case studies were presented: EIT at moderate densities and SFM at very high densities.

Finally, an experimental study of EIT in rubidium vapour was conducted using two cw Ti:sapphire laser sources. A counter-propagating experimental geometry minimised the power requirements for the coupling laser source and a reduction of up to 70% in the resonance absorption was realised. Focusing and de-focusing of the probe laser beam was observed as it was tuned through the transparency window and the mechanism for this was traced to the radial beam profile of the coupling laser. This effect that we name "electromagnetically-induced focusing", is believed to be a novel and significant observation, of importance in the field of EIT, phasonium and inversionless lasing. Specific applications for this continuously variable lens, controlled by one laser and experienced by another without associated absorption on either beam, may also arise.

9.1. Suggestions for Further Work

Once again, suggestions for relevant further work were indicated in earlier chapters. However, a collected summary of them is presented below.

With the observation of hysteresis in the mode-hopping behaviour of the ring Ti:sapphire laser, further work could be conducted on this and the mechanisms behind the bistability. Possibly a simpler cavity could be adopted easing conceptual difficulties in the theoretical treatment.

Within the SFM experiments, further work could be conducted in two main areas. Firstly, the radial effect observed in the phase matching behaviour could be studied and the causes illuminated. This may require careful control of the vapour conditions and laser beam quality to ensure that these were not the root causes. Secondly, the resonant SFM experiments could be repeated using a clean three-level atomic system. This would suggest an atom without nuclear spin so that hyperfine structure could be avoided and would allow a quantitative comparison of theory and experiment, that was not possible in sodium due to the many complicating sub-levels.

Both of the theoretical chapters (6 and 7) invite experimental demonstration of their predictions. The use of EIT to enhance SFM processes requires a powerful coupling laser source and is perhaps not appropriate to cw lasers. However, Q-switched or amplified single-frequency lasers should have ample power and sufficient coherence to provide the appropriate coupling radiation. The study of the local-field effect on EIT, however, could be conducted in any experiment within which a high level of transparency is achieved. If a tighter focusing geometry is adopted in rubidium and the transparency level significantly extended then a study at higher temperatures may be possible. Returning to theoretical work, the generalised equations themselves require further analysis of the effects of the new terms and further high density optical phenomena, such as the enhancement of inversionless lasing already predicted [2], may be predicted.

Perhaps it is within the EIT experiments that the prospects of further work are most fertile. Due to the lack of experiments in this area there are many theoretical predictions yet to be tested and many experimental schemes to be studied. Some possible ideas for further study are listed below:

- A three-level scheme without hyperfine structure could be probed by cw radiation. This would provide a high-resolution test of the theoretical curves. An atom without nuclear spin and with transitions amenable to the chosen laser sources (and available powers) must be identified.

- Experiments in an atomic beam could allow a high-resolution test of the theoretical predictions. Pure three-level atom systems can be probed via circular polarisation and the power requirements on the lasers are much reduced. However, high stability specifications are imposed on these lasers.

- Other level schemes in rubidium can be probed with the available laser sources. These are shown in figure 9.1 and would allow a study of all three of the cascade, lambda and vee configurations. To retain the cancellation of Doppler broadening attained via a counter-propagating scheme in the cascade atom, the lambda and vee schemes must be probed in a *co-propagating* manner.

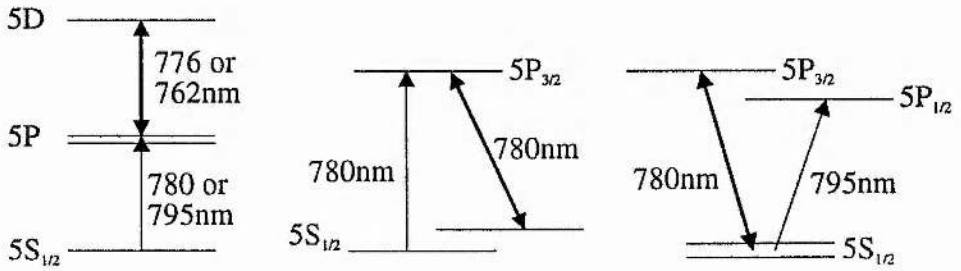

Figure 9.1: Three schemes for EIT in rubidium using the two Ti:sapphire laser sources.

- Using a Mach-Zender interferometer arrangement the refractive index changes

associated with EIT could be measured. This could allow a proof-of-principle experiment on the magnetometer application proposed [3] for such a scheme.

- The addition of incoherent pumping, via a discharge or radio frequency coils, to an EIT experiment could allow the observation of inversionless gain, under appropriate atomic parameters [4].

- Electromagnetically-induced focusing deserves further study both theoretically and experimentally. A detailed theoretical treatment, capable of quantitative predictions, should be derived and tested against experimental evidence. This may predict novel lensing effects due to the lens profiles in the media. An interesting experimental proposal is the idea of using non-Gaussian coupling laser modes, eg. doughnut modes, to possibly give stable trapping of the probe beam. The observation of a stable filament of trapped probe light, free from absorption would be of significance.

REFERENCES

[1] Alistair J. Poustie, *Magnetic Field Induced Sum Frequency Mixing in Sodium Vapour*, PhD thesis, University of St. Andrews, 1990.

[2] Jonathan P. Dowling and Charles M. Bowden, Near dipole-dipole effects in lasing without inversion: An enhancement of gain and absorptionless index of refraction *Phys Rev Lett* **70**, 1421 (1993).

[3] Marlan O. Scully and Michael Fleischhauer, High-sensitivity magnetometer based on index-enhanced media *Phys Rev Lett* **69**, 1360 (1992).

[4] A. Imamoğlu, J. E. Field, and S. E. Harris, Lasers without inversion : A closed lifetime broadened system *Phys Rev Lett* **66**, 1154 (1991).

Appendix A

Rules for N Level Density Matrix Models

A. Rules for N Level Density Matrix Models

A.1. Introduction

This appendix contains a set of rules and general guidance on how to construct the n^2-1 real simultaneous equations to describe the steady-state of an arbitrary n level atom subjected to a number of coherent electromagnetic fields (maximum $n-1$) using the rotating wave approximation under the density matrix formalism. They have been empirically derived following the derivation and definitions in Chapter 2. Specifically, the system and solution matrix are created here and may then be incorporated in a numerical solution algorithm to probe the systems response.

The rules expounded herein are fairly general but should only be used along with a working knowledge of the derivation that they are short-cutting. They are very useful in speeding the process of implementing a model on a new atomic system but care should be taken that they are not applied without reference to the physical system so that conceptual anomalies are not introduced. If in doubt, check by the full derivation. Several assumptions are implicit in this Appendix, of which the strongest governs the number and location of the incident fields. The fields are considered sufficiently different in frequency so that only one may interact strongly with any transition. (However, one field may interact with more than one transition, as long as another one does not impinge on either transition.) Furthermore, the matrix elements and Rabi frequencies are assumed real which is valid as long as a

maximum of $n-1$ fields impinge on the n level atom. This also removes the need for considering phase matching. Neither of these restrictions rule out the majority of systems that are likely to be considered and the rules could be extended by further work to remove them.

A.2. Notation

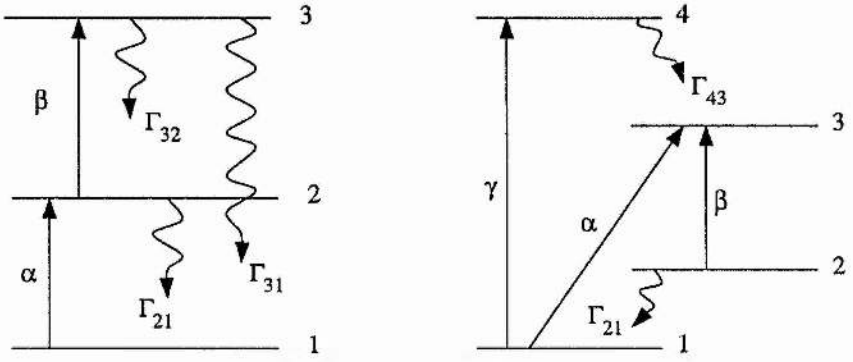

Figure A.1: Two sample atomic systems. On the left a cascade three-level system and on the right a 4 level one corresponding loosely to the laser scheme for Nd:YAG.

Throughout this appendix reference will be made to the two model examples, as shown in figure A.1. The four-level one would require the derivation longhand of 16 equations and demonstrates the power of this technique. The atomic levels are always numbered in the order of energy, from the lowest to the highest. If the order is broken the convention used to define the signs of some elements will be inaccurate.

In order to create the system an altered hamiltonian matrix, J, will be defined to formalise the optical field connections. J is defined as an $n \times n$ matrix where the diagonal elements are zero and the off-diagonal elements the half Rabi frequency of the optical field connecting the corresponding levels, ie.:

$$J_{ij} = \begin{cases} 0 & i = j \\ \frac{\mu_{ij} E^0_{ij}}{2\hbar} & i \neq j \end{cases} \tag{A.1}$$

The field connecting levels i and j has been defined as:

$$E_{ij}(z,t) = \frac{E_{ij}^0}{2}(\exp(i[\omega t - kz]) + \text{c.c.}) \tag{A.2}$$

and the dipole matrix element controlling the strength of interaction is μ_{ij}. Hence for the three-level system J would be:

$$J = \begin{bmatrix} 0 & \alpha & 0 \\ \alpha & 0 & \beta \\ 0 & \beta & 0 \end{bmatrix} \tag{A.3}$$

where α and β are the respective half Rabi frequencies. (The four-level system also has third field with half Rabi frequency γ, not to be confused with the coherence decay rates γ_{ij}.)

A.3. Matrix Equation Construction

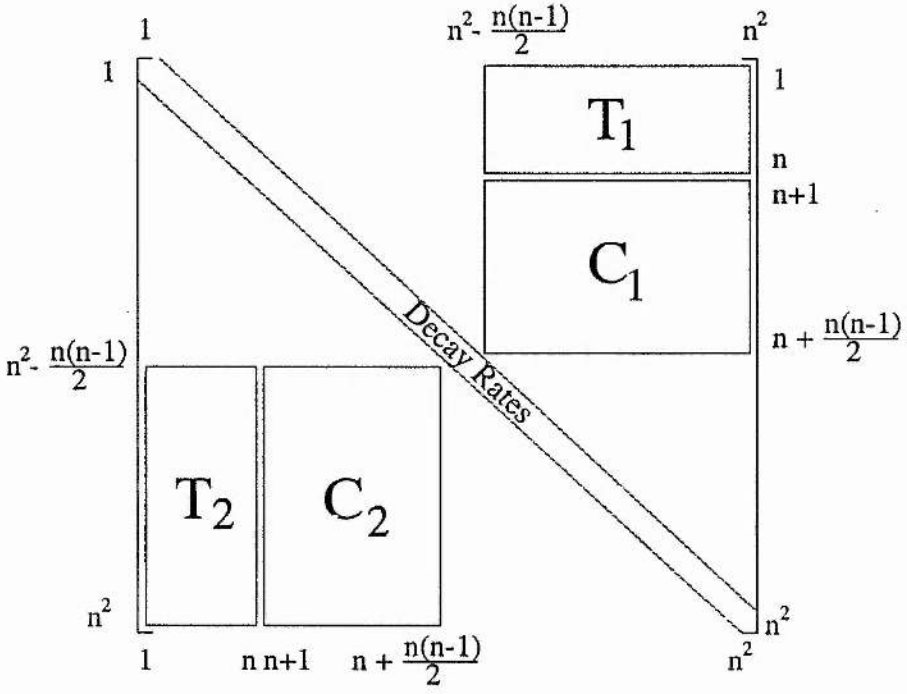

Figure A.2: The subdivisions of A used in creating the system.

The full system, in steady-state, is described by n^2 real simultaneous equations. In matrix form:

$$Ax = b \tag{A.4}$$

where

$$\begin{aligned} A &= \text{system matrix} \\ b &= \text{equation right hand sides} \\ x &= \text{density matrix elements} \end{aligned}$$

The convention for ordering of the density matrix elements I shall use is:

$$\left.\begin{array}{l} \rho_{11} \\ \rho_{22} \\ \vdots \\ \rho_{nn} \end{array}\right\} \text{Occupation Probabilities}$$

$$\left.\begin{array}{l} \rho^r_{12} \\ \rho^r_{13} \\ \vdots \\ \rho^r_{1n} \\ \rho^r_{23} \\ \vdots \\ \rho^r_{(n-1)n} \end{array}\right\} \text{Real Part of Coherences}$$

$$\left.\begin{array}{l} \rho^i_{12} \\ \rho^i_{13} \\ \vdots \\ \rho^i_{1n} \\ \rho^i_{23} \\ \vdots \\ \rho^i_{(n-1)n} \end{array}\right\} \text{Imaginary Part of Coherences}$$

When the equations are written in the order dictated by this convention the matrix A of the coefficients displays a certain symmetry and allows for partitioning

into three submatrices. The position of these subsets is defined in figure A.2. *Any element falling outside these parts is zero.*

The first part is the diagonal elements, A_{ii}. They contain decay rates for the populations and coherences. Next are the two rectangular matrices T_1 and T_2. They are related as follows:

$$T_1 = -2T_2^T \tag{A.5}$$

and deal with the transfer of population (where the superscript T denotes transpose). The C matrices are square, of size $n(n-1)/2$, deal with coherence creation and feedback and related by:

$$C_1 = -C_2^T \tag{A.6}$$

The writing down of each of these shall be now explained in the following subsections.

A.3.1. A_{ii}, the Decay Rates

For the open atomic system where the atomic levels decay to unspecified locations at rates Γ_{ii} this system is particularly simple (see [1]). On row i goes the decay rate for that level/coherence. Due to conventions used later and to ensure continuity these are *positive* quantities. For a 3x3 open system we obtain:

$$\begin{bmatrix}
\Gamma_{11} & & & & & & & & \\
 & \Gamma_{22} & & & & & & & \\
 & & \Gamma_{33} & & & & & & \\
 & & & \gamma_{12} & & & & & \\
 & & & & \gamma_{13} & & & & \\
 & & & & & \gamma_{23} & & & \\
 & & & & & & \gamma_{12} & & \\
 & & & & & & & \gamma_{13} & \\
 & & & & & & & & \gamma_{23}
\end{bmatrix}$$

where Γ_{ii} is the population decay rate and γ_{ij} the coherence decay rate. This is usually approximated by:

$$\gamma_{ij} = \frac{\Gamma_{ii}}{2} + \frac{\Gamma_{jj}}{2} + \text{deph}_{ij} \tag{A.7}$$

with deph_{ij} being the dephasing rate on the i-j transition eg. by collisions.

If, instead, the system is a closed one with level-to-level decay rates being known then these are simple put in the first N rows connecting the relevant population terms, remembering decays are positive under this convention. For example, the three-level system would be:

$$\begin{vmatrix} 0 & -\Gamma_{21} & -\Gamma_{31} & 0 \\ 0 & \Gamma_{21} & -\Gamma_{32} & 0 \\ 0 & 0 & \Gamma_{31}+\Gamma_{32} & 0 \\ 0 & 0 & 0 & \gamma_{12} \\ & & & \ddots \end{vmatrix}$$

It is quite straightforward to construct this by reference to the Liouville equation for each element.

A.3.2. T, the Transfer Matrices

The matrices T_1 and T_2 govern the transfer of population between the levels. Construction for T_1 will be given in detail below.

T_1 is a $(n(n-1)/2) \times n$ matrix. Number the horizontal and vertical axes by the population or coherence, respectively, that the row/column refers to, ie. the density matrix component ρ_{ij} that the element is the coefficient for in the multiplication Ax. For the four-level system this is:

$$\begin{array}{c} 11 \\ 22 \\ 33 \\ 44 \end{array} \begin{bmatrix} & & & & & \\ & & & T_1 & & \\ & & & & & \end{bmatrix}$$

$$\begin{array}{cccccc} 12 & 13 & 14 & 23 & 24 & 34 \end{array}$$

The individual elements can then be filled in. If levels 1 and 3 are connected by the field with Rabi frequency α then -2α would go in the 11 row and 2α in the 33 row, both in the 13 column. More generally for column ij the element in row ii is $-2J_{ij}$ and row jj is $2J_{ij}$, the others being zero. Thus for the four-level system the T_1 matrix is:

$$\begin{array}{c} \\ 11 \\ 22 \\ 33 \\ 44 \end{array} \begin{bmatrix} 0 & -2\alpha & -2\gamma & 0 & 0 & 0 \\ 0 & 0 & 0 & -2\beta & 0 & 0 \\ 0 & 2\alpha & 0 & 2\beta & 0 & 0 \\ 0 & 0 & 2\gamma & 0 & 0 & 0 \end{bmatrix} \\ \begin{array}{cccccc} 12 & 13 & 14 & 23 & 24 & 34 \end{array}$$

The signs that have been used were decided by the convention adopted with the decay rates. Once this is done T_2 follows by equation A.5.

A.3.3. C, the Coherence Matrices

The C matrices are square, of dimension $n(n-1)/2$, and are related by equation A.6. They split into two for composition, the diagonal — containing the detunings — and the off-diagonals, for the coherence creating fields. To ease the task of writing in the elements it is convenient to label the rows and columns with the coherence that it relates to, in the same way that the horizontal elements were labelled for T_1 above. More formally:

row/column	connected levels, $\|i_1>$ and $\|i_2>$
1	1,2
2	1,3
⋮	⋮
$N-1$	1,N
N	2,3
$N+1$	2,4
⋮	⋮
$\frac{N(N-1)}{2}$	$N-1$,N

The following rules refer to C_2 and once this is laid out C_1 follows by equation A.6. First, the leading diagonal which contains the detuning terms. If there is a field $E_{i_1 i_2}$, connecting levels $|i_1>$ and $|i_2>$ with a frequency $\omega_{i_1 i_2}$ then the detuning for the element on the diagonal in row labelled $i_1 i_2$ is $\Delta_{i_1 i_2}$ where:

$$\Delta_{i_1 i_2} = \omega_{i_1 i_2} - \omega^0_{i_1 i_2} \tag{A.8}$$

and $\omega^0_{i_1 i_2}$ is the energy gap between levels $|i_1>$ and $|i_2>$. If there is no field directly connecting the two levels then a sum of fields is used. For example, between levels $|2>$ and $|4>$ in the four-level scheme the detuning term is $\Delta_{24} = \Delta_{14} + \Delta_{23} - \Delta_{13}$. One way to think of this is as trying to make the energy gap ω^0_{24} using ω^0_{13}, ω^0_{23}, ω^0_{14} as there are fields bridging these gaps. Thus the additions and subtractions are defined. Therefore, for the four-level system:

$$\begin{array}{c} \\ 12 \\ 13 \\ 14 \\ 23 \\ 24 \\ 34 \end{array} \begin{bmatrix} \Delta_{13} - \Delta_{23} & & & & & \\ & \Delta_{13} & & & & \\ & & \Delta_{14} & & & \\ & & & \Delta_{23} & & \\ & & & & \Delta_{14} + \Delta_{23} - \Delta_{13} & \\ & & & & & \Delta_{14} - \Delta_{13} \end{bmatrix}$$

(Note that the horizontal axis is numbered in the same way as the vertical axis for the C matrices.)

The off-diagonal element i, j contains the Rabi frequency connecting the coherences referred to by that element, if they exist. If element i, j refers to coherence $i_1 i_2$ on the vertical side and $j_1 j_2$ on the horizontal side then:

If $i_1 = j_1$ element i,j contains $J_{i_2 j_2}$

$i_2 = j_2$ $\quad -J_{i_1 j_1}$

$i_1 = j_2$ $\quad J_{i_2 j_1}$

$i_2 = j_1$ $\quad -J_{i_1 j_2}$

otherwise element i,j contains zero.

where J_{km} is defined as above. Hence, for the four-level system C_2 is:

$$\begin{bmatrix} \Delta_{13} - \Delta_{23} & \beta & 0 & -\alpha & \gamma & 0 \\ \beta & \Delta_{13} & 0 & 0 & 0 & -\gamma \\ 0 & 0 & \Delta_{14} & 0 & 0 & -\alpha \\ \alpha & 0 & 0 & \Delta_{23} & 0 & 0 \\ \gamma & 0 & 0 & 0 & \Delta_{14} + \Delta_{23} - \Delta_{13} & -\beta \\ 0 & \gamma & -\alpha & 0 & -\beta & \Delta_{14} - \Delta_{13} \end{bmatrix}$$

A.3.4. b, the Solution Vector

The solution vector b is straightforward, containing all zeros initially, unless Γ_{ii} general level decays are in use. In which case $b_i = \Gamma_{ii}\rho_{ii}^0$ where ρ_{ii}^0 is the thermal equilibrium population of level i. If spontaneous decay chains Γ_{ij} are used to move population in a cascade manner then there is no need for the specific equilibrium populations to be included.

A.4. General Notes

- Remember each row is an equation!
- While it is an n^2 system matrix created above, using conservation of population as embodied in the trace normalisation of the density matrix, $\rho_{11} + \rho_{22} +$

$\ldots \rho_{nn} = 1$, one degree of freedom is removed. Hence only $n-1$ of the n populations are independent and so row 1 can be removed. Column 1 is also removed using the substitution $\rho_{11} = 1 - \sum_{i=2}^{i=n} \rho_{ii}$ (which will add elements to the solution vector b, as well as altering terms in the first few columns of A). This leads to a $n^2 - 1$ system with savings in computer time as the time taken to solve the matrix will be an operation of the order of the matrix size of A squared.

- The Doppler shift can be included in the detunings by changing the field frequency ω_{ij} to its Doppler shifted value $\omega_{ij} - k_{ij}V_z$ where k_{ij} is the wavevector of the field and V_z the atomic speed. Thus numerical integrations over the Maxwellian velocity distribution can be performed using the algorithm in Chapter 2.

- If may seem at first sight that the decays of Γ_{ii} and the movements of T_1 contradict each other. eg. that the decay out of level 2 is positive and the 2α term which brings in population by excitation. However, if ρ_{ij}^{i} is an absorption it is negative, so both terms will be in anti-sense when multiplied by their appropriate density matrix element and the movements are indeed physical.

- If no chain of fields connects two levels the C_2 diagonal element is merely $-\omega_{ij}^{0}$. This is normally only used for the case of two hyperfine split levels where the coherence oscillations are much lower in frequency than optical oscillations.

- If three or more fields combine in the atom to give a parametric interaction phase mismatches should be introduced (giving rise to $\cos \Delta kz$ and $\sin \Delta kz$ terms) and complex Rabi frequencies are necessary. The whole system is more complex and these rules must be extended to deal with the system.

- Always keep in mind where the element is coming from. Derive a row from the Liouville equation if there is an uncertainty about an element within it!

REFERENCES

[1] Alistair J. Poustie, *Magnetic Field Induced Sum Frequency Mixing in Sodium Vapour*, PhD thesis, University of St. Andrews, 1990.

Appendix B

Publications and Presentations

B. Publications and Presentations

B.1. Publications

The following publications have been published, or have been submitted, concerning the work described in this thesis. They are listed in chronological order.

Enhanced conversion efficiency in three-wave mixing via electromagnetically reduced fundamental wave absorption

Richard R. Moseley, Bruce D. Sinclair and Malcolm H. Dunn

Optics Communications **101** 139–143 (1993)

Effects of different phase-matching conditions in sum-frequency-mixing systems in vapors

Sara Shepherd, Richard R. Moseley, Bruce D. Sinclair and Malcolm H. Dunn

Physical Review A **49** 3002–3010 (1994)

Local field effect in the three-level atom

Richard R. Moseley, Bruce D. Sinclair and Malcolm H. Dunn

Optics Communications **108** 247–252 (1994)

Interference between excitation routes in resonant sum frequency mixing
Richard R. Moseley, Sara Shepherd, David J. Fulton, Bruce D. Sinclair and Malcolm H. Dunn
In press, Physical Review A (1994)

Spatial consequences of electromagnetically-induced transparency: Observation of electromagnetically-induced focusing
Richard R. Moseley, Sara Shepherd, David J. Fulton, Bruce D. Sinclair and Malcolm H. Dunn
In press, Physical Review Letters (1994)

B.2. Conference Presentations

High-resolution investigation of contrasting routes for sum-frequency mixing in sodium vapor
Richard R. Moseley, Sara Shepherd, Bruce D. Sinclair and Malcolm H. Dunn
in Quantum Electronics and Laser Science Conference (QELS), Technical Digest Series Vol. 12, paper QFE4 (Optical Society of America, Washington DC, 1993).

Contrasting routes for sum frequency mixing in sodium vapour
Richard R. Moseley, Sara Shepherd, Bruce D. Sinclair and Malcolm H. Dunn
Poster 93 in Eleventh UK National Quantum Electronics Conference (QE–11), Belfast 1993.

Electromagnetically reduced fundamental wave absorption in three wave mixing
Richard R. Moseley, Bruce D. Sinclair and Malcolm H. Dunn
Poster 141.1 in Eleventh UK National Quantum Electronics Conference (QE–11), Belfast 1993.

Possibilities of electromagnetically-induced transparency using continuous-wave lasers
Richard R. Moseley, Sara Shepherd, David J. Fulton, Bruce D. Sinclair
and Malcolm H. Dunn
in Strong Field NLO, half-day meeting of the Quantum Electronics Group of the Institute of Physics, (Imperial College, London) June 1994.

Interference between excitation pathways in resonant sum frequency mixing in vapours
Richard R. Moseley, Sara Shepherd, David J. Fulton, Bruce D. Sinclair
and Malcolm H. Dunn
in 5th European Quantum Electronics Conference (EQEC), Technical Digest, paper QMH2 (IEEE, Piscataway, 1994).

Spatial Consequences of Electromagnetically-Induced Transparency: Observation of Electromagnetically-Induced Focusing
Richard R. Moseley, Sara Shepherd, David J. Fulton, Bruce D. Sinclair
and Malcolm H. Dunn
in 5th European Quantum Electronics Conference (EQEC), Postdeadline Paper EPD1 (IEEE, Piscataway, 1994).